Argonne
NATIONAL LABORATORY
Advanced Photon Source Upgrade

Advanced Photon Source Upgrade Project

Preliminary Design Report

September 2017

Chapter 6: Experimental Facilities

Document Number : APSU-2.01-RPT-002
ICMS Content ID : APSU_1705610

Table of Contents

List of Figures

List of Tables

Acronyms and Abbreviations

2D	Two Dimensional
3D	Three Dimensional
ADR	Accelerator Detector Research
ALARA	As Low As Reasonably Achievable
ALD	Atomic Layer Deposition
AML	Activated Materials Laboratory
APS	Advanced Photon Source
APS-U	Advanced Photon Source Upgrade
Argonne	Argonne National Laboratory
ASD	(ANL) Accelerator Systems Division
BDA	Beam Defining Aperture
BCDI	Bragg Coherent Diffraction Imaging
BES	Office of Basic Energy Sciences
BESAC	Basic Energy Science Advisory Committee
BSC	Beam Conditioning System
CD-n	DOE Critical Decision (n = 0, 1, 2, 3, 4)
CDI	Coherent Diffractive Imaging
CHEX	Coherent High-Energy X-ray
CIGS	Cu(In, Ga)Se2
CMR	Colossal Magnetoresistance
CNM	Center for Nanoscale Materials
COR	Center of Rotation
CRL	Compound Refractive Lens
CSE	Chemical Sciences and Engineering Division
CSSI	Coherent Surface Scattering Imaging
CVD	Chemical Vapor Deposition
DBA	Diffracted-Beam Aperture
DCM	Double Crystal Monochromator

DMM	Double Multilayer Monochromator
DOE	U.S. Department of Energy
DWBA	Distorted Wave Born Approximation
EBSD	Electron Backscatter Diffraction
EDD	Energy Dispersive Detectors
EE	Experimental Enclosure
ER	Error Reduction
ES	Experimental Station
ESAC	Experimental System Advisory Committee
FE	Front End
ff-HEDM	far-field high-energy x-ray diffraction microscopy
FFT	Fast Fourier Transform
FOE	First Optics Enclosure
FPGA	Field Programmable Gate Array
FWHM	Full Width Half Maximum
GA	Generic Algorithm
GB	Gigabyte (10^9 bytes)
GISAXS	Grazing-Incidence Small-Angle X-ray Scattering
GIXPCS	Grazing-Incidence X-ray Photon Correlation Spectroscopy
GUI	Graphical User Interface
H	Horizontal
H-BDA	Horizontally Beam Defining Aperture
HE	High Energy
HEDM	high-energy x-ray diffraction microscopy (prefixes nf-, ff-, and vff- denote near-field, far-field, and very-far-field technique variants)
HERIX	High Energy Resolution Inelastic X-ray Spectrometer
HEXM	High-Energy X-Ray Microscope beamline
HGVPU	Horizontal Gap Vertically Polarized Undulator
HHL	High Heat Load

HIO	Hybrid Input-Output
HV	High Vacuum
ID	Insertion Device
ISF	Intermediate Scattering Function
ISN	*In Situ* Nanoprobe
KB	Kirkpatrick-Baez
KL	Kinoform Lens
LDRD	Laboratory-Directed Research and Development
LLD	Lower Level Discrimination
LN2	Liquid Nitrogen
μ-CT	computed micro-tomography
MBA	Multi-Bend Achromat
MBE	Molecular Beam Epitaxy
MDI	Materials Discovery Institute
MH	Mini Hutch
MLL	Multilayer-Laue-Lens
MM-PAD	Mixed-Mode Pixel Array Detector
NA	Numerical Aperture
nf-HEDM	near-field high-energy x-ray diffraction microscopy
NFO	Nanofocusing Optic
NMPZ	Non-Minimum Phase Zero
NNSA	National Nuclear Safety Administration
NSLS-II	National Synchrotron Light Source II
NSUF	Nuclear Science User Facilities
PAD	Pixel Array Detector
PCS	Photon Correlation Spectroscopy
ph	photon
PLD	Pulsed Laser Deposition
R&D	Research and Development

RIXS	Resonant Inelastic X-ray Scattering
rms	Root Mean Square
RSS	Radiation Safety System
SAC	Scientific Advisory Committee
SA-XPCS	Small-Angle X-ray Photon Correlation Spectroscopy
SAXS	Small-Angle X-ray Scattering
SC	Superconducting
SCU	Superconducting Undulator
SCAPE	Superconducting Arbitrarily Polarized Emitter
SCM	Single-Crystal Monochromator
SEM	Scanning Electron Microscope
SF	Spatial Filter
SME	Subject Matter Experts
SMS	Sample Manipulation System
SNR	Signal-to-Noise Ratio
SOE	Second Optics Enclosure
SR	Storage Ring
SSA	Secondary Source Aperture
ST	Scattering Tomography
TB	Terabyte (10^{12} bytes)
TBD	To Be Determined
TEM	Transmission Electron Microscope
TM	Transition Metal
TXM	Transmission X-ray Microscope
UFXC	Ultra Fast X-ray Camera
UHV	Ultra-High Vacuum
V	Vertical
V-BDA	Vertically Beam-Defining Aperture
vff-HEDM	very-far-field high-energy x-ray diffraction microscopy

VIPIC	Vertically Integrated Photon Imaging Chip
WA-XPCS	Wide-Angle X-ray Photon Correlation Spectroscopy
WAXS	Wide-Angle X-ray Scattering
WB	White Beam
WBS	Work Breakdown Structure
XBIC	X-ray Beam Induced Current
XBIV	X-ray Beam Induced Voltage
XEOL	X-ray Excited Optical Luminescence
XFEL	X-ray Free Electron Laser
XMAT	eXtreme MATerials beamline concept/initiative
XMCD	X-ray Magnetic Circular Dichroism
XMLD	X-ray Magnetic Linear Dichroism
XPCS	X-ray Photon Correlation Spectroscopy
XRD	X-ray Diffraction
XRF	X-ray Fluorescence
XRIM	X-ray Reflection Interfacial Microscopy
XRMS	X-ray Resonant Magnetic Scattering
XSD	(ANL) X-ray Science Division
YAG	Yttrium Aluminum Garnet
ZP	Zone Plate

6 Experimental Facilities

6-1 Experimental Facilities Overview

The U2.04 Experimental Facilities portion of the APS-U Project consists of two major areas: 1) Feature Beamlines and 2) Beamline Enhancements. The Feature Beamlines portion of the Project includes all APS-U beamlines that are either entirely new, or are existing APS beamlines that are being significantly modified. The Beamline Enhancements are upgrades to existing beamlines that are more modest in scope, but that will have a significant impact on that beamline to allow it to more fully utilize the capabilities of the APS-U storage ring (SR).

In this section, the scope selection process for both areas will be described along with a discussion of the roadmapping exercise used to determine the location of Feature Beamlines.

6-1.1 Feature Beamline Selection

For nearly twenty years there have been workshops concerning possible new beamlines for the APS. The decision to pursue a low-emittance, storage-ring lattice directed the focus of these workshops to beamlines that would take advantage of the vastly increased coherence of the APS-U storage ring. In particular, a set of well-attended workshops in May, 2015 generated formative plans for specific beamline needs and contributed many ideas to the APS-U science case (see Chapter 3).

In designing a process for selection of APS-U beamline scope, a guiding principle was used: the process should result in “New beamlines and major upgrades with resultant world-leading capability that utilize the key aspects of the APS-U storage-ring improvements.” Furthermore, stated goals for the process were that the process:

- Solicit the best ideas from the community of potential users,
- Be open and transparent to the degree possible,
- Meet the relevant DOE project deadlines,
- Effectively use the APS and APS-U advisory committees, and
- Meet the overall strategic needs of the APS.

With the guiding principle and goals in mind, a two-stage process was used. In the initial stage, a call was issued for beamline white papers that were limited to ten pages in length. In the second stage, proposers of selected white papers were invited to develop their white paper into an expanded proposal (nominally limited to 30 pages). To evaluate contributions from both stages, a scientifically-diverse, ad-hoc committee of x-ray science experts was assembled (see Table 6.1). Membership of the committee included members of the APS/APS-U Experimental Systems Advisory Committee (ESAC), APS Scientific Advisory Committee (SAC), and subject-matter experts (SMEs). Table 6.2 lists the selection evaluation criteria given to the committee.

Thirty-six papers were submitted to the initial white-paper stage. After evaluation by the ad-hoc committee and subsequent discussion among the APS/APS-U management with the APS SAC,

Table 6.1. APS-U Beamline Selection Review Committee

Name	**Affiliation**	**Relationship**
Gene Ice	ORNL (retired)	ESAC
Piero Pianetta	SLAC/SSRL	ESAC
Jean Jordan-Sweet	IBM	SAC
Janos Kirz	LBNL/ALS (retired)	SAC
Sine Larsen	U of Copenhagen	SAC
Mark Daymond	Queens University	User/SME
Rob McQueeney	Iowa State University	User/SME
Don Brown	LANL	User/SME
Qun Shen	BNL/NSLS II	SME
Sean McSweeney	BNL/NSLS II	SME
Steve Kevan	LBNL/ALS	SME
Mike Toney	SLAC/SSRL	SME
Uwe Bergmann	SLAC	SME

Table 6.2. Feature Beamline Selection Evaluation Criteria

Scientific/Technological importance of program:	Does the research enabled by the proposal address important scientific, technical and/or industrial problems? Is the program in alignment with the “Early Science at the Upgraded APS” document? If not, provide input as to why the proposed beamline should be considered.
The use of APS-U characteristics and potential for this beamline to be world-leading or world-class:	Does the proposed program and associated beamline use the characteristics of the APS-U (high energy, brightness, coherence,etc.)? Will the proposed performance result in a world-leading/world-class beamline that fulfills the scientific/technical program?
Feasibility of design and required R&D activities to mitigate risks:	Are the proposed beamline performance goals technically feasible? Is there a high degree of certainty that the performance goals can be obtained? Are there specific R&D activities that are required to achieve the proposed goals? If so, have those activities been identified in the proposal and a path forward described to meet those goals and mitigate the risks?
Strength of team and expected productivity:	Are the team members recognized leaders in the field? What do you foresee as the user demand and communities served? Will it require the development of a new community to fully utilize this beamline? What are your expectations from this beamline with respect to high-impact papers and/or technological impact?
Quality of the beamline design*:	Will the proposed performance result in a world-leading beamline that fulfills scientific/technical program? Are those design specifications technically feasible? Is the design optimized or have compromises been made? Is it cost effective (i.e. is there good bang for the buck)?

* This criterion was added at the expanded proposals stage.

seventeen were selected for further developments. Of these, three proposals in the area of wide-field imaging were asked to merge and two proposals emphasizing time-resolved methods were asked to merge. In total, fourteen invitations were given for proposers to develop expanded proposals. It should be noted that in several cases, APS/APS-U management gave directed feedback to proposers to refine alignment to APS strategic plans. For the development of expanded proposals, the APS-U provided engineering and optics-simulation support to the proposers. In addition, each of the fourteen proposals was presented to the user community for feedback during a workshop at the APS/CNM Users Meeting.

Leaders of each of the fourteen proposals made a presentation to the ad-hoc committee, after which the committee scored each proposal in the areas of the evaluation criterion. APS/APS-U management used this input along with top-down cost estimates provided by the APS-U staff to present a list of proposed scope to the APS SAC. After a discussion with the SAC, the Feature Beamline scope was finalized and is shown in Table 6.3.

Table 6.3. APS-U Feature Beamline Scope

Name	**Proposal Title**	**Technique**
CH EX	Coherent High Energy X-ray Sector for In Situ Science	*In situ*, surface high-energy coherent scattering
Polar	Polarization modulation spectroscopy	Magnetic spectroscopy
HEXM	A High-Energy X-ray Microscope	High-energy microscopies & CDI
XPCS	Development of a Small-Angle X-ray Photon Correlation Spectroscopy Beamline for Studying Dynamics in Soft Matter Wide-Angle X-Ray Photon Correlation Spectroscopy and Time-Resolved Coherent X-Ray Scattering Beamline	Small-angle XPCS, Wide-angle XPCS
Ptychoprobe	PtychoProbe	Ultimate resolution, forward scattering ptychography/spectromicroscopy
InSitu	In Situ Nanoprobe Beamline	*In situ*, forward scattering ptychography/spectromicroscopy Long working distances
CSSI	Coherent Surface Scattering Imaging Beamline for Unraveling Mesoscopic Spatial-Temporal Correlations	Coherent GISAXS,XPCS
ATOMIC	Atomic – A beamline for extremely high resolution coherent imaging of atomistic structures	Diffraction microscopy & CDI Bragg CDI
3DNano	3D Micro & Nano Diffraction	Upgrade of current 34-ID-E

6-1.2 APS-U Roadmap

The process of siting the Feature Beamlines is known as the "APS-U Roadmap." As an upgrade to an existing facility, the implementation of the APS-U Feature Beamlines scope presents challenges as well as significant opportunities. Currently, only two ID ports at the APS are not occupied by an operating beamline. It is obvious that at least six of the Feature Beamlines will need to be placed at sites that are currently being used. An additional complicating factor is that for two of the selected Feature Beamlines, strong technical cases have been made for extending those beamlines beyond the current APS Experimental Hall. These "long beamlines" (HEXM and InSitu), will have end stations in a new building built adjacent to the current APS building. As will be discussed below, there are a limited number of places around the APS where a beamline can be existed beyond the existing building, and neither of the currently unoccupied ports are suitable for such extension. In summary, the main considerations in developing the APS-U Roadmap were the following:

- Maximizing Feature Beamline performance, leading to world-leading and world-class APS beamlines,
- Constraints of the APS-U Feature Beamline budget,
- Impact on existing beamlines,
- Long beamline location,
- Reuse of existing infrastructure,
- Compatibility with XSD strategic plans, and
- Compatibility with CAT plans.

It was clear from the beginning of the process that locations of the long beamlines were key to determination of all of the other issues, and had the potential to cause the most difficulty. It was decided that the only practical approach was to site the two long beamlines adjacent to one another so that they could share infrastructure, in particular, a new building adjacent to the current APS building. APS-U staff worked with John Sidarous of the APS Site Operation Group and Studio GC, a Chicago-based architectural firm, to evaluate every APS ID beamline site for suitability based on a variety of factors, including: environmental issues (e.g., wetlands), impact on non-APS infrastructure (e.g., roads, utility lines, sewers), impact on APS infrastructure (e.g., lab office modules), topography, and impact on existing beamlines.

Three locations were identified as the most suitable and these locations were subjected to detailed analysis. The locations were 3&4-ID, 19&20-ID, and 30&31-ID. The results of this are given in [20], with the 19&20-ID site being the clearly preferred option. In addition to the siting study, conceptual plans were developed for a platform, stairs, and elevators to allow access for areas blocked by the long beamlines.

With the locations of the long beamlines determined, other siting decisions become possible, and after deliberations among APS/APS-U management and affected stakeholders, the roadmap shown in Table 6.4 was developed. The roadmap given in Table 6.4 is the assumption for the beamline sections given in the rest of this chapter and will be the basis for the designs, cost, schedule, and other documentation for the CD-2 phase of the Project. As developments occur with existing APS programs, the APS-U Roadmap may be adjusted in response to opportunities that arise, and APS-U plans will be adjusted accordingly using the standard APS-U Project change request process.

Table 6.4. The proposed APS-U Roadmap

Program	**Selected Location**	**Affected Existing APS Program**	**Comment**
In Situ	19-ID	SBC-CAT	Long beamline
HEXM	20-ID	Current 20-ID	Long beamline Current 20-ID program will relocate to 25-ID.
Polar	4-ID	4-ID-C	The IDs for the Polar program will occupy the entire 4-ID straight section, requiring relocation of the 4-ID-C soft x-ray branch.
XPCS	8-ID		Currently location of XPCS program. SAXPCS and WAXPCS programs combined.
CSSI	9-ID	USAXS	USAXS tentatively slated to move to 12-ID
		Bionanoprobe	Bionanoprobe slated to move to 2-ID
CHEX	28-ID		28-ID currently unoccupied
Ptychoprobe	33-ID	Current 33-ID program	Current 33-ID will be absorbed into existing XSD diffraction beamlines.
ATOMIC/ 3DMicroNano	34-ID		Both programs are based on instruments currently located on the canted 34-ID beamline

6-2 ATOMIC: A beamline for extremely high resolution coherent imaging of atomistic structures

6-2.1 Executive Summary

The ATOMIC beamline will enable extremely high-resolution ($<$1 nm) investigation of materials structure and high resolution ($<$10 nm) imaging of a material's *operando* conditions. The APS MBA lattice will produce an unprecedented amount of coherent flux in the hard x-ray region. This will enable coherent diffractive imaging (CDI) of material structure at a resolution approaching atomic dimensions within a reasonable measurement time (10s of minutes).

ATOMIC will address structural questions intersecting nearly every branch of science. We have outlined several where we believe the impact will be transformative. One such example is catalysis, which would enable one to literally see into the functional nature of these materials while they are active. We will address important questions in structural materials, such as the influence of grain boundaries, defects, and the nucleation of voids leading to failure. Dislocation dynamics play a critical role in materials failure. ATOMIC will be capable of imaging their interactions with point defects as well as clusters of defects. Extremely high-resolution coherent imaging expands our understanding of failure mechanisms in amorphous materials like bulk metallic glasses, which are among the strongest materials known. Finally, magnetic and other properties of correlated electron systems typically scatter x-rays weakly, hindering local understanding of spin and lattice coupling in these systems. ATOMIC will facilitate the performance of high resolution imaging measurements on them on practical time scales. The ATOMIC beamline, together with the tremendous coherent flux of the APS MBA lattice, will literally make the invisible, visible.

The ATOMIC beamline is conceptually simple. The major components consist of an undulator source, a set of slits, a monochromator, and a focusing system to tailor the coherent x-ray beam to the sample, a stage to manipulate and orient the sample, and a detector to capture the coherently scattered photons. We outline aggressive, no-compromise design goals for both the optics and sample manipulations based on technologies that are past their proof-of-principle stage. We identify R&D required to take these components from the design stage to full-fledged instrumentation in support of the science program. A key feature of the ATOMIC beamline is a variable numerical aperture focusing system capable of more than one decade of continuous tuning of the focal spot size. This system, based on Kirk-Patrick Baez (KB) mirror pairs, combined with beamline optics to provide the necessary coherent beam properties, will enable the ambitious scientific program outlined above. ATOMIC will be alone in the world as a dedicated coherent imaging beamline for studies of atomistic structure in materials based on state-of-the-art technical capabilities and a synchrotron x-ray source.

This section outlines the scientific objectives and case for ATOMIC, the beamline technical capabilities and key performance specifications, the source and front-end requirements, the beamline layout and optics, experimental station instrumentation, detector and data acquisition planned, and R&D work needed to realize the above. A drawing of the beamline layout and a component list are covered later in this section.

6-2.2 Scientific Objectives and Capabilities

6-2.2.1 Science case for beamline (See Section 2.2)

Interrogating modern functional materials to unravel the tangle of structural, chemical, and physical properties is currently a major endeavor[21]. Few structural techniques possess sensitivity to local atomic structure across tens of nanometers to micrometers of sample volume while also permitting *operando* investigations. Billinge et al. summarize this endeavor nicely in their review in *Science Magazine* entitled "The Problem with Determining Atomic Structure at the Nanoscale"[21]. Typically atomic and mesoscale information is gathered by a variety of techniques on micrometer and millimeter size samples. Modeling and simulation are then employed to extract a plausible story of the structural and functional properties of that sample. There is a strong need for techniques that can acquire atomistic structural information across many length scales in full three-dimensional detail. If these same techniques can function with *operando* environmental cells, they will have a transformative impact on many disciplines of science. The ATOMIC beamline aims to be that tool.

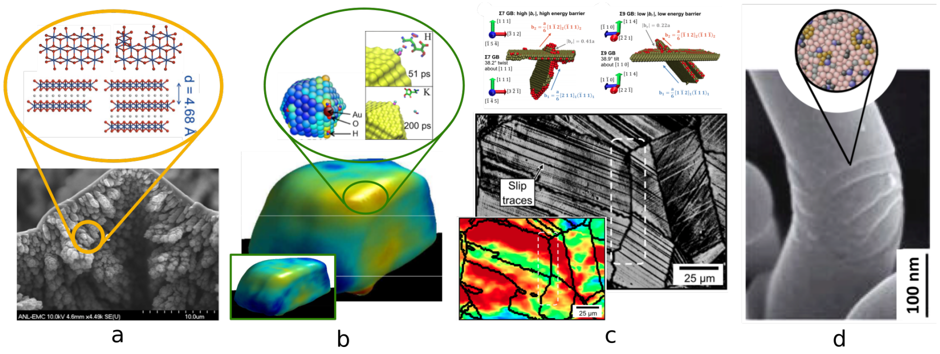

Figure 6.1. (a) SEM of cobaltate "artificial leaf" films. Models shown above of organized active domains and their potential stacking[1, 2]. (b) A 300nm gold crystal, imaged with BCDI, before (inset) and after exposure to ascorbic acid. Surface color represents lattice strain. Reactive MD simulation (above) explains increased strain at corners is due to hydroxyl ions chemisorbed to the surface[3]. (c) SEM showing slip planes transiting grain boundaries in regions of high strain(inset) imaged with EBSD. MD simulations (above) are used to understand energies associated with dislocations crossing grain boundaries of different types[4]. (d) Plastic failure of metallic glasses occurs with shear bands. The atomic organization of such failure modes is still unknown (inset cartoon)[5].

6-2.2.2 Description of user community

Beyond the experiments described in detail in Section 2.2, coherent imaging is currently contributing to many branches of science. The current coherent imaging end station at APS contributes to studies in nano-materials, energy materials, chemical and catalysis materials, x-ray optics, and to a lesser extent, some life science themed studies. The emphasis is on *operando* as well as *in situ* characterization. The community continues to grow. The APS Upgrade will effectively move coherent imaging from a specialist technique to the mainstream method for nanoscale structural characterization. Challenging coherent imaging experiments today will be the routine experiments of the APS Upgrade in the future.

High Pressure The high pressure community possesses almost no high resolution imaging capabilities. Both the diamonds and gaskets in modern panoramic high pressure cells greatly hinder direct imaging methods. Coherent imaging however, particularly using Bragg peaks of samples within diamond-anvil cell, has rendered nanoscale investigations possible[22, 23].

Wenge Yang — 1000 talents Award Staff Scientist, Shanghai Laboratory of HPSTAR & High Pressure Synergetic Consortium, Carnegie Institution of Washington.

Correlated systems and complex materials Paul Evans, Department of Materials Science and Engineering, University of Wisconsin at Madison. Structure and response of complex oxides under extreme fields.

Phil Ryan, X-ray Science Division, Argonne. Magnetic x-ray scattering, thin films, and electronic structure of correlated systems.

Oleg Shpyrko, Shpyrko Research Group, UC San Diego Nanoscale dynamics, energy materials, metallic glasses, quantum fluctuations, novel coherent x-ray scattering methods.

Edwin Fohtung, Department of Physics, New Mexico State University. Research focuses on nanoscale physics of ferroelectric and multiferroic systems.

Joshua Turner, LCLS, Stanford Linear Accelerator Laboratory. Ordering and phase transitions in correlated electron systems, x-ray resonant scattering.

Ian McNulty, Center for Nanoscale Materials, Argonne National Laboratory. Coupling of magnetism and strain in nanomagnetic and correlated electron materials. Ordering behavior at phase transitions.

Energy Materials Coherent imaging of *operando* energy storage materials.

Andrew Ulvestad, Synchrotron Radiation Studies Group, Materials Science Division, Argonne Material interfaces and catalysis for energy conversion and storage.

Oleg Shpyrko, Shpyrko Research Group, UC San Diego Nanoscale dynamics, energy materials, metallic glasses, quantum fluctuations, novel coherent x-ray scattering methods.

Paul Fuoss, Synchrotron Radiation Studies Group, Materials Science Division, Argonne Epitaxial films and crystal growth, novel coherent x-ray scattering methods.

Felix Hofmann, Department of Engineering Science, University of Oxford, irradiation damage in structural materials, nano- and dislocation mechanics.

Chemistry and Catalysis Hoydoo You, Synchrotron Radiation Studies Group, Materials Science Division, Argonne Material interfaces and catalysis for energy conversion and storage.

Prof. Hyunjung Kim, Sogang University, Zeolites and metallic catalysts.

Life Science Recent progress has been made in imaging biological macromolecule crystals using CDI. The APS-U will improve this through more efficient collection of scattered photons, given that the limiting factor with these samples is damaging dose[24].

H. D. Coughlan, C. Darmanin,N. W. Phillips, B. Abbey - Australian Research Council Centre of Excellence in Advanced Molecular Imaging, Department of Chemistry and Physics, La Trobe University, Melbourne 3086, Australia.

6-2.2.3 APS-U characteristics

The experiments outlined in our science case have a tremendous need for coherent flux, both from the standpoint of reaching atomic resolution[6, 25, 26] by CDI, and pushing current detection limits to that of single-defect, chemical species identification, or spin and orbital-sensitive measurements. The proposed APS Upgrade source will not only revolutionize the science done with coherent imaging, but also drive the evolution of the method itself. We will be able to manipulate and use the coherent modal composition of the beam like never before. Polychromatic and multimodal coherent imaging methods have been demonstrated are under further development[27, 28, 29]. The relatively narrow bandwidth of the spectral components of the new source will make these methods even more promising.

It is not optimistic to expect sub 10-nm resolution imaging of operando materials in tens of seconds with this instrument. Atomic resolution imaging of 50-nm volumes could be achieved in tens of minutes. This capability nicely complements operando Transmission Electron Microscopy (TEM) where strong beam-matter interactions limits the technique to a few to tens of nanometer resolution.

Dietze et al.[6] have recently published a comprehensive study on the required photon flux to image both crystalline and amorphous high-z materials with coherent diffraction at atomic resolution. In this study, the authors performed realistic simulations of coherent diffraction data that was then phased using current methods to retrieve and image the sample. For this reason, this article is highly valuable for estimates regarding what can be achieved with coherent imaging at the APS-U. The required photon fluxes have been specified by the fidelity of the resulting image of the atoms in the sample. Figure 6.2 is assembled from Dietze et al.[6] The authors have determined that to faithfully image a 20 nm gold crystal, one needs an incident time-integrated flux of about 10^{18} ph/μm^2. This corresponds to about 40 s of integration for a full 3D atomic resolution image using the estimated APS-U coherent flux at 10 keV, taken from the plot in Figure 6.3. Of course this assumes absolutely no losses in focusing of the beam to exactly the size of the sample and also perfect efficiency in collection of the scattered photons. Even if we only come within an order of magnitude of perfection, we may still achieve atomic resolution in a reasonable time period. In the case of atomic resolution imaging of an amorphous gold sample, Dietze et al. found that the situation improves by a further order of magnitude, achieving faithful images of their sample with just 10^{17} ph/μm^2 of time integrated flux. This is summarized in Figure 6.2. where the achieved image resolution is found to plunge by nearly an order of magnitude upon reaching the threshold flux in each case. This improvement for amorphous samples is explained at least qualitatively by the fact that very little information is actually contained in the Bragg peaks of a crystalline scattering pattern while they also contain a large fraction of the scattered photons. For an amorphous sample, those photons are available to scatter into a signal of many length scales.

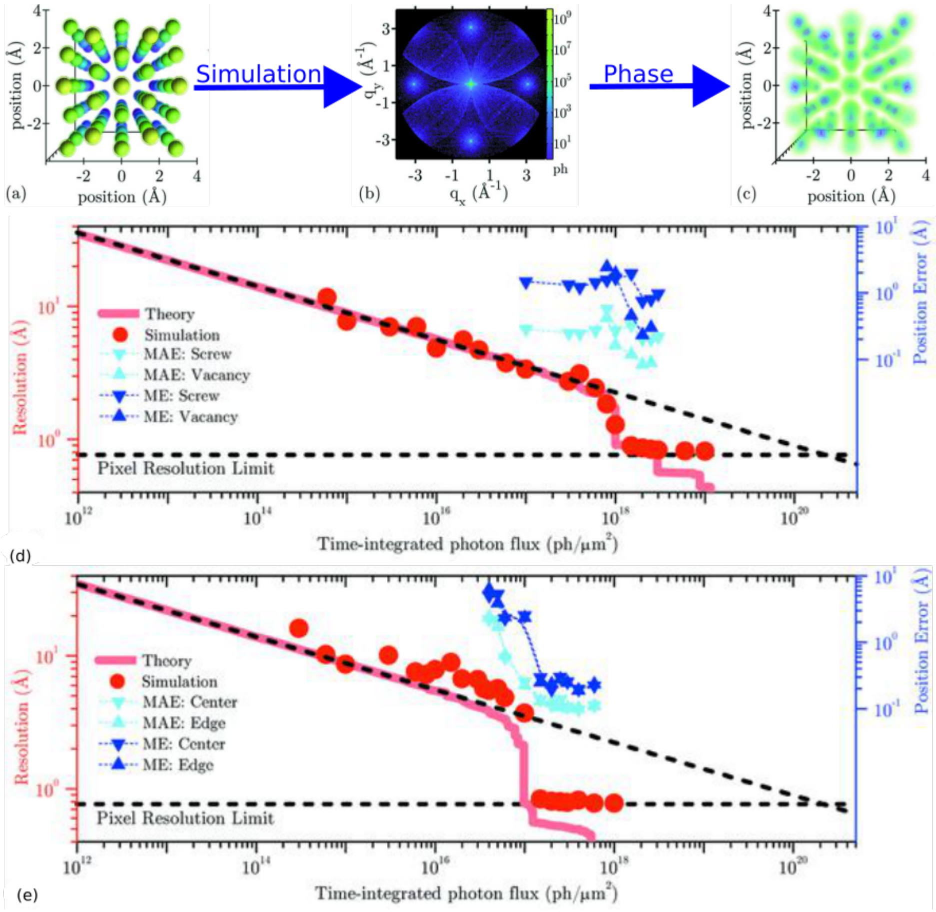

Figure 6.2. Assembled from Dietze et al.[6]. (a) The criterion for sufficient signal to image at atomic resolution was obtained by (b) accurately simulating coherent diffraction from an atomistic model and (c) conducting phase retrieval to recover the image. (d) The obtained resolution as a function in time integrated photon flux on a crystalline sample. (e) The same as (b) for an amorphous sample of the same atomic composition. Inset in (d) and (e) is the position error associated with different defects or locations in the sample.

Dietze et al. also found that the total time, or number of scattered photons, to image at atomic resolution did not significantly increase with the size of an amorphous material and only linearly increased with the size of crystalline samples[6].

The following analysis is included in the Early Science at the Upgraded Advanced Photon Source document[30][Page 51, 7].

APS Upgrade-enabled CDI measurements with atomic (or near-atomic) resolution have the potential to characterize the atomic rearrangements associated with yielding of an amorphous metal. As envisioned here, samples will be cylindrical, with diameters and lengths of 20 nm and 50 nm, respectively. The glass will be subjected to applied strain that is either in compression, using a nanopillar of the type commonly employed in stress-response measurements of amorphous metals,

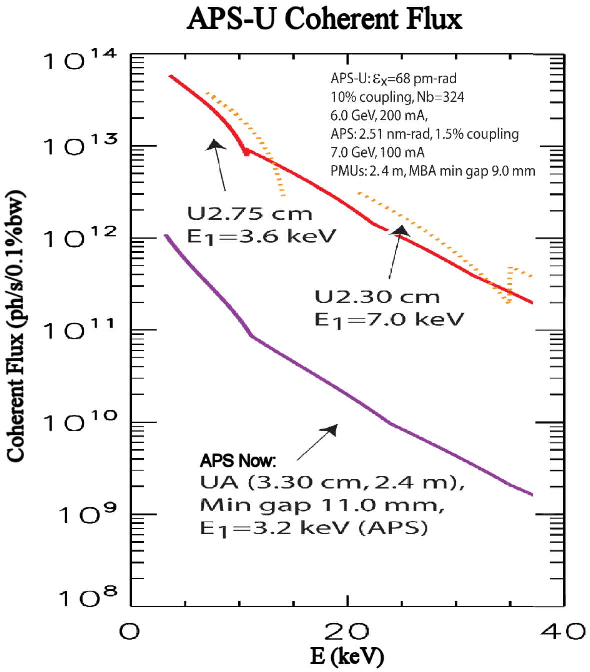

Figure 6.3. The anticipated coherent flux tuning curves of the APS Upgrade for a representative undulator sources.

or that is in tension, where "dog bone-shaped" samples would isolate the failure region to a desired cylindrical segment. In either case, CDI reconstructions would be performed as a function of fixed strain, as the stress is simultaneously monitored so that rearrangement events can be directly connected to nonlinear mechanical response.

As an assessment of the feasibility of such measurements, we have calculated the expected scattering intensities in coherent diffraction patterns from a sample of amorphous metal, based on molecular dynamics simulations. The simulation results contain the positions of 96,000 atoms within an approximately 8 x 8 x 26 nm^3 specimen of the widely studied metallic glass composition Cu64Zr36 before and after yielding under an applied shear stress.

The diffraction patterns, which are shown on a log scale and extend to a maximum wave-vector qmax = 1.26 A^{-1}, were calculated based on a 20 x 26 nm^2 incident beam on the specimen with a total dose of 10^{13} photons/nm^2. Patterns with such scattering intensity to this q_{max} can be used to reconstruct the real-space atomic configuration with a precision of 0.1 A^{-1} in the atomic positions. Assuming that the top half of a cylindrical sample is being imaged, so that the beam and sample size approximately match (and so that the total number of atoms being imaged is about six times the number in the simulation), and using the expected coherent flux at APS-U that can be focused into a 20 x 26 nm^2 spot of 2x10^{12} photons/s (0.01% BW), we estimate that the total exposure time needed to collect such a dataset from the nanopillar will be approximately 7 min. Further, assuming one obtains roughly 10 such datasets from different orientations to make a tomographic 3D reconstruction, the total time for a measurement at each strain position will be about 1 h. We therefore expect that atomic-resolution images of the amorphous metal nanopillar at multiple strain amplitudes, and at multiples stages of yielding, should be feasible.

While coherent imaging remains a primary driver for most low emittance synchrotrons worldwide, none are planning fully dedicated coherent diffractive imaging instrumentation with the technical capabilities of ATOMIC. Coherent imaging is typically considered in the context of nanoprobes or small angle x-ray scattering (SAXS) instrumentation where coherent diffractive imaging will not be the primary function of the beamline. The only notable exception to this is the proposed BCDI beamline at the National Synchrotron Light Source (NSLS2) at Brookhaven National Laboratory. When constructed, this beamline will be a fully dedicated coherent image beamline with both the ability to measure Bragg peaks of crystalline samples and capabilities for scanning coherent diffraction (ptychography). The APS-U source will be at least one order of magnitude brighter than NSLS2 at 10 keV, giving obvious advantages to ATOMIC at hard x-ray wavelengths, though ATOMIC will nicely compliment the BCDI instrument at NSLS2. The NSLS2-BCDI instrument is planning to operate in the 6-15 keV energy range with intended focal spots of 1-7 Îijm. This beamline will also include laser pump, x-ray probe coherent imaging capabilities for time resolved studies of materials properties.

There are major advantages to a dedicated beamline for coherent imaging. ATOMIC will be able to implement state-of-the-art optics and sample manipulation without compromising other measurements. Those components will be reliably configured and maintained for a suite of experiments. In fact, the greatest advantage of the current APS coherent imaging beamline, 34-ID-C, compared to others in the world, is its dedicated nature. The fact that core capabilities of the beamline are never altered, and only slowly improved, has enabled a substantial scientific productivity in the last five years. (There have been more than 55 publications, most with high impact factors). While beamlines at ESRF can deliver greater coherent flux and SLS beamlines have more capable detectors, the APS beamline (34-ID-C) is permanently "set up" and ready for measurements. Among other opportunities, this enables development of dedicated capabilities such as environments for specific measurements.

6-2.2.4 Key beamline characteristics

To achieve the high resolution imaging goals of this beamline, it is vital to deliver maximal coherent flux to a precisely determined area, or volume, of the sample. The beamline will enable imaging across multiple length scales of complex samples under *operando* conditions. The proposed zoom KB system in the ATOMIC beamline promises to enable this with a continuously variable spot size from 50 nm to 1.5 μm. While in principle ptychography methods will be used for coherent imaging of arbitrary fields of view within a sample, the overhead associated with scanning overlapping regions of the sample will greatly reduce the temporal resolution of *operando* experiments on functional materials. ATOMIC will be capable, through the zoom KB system, of imaging samples that are less than 50 nm to greater than 1 μm in size in a single scan to accumulate high resolution data. For samples larger than our proposed 1.5 μm spot size, we will use ptychography methods with optimized x-ray beam size for a given experiment.

The beamline will support the use of broadband Laue diffraction to obtain crystallographic orientations of the samples prior to coherent diffraction measurements and enable polychromatic CDI methods currently under development. A randomly oriented crystallographic sample, such as those described in our science case, will be nearly impossible to measure unless one can determine the orientation of the crystallographic axis. By using broadband illumination, multiple Bragg peaks of the crystal will simultaneously be excited and can be used as a map of the samples' lattice orientation. Once analyzed, one can dial up any desired Bragg orientation with a monochromatic beam and do coherent diffraction measurements. Micro-Laue diffraction, as shown in Figure 6.4, has been extensively developed at the APS over the last two decades and can achieve the orientation accuracy required for our experiments[7]. The existing instrument has been used recently to determine orientations of samples for CDI experiments. Great care must be taken to ensure the sample mounting is compatible with both instruments, and therefore orientations are typically accurate to a few degrees. *In situ* Laue diffraction orientation would be used every day if it were available at the CDI instrument today.

Laue microdiffraction measurement will not be conducted at high spatial resolution at ATOMIC, so the smallest beams will not be necessary with broadband illumination. This will relieve a need to deal with the high power in the broadband illumination throughout the final optics to the sample.

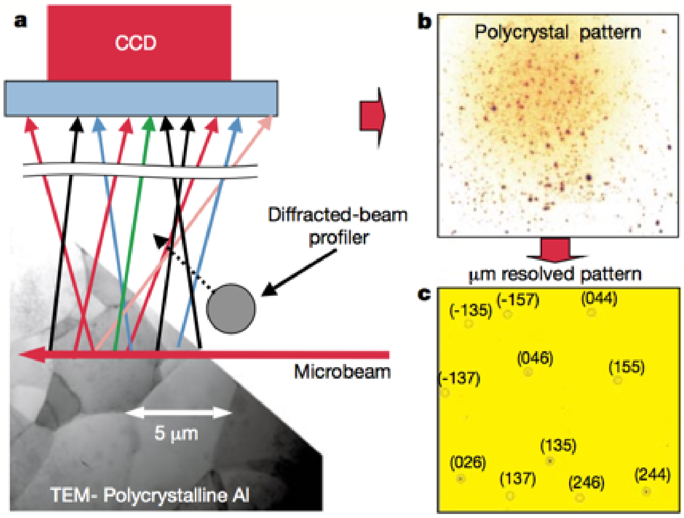

Figure 6.4. Taken from Figure 2 of Larson et al.[7]. (a) The usual broadband Laue microdiffraction measurement, with a beam profiler to determine 3D structure. (b) A Laue diffraction pattern of a polycrystalline sample. (c) indexed diffraction pattern from just a single grain in the sample extracted from the polycrystalline diffraction pattern in (b).

The broadband capabilities of the beamline will also enable polychromatic coherent diffractive imaging measurements.

We anticipate that as many as 10 spatial coherence modes or the full spectral width of a harmonic can be used in some CDI experiments by exploiting recent advances in phase retrieval algorithms and measurement methods[27, 28]. This will enable use of more total flux from the source, e.g. for weakly scattering samples. Use of broadband coherent flux will also enable full 3D imaging without rocking the sample. This can be employed for *operando* measurements or mechanically forced materials at the ATOMIC beamline[31].

An experiment that highlights the unique capabilities of ATOMIC was envisaged in the development of our science case. We will be able to image a binary alloy nanocrystal, such as silver-gold, at extremely high resolution to characterize the morphology and individual defects within the crystal. We would then like to perform *operando* electrochemical dealloying and analyze the nature of the dealloying process that selectively removes silver from the lattice. We can do this either in real time at modest resolution, or incrementally stop the process and image at extremely high resolution, approaching the spacing of individual atoms within the sample. Using anomalous CDI, we can track the local density of silver atoms that remain in the lattice after partial dealloying and analyze the transport mechanisms underlying the dealloying process. Does the dissolution initiate and progress from specific facets of the crystal, or are the edges and corners particularly important? What is the role of defects in the as-grown material in this process? Where, and perhaps how, do defects arise in the sample as the dealloying occurs? Once the silver is gone, the gold will be left as a nano-porous structure. We can then conduct catalysis on this material, such as the decomposition of ascorbic acid, and watch as the lattice responds at active sites throughout the 3D volume of the material. The density of active sites and the rate at which they become active can be studied at very high resolution. The same nano-porous gold will then be coarsened *operando* by heating followed by further catalysis cycles to understand how the morphology of the coarsened gold impacts the density of active sites or the rate at which they are utilized. Of course, this exact process can be repeated with crystals of different sizes, utilizing the zoom optics of the beamline, to understand how the initial size impacts the entire process. The Laue diffraction for orientation determination will allow us to select crystals at will, without regard for special sample preparation to control the crystal growth directions.

The beamline will efficiently deliver a coherent beam with a photon energy between 5 - 25 keV into the end station. The high end of this range serves two purposes for ATOMIC. One is the need to obtain broadband Laue diffraction for determination of sample orientation. The higher order Bragg reflections will be excited with high energy x-rays. These are extremely valuable for accurately determining crystal orientation. The other need is for penetration into environmental cells, such as the catalysis chamber envisioned in our science case. Experiments that simply need to occur in glass, silicon, or high pressure diamond anvil walled chambers can be easily probed with 25 keV x-rays, where the source will have a coherence on par with today's APS at 5 keV.

The low end of this spectrum is intended for taking advantage of an increased scattering cross section of light elements and to access absorption edges of elements like Manganese and Vanadium, which have important properties in correlated electron systems.

6-2.3 Source & Front End Requirements

6-2.3.1 Insertion Device

The proposed science program will be best served by an insertion device (ID) that delivers the highest achievable coherent photon flux over the 5-25 keV energy range. These coherent flux requirements are driven by the goal of reaching atomic resolution images. This energy range will enable access to resonances down to the V and Mn K-edge at the lower end of the range, and efficient crystallographic orientation of samples by Laue methods with broadband radiation and penetration into environmental cells at the upper end of the range.

To minimize losses in horizontally oriented optics and monochromators, a horizontally oriented undulator used to produce vertically polarized x-rays will be considered. Losses to a horizontal monochromator can be as great at 40% at the lower x-ray energies used at ATOMIC. The losses can grow tremendously at higher reflections that would be used for smaller energy bandwidth or greater temporal coherence.

6-2.3.2 Other source requirements

The source stability requirements for the ATOMIC beamline are met by the planned source stability specifications, i.e. $<=$ 10% variation in the source size and divergence.

6-2.3.3 Front End Requirements

The beamline front-end should be windowless to minimize scattering and introduction of phase structure in the coherent x-ray beam.

6-2.4 Beamline Layout

The current APS source lends itself to use of the entire extent of the beam in the vertical direction and defining the source in the horizontal direction for nano-focusing. This has been optimally achieved using a focusing mirror and aperture in the horizontal[32]. The substantially smaller horizontal emittance of the APS-U source offers much greater freedom to manipulate the beam to an optimal coherence configuration before focusing into the experiment.

The optical layout of the ATOMIC beamline is designed to take advantage of this freedom by selecting a beam with a well-defined set of coherence modal properties and matching it efficiently to the experiment. The following section outlines the conceptual scheme and principal components of the beamline optics.

6-2.4.1 X-ray Optical Layout

The following beamline optical design is based on three sections with associated optical functions that target the science program of ATOMIC: (i) spatial coherent mode selection, (ii) temporal coherence selection (monochromatization), and (iii) focusing. Figure 6.5 shows the approximate locations of the components of each section and their distances from the source, defined to be the center of the straight section containing the undulator.

Coherence mode selection is accomplished with two sets of beam defining apertures (slit pairs) separated by a drift path, to allow the beam to propagate freely between them. The first white-beam slit pair, S1, located ∼27 from the undulator source, can be closed to define a secondary effective source or be opened to accept a partially coherent beam to the optics and experiment downstream. The second slit pair, S2, located at ∼51 m from the source, can also be closed or opened to accept a fully or partially coherent beam from the first slit pair. Together, the purpose of the two slit pairs is to define the coherence properties of the beam, ranging from a single coherent mode to as many as several modes in both the horizontal and vertical planes, depending on the x-ray energy and coherence requirements of the experiment.

Temporal coherence selection is accomplished by a double-crystal monochromator (DCM), and optionally, a double multi-layer monochromator (DMM) located after slit pair S2 at ∼51 m from the source. A temporal (longitudinal) coherence length of $\lambda^2/\Delta\lambda \sim 0.5\mu m$ at 10 keV, which is met by a Si(111) DCM, will be sufficient to reach atomic resolution with a sample diameter of 50 nm. Higher-order crystal reflections can be utilized if a longer temporal coherence length is required.

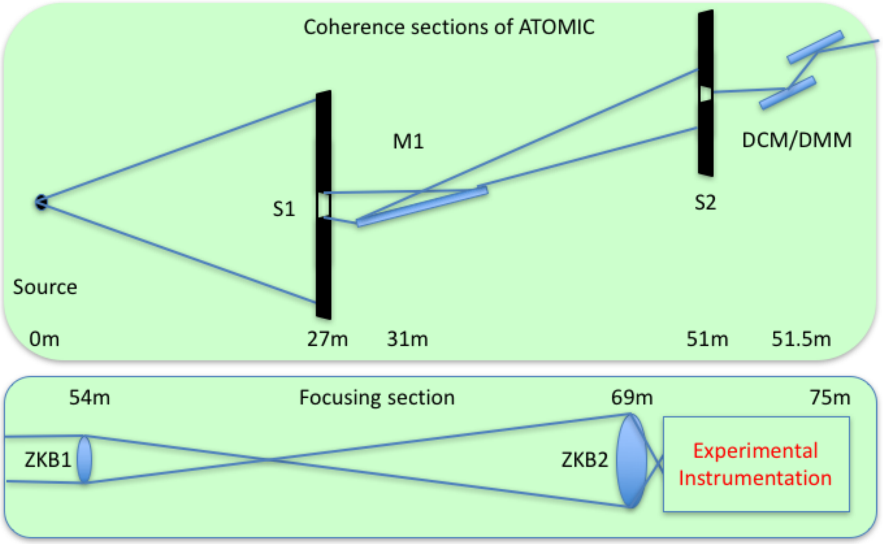

Figure 6.5. ATOMIC beamline optical layout. The components of the coherence mode selection, monochromatization, and beam focusing sections of the beamline, as well as their distances (in meters) from the source.

A harmonic rejection/horizontal offset mirror will be just downstream of the slits S1 to increase the offset from the beam feeding the 3DMN experimental station (34-ID-D). This mirror also serves to further reduce the power load on the downstream apertures and optics when the beamline is operating at high energies with small undulator gap. ATOMIC will include a set of removable silicon filters in the upstream section of the beamline to remove the power load in the lower harmonics. The DCM/DMM are conventional although likely designed for horizontal dispersion and deflection with minimal offset. Horizontal deflection may offer the greatest angular stability against gravity sag and vibration communicated through the experimental floor. Detailed simulations will be required to determine the cooling needs of both the mirror and monochromators to maintain an estimated maximum figure error of 100nrad. Ideally they will need very modest cooling that is readily accomplished with a high degree of stability.

The focusing of the source to the sample will be performed with a variable numerical-aperture focusing optical system [33], also known as "zoom KB" optics [8, 33, 34]. This approach enables the coherent size and dimensions of the beam to be efficiently tuned to specific samples and volumes of interest. Recently, a zoom KB system was demonstrated at SPring-8 that achieved a zoom range from 100 - 1400 nm [33]. While not implemented for user operations at a beamline, these results suggest a feasible and flexible approach to matching beam size to samples for the scientific program envisioned for ATOMIC.

6-2.4.2 Beamline Physical Layout

Overall Layout

A preliminary layout of the beamline is shown in Figures 6.6 and 6.7. Much of the final design for the ATOMIC branch will depend on the specification of the zoom KB system resulting from R&D. The key components of the beamline are shown in Table 6.5.

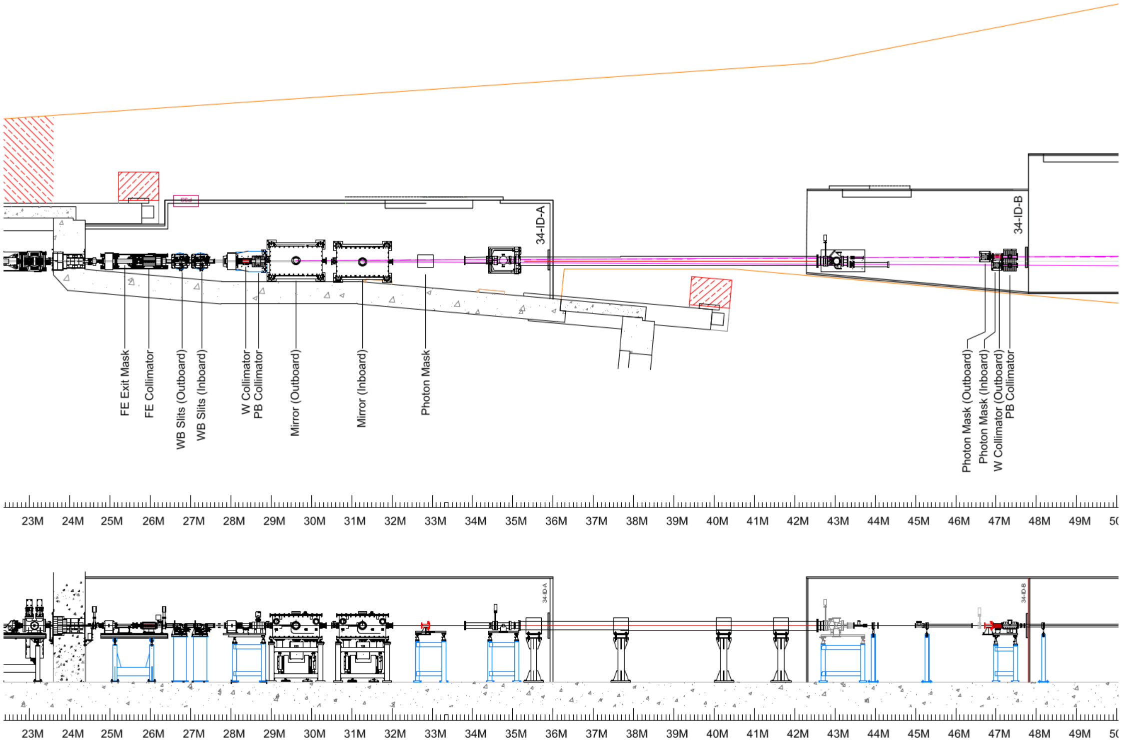

Figure 6.6. Preliminary layout of the FOE showing slits (S1), collimator, beam position monitor, and white beam mirror.

First Optics Enclosure and Infrastructure Major Components

The ATOMIC beamline will be served by three shielded enclosures (hutches): the first optics Enclosure (FOE), second optics enclosure (SOE), and experimental enclosure (EE). The first component in the FOE contains a windowless, differentially pumped section that interfaces the storage ring front end to the beamline. The FOE will also house a high power white-beam (WB) compatible precision slit intended to reduce both the power and coherent modal content of the beam. A white-beam compatible horizontally deflecting mirror will provide harmonic rejection and separation from the 3DMN beamline on the other branch of the canted source.

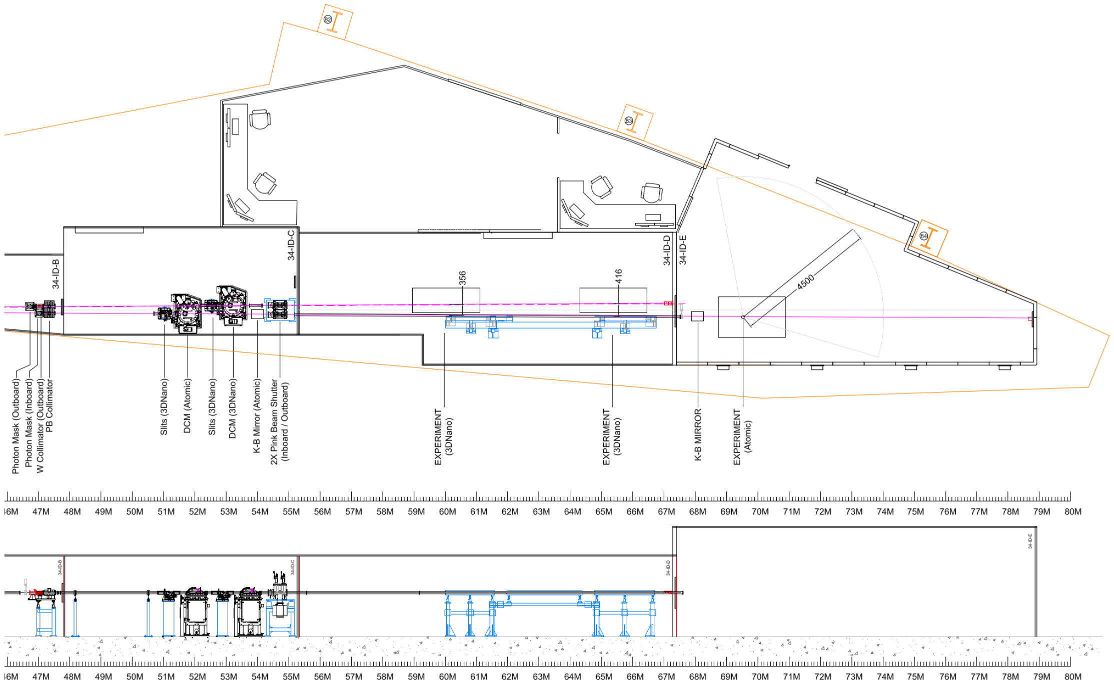

Figure 6.7. Preliminary layout of SOE and the experiment enclosures. The SOE houses the coherence defining aperture (slit S2), monochromators, and first KB mirror pair (ZKB1)at 54m. The experimental enclosure will contain the final KB and diffraction instrumentation at roughly 70 m.

Table 6.5. Principal beamline components, designations, and their distances from the source

Enclosure	**Distance (m)**	**Name**	**Component**	**Function**
FOE			First optics enclosure	Radiation shielding
	27	S1	Slits	Primary spatial coherence selection
	31	M1	White beam mirror	Harmonic rejection and beam separation
	32	BPM1	Beam position monitor	Beam position/angle diagnostics
SOE			Second optics enclosure	Radiation shielding
	51	S2	Slits	Secondary spatial coherence selection Power filtering, harmonic rejection
	51.5	DCM	Double crystal monochromator	Temporal coherence selection (narrow bandwidth)
	52	DMM (not shown)	Double multilayer monochromator	Temporal coherence selection (moderate bandwidth)
	53	Polarizer (not shown)	Diamond phase plate	x-ray beam polarization control
	54	ZKB1	Zoom KB: upstream mirrors	Focusing optics (upstream)
EE			Experimental enclosure	Radiation shielding, experiment isolation
	68	BPM2	Beam position monitor	Beam position/angle diagnostics
	69	ZKB2	Zoom KB: down-stream mirrors	Focusing optics (downstream)
	69.050	DIFF	Diffractometer	Reciprocal space selection
	72-75	DET	Detector	Swallows the photons

Second Optics Enclosure (SOE 34-ID-B)

The SOE will house the small offset monochromators for both the ATOMIC instrument and 3DMN end stations. On the ATOMIC branch there will also be a precision slit acting as the entrance aperture for the first pair of KB mirrors in the ATOMIC zoom KB system that is also in the SOE.

Selectable, arbitrary polarization will enable dichroic Bragg coherent diffractive imaging experiments on magnetic and other systems characterized by molecular and orbital anisotropies. In particular, circular polarization is important for study of ferromagnetic states. Circularly polarized x-rays with energies up to ∼12 keV will cover the major edges of interest for hard x-ray resonant scattering. Bragg coherent diffractive imaging measurements have been performed on crystalline samples with both linearly and circularly polarized x-rays and researchers found that the images of strain in the crystals are unaffected by the circular polarization of the x-rays. Circular polarization can be produced with a dedicated insertion device, though magnetic studies will likely not be our daily measurements at 34-ID. A diamond phase plate to produce left and right circularly polarized light, as well as arbitrary linear polarization, will be installed in the SOE after the monochromators. A diamond phase plate has been tested for coherent imaging applications at APS 34-ID-C[35].

ATOMIC Beamline Experimental Enclosure

The generic "size" of an experiment conducted at ATOMIC will be 10cm, so the final zoom optic will need a working distance of 50 mm. This specification is likely within reach for a zoom KB system with a tunable spot size from 50 nm to 1.5 μm similar to the one illustrated in Figure 6.8 [8, 33]. An ultra-stable diffractometer to orient the sample in such a beam and maintain alignment with the beam while performing *operando* experiments may be based on the inverted joystick design of Blank et al.[9].

Beamline Components

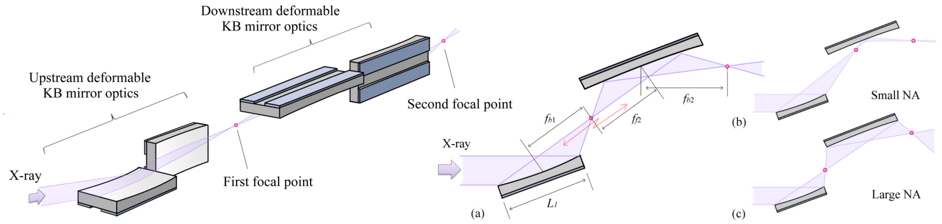

Figure 6.8. Zoom KB schematic[8]. The total numerical aperture of the system is tuned by modifying the shapes of the mirror pairs, separately in horizontal and vertical, to move the first focus relative to the first mirror, thereby adjusting the effective numerical aperture of the second mirror.

Zoom KB The Zoom KB system specification has been refined for the current layout of the ATOMIC branch of 34-ID. Three parameters have been investigated with an analytical simulation in Mathematica. The separation between the mirror pairs, the lengths of each of the mirrors, and the potential to make the angles adjustable to maximize beam transmission at lower x-ray energies are all important factors. All of these have been optimized for the intended 50 nm to 1.5 μm spot size range required of the system. A Shadow-hybrid wave optical simulation of the optimized mirror design has also been conducted in order to verify the results.

The Mathematica simulation was first verified against the experimentally achieved focus obtained in reference[36]. Figure 6.9 illustrates the agreement with the experiment and the fact that the analytical model, not surprisingly, under-predicts the smallest achievable spot size.

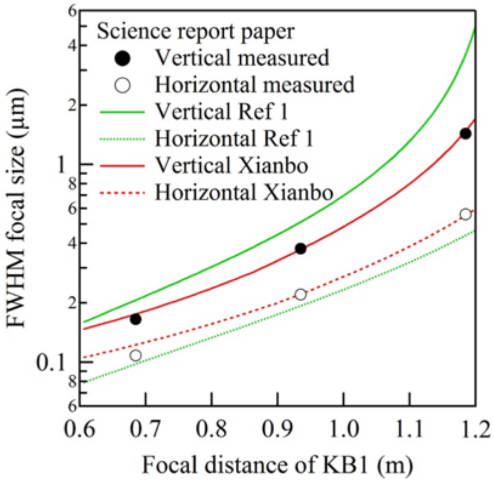

Figure 6.9. Comparison between simulation and experiment for a Zoom KB system.

The first parameter investigated was the separation between the mirror pairs. The range of numerical apertures that can be achieved in such a system is proportional to the separation. Our simulations shown in Figure 6.10 illustrate that 15 m is capable of providing the required range with better performance in overall transmission of the x-ray beam than the minimum required separation of 5 m. Additionally, 15 m is sufficient separation to allow the 3DMN instrumentation on the other canted branch to occupy the space in between.

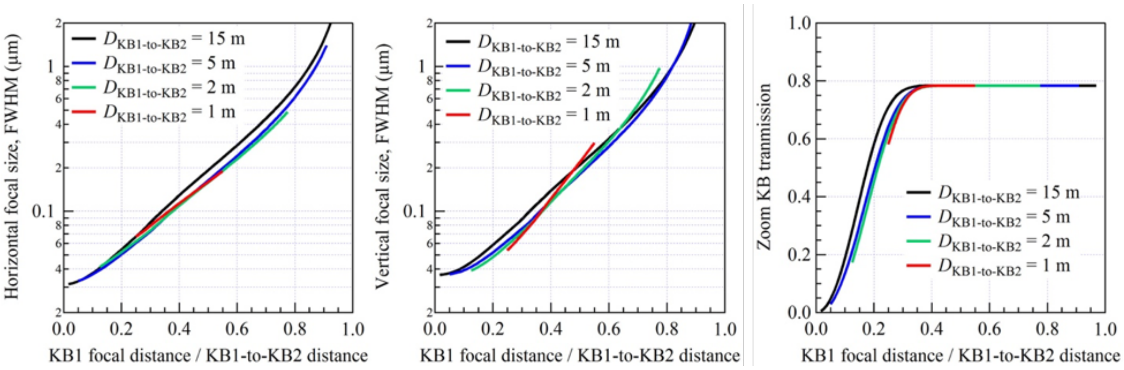

Figure 6.10. Available Numerical Aperture (NA) of a Zoom KB system as a function of separation of the mirror pairs for horizontal (left) and vertical focusing (center). The overall transmission as a function of mirror separation (right).

There is significant freedom to assign the lengths of the first pair of mirrors since the focal length will not be fixed and will in fact vary over many meters as the system is adjusted. Optimization is done assuming 3 mrad incidence angles for all mirrors. To accept a single coherent mode at 5 keV x-ray energy (the longest coherence lengths the beamline will need to deal with), the system will require mirrors that are 62 mm long in the horizontal focusing direction and 142 mm in the vertical. To allow greater flexibility in selection of coherent modes delivered to the experiment, we will implement 350 mm long mirrors in each direction. These are sufficient to accept between 74% and 99% of the entire beam across the energy range in which the beamline will operate. Table 6.6 summarizes these fractions.

Table 6.6. Mirror pair 1 beam acceptance

Mirror acceptance	$L_{\mathrm{KB1H}} = 350$ **mm**			$L_{\mathrm{KB1V}} = 350$ **mm**		
	5 keV	10 keV	25 keV	5 keV	10 keV	25 keV
Brightness mode	77%	89%	97%	80%	92%	99%
Timing mode	78%	90%	98%	74%	85%	93%

The lengths of the final KB pair have multiple requirements. The downstream mirror will be the final horizontal focusing element. It needs to both meet the required spot size and working distance (50 mm) from the end of the mirror. The length of the second horizontal focusing mirror did not affect the ability of the vertical system to achieve the required spot size. It does however effect the final flux density. As the mirror length grows longer, the overall transmission increases as a function of first mirror focal distance, which determines the NA of the final mirror. But the required first mirror focal distance increases at a greater rate as the second mirror grows longer (needing a longer final focal length) and this leads to greater loss of photons at the smallest desired spot size of 50 nm. Optimization of the final horizontal mirror length, illustrated in Figure 6.11 (right), for flux density in the focal spot determined that 140 mm is the optimum length.

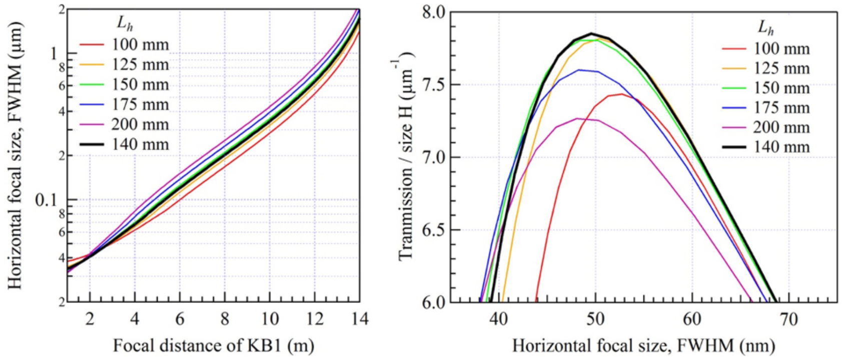

Figure 6.11. Final focal spot size (left) as a function of first focal distance for a range of second horizontal mirror lengths. The flux density in the horizontal (right) for different second horizontal mirror lengths.

Assuming 140 mm for the second horizontal mirror, it was found that the longest available mirror for the final vertical focusing is ideal, with 500 mm providing the required spot size and greatest flux density as shown in Figure 6.13. To be conservative, the system was optimized with a 400 mm second focusing mirror. Shadow-hybrid simulations were performed for the optimized configuration. The peak flux into a 50 nm spot is estimated to be about 4.9e12 ph/s. This flux would permit 3D atomic resolution imaging in about 1000 seconds based on the estimates in Dietze et al.[6]. The final simulated spot is shown in Figure 6.12 both for a perfect mirror and in the case of a presumed figure error in the mirrors.

Since the entire mirror system will be tunable, there is one more knob that can be turned to improve the total transmission of the system. One can adjust the incidence angles of the mirrors to increase

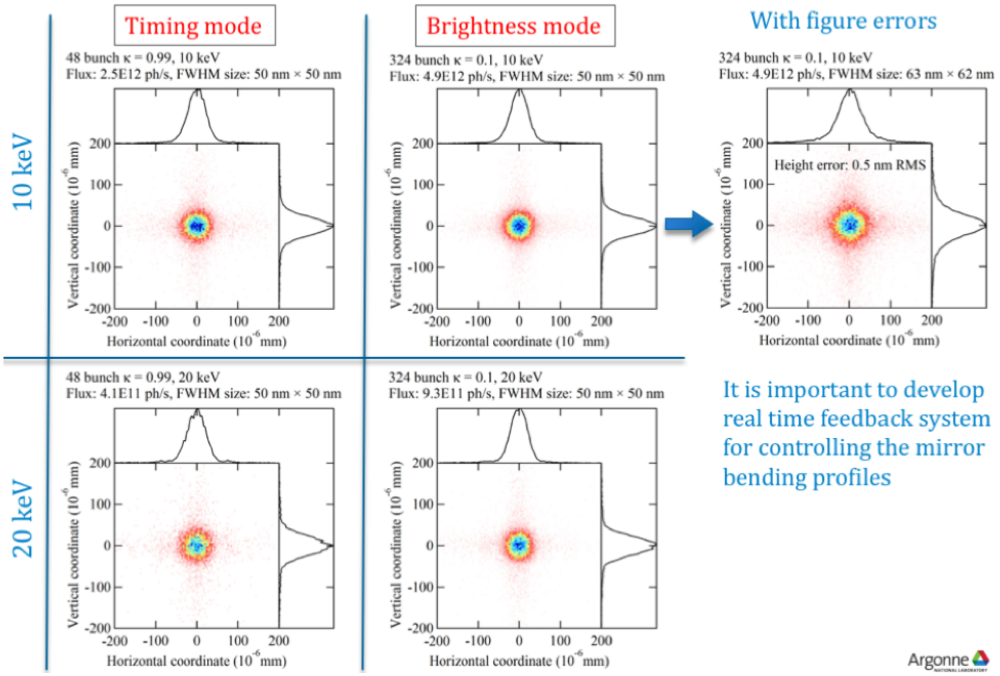

It is important to develop real time feedback system for controlling the mirror bending profiles

Figure 6.12. Shadow-Hybrid simulation of optimized configuration at 10 keV and 20 keV x-ray energy.

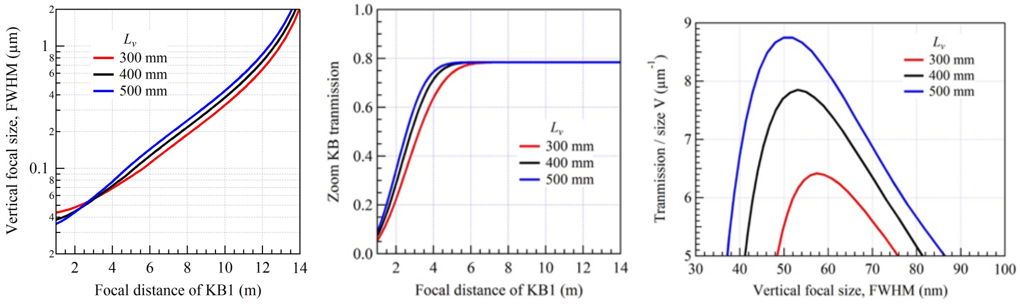

Figure 6.13. (Left) Vertical focal size on abscissa, as a function of first mirror focal distance. (middle) The total system transmission as a function of first mirror focal distance (or final spot size since they are directly related) shown for several vertical focusing mirror lengths. (right) the flux density in the vertical for several second vertical mirror focal lengths.

their total acceptance. For instance, when running at 10 keV for experiments, the incidence angle of all mirrors can be set to 5 mrad instead of the 3 mrad specified to allow the full x-ray energy range of the beamline to pass. The results of simulations for 3 mrad, 4 mrad and 5 mrad incidence angles for all mirrors are shown in Figure 6.14. In addition to greater total transmission, greater incidence angles may enable spot sizes smaller than 50 nm.

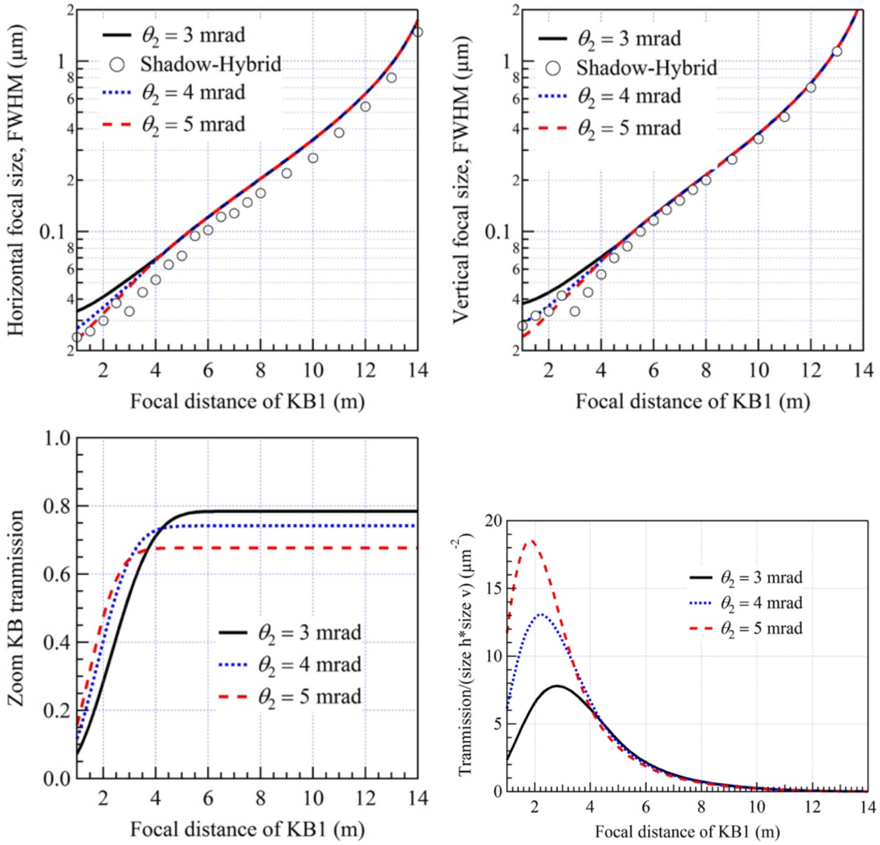

Figure 6.14. Effect of mirror angle on the final focused flux density.

Changing the incidence angles of the first mirror pair will necessarily require the positions of the second mirror pair to be shifted to intercept the beam. Common knowledge would discourage the addition of translation stages under the mirrors due to presumed poor stability of another motion axis. Recently however, translation stages composed of granite and air bearings have been implemented on the Velociprobe prototype instrument at APS. These stages have shown micrometer repeatability and a high degree of stability. Figure 6.15 shows a photo of the Velociprobe instrument. One can identify the vertical wedge axis and the translating gantry on top which positions the optics relative to the sample stages.

There will be precision apertures at strategic positions between the KB pairs to apodize the intermediate focus. Khakurel et al. have shown that the slit diffraction pattern, which is demagnified by the KB pairs, is sufficiently intense to strongly affect the visibility of the coherent diffraction pattern. As a result, the detector distances must be increased dramatically to oversample the diffraction pattern of not just the central bright spot, but also the side lobes of the incident beam. As shown in Figures 6.16 and 6.17 apodizing slits at the intermediate focus solves this problem. Our apodizing

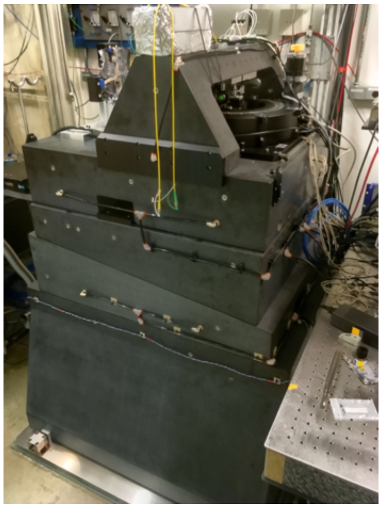

Figure 6.15. The Velociprobe instrument at APS with stable granite components capable of micrometer reproducible movements.

slits will be either strategically placed to take advantage of the most commonly used spot sizes or carefully designed to be translated parallel to the beam without interfering in the beam offset of the micro/nano instrumentation.

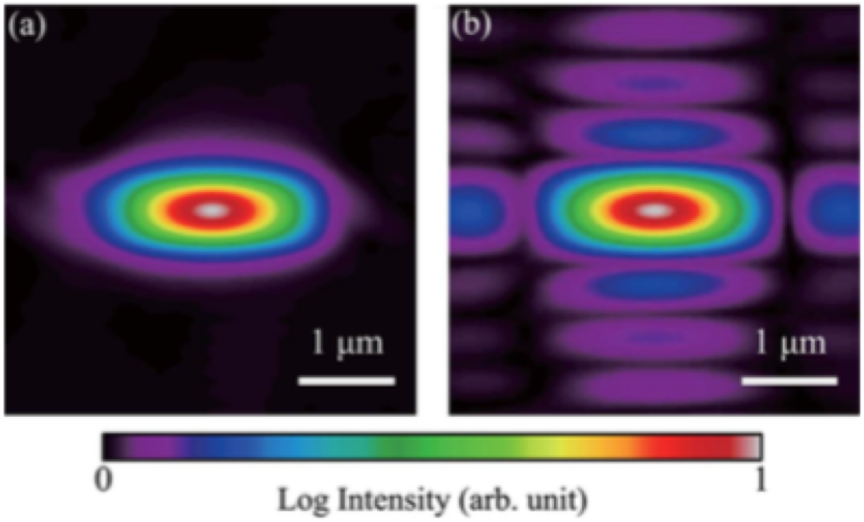

Figure 6.16. Simulated focal spots from an apodized (left) and non-apodized (right) zoom KB system.

Instruments

Goniometer Recording the huge volumes of reciprocal space for atomic resolution will require that the alignment between the sample and the beam is maintained with high accuracy, even while the sample is rotated relative to the beam. In the more modest resolution imaging case, crystalline samples will require orientation afforded by a three-axis goniometer. It is anticipated that scan

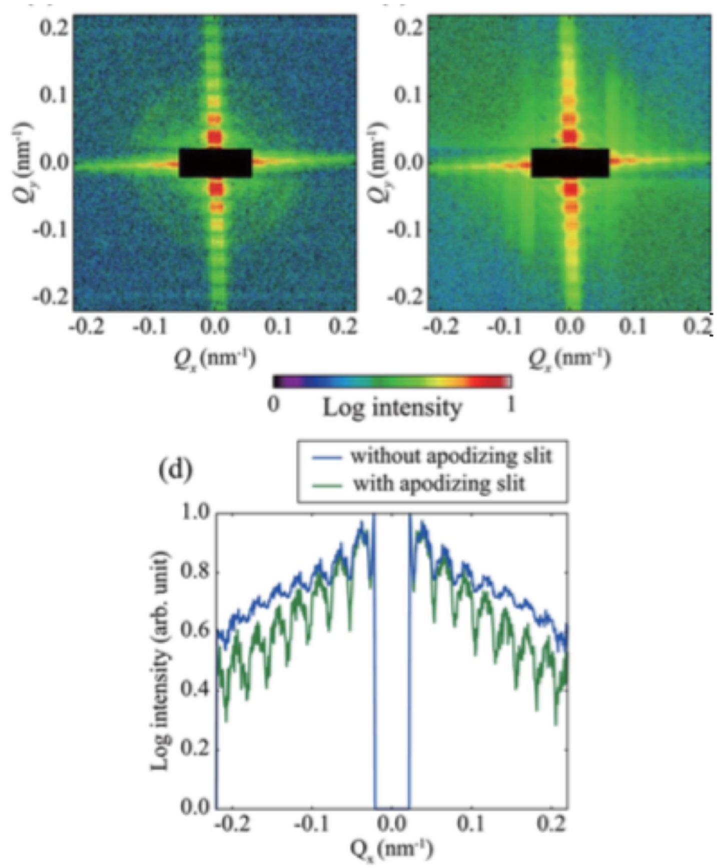

Figure 6.17. Experimental coherent diffraction measured from apodized (top left) and non-apodized(top right) zoom KB mirrors. The lower plot illustrates the remarkable improvement in diffraction pattern visibility.

times will be on the order of one hour for our highest resolution imaging. Therefore, the goniometer will need stability of tens of nanometers over this time scale. This will require the development of an ultra-stable goniometer. Previously, an inverted joystick goniometer was developed, shown in Figure 6.18, for ultra-precise orientation of an centimeter scale analyzer crystal[9]. This device may prove to be inherently stable and scalable to experimental dimensions. With only three points of contact supporting the moving surface, and the ability to produce a highly polished hemispherical cradle, one may envision an extremely stable, highly characterized, low eccentricity, three axis goniometer where the traditional "sphere of confusion" is not a concern. As a reference, the Hubble space telescope mirror has a figure error of about 30 nanometers. So such a spec may therefore be achieved for the hemispherical cradle of this goniometer.

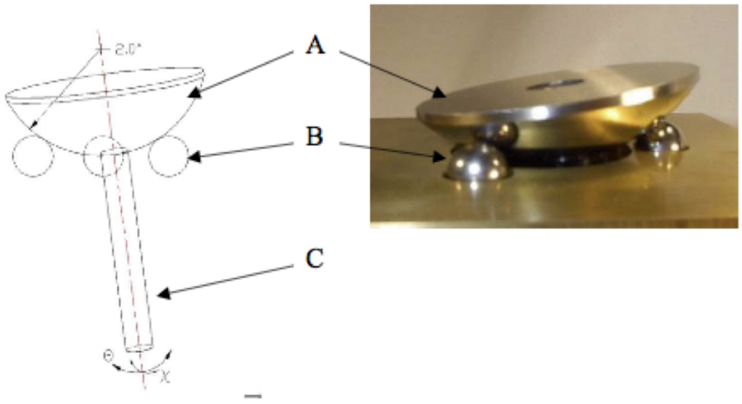

Figure 6.18. An example of an inverse-joystick goniometer. A third axis could easily be added by rotating the hemisphere about a line parallel to the joystick arm[9].

On top of the goniometer there will be three axes of sample positioning to ensure the sample is placed at the center of rotation (COR) and in the x-ray beam. The stages may be flexural construction with several millimeters of range and nanometer incremental stepping capability. The actuators will also need to be controlled in a manor in which continuous (fly) scanning can be accomplished. To accommodate various sample environments on top of the stages, they will need to be low profile and able to support a substantial load(>1kg). Sample environments with integrated positioning will also be explored. A discussion of opportunities for sample-beam position registration is included below.

Beam-sample position monitor Currently, CDI measurements are done with a beam that overfills the sample, often by more than a factor of two. Therefore, small motions of the sample in the beam simply do not matter and the stability of the entire instrument is somewhat less critical. At ATOMIC the beam size is intended to be optimized to the sample, or through ptychography, to the area of interest in the sample. Monitoring the sample-beam position will be critical to optimizing the measurements.

There are several options for this that can be explored. The exit window of the KB system could be an x-ray BPM. Diamond photon BPMs have been demonstrated with 50nm rms accuracy and may achieve the 15 nm limit given by the noise floor of the RF sensors used in the design[37]. The entrance window for an environmental cell could also be an integrated photon BPM. BPMs could also be integrated with the goniometer and inserted into the beam once the sample is oriented, and then readout can be gated against intentional motions of the sample angles.

It is also possible to monitor the position of the proposed spherical goniometer relative to the cradle in which it sits with very high accuracy. Similarly, the positions of the top of the sample stages relative to the platform of the goniometer can be monitored through interferometry. The accuracy by which the position of the composite system can be determined will need to be explored.

Detector positioning Several diffraction beamlines around the world have explored the use of robotic arms for detector positioning. The current systems have not been extremely well integrated as complete diffractometers. Since ATOMIC will not target single view imaging of samples larger than 1.5μm (larger samples being imaged via ptychography), it is not anticipated that detector distances in excess of 5m will be needed. This is well within range of a purpose build conventional two circle detector arm.

The diffractometer recently installed at ESRF ID-1 is a model for how a modern diffractometer can be built. The system is composed of an intertwined large detector arm with a granite platform to hold the sample manipulation stages and final optics for the experiment. The detector positioning is completely separated from the platform for the sample and optics. Only the floor can transmit vibrations from one to the other, and this can be minimized by placing the granite on a bed of sand for instance. Figure 6.19 is an image of the ID-1 diffractometer. The granite block and separate detector circles are visible. ATOMIC is will implement a similar design optimized for the goniometer and optics.

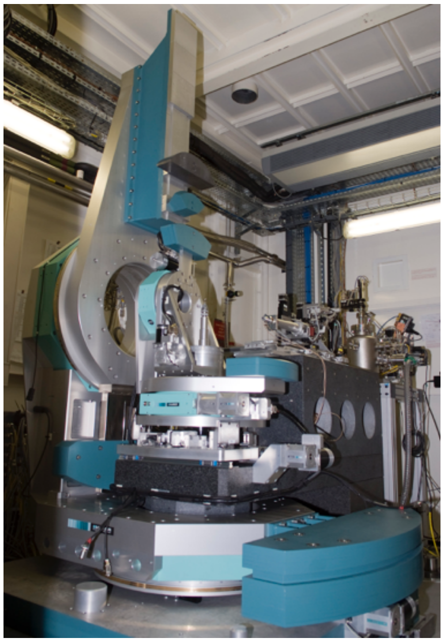

Figure 6.19. The new diffractometer at ESRF ID1. The black granite block supports both the x-ray optics and sample manipulations. The detector circles are completely separated from the optics and sample platform.

6-2.4.3 Additional

Detectors

The greatest photon density expected on the detector is the fully transmitted coherent beam with the zoom KB system configured for the largest spot size (least divergence) assuming minimal absorption by the sample. Even for the 50 nm focusing, the divergence is about 2.3x2.5 mrad, so at a detector distance 0.2 m (slighter greater than factor three oversampling of a 50 nm object) the beam striking the detector is about 460x500 μm. This leads to very poor flux per pixel at 12 keV. The 50 nm beam with no attenuation falling on a 75 um pixel detector would impart 7e10 ph/s/pixel onto the detector. For the 1.5 um focusing, the divergence is about 65x70 μrad, so at 4 m detector distance the beam occupies about 260x280 μm on the detector. The flux in this case will fall on just sixteen 75 μm pixels and be completely unmanageable at 2.0e11 ph/sec/pixel.

In practice, the photon density will not be this severe, but even modern, off-the-shelf detectors like Eiger from Dectris can only linearly detect about 3e6 ph/s/pixel, based on specifications published on the Dectris web page. The unattenuated flux of the APS-U is still out of reach to even cutting edge detectors today. The best count rate achieved by a detector today is about 1x10^8 ph/sex/pixel [38].

It must be emphasized that current, off-the-shelf, detectors are not going to be capable of dealing with the signals the APS-U will produce. Only the cutting edge detectors of today can even come close. There needs to be investment in advancing the cutting edge of today to the workhorse detector of the APS-U era.

An estimation of the required distance of a detector can be made using the formula for the spacing of the fringes of a single-slit diffraction pattern, or sinc function.

$$sample\ size = \frac{\lambda * det\ dist}{fringe\ spacing}$$

Assuming 75 μm pixels and a sampling criterion of three pixels between speckles (bright – dark – bright) at 12 keV for the intended range of x-ray spot sizes, a detector distance of 0.112 meters for 50 nm spot and 3.375 meters for a 1.5 μm sample is calculated. Typically, data is sampled at greater than the theoretical minimum required for the method. Higher-order Bragg peaks give a linearly greater sensitivity to lattice distortions in the sample. For example, to reach the next-order Bragg peaks in gold (333 and 400) at 12 keV, the two-theta angles are 60 - 80 degrees.

Computing & Controls & Data Acquisition

For Bragg CDI, the phase-retrieval step represents perhaps the most challenging part for the non-specialist user. As such, we plan to provide a standard set of algorithms that are known to work well in a diverse set of applications.

Currently the most effective phase retrieval methods in use for CDI are based on a genetic algorithm that begins by using the data with different sets of random phases to form the first population of images. The population (anywhere between 5-50 independent starts) is then iterated using a combination of Error Reduction (ER)[39] (the original Gerchberg-Saxton algorithm) and the Hybrid Input-Output (HIO) algorithm prescribed to Fienup[39]. Every 5 iterations, the support is updated via the shrinkwrap method[40]. The procedure continuously switches between 10-20 iterations of ER followed by 90-100 iterations of HIO. This is repeated 3-4 times for each member of the population of images. After the final iteration, the best member of the population is chosen according to a particular metric. For highly strained crystals, selecting the best reconstruction according to the "sharpness metric" has been shown to converge to the correct image with a higher success rate than using the standard error metric as a criterion[41]. The sharpness metric is only effective in the case of a sample with uniform density throughout, however. Therefore, the user will need to choose the metric based on the sample at hand and anything that is known about the sample. Once the best member of the population has been selected, it is combined with each of the other images to form the next generation and the entire process is repeated. Typically, running 5-50 population members for 5-10 generations to get the final image is advised. This is computationally intensive, so we plan to run a reduced version of this to provide lower confidence images as the data is being taken at the beamline. The ptychography phase retrieval needs of ATOMIC will mirror those of the Ptychoprobe and In-situ Nanoprobe beamlines. In this regard there will be a strong synergy and cooperation in technical development.

Data from the current CDI beamline at APS provides useful examples. In a population of 3 random initial images run for 3 generations of the phasing algorithms, using an array size of 256x256x64, the algorithm can run one member of the population in about two seconds on an NVIDIA Titan Black GPU card interfaced with the MATLAB GPU computing toolbox. A factor of 10 improvement in speed is expected by porting the code to a dedicated compiled C++ library. The best data collected in recent runs at 34-ID-C are too large for the memory of a Tesla K40 GPU card to run the HIO algorithm.

Finally, because each member of the population does not depend on any other member, each GPU card can iterate on as many members of the population of images as can fit in memory on the card. We expect that this should allow a good quality image to be reconstructed in minutes after the data is taken. This length of time is key as it allows the users to decide if the crystal under investigation is "good enough" and/or gauge how quickly the dynamics under study are happening and adjust the experiment to maximize beam time accordingly.

In addition to improving the speed of the phase retrieval algorithms, a fully dedicated pipeline for data transfer and phase retrieval will be developed. With data rates expected to exceed five data sets per minute, the time required to convert those data sets into images becomes prodigious.

6-2.5 R&D Needs

The main technical areas that have been identified for investment in research and development (R&D) are the zoom KB focusing system, the high stability, low-eccentricity goniometer for the diffractometer, and CDI phase retrieval algorithms optimized for both speed and ease of use in CDI.

A key R&D question to address is the feasibility of scaling up the Matsuyama et al. variable numerical aperture zoom KB design to achieve the numerical aperture (NA) required to deliver a 50 nm spot to the sample with a working distance of 50 mm in a functional instrument for user experiments. The proposed system will include *in situ* profile monitoring to maintain the state of the system and enable near real-time zoom capabilities without a need to realign the beam and sample when the spot size is modified.

Specifications for the sample goniometer were included above, as well as ideas for implementation. Conventional wisdom says that it is impossible to accurately monitor, and provide feedback, on a position on top of a multi-axis goniometer. We believe that a path towards achieving this is afforded by the inverse joystick goniometer, but research and development will be necessary to determine the limits of this capability.

There is significant room for improvement in the genetic algorithms used in CDI phase retrieval. New fitness metrics will need to be developed for guiding the population to a high confidence solution of arbitrary samples. Perhaps metrics with atomistic constraints will be necessary for the very highest resolution datasets. For example, users have observed current GA metrics are insufficient when networks of dislocations are present in the sample. This requires further investigation. Entirely new concepts for coherent diffraction data analysis need to be explored. For example, one could return to the old days of fitting data to a model, but now do this with a library of models composed of atomistic structures formulated from molecular statics simulations of materials properties. The fitting could be done by machine learning techniques such as the convolutional neural networks to directly interrogate the features present in the data sets and piece together an image of the sample, based on knowledge acquired from the library of models and previous data sets from the material of interest.

ATOMIC will deliver an extremely high photon flux density on-sample, approaching $2 \text{x} 10^9$ ph/s/nm^2. Based on a growing body of experimental evidence [24], as well as quantitative estimates [25, 42], we expect that this flux density will be significantly above the threshold for causing observable radiation damage in most soft condensed materials and many hard materials. R&D will be necessary to determine the limits of signal vs. radiation dose to scale up to experiments with ATOMIC. In addition, the power in the focused beam (8.0 mW over an area of 50 x 50 nm^2 at 10 keV) will be significant even when only a small fraction of this power is absorbed by the sample. Thermal management of samples will, for the first time, become important for some experiments. We will aggressively investigate strategies to mitigate radiation damage and thermally induced changes to samples, including use of inert and reducing gaseous environments, electrochemical protectants, and cryo-preservation where appropriate.

6-3 The 3D Micro Nano Diffraction

6-3.1 Executive Summary

The 3D Micro & Nano Diffraction beamline is designed to directly address a wide range of spatially inhomogeneous materials problems at the mesoscopic length scale. These are problems in materials science, physics, geoscience, and most other fields of science where previous x-ray diffraction techniques are insufficient due to the short length scale of the inhomogeneities in the materials. This inhomogeneity is an important or intrinsic part of the material's properties, and so must be studied on its length scale; large perfect samples are either impossible to make or do not represent the real material. Due to the current extreme difficulty or impossibility of making these measurements we plan to use the bright APS-U source to provide small intense x-ray spots (50 –200 nm) to investigate the important spatial variations of strain and structure that define this wide range of scientifically and technologically important materials.

6-3.2 Scientific Objectives & Capabilities

6-3.2.1 Science Case for Beamline

In the first part of the last century, great advances were made in understanding the mechanical and electrical properties of materials by assuming a simple perfect crystal structure. However, it was always recognized that the real properties of a material often depend critically upon the defects and spatial inhomogeneities that were either induced or inherent in the material. For example, the strength of copper changes drastically with even the simplest work hardening, and in strongly correlated electron systems, local phase separation and competition give rise to exotic macroscopic electronic properties such as colossal magnetoresistance (CMR), or ferroelectric domains to name just two. For these and many other examples, just knowing the average strain or the average structure is not sufficient for understanding the new and interesting properties; one needs to know the local spatial distribution of strain and structure. The common theme in all of these cases is that inhomogeneous local interactions give rise to fundamentally interesting and technologically important physical phenomena. Moreover, in all of these cases, the "3D micro-and nano-diffraction" capabilities provided by this beamline will provide critically needed, previously unavailable, quantitative descriptions of these local mesoscopic interactions. Illuminating the underlying microstructural mechanisms is imperative for understanding materials behavior, guiding the development of new materials, improved processing techniques and developing predictive modeling capabilities.

The very small x-ray beams will provide the resolution in both real-space and reciprocal-space to address scientific problems such as: The distribution and evolution of crystalline defects (e.g. dislocations) and elastic strains at the nanometer and micrometer length scales within deformed metallic structures that have broad implications for developing a better understanding of mechanical behavior as a function of plastic deformation. The ability to probe high-pressure materials in diamond anvil cells at even higher pressures, and thus smaller samples sizes. The internal strains in different types of electronic devices. The internal strains in complex oxide materials occurring in nanoelectronic devices, fuel cells, and novel ferroelectric devices, as well as the strains leading to phase separation in new complex oxides. To spatially resolve the internal strains that occur in the novel microstructures arising from additive manufacturing. Coherent scattering from embedded precipitates to determine the precipitates internal strain and orientation.

6-3.2.2 User Community/Stakeholders

The techniques and capabilities in this proposal are extremely versatile and will provide opportunities in almost all branches of materials-related science. The option to use either monochromatic or polychromatic focused beams greatly expands the range of science and samples that can be investigated. Previous and ongoing work at 34-ID and 2-ID has already appealed to many different areas in materials physics, including mechanical properties in metals, correlated electron behaviors in complex oxides, semiconductor device physics, structure inside individual nanocrystals, and high-pressure research.

The proposed beamline would greatly benefit the metals deformation community. The 3D microdiffraction capabilities represent the only experimental technique that allows both scanned polychromatic and monochromatic operations, thus enabling both orientation and *absolute* lattice parameters ($\Delta d/d=10^{-4}$) from depth-resolved sample volumes. As one example of the new measurement capabilities possible with this instrument, experiments at 34-ID-E have already demonstrated the ability to measure all nine components of the elastic strain tensor from ~300 nm sample volumes within individual dislocation cell interiors, revealing unexpected and exciting large stress excursions that are not predicted by existing deformation theories. Refining these measurements to even smaller length scales (with volumes ~100 nm across) would allow researchers to extend strain tensor measurements to the critical dislocation cell wall structures where these stresses originate.

As an example of the importance of this instrument to the user community, NIST has committed to spend at least $500 K over the next few years to work with APS staff to develop and install an *in situ* nanoindentation system on 34-ID-E. This new nanoindenter system will provide an unprecedented look at how metal systems deform *in situ* during nanoindentation. In addition, *in situ* nanoindentation measurements on semiconductor materials such as Si would also allow direct identification of the mysterious transient high-pressure phases that develop under the nanoindenter.

The submicron and 3D facilities will provide new scientific opportunities in many other areas involving mechanical properties, including fracture, creep, crack propagation, advanced ceramics and alloy development. For example, developing a polychromatic nano-diffraction (~50 nm) user capability would also allow groundbreaking studies on new advanced alloy systems including additive manufacturing that are now being developed for industrial use. Many of these alloys (especially advanced high-strength steels) have extremely complex microstructures with multiple phases, partially lamellar microstructures, and precipitates. These small-scale microstructural features work together to provide the high strength/weight ratio, formability and crash worthiness characteristics necessary for improved mileage and safety in next-generation automotive applications. The high spatial resolution of the nano-diffraction instrument would allow the interplay between these microstructural features to be explored directly, providing unparalleled information for guiding the development of these advanced materials.

The condensed matter physics community is actively engaged as users of submicron diffraction capabilities and will benefit tremendously from the availability of smaller beams, particularly in areas involving strongly-correlated electron systems. This community appreciates the underlying role of nanoscale phase separation and competition in the emergence of fundamentally interesting and technologically useful exotic macroscopic electronic properties. Phenomena such as colossal magnetoresistance (CMR), ferroelectric domain switching, multiferroics, metal-insulator transitions, phase change materials and superconductivity all provide exciting scientific challenges and potential for novel applications. In all of these phenomena, local structural inhomogeneities are believed to play a central, controlling role.[43] The high-resolution local probes proposed for 34-ID will be ideally suited for studies revealing how domain and phase interactions give rise to these emergent behaviors. In many cases, the relevant length scales are of order ~50-100 nm. Thus, the proposed implementation of both polychromatic and monochromatic nano-diffraction instruments will be an ideal match to the needs of this community. Other condensed matter research areas which will benefit directly from the proposed submicron and 3D diffraction capabilities include high-pressure research, studies on solar cell photovoltaic efficiency [44] and understanding epitaxial film growth mechanisms.[45] The condensed matter community has also benefited greatly from various scanning probe microscopies (e.g. piezo force microscopy), and the APS may wish to consider incorporating an *in-situ* scanning probe instrument at 34-ID in the future.

The nanoscience and nanotechnology communities will likely realize the most direct benefit from the development of polychromatic and monochromatic nano-diffraction capabilities at 34-ID. Although this community is broadly-defined and overlaps somewhat with other communities, the need for quantitative characterization of nanostructures is the justification for co-locating the Center for Nanoscale Materials (CNM) with the APS. This community is already well acquainted with high-resolution imaging using electron-based imaging techniques, but realizes the need for quantitative, penetrating, nondestructive, imaging instruments. The availability of a polychromatic probe will enable studies of randomly aligned nanostructures. Examples of nanoscience research which will be enabled by the proposed nano- and 3D diffraction capabilities include strain mapping in CMOS semiconductor devices with ~30 nm features as described above and interfacial structural changes due to dynamic ionic conductivity that are relevant to applications in fuel cells, batteries and catalysts.

We are convinced that the impact on research communities will eventually extend to all branches of materials-related science. The growth of community involvement is often related to the flexibility and availability of a technique. The proposed 3D micro- and nano-diffraction tools are extremely versatile, but are limited in availability. The 3D polychromatic approach provides the Laue diffraction pattern generated by each submicron volume element within a sample (i.e. point-to-point scanning). The class of all materials with crystalline (or semi-crystalline) grains in the 40 nm to few μm range is incredibly broad. We believe that the scientific impact of submicron techniques at 34-ID on a wider range of disciplines has in the past been constrained primarily by user beam time availability. The cutoff for proposals receiving time at 34-ID-E has typically been a rating of 1.4 (closer to “extraordinary” than to “excellent”) in recent cycles. Thus, excellent science is being delayed or rejected. We expect that new micro- nano-diffraction capabilities should only attract new users, and provide the existing users with more opportunities for exciting science. We believe that this facility will also attract users from diverse materials communities including geosciences, environmental science, biology, biomaterials, archeology, and art history. Local structural inhomogeneities control materials properties and performance in all of these disciplines. Geologists and environmental scientists need 3D maps to reveal mineral interactions; bones are hierarchical structures containing nanocrystals; and archaeologists and art historians need nondestructive characterization to understand past techniques involving material processing.

With the closing of 2-ID-D to micro-diffraction, there is now an influx of displaced users with micro-diffraction experiments requiring a probe under 200 nm. So the user base for the current 34-ID-E facility is expected to grow significantly in just the next few months, and the enhanced capability provided by the upgrade (smaller spots and greater intensity) will only increase the demand.

All of the current users that have been contacted are all strongly in favor of improving their favorite instrument by a factor of 100. To quote Conal Murray from IBM, "a smaller spot size will be very important to our efforts as the volumes we need to interrogate are also shrinking."

The white/monochromatic micro-diffraction beamline with depth resolution (giving 3D volumes of strain and orientation) currently operating at the APS is unique in the world. Increasing it efficiency by more than a factor of 100 should cement its place as the world leader. For descriptions see [46, 47, 48, 49]

In April 2017, there was a workshop to engage users that attracted many current and potentially future users of this planned facility. This includes scientific programs that were not even mentioned in the scientific case.

6-3.2.3 Use of APS-U Characteristics

The most obvious characteristic of the APS Upgrade is the MBA lattice. The MBA lattice is designed to provide an x-ray source that is ~100 times brighter than the existing source.

The prime characteristic of this proposal is its use of a suite of small-beam, scanning probes with diameters of 50 nm to ~150 nm. This small probe is obtained by creating an image of the source at the sample position. For an imaging optic at 62 m from the source with a focal length of 150 mm, the spot at the sample will be an image of the source demagnified by a factor of 62/0.150 = 413. So, a 27 μm FWHM source size becomes a 65 nm spot at the sample. The brighter the source, the brighter the focused spot. Further, this decrease in probe size is accompanied by an increase in the intensity. Since the source has a smaller divergence, more of the emitted x-rays hit a Kirkpatrick-Baez (K-B) mirror of a given size, so the intensity increases. In general, the total brightness of the focused x-ray spot should scale as the brightness of the undulator source, again because the spot is an image of the source. This discussion of beam intensity and spot size is exactly the same whether the focusing optic is a K-B mirror pair, a zone plate, or a compound refractive lens; increases in source brightness transfer directly to an increased brightness in the focused spot.

The greatly increased coherence of the incident beam is another prime characteristic of the MBA source. As mentioned in section G of the science case above, there are coherent scattering experiments planned for this beamline. Measurements taken at 34ID-E with the current differentially deposited K-B mirrors at 8 keV showed a horizontal coherence length of $\xi_\mathrm{h} > 50$ μm with 50 μm horizontal slit at 28 m which decreased to $\xi_\mathrm{h} = 26$ μm after opening the slit to 250 μm. In the vertical direction, the coherence length was $\xi_\mathrm{v} = 35$ μm without any vertical slit. This unexpectedly small vertical coherence length was attributed to vertical vibrations in the monochromator. With a more stable monochromator, the vertical coherence length should increase. Using the focused beam (the D-station at 62 m) for coherent scattering should only require the installation of a suitable area detector that can be located 2 – 3 m from the sample and positioned to intercept the diffracted beam

6-3.2.4 Key Beamline Characteristics

The micro-nano diffraction project will consist of two instruments on one canted beam line. All windows will be carefully designed to preserve the wavefront to ensure that the source characteristics are not deteriorated. Upstream of the monochromator there should only be slits or differentially pumped apertures and one LN2 cooled Si mirror.

The first station at 60 m will be for micro-diffraction. It will provide pink or monochromatic x-rays focused into a <200 nm spot with a large working distance. The monochromator will be designed so that it can be switched between pink and monochromatic beams in a few seconds. This monochromator will feed both instruments in the experimental station. The focused spot should not move (or move in a predictable manner) when switching between pink and monochromatic modes. Thus, the *same* location on the sample can be examined with pink and mono beams. The desired monochromatic energy range is [5.3 – 30] keV. 5.3 keV gives access to elemental edges down to Vanadium. The high energy of 30 keV is set by the critical angle of the mirrors. Although the critical energy of the mirrors is less than 30 keV, there is still some usable flux up to 30 keV.

The second station at 66 m will be for nano-diffraction. It will again provide pink or monochromatic x-rays focused into a ~50 nm spot and a reduced working distance. The focused spot again should not move (or move in a predictable manner) when switching between pink and monochromatic modes. Thus, the *same* location on the sample can be examined with pink and mono beams. The desired monochromatic energy is again [5.3 – 30] keV.

The monochromator (which should be substantially identical to the one on the neighboring ATOMIC beam line) will be similar to the existing small offset monochromator currently located in 34-ID-D. A redesign of the existing monochromator will be needed to provide the clearance for the x-ray beam of the inboard canted line, and to improve stability, and speed and repeatability when changing or scanning energy. Both monochromators must be *very* stable so that the projected source does not appear to move which would degrade the focused spot and the coherence.

Both instruments will require a sample stage with ~10 nm resolution capable of supporting and scanning both small samples and more substantial environmental cells (e.g. diamond anvil cells). A scanning knife-edge stage will also be required with <10 nm resolution but a longer travel and smaller load capacity than the sample stage. All stages and supports must be stable and scannable.

The expected flux for pink beam is ~10^{14} (ph s^{-1}) and for monochromatic beam it is ~10^{12} (ph s^{-1}). This is approximately 50 times greater than current operations with a 500 nm spot size.

In addition to the factor of 100 that comes from the MBA, there are also three other areas where an additional enhancement is planned.

Improved K-B Mirrors

The current K-B mirrors are spherical Si substrates that have been differentially coated with Pt to provide the desired elliptical figure. These mirrors currently provide a spot size of only ~500 nm, and then only when apertured to ~60 x 60 μm^2. By obtaining state of the art mirrors we will not only be able to reach a smaller spot size, but we can simultaneously open the 60 μm aperture to fully illuminate the mirrors while increasing the flux by a factor of ~9 without degrading the spot size.

Multiple Knife-Edge Structure, or Coded Aperture

The current knife-edge is used to provide depth resolution that is a key feature of both the current and new beamlines. When scanning the knife-edge, the step size is determined from the desired depth resolution, but the distance of the scan is determined mostly by the width of the angular fan hitting the detector. With a smaller spot, we will need a correspondingly finer depth resolution, and thus a smaller step size in a knife-edge scan. However, the angular range on the detector is not changed, and so the length of the scan is also unchanged. Thus a resolution improvement from 500 nm to 100 nm will require 5 times as many images at each sample position. To alleviate this problem, we propose to make a structure comprising multiple knife-edges spaced to cover the entire angular range but only requiring a scan with 1/5 as many positions. This is similar to a coded aperture used in x-ray astronomy, but simpler since this is only a 1D problem.

Improved Detector

The current amorphous Si area detectors have a large thermal noise that makes it difficult to measure weak signals. One method to measure weak signals contaminated with noise is to increase the counting time. This problem will become more acute as the required depth resolution shrinks and the signals get weaker. In general, the diffracted intensity goes down by the volume of material, but we suffer no reduction as we focus the x-rays to smaller sizes since no photons are lost. However, as we reduce the desired depth resolution the scattering does decrease linearly with the depth resolution. So, a factor of 5 reduction in depth resolution will mean a factor of 5 reduction in scattered signal strength. With a resolution of 100 nm, all of our samples will look 5 times weaker than at 500 nm resolution. The solution to this is to use a pixel detector where the noise is intrinsically much lower and the frame rate is high enough to make efficient use of our intense focused beam. The improvement from this detector is hard to estimate, but it will probably lie in the range of X5 - X15 depending upon the experiment.

With a factor of 100 increase from the MBA, a factor of 9 from better K-B mirrors, a factor of 5 from the knife-edge structure, and a factor 10 from the detector we anticipate an overall enhancement of 100x9 = 900 for most experiments, 900x5 = 4,500 for many experiments and perhaps 4,500x10 = 45,000 for some experiments as compared to the current situation.

6-3.3 Source & Front-End Requirements

6-3.3.1 Insertion Device

The insertion device should be a standard undulator, probably of 27 mm period in a Multi-Bend-Achromat (MBA) storage ring running at ~6 GeV. This undulator will be, of course, tunable so that the undulator spectrum can match the monochromator setting. It should also provide for tapering to broaden the spectrum for measuring Laue patterns. The undulator gap will also be frequently scanned.

3dn:other-special-source-requirements.

6-3.3.2 Other special source requirements.

In addition to providing a beam to the monochromator, we will also focus the pink beam directly onto the sample, for the purpose of measuring standard Laue patterns from microscopic volume elements. For measuring Laue patterns on the top detector, most of the signal is in approximately the 12-17 keV range. In general, at lower energies, there are few reflections that scatter at a 2θ of 90°, and at higher energies the Q of the reflection is so large that the atomic form factor becomes weak. In monochromatic mode, a highly-peaked spectrum is obviously desirable, but in pink-beam mode a broader spectrum is preferred.

6-3.3.3 Front End Requirements

A standard front-end will be requested. A differentially pumped aperture at ~25 m will be preferred over a window to preserve the source brightness and beam coherence. However, a small diamond window would reduce the heat load on the LN2 cooled Si mirrors, this would be preferred if the diamond quality is high enough

6-3.4 Beamline Layout

6-3.4.1 X-ray Optical Layout

The basic optical layout of the two branches is shown in Figure 6.20. This section describes the basic beamline layouts, with more detailed specifications for the individual components given in later sections.

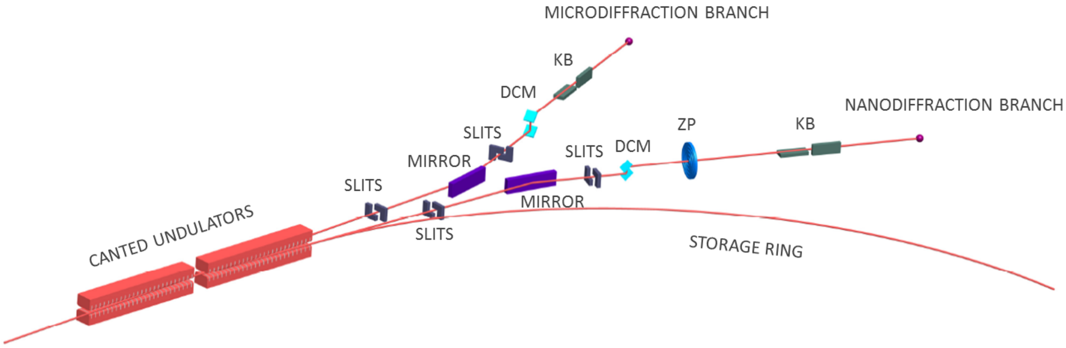

Figure 6.20. Basic optical layout of the two branch lines for micro-diffraction and nano-diffraction.

Since the IDs at Sector 34 are canted by only 1 mrad, two horizontal deflection mirrors in 34-ID-A will be used to further separate the 34-ID-D 3DMN beamline from 34-ID-E (ATOMIC) beamline. The existing liquid nitrogen (LN2)-cooled beam-splitting mirror, which is currently used for coherent diffraction activities on the outboard beamline, will be replaced by two LN2 cooled Si mirrors one deflecting outboard and one inboard to give a total of ~11 mrad between the two pink beams. These two LN2 cooled mirrors will need sufficient angular stability to not broaden the source, and also accurate surface figures. It may prove desirable to have the mirrors slightly curved to collimate the x-rays.

A switchable, small-offset Si 111 monochromator covering the energy range of 5.3–30 keV will be installed in the 34-ID-C optical enclosure to provide monochromatic x-rays to the 34-ID-D station. The monochromator will pass either a pink beam or a monochromatic beam (thus switchable) through the same exit slit and will be either water or LN2 cooled.

A K-B micro-focusing mirror instrument will be installed in the front of 34-ID-D for Laue micro-diffraction measurements in either polychromatic or monochromatic mode. The system will have a focal spot of <200 nm and should reach 100 nm with sufficient working distance for small environmental chambers.

A new K-B nano-focusing mirror system will be installed in the rear of 34-ID-D for Laue nano-diffraction measurements in either polychromatic or monochromatic mode. The system will have an initial focal spot of <100 nm with a future target of ∼50 nm.

This proposal envisions using the outboard branch of the existing 34-ID canted ID line with one large user enclosure for the experimental work, providing instruments at 60 m and 66 mm as shown in Figure 6.21. The existing 34-ID-D & 34-ID-E stations will be joined, and a 2 m extension will be added to the end to form the new larger 34-ID-D station. The front of D- station will have an instrument for the larger spot sizes of ≤200 nm with a working distance of ≥ 50 mm, and would contain a single pink or mono Kirkpatrick-Baez (K-B) mirror set used for 3D micro-diffraction. This upstream instrument will also be capable of performing some coherent diffraction measurements.

At the rear of the new D-station there will be a dedicated nano-diffraction instrument using a K-B nano-probe for ultra-high-resolution studies of advanced materials. The greater distance and reduced working distance will increase the demagnification providing a smaller spot size of ∼50 nm. This instrument will also require special temperature stabilization and likely an enclosed control area to maintain that stable temperature.

To provide a greater separation between the two canted beamlines there will be two LN2 cooled Si deflecting mirrors in the first white enclosure at ˜30 m providing a separation of ˜400 mm in the first user station (D- station). These mirrors may be either flat, or perhaps figured to provide some pre-focusing or collimation of the white beam. An additional reason for these mirrors is to protect the K-B focusing optics from the raw white radiation that can cause damage to the precisely figured K-B mirrors.

The micro-monochromator that currently feeds the existing 34-ID-E station will not be suitable for the new beam line because it cannot pass the inboard undulator beam, and it is not stable enough to preserve the increased brightness of the MBA. It will be necessary to build a slightly smaller micro-monochromator with enhanced stability to feed the user station. This will again use Si 111 crystals, and it should have a modest cost due the small size. This micro-monochromator will have negligible translational shift in the output over the desired 5.3–30 keV energy range. Additionally, the micro-monochromator can be automatically removed from the x-ray beam to send the pink beam down to the user instruments. Due to the similar specifications, the monochromator described here should be substantially similar to the one feeding the neighboring ATOMIC project on the inboard part of the cant (ATOMIC will use the new 34-ID-E station).

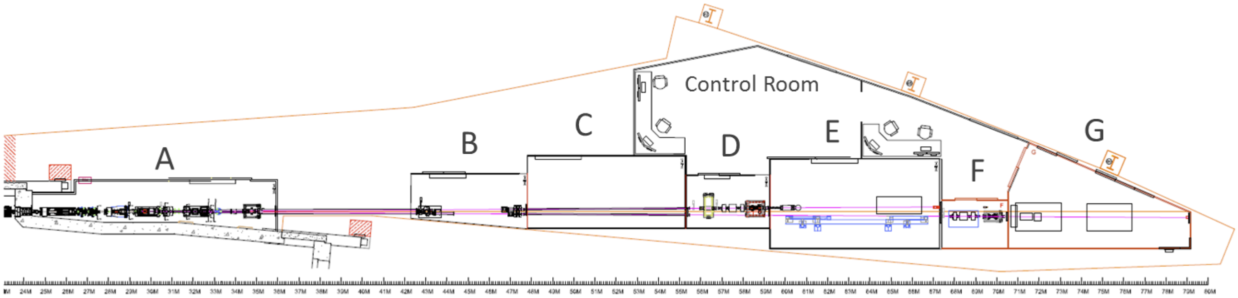

Figure 6.21. Possible sector 34 layout showing user experimental stations in E and G and new LN2 cooled Si mirrors in A. Micro-monochromators are located in C. Stations A-E already exist, F & G would be new construction.Possible sector 34 layout showing user experimental stations in E and G and new LN2 cooled Si mirrors in A. Micro-monochromators are located in D and F. Stations A-E already exist, F & G would be new construction.

Stability of the K-B mirror mounts are extremely important, and this is currently being evaluated by using a new flexure based mirror stage that has been recently installed at the current 34-ID-E.

The instrument at ~60 m will be a fairly standard K-B mirror system feeding an xyz sample stage with a scanning knife-edge. Using state of the art mirrors, this system should provide a ≤ 150 nm spot with a ≥ 50 mm working distance. This could accommodate *in-situ* experiments requiring small environmental chambers.

For the second user experimental instrument at 66 m, there will be a set of advanced K-B mirrors with ultra-low slope errors of ~0.05 μrad. This will bring the focal size down to $<$50 nm with a reasonable working distance of ~30 mm. A sample xyz stage and a scanning knife-edge (differential aperture) with 5 nm precision will be required for the measurement in all three dimensions. This system will also require a low noise detector (similar to a Pilatus 6M) to allow measurement of low intensity signals from the smaller volumes and from weaker scatters. Having a large solid-angle coverage and moderate pixel size is preferred.

Liquid Nitrogen Cooled Horizontally Deflecting Mirrors

To provide a greater separation between the two canted beamlines there will be two LN2 cooled Si deflecting mirrors at ~30 m providing a separation of ~400 mm in the first user station (D-station). These mirrors may be either flat, or perhaps slightly figured to provide some pre-focusing or collimation of the white beam. An additional reason for these mirrors is to protect the K-B focusing optics from the raw white radiation that can cause damage to figured K-B mirrors. They will require great stability, particularly against horizontal rotations. For a mirror at 30 m from the source, an rms rotational vibration of 0.8 μrad will broaden the source by 50 μm (which is the MBA source width). So, a horizontal rotational stability of 20 μrad will be required.

Heat load on these mirrors is an issue, that is why they are cooled by liquid nitrogen. This technique has proven adequate for the existing Bragg CDI program, and we intend to use the same technique in this project.

Monochromator

The micro-monochromator currently feeding the existing 34-ID-E station will not be suitable for the new beam line because it cannot pass the inboard undulator beam that feeds ATOMIC, and it is not stable enough to preserve the increased brightness of the MBA. It will be necessary to build a slightly different micro-monochromator with enhanced stability to feed the user station. This will again use Si 111 crystals, and it should have a modest cost due the small size. This micro-monochromator should provide negligible translational shift in the output over the desired 5.3–30 keV energy range. Additionally, the micro-monochromator can be automatically removed from the x-ray beam to send the pink beam down to the user instruments. This monochromator should be substantially similar to the one required for the ATOMIC project on the inboard part of the cant, and so a common design should be possible. The main undecided issue is whether to use water or LN2 cooling on the monochromator. Calculations need to be made whether water will be sufficient to avoid a thermal bump on the first crystal. If water cooling is insufficient, then LN2 will be used. We also need to decide upon the orientation, either horizontally deflecting or vertically deflecting. Traditional monochromators deflect vertically due to the smaller vertical source divergence and to avoid of losses due to the polarization correction $\sim cos^2(2\theta)$. With the MBA lattice, the source divergence is small in both directions, and at 5.3 keV, the polarization loss will be ~1/2, for 8 keV the loss is 1/4, and at 12 keV it is only 10%. The main reason for considering horizontal diffraction is the hope of improved angular stability with only a minor loss of efficiency [11]. The choice of 5.3 keV for the lower limit is governed partly by the geometry of getting the x-rays through the crystals, but mostly by the rapid increase in θ with decreasing energy. Note that increasing the monochromator upper-energy limit from 25 to 30 keV only changes the angular range by 0.75°, whereas changing the monochromator lower energy limit from 5.3 to 6.3 keV changes the angular range by a much larger 3.6°. The energy resolution of the usual Si 111 double bounce monochromator is $\Delta E/E \approx 10^{-4}$, which is well matched to the desired q-resolution. While desirable for a variety of experiments purposes, energies towards 5.3 keV are not as important as the somewhat higher energies to the overall mission of the beamline, and if compromises on energy range are required, the lower limit can be raised somewhat.

The main monochromator requirements are:
Switchable between white and pink beam with negligible exit beam motion
Small offset, ~1.1 mm.
White and pink beams exit the monochromator collinearly
Energy range 5.3–30 keV (although the low energy limit may be raised, if needed)
Rotational vibrational stability of 0.2 μrad rms about the θ axis
Sufficient cooling on first crystal to avoid a thermal bump.
Does not need to accept the entire beam (only < 300 X 300 μm^2 are needed).
Allow passage of neighboring canted beam.

K-B Mirrors

The K-B mirror optics will directly image the source in the undulator. A secondary source would allow better source control for the K-B optics, but at the expense of a reduced x-ray flux and added complexity. This design is matched to the MBA specifications. With the calculated source parameters, the expected spot sizes at the two instruments are summarized in Table 6.7 and Table 6.8.

Assuming one set of K-B mirrors at 62 m from the source with a horizontal fl = 70 mm and vertical fl = 142 mm. The following spot sizes for 48 and 324 bunch modes at 6 keV are calculated in Table 6.7. Note that the x-ray source size does have a small energy dependence, so at 16 keV, the source size will be ~15% *smaller* than the values in the table, and thus the sample spot sizes will also be reduced. The rms slope error for the K-B mirrors are assumed to be 0.1 μrad, which is currently commercially available.

Table 6.7. Focus at sample, FWHM at 62 m from source assuming mirrors with 0.1μrad rms slope error.

	source FWHM (μm)	**demag at 62 m**	**focus with 0.1μr rms (nm)**	**Diffraction limit (nm)**
48 Bunch				
Horiz.	43.6	886 (fl=70 mm)	52	52
Vert.	26.9	436 (fl=142 mm)	67.8	42
324 Bunch				
Horiz.	51	886	59.2	
Vert.	13	436	41.1	

This leaves 50 mm clearance between the end of the second K-B mirror and the sample spot. Increasing this clearance by another 40 mm increases the working distance, but reduces the demagnification. The horizontal demagnification reduces from 886 to 564, increasing the horizontal spot size from 52 to 80 nm and 59 to 93 nm. Similarly, the vertical demagnification is reduced from 436 to 341, giving vertical sizes of 87 and 53 nm. It may still be best to use the shorter 50 mm clearance to reduce the stability requirements on all of the optics, particularly the stability of mirror angles.

For the station at 66 m the horizontal fl is reduced to 55 mm, the vertical is reduced to 120 mm and the distance to the source increases changing the demagnification and producing the smaller spot sizes shown in Table 6.8. Note that the rms slope error is assumed to be only 0.05 μrad that is currently not guaranteed by the manufacturer, but should be obtainable.

Table 6.8. Focus at sample, FWHM at 66 m from source assuming mirrors with 0.05μrad rms slope error.

	source FWHM (μm)	**demag at 66 m**	**focus with 0.05μr rms (nm)**	**Diffraction limit (nm)**
48 Bunch				
Horiz.	43.6	1200 (fl=55 mm)	36.7	41
Vert.	26.9	550 (fl=120 mm)	50.4	37
324 Bunch				
Horiz.	51	1200	42.8	
Vert.	13	550	26.5	

Using the focused beam (in the 62 m station) for coherent scattering only requires the installation of a suitable area detector that can be located 2 – 3 m from the sample and positioned to intercept the diffracted beam. To scan through a particular reflection, we plan to scan energy, leaving the sample fixed.

6-3.4.2 Beamline Physical Layout

Overall Beamline

The physical layout of the beamline is shown in earlier section and in Figure 6.21.

Major Component List

A-station White beam slits at front (~26 m)
Outboard deflecting LN2 cooled Si mirror (~30 m)

B-station Possible diagnostic (~43 m)

C-station “micro-mono”, monochromator with integral slits.
Photon shutter used for accessing D-station.

D-station (main experimental station) Micro-diffraction instrument, with K-B mirrors, stages, detectors:
1 Large area detector above sample
2 medium area detectors somewhat to the sides.
1 fluorescence detector (close to sample)
1 medium size area detector in the forward scattering direction with horizontal motion

Coherent scattering detector:
Movable medium size area detector.

Nano-diffraction instrument, with K-B mirrors, stages, thermal enclosure, detectors:
1 Large area detector above sample
2 medium area detectors somewhat to the sides.
1 fluorescence detector (close to sample)
1 medium size area detector in the forward scattering direction with horizontal motion

First Optics Enclosure and Infrastructure (A-station)

As seen in Figure 6.21, the first optics enclosure (A- station) is a white beam station that will contain a window or differentially pumped aperture, two LN2 cooled Si mirrors, and adjustable slits for each of the canted lines. It will also contain masks and collimators as needed for safety requirements. The vacuum will be ultra-high vacuum (UHV) all the way down to the experimental station (D-station). After the LN2 cooled Si mirrors, the masks and collimators should change the beam from white to pink. This means that any new enclosures need only be pink beam capable, not white.

In this and the following stations, Bremsstrahlung collimators and other apertures will be placed as determined by ray tracing following standard APS radiation shielding guidelines.

B-Station

This is an existing white beam station that will provide space for a mask, and collimator. It may also hold a beam diagnostic module for beam alignment. All beam transport will be in UHV.

C-Station

This is an existing experimental station that is to be repurposed for beam line optics. It will contain the small-offset monochromator with its associated slits, and the pink-beam shutter that stops the x-rays for accessing the following experimental station (D- station). All of the beam path in this station will be in UHV, and this station is already white beam compatible.

End Station (D-station)

There will be two experimental sites in the D station. The first (upstream) is the micro diffraction instrument. It will be for more conventional micro/nano diffraction with the capability of also doing coherent scattering from selected small particles. This experimental site will use a K-B mirror pair to provide an ~150 nm spot on the sample.

The second instrument is the nano diffraction instrument located at the end of the station. It is configured for the smallest beam sizes. It will have a short focus K-B mirror pair to provide a spot on the sample of ~50 nm.

This station will require a shielded beam pipe to pass the x-rays from the inboard undulator on to the new E station. With the 1 mrad cant and the two white beam mirrors, the separation at 58 m will be 414 mm (assuming all horizontal mirrors at 2.5 mrad).

The D station will require temperature control to maintain dimensional stability of the instruments. Temperature stability of 0.05 ℃ is required, this cannot be done using current APS air handling units.

This station is currently white beam capable, so the major radiation safety issue will be the pink beam transport for the inboard line. This will be similar to the shielded white beam transport currently in 34-ID-C. The UHV will end at a window at the front of this station, all subsequent beam transport will be in either He or rough vacuum. The only other UHV will be the K-B mirror box, which will be a small standalone UHV system.

Micro-diffraction instrument The first instrument in D station is the low-resolution instrument. It will be similar to the existing 34-ID-E instrument, but with multiple improvements, better mirror, better K-B mirrors, better detectors, and a movable detector for doing coherent diffraction on identified particles.

This instrument will use a K-B mirror pair to provide an ~150 nm spot on the sample. Since coherent diffraction is expected, there will be a detector at ~3 m from the sample that can be moved to intercept the diffracted beam. This movable detector will be mounted on a robot or large x-y translator to position the detector on a single diffraction spot. The main detector will be fixed mounted above the sample position which is necessary for depth-resolution.

The fixed detector does *not* have to have small pixels, what is important is having more pixels. The height is adjusted to make 1-pixel equivalent to ~10^{-4} in $\Delta d/d$, and then with many pixels you will also span a large angular range. The angle between pixels determines your ability to measure the strain of a particular reflection. The angular span of the detector determines your ability to measure shear and other off-diagonal strain components.

Nano- diffraction instrument The second instrument in D station is the high-resolution instrument, which will be configured for the smallest beam sizes. This experimental site will have a separate thermal enclosure to provide the best thermal stability. Temperature regulation of 0.02 ℃ is required. It will have a short focus K-B mirror pair to provide a spot on the sample of ~50 nm. It will also require a very-low noise detector to see the small signals.

6-3.4.3 Additional

Detectors

All measurements require large low noise high count rate detectors. There is no obvious need for development of special detectors.

The main detector located above the sample should be similar to a Pilatus 6M; it has many pixels, low noise, and high frame rate. For the two side detectors, two smaller detectors such as the 1M or 2M are sufficient. These three detectors surrounding the sample at the micro or nano diffraction instruments do not need particularly small pixels. The current Perkin-Elmer detectors have 200 μm pixels which work fine; the detector distance is adjusted to provide the desired 10^{-4} resolution in Q. To get accurate off diagonal strain components, the detector should cover as large a solid angle as practical to allow measuring a wide range of q-vectors. These two conditions imply that a detector with a large number of pixels is desired; this is the important criteria. A detector speed of < 200 Hz should be sufficient to keep up with the expected signal.

We also plan of providing a medium size area detector for measuring the forward scattered beam. This will provide valuable information for thin samples, and is essential for some of the programs such as the high-pressure work.

The movable detector for coherent measurements should have smaller pixels appropriate for doing coherent scattering measurements, but does not need to be especially large or fast. The limitation on pixel size is given by the distance (~3m) and the expected particle size. See the discussion of detectors in the ATOMIC project. For a particle size of 1.5 μm and a pixel size of 75 μm, the detector distance should be 3.3 m at 12 keV.

Additionally, require a fast fluorescent detector to provide elemental maps. The fluorescent signal is sometimes part of the experimental result, and is sometimes used to find fiducials for locating a specific location on a sample. A detector similar to a Vortex is appropriate. A 1 mm thick detector is preferred for detecting higher energy emission lines.

Computing

In general, the control system will be a standard APS EPICS control system. There will be a need for fly-scanning on the knife-edge, monochromator, and on at least one of the three sample positioners. The biggest challenge on the motion system will be to:
1) position the sample and knife-edge to less than the x-ray spot size (<200 nm), and
2) avoid thermal-drifts so that the sample does not drift away from the x-ray spot during the measurement.

The data rate from either of these two instruments may get quite high. Running a Pilatus 6M continuously at 100 Hz for 24 hours produces 113 TB of data (with an 80% duty factor), with 3 detectors that increases to 189 Tb/day. So, generating 10 TB/day should become common, and 100 TB becomes a quite possible goal. The detector images will all have to be processed promptly so that the user can see the results in near real time. This will require a fast connection between the detectors and the disk array, and a fast connection to the compute nodes to keep up. The data rate is expected to be steady state, and not composed of bursts. It is likely that it will become necessary to analyze the images without ever saving all the images to disk; i.e., first storing the images directly to memory for processing, and saving only the fitted peak positions to disk..

The expected workflow will depend upon the type of measurement. A 3D white beam diffraction experiment should consist of a series of knife-edge fly-scans, with each fly-scan consisting of between 50 and 2000 images. After each knife-edge scan the sample is moved a small distance in the transverse direction, and the knife-edge scan is repeated. These images are then depth-resolved to provide individual Laue patterns on an xyz grid in the sample. The individual Laue patterns are indexed which gives the user the crystallographic orientation of each volume element. The coded aperture development is intended to reduce the need for 2000 images in a knife-edge scan down to 400.

For measurements of absolute strain, the process will be similar, but with the addition of energy scanning the monochromator. For individual reflections, this means that only a small ROI of the detector is needed, and the knife-edge scan is also reduced.

Specific Safety Requirements

A normal APS safety envelope should be sufficient. There are no special hazards anticipated. While the occasional radioactive sample will probably be measured, such samples will arrive sealed in such a manner that no special permanent facilities will be required.

Specific Conventional Facilities Requirements

In general, we are concerned about vibration and temperature fluctuations.

Due to the need for long term position stability in all of the instrument, the station will require a temperature stabilized buffer area around the entrance. A temperature stability of 0.1 ℃is required; this is achievable using the current APS air handling units. This enclosed area will also be where the experimenters sit while operating the instruments.

The inside of the station will require better temperature stability, perhaps 0.03 or 0.05 ℃. This will require moving as much electronics as possible out of the station and including a separate air handling unit to stabilize the station temperature. A 100 mm long piece of aluminum will expand by 100 nm with a temperature change of 0.04 ℃ ($\alpha = 24\text{e-}6\ \mathrm{C}^{-1}$).

The nano-diffraction instrument will have to be surrounded by an additional temperature barrier and have an additional unit to stabilize the temperature of the nano-diffraction instrument to at least 0.02 ℃.

Since vibration is clearly important, both instruments will be mounted on large granite rocks. The old table at 34-ID-E with steel post legs provided ~50 nm rms vibrations, granite should be better.

Support facilities

This project should not require any special laboratory or sample preparation facilities beyond a work area outside the station for sample mounting.

6-3.5 R&D Needs

6-3.5.1 Knife-edge / coded aperture development.

To improve throughput on 3D measurements we propose to develop a coded aperture type structure to replace the existing knife-edge. A coded aperture may be able to speed up the depth measurements by a factor of 5 with the possibility of providing better signal to noise, and the hope of providing some energy information about the scattered x-rays.

6-4 Coherent High-Energy X-ray Sector for *In Situ* Science (CHEX Sector)

6-4.1 Executive Summary

The Coherent High Energy X-ray (CHEX) Sector for *In Situ* Science will advance the frontier for *in situ,* real time studies of materials synthesis and chemical transformations in natural operating environments using the unprecedented coherence of the high-energy X-ray beams provided by the APS Upgrade. Research areas addressed include epitaxial film growth, bulk crystal growth, synthesis of materials by advanced methods, etching and corrosion, electrochemistry, geochemistry, energy storage, and catalysis. Coherent diffractive imaging and photon correlation spectroscopy (PCS) will provide transformative insight into a material's structure, heterogeneity and disorder, chemical and long-range interactions, dynamics, and evolution under real-world conditions and time frames. Undulator sources, beamline optics, diffractometers, and detectors will be optimized for coherent X-ray techniques at the high energies (15-60 keV) needed for *in situ* studies. By using canted undulators and multiplexing monochromators, four simultaneously operating branch beamlines will efficiently accommodate eight instruments on a single APS sector and amplify the beam time available for programs to address high-impact problems. Infrastructure needed for *in situ* measurements of synthesis and transformations will be provided, such as chemical exhaust, gas sources and safety systems, and sample chambers suitable for coherent beam studies. The beamline layout fits onto APS Sector 28, close to related materials synthesis and characterization facilities at the Center for Nanoscale Materials. The CHEX Sector will capitalize on the world-leading brightness and coherent flux of the APS-U at high photon energies to enable studies not feasible at other facilities.

6-4.2 Scientific Objectives & Capabilities

6-4.2.1 Scientific Case for Beamline

In November 2015, the DOE Basic Energy Sciences Advisory Committee (BESAC) published *Challenges at the Frontiers of Matter and Energy: Transformative Opportunities for Discovery Science*, a report that highlighted an essential and growing need for *in situ* studies in materials science and chemistry:

> *While it will always be valuable to examine a structure after the fact, it is increasingly important that we develop characterization tools to evaluate the evolution of structure and function in real time. If this capability can be achieved, it creates the critical link between computational design and experimental realization, and significantly accelerates the pace of materials discovery, especially for hierarchically assembled materials and complex chemical transformations.* [50]

The scientific goal of the Coherent High Energy X-ray (CHEX) sector is to advance the frontier for *in situ,* real time studies of dynamics using the unprecedented coherence of the high-energy X-ray beams provided by the APS Upgrade. Such research promises breakthroughs in discovering, developing, and understanding the materials and processes that are needed to address our global challenges in energy, environment, health, and security.

The scientific impact of the proposed facility for coherent high-energy *in situ* studies will be broad, cutting across the sections of the APS-U Early Science document [51] on advanced materials, chemistry, condensed matter physics, and environmental science, bringing together researchers in these areas with common underlying scientific questions and technical approaches. Here we focus on two major areas: *in situ* materials synthesis, and transformations under real conditions. Specific areas include:

within ***in situ* studies of materials synthesis**:

- 2D materials, metastable materials, mesoscale heterostructures
- Film deposition and bulk crystal growth
- Electrochemical growth, nanoparticle growth, additive manufacturing

and within **transformations under real conditions**:

- Reactive ion etching, lithography, corrosion
- Energy storage, geochemistry
- Structural evolution during catalysis
- Materials under irradiation

An overarching scientific theme crosscutting these areas is the need for understanding the critical roles of heterogeneity, interfaces, and disorder. This need is articulated in the report put out by BESAC:

> *Real materials, both natural ones and those we engineer, are usually a complex mixture of compositional and structural heterogeneities, interfaces, and disorder across all spatial and temporal scales. It is the fluctuations and disorderly states of these heterogeneities and interfaces that often determine the system's properties and functionality. ... Developing new approaches to understanding interfacial structure, its heterogeneity and disorder, chemical and long-range interactions, dynamics, and evolution under real-world conditions and time frames represents a Transformative Opportunity.* [50]

Penetrating high-energy X-rays have proven to be a powerful tool for *in situ* studies, revealing atomic scale structure and dynamics under actual operating environments in a broad range of current research at APS. While there has been continued improvement in spatial and time resolution, techniques using incoherent X-ray beams that are sensitive to averages over the illuminated volume have often required that we study ideal crystals or interfaces that are as homogeneous as possible over macroscopic regions and time scales. For example, to observe atomic mechanisms at an interface, it has typically been necessary to study a model interface that is flat and uniform over a large area, and simultaneously undergoes the same process at all locations. For the great variety of systems and processes that are inherently inhomogeneous, only the average behavior can be observed.

The advent of high-energy coherent X-ray beams at the APS Upgrade will deliver unprecedented new opportunities to investigate the spatial and temporal inhomogeneity in "real" systems with defects, disorder, and hierarchical nanostructure. We can anticipate that these new experimental capabilities in imaging and dynamics using coherent X-rays will converge with ever-more-powerful computer modeling and simulation capabilities to greatly accelerate the pace of discovery.

Here we take a closer look at some of the major scientific opportunities in materials synthesis and chemical transformations.

In Situ Studies of Materials Synthesis

> *To date, chemistry and materials research has focused on understanding and manipulating the relationship between structure and function, with the goal of predicting where the atoms should be placed in order to achieve a desired property. Scant attention has been directed toward the predictive science of synthesis—that is, toward understanding how to get the atoms where they need to go to achieve a desired structure. ... In situ and real-time monitoring of growth and synthesis processes is essential to understand and ultimately control chemistry and materials synthesis. [50]*

Not only do we need to understand the proper arrangements of atoms in materials and nanostructures that give the desired functionality, but as the BESAC report points out, we also need to learn how to synthesize and stabilize these arrangements. Rather than a trial-and-error approach, developing the science underlying materials synthesis promises the most extensive and sustainable progress.

New capabilities provided by the APS Upgrade will dramatically impact the science of synthesis. The orders-of-magnitude increase in X-ray brightness at high energies will enable *in situ* coherent X-ray studies of synthesis mechanisms down to the atomic scale with sub-microsecond time resolution. As described below, coherent imaging and correlation spectroscopy techniques will reveal unprecedented detail regarding atomic arrangements and dynamics. In parallel, orders-of-magnitude increases in computing power are enabling *ab-initio* simulations not just of ground-state materials structure and properties, but also of the competing chemical reactions and materials kinetics that occur during synthesis. Both coherent X-ray techniques and atomic scale modeling enable us to see beyond the average behavior of a fluctuating system and reveal the microscopic arrangements, correlations, and dynamics underpinning the synthesis process. The combination of *in situ* observation of structure and dynamics during synthesis with advanced computational studies will usher in a powerful new framework for discovering, isolating, and optimizing desired growth pathways and outcomes.

The primary issues in materials synthesis, such as phase selection and microstructure development, typically revolve around a competition between different underlying atomic-scale processes. A dominant theme in heteroepitaxial film growth, critical for synthesis and function of advanced devices, is the simultaneous control of strain, composition, dislocation nucleation, and the growth instabilities that favor nonuniformity. An important example is the growth of superlattices and heterostructures that are designed using advanced theoretical approaches to have properties targeted for specific applications- for example, enhanced ferroelectricity or superconductivity. The formation of atomically abrupt interfaces required for high performance materials results from a competition between surface diffusion, island nucleation, mechanical constraints, epitaxial strain, and fluctuations in deposition rates [52, 53]. *In situ* observation of a variety of vapor phase growth processes (e.g. pulsed laser deposition, molecular beam epitaxy, and atomic layer deposition) provides a powerful tool for characterizing and addressing challenges to synthesizing complex heterostructures. Likewise, heterogeneous nucleation at interfaces is critical for thermodynamic phase and crystal orientation control in bulk crystal growth and in synthesis of two-dimensional materials on substrates. The ability to image these fluctuations dynamically will transform our ability to create the desired structures. These new capabilities, made possible by the high coherent flux from the APS Upgrade, will be enabled by the CHEX facility.

Successful materials synthesis often involves finding the "trick" that allows formation of a metastable phase, such as alloying InN into the active layers of efficient solid-state lighting devices [54], or building cation and anion sublattices under vastly different conditions in bulk magnetic oxides [55]. Rational design of metastable materials synthesis processes requires understanding the specificity of different sites and interfacial defects to catalyze certain reaction pathways. Imaging the complex, non-equilibrium interface chemistry in the growth environment will be crucial for forming new metastable materials via chemical vapor deposition and electrochemical and nanoparticle growth, and in developing new synthesis methods such as 3D printing for additive manufacturing. Selective growth of bulk crystals requires identification of nucleating species to direct synthesis of new or targeted materials, or monitoring of dopant profiles during growth to isolate homogeneous specimens. *In situ* observation of these processes will shed light on phase selection and allow isolation of metastable compounds. Alternatively, monitoring of crystal habit, grain boundaries, and extended defects are key opportunities for *in situ* study of bulk crystal growth processes such as Bridgman growth. In this case, optimized growth can be achieved by combining real-time *in situ* feedback with newly developed predictive modeling approaches [56]. Coherent diffractive imaging of the developing nanoscale strain fields during growth will provide a powerful tool for these studies.

Transformations under Real Conditions

The need for *in situ* studies of materials and chemical transformations spans across a wide range of research activities. These include the atomic-scale understanding of advanced lithographic processes such as reactive ion etching and additive manufacturing, complementary to the science of thin film synthesis; understanding the relationship between surface site structure and reactivity during heterogeneous catalysis, and the evolution of the catalyst structure; the formation mechanisms of metastable microstructures under extreme conditions such as ion irradiation; as well as heterogeneous phase transitions and chemical reactions in energy storage and geochemical systems. The power of coherent, high-energy X-ray techniques to image and observe dynamics at the nanoscale under operating conditions provides a transformational opportunity in all of these areas. Here we describe some example opportunities in greater detail.

The BESAC report states that “*understanding the basic properties of rock formations in contact with reactive fluids is critical to ensuring safe long-term storage of CO_2 and will require new approaches to measuring the surface and near-surface properties of minerals and fluids under realistic conditions using synchrotron X-rays, combined with molecular models of the interactions.” [50]* The ability to understand and control the processes that underlie rock-fluid interactions in natural systems is limited by the inherently high heterogeneity of these systems and the opacity of such systems to most experimental probes. While traditional (incoherent) high-energy X-ray and neutron techniques can penetrate such samples, they typically elucidate spatially averaged rock properties (e.g., mean particle size, porosity). A molecular-scale understanding of interfacial reactivity has been obtained only for flat homogeneous single crystalline mineral-water interfaces. A robust understanding of the reactivity of complex rock architectures will need to connect this mechanistic understanding of mineral-water reactivity to porous geomaterials, relevant to our understanding of geological transport of energy-related materials (e.g., CO_2, radiological waste, etc.). In these systems, reactivity is controlled by the interplay between the hierarchy of pore structures, and the resulting fluid flow patterns and the fluid-mineral interactions that can be strongly modulated by nanoscale confinement. The coherent hard X-ray beams from the CHEX facility at the APS-U will provide a fundamentally new opportunity to extend such a molecular-scale understanding to the complex structures in the "real" rock interfaces found in natural systems, and can be used to directly test our predictive capabilities on well-defined systems. Here, the robust use of coherence enables multiple imaging modalities capable of elucidating reactivity with resolutions spanning from nanometers (e.g., coherent diffraction imaging) to micrometers (e.g., transmission X-ray microscopy) and even to macroscopic distances (e.g., tomography). The new coherent capabilities will allow the principles governing reactivity (e.g., nucleation, growth, dissolution) to be discovered through direct *in situ* observations at the conditions of interest (e.g., under confinement, flow, etc.) and ultimately in real-time.

Similar considerations also apply to the complex processes that occur in the intricate environments of energy storage systems. In addition to the challenges inherent to natural rock-water systems, energy storage systems have degrees of complexity associated with extreme gradients of applied potentials, the driven transport of the active ions (e.g., Li^+ or O^-), the substantial volume changes and complex phase transformations that occur during ion insertion and removal within the electrode, and the coupled spatiotemporal responses within these complex structures. These challenges limit the performance of the energy storage system (e.g., in terms of stored energy, number of charge-discharge cycles that can be accessed, or magnitudes of voltage losses at the electrodes). As in the case of the natural rock-water systems, the use of coherent high-energy X-ray techniques opens up the possibility to understand, from direct observation, the deterministic processes that occur associated with the specific structures, rather than the average response of the system. Thus, the use of coherent imaging should enable the discovery of the principles that will allow the full theoretical performance of these systems to be achieved.

Corrosion and fouling impose enormous costs on society that exceed 3% of GDP in the United States [57]. The ability of coherent X-rays to penetrate thick layers and create real-time images of nanoscale to millimeter structures will allow an upgraded APS to address the grand challenges in corrosion science identified by the National Academy of Sciences [57]. Corrosion and fouling mechanisms are exceptionally difficult to predict and control because they have strong electrochemical and mechanical couplings that guide diffusion of the reactants, determine the shape of particles, and strongly influence their internal atomic and mesoscopic arrangements. A particular challenge in understanding corrosion is the multiple length scales and multiple time scales. The initial processes that happen quickly and over relatively short length scales have been studied with traditional surface science probes. However, corrosion problems quickly become much more difficult to study as the corrosion layers build up and large gradients in chemical potentials (particularly the oxygen chemical potential) and mechanical stresses are introduced into the problem. The facility we propose will enable the study of both the initial, rapid formation of corrosion products and, through flexible sharing of the beamline capabilities, the long-term (days and weeks) evolution of those products.

Coherent, High Energy X-ray Techniques for Heterogeneous Systems

In general, coherent X-ray techniques will provide powerful new probes to characterize defects and heterogeneities in materials. Classical scattering techniques with incoherent X-ray sources give the structure averaged over many coherence volumes, and are thus most sensitive to the long-range order in systems that remains the same over many X-ray coherence volumes, such as the interior structure of crystals, or layered structures parallel to a flat interface. Only average properties, such as mean particle size or spacing, can be obtained regarding structures without long-range order. The use of a coherent X-ray beam can give full information about the exact structure within the illuminated volume, including features and arrangements without long-range order that are averaged out in classical measurements.

Thus, we can anticipate especially high impact from the new APS Upgrade source characteristics in studies of disorder and defects in heterogeneous systems. Examples of important research areas include complex processes such as non-uniform solid-state reactions in polyphase systems, geochemistry of natural materials, and growth of polycrystalline aggregates through advanced additive manufacturing methods ("3D printing"). Coherent techniques, such as BCDI imaging of individual grains and XPCS studies of diffusive and deformation dynamics, will open new avenues for studies of these systems.

For example, a new deterministic understanding of geochemical reactivity of natural rock samples will relate observed properties to actual structures (instead of statistical measures of the structure, e.g., pore-size distributions). Ptychographic approaches will be used to image the full 3D structure of geomaterial matrices. Coupled with the high brilliance and coherence at hard X-ray energies ($\sim$20 keV), such approaches will enable in-situ studies (e.g., before, during and after reactions) to *observe* the real-time dynamics and evolution of heterogeneous reactivity (e.g., growth, dissolution) in these systems. Such observations can, in principle, relate the nucleation and evolution of such reactions to structural observables such as matrix, particle and pore arrangements, flow patterns, and the spatially variable strain within the mineral matrix. Similar measurements also can be used to understand the structure and reactivity of nanoparticulate materials (ranging from anthropogenic-, inorganic- and bio-materials) within their natural setting, such as complex soil matrices. Such observations, when coupled to parallel measurements of spatially resolved signals (e.g., diffraction, fluorescence), enable robust observations of structure and composition to provide a complete understanding of reactivity in these systems.

An example of recent success in this area is the nanoscale imaging of strain distributions, dislocations, and phase transformations in individual grains during charging and discharging of battery cathode materials [58]. The CHEX sector will enable broad use of such coherent X-ray techniques using the penetrating high-energy beams needed for *in situ* studies of heterogeneous systems.

Transformative Opportunity of Coherent, High Energy X-ray Techniques

Coherent X-ray techniques will allow us to observe the atomic-scale dynamics during materials synthesis and transformations with much higher fidelity than has been previously possible. These techniques provide qualitatively new information regarding the structure and dynamics of the defects and disorder that mediate crystal growth and phase transformations. For example, on what type of sites do nuclei form? On what region of a nanoparticle surface does a catalytic reaction occur? Coherent techniques are sensitive to the exact arrangement of nanoscale structure, rather than just spatially averaged quantities such as defect density [59]. Coherent diffraction imaging (CDI) can show the arrangement, while X-ray photon correlation spectroscopy (XPCS) is sensitive to changes in the arrangement.

Ongoing rapid development of these techniques, e.g. time-resolved CDI [3], 3-dimensional Bragg ptychography [60], polychromatic CDI [29], combined full-field X-ray microscopy and CDI [61], coherent grazing-incidence small-angle scattering [62], high speed XPCS [63], and analysis of complex 2-time, 2-q correlations in XPCS [64, 65], promise to further extend their capabilities. By providing greatly increased coherent flux at the penetrating, high photon energies (15-60 keV) needed for *in situ* studies, the CHEX sector of the APS Upgrade will bring these powerful techniques to bear on the new frontiers of materials synthesis and transformations.

6-4.2.2 Description of User Community and Stakeholders

Discussion with the research community regarding needs for advanced facilities for *in situ* synchrotron X-ray studies has been ongoing since the original workshops to outline future scientific directions for APS beginning a decade ago. These included workshops on *in situ* characterization of interface structures and catalysis [66, 67], interfacial and surface science [68], and *in situ* studies of interfacial reflectivity [69]. Community excitement for *in situ* studies of materials synthesis and chemistry was a highlighted topic in the summary workshop to define the science case for the APS Upgrade [70], and was a primary driver for a proposal to develop an X-ray Interface Science sector at APS [71], which was included in the conceptual design for the APS Upgrade[72]. The planning for this facility was continued at a dedicated workshop [73] that included reports from the community on Buried Interfaces, Electrochemistry and Geochemistry, Materials Synthesis, and UHV Nanoscience. These helped inform its preliminary design [74] and develop many of the design concepts listed above. The *in situ* studies community has been involved in continuing workshops on the new horizons opened by coherent X-ray techniques [75] and to envision their scientific impact as part of the APS-U science case [51].

Enthusiastic community support for upgraded facilities at the APS for *in situ* studies has emerged at all of these workshops. Since the development of the initial CHEX white paper, we have continued to solicit community input. The CHEX proposal is synergistic with two other APS-U beamline proposals that focus on *in situ* studies, the In Situ Nanoprobe (ISN) and ATOMIC. CHEX enables coherent X-ray scattering at photon energies up to 60 keV, while ISN and ATOMIC are designed for nanoprobe and Bragg CDI studies, respectively, at lower photon energies. Together, the leaders of these three proposals convened a workshop on May 10-11, 2016 at the APS Users Meeting, "*In Situ* Studies of Materials Transformations using Coherent X-rays," to explore the future applications of coherent X-ray techniques, such as photon correlation spectroscopy and coherent diffractive imaging, for *in situ* studies of materials dynamics. This workshop explored three general science areas—catalysis and interface chemistry, materials synthesis, and dynamics in complex materials—with 12 presentations by experts, and a discussion session. Forefront work was presented in areas such as nanodiffraction for phase and strain mapping in microelectronics, Bragg CDI studies revealing effects of surface reactions on strain in nanocrystal catalysts, and XPCS studies of surface morphology and reconstruction dynamics during film growth and etching. There were several connections between the areas, such as the importance of both fluid-solid and solid-solid interfaces in next-generation batteries, and the synthesis of materials through both fluid-solid and solid-state reactions at interfaces. Collaborations were discussed among the participants in areas such as creating standard software packages for coherent diffractive imaging reconstruction, and developing instruments for *in situ* studies with coherent X-rays.

The May 2016 workshop further informed the goals and design of the CHEX sector. Needed beamline capabilities discussed included:

- A variety of *in situ* environment stages / chambers (heating, chemistry, electrochemistry, ...) with designs that are easy to swap onto a shared goniometer and to duplicate for multiple, potentially incompatible uses
- Small sphere-of-confusion goniometers
- Space for larger *in situ* instruments / chambers, e.g. MBE, PLD
- Multiplexing of experiments for high productivity
- Large optics-to-sample working distances
- Small pixel detectors, large/variable sample-to-detector distances
- Multiple detectors for simultaneous CDI, XPCS at different Q
- Pink beams for enhanced signal, for Laue crystal alignment in BCDI
- For some but not most experiments, photon energy tunability
- *In situ* alignment microscopes (optical, possibly SEM and AFM)
- Manipulation and stability of samples, e.g. particles in environment

Formation of user groups interested in specific instruments was discussed. Another outcome of the workshop was the addition of Gyula Eres to the list of Principal Developers for CHEX. Dr. Eres brings expertise and interest in *in situ* film growth studies by pulsed laser deposition (PLD).

Based on the workshop input, and an evaluation of the current and future research communities, we anticipate that the capabilities of the CHEX sector will be highly oversubscribed. Table 6.9 lists 14 example instruments, serving five major research communities, which are envisioned to operate at CHEX. We are developing a list of potential users of the CHEX facility, which will form the basis of a CHEX sector user advisory committee. The current list is given in the Appendix.

We have assigned members of our principal developer team to act as contacts and coordinators for each of these communities in the development of the needed instruments and capabilities. For developing the overall design of the CHEX facilities, we have categorized the instruments roughly as shown in the table, based on:

- Whether the instrument / chamber can be mounted on a shared goniometer, or is sufficiently complex to require a specialized integrated goniometer
- The approximate photon energy range needed, either 15-35 or 35-60 keV
- Whether photon energy tunability is a major advantage

Some details of these 14 example instruments are discussed below. The CHEX layout will provide 8 locations for these instruments, listed in Table 6.9 and described below, 4 of which can operate simultaneously. The capabilities of the various endstations have been designed to meet these needs.

Thin film synthesis and etching is one of the largest research communities addressed by CHEX. There are many well-developed film growth methods, and because most operate in environments that are incompatible with electron-based characterization techniques, *in situ* X-ray studies are a critical tool. Techniques such as molecular beam epitaxy (MBE) and pulsed laser deposition (PLD) are powerful methods for synthesizing advanced materials and heterostructures with many chemical components, such as complex oxides. Because these growth systems are large and elaborate, *in situ* X-ray studies benefit from integrated goniometers. Because of the many chemical components, photon energy tunability is especially valuable for resonant scattering capability. Other film growth techniques, such as chemical vapor deposition (CVD), atomic layer deposition (ALD), sputter deposition, and solid-state reactions, can be effectively studied in more compact chambers that can share a large goniometer sample platform. Likewise, techniques for thin film lithography, such as reactive ion etching, atomic layer etching, and sputter erosion, can be implemented with relatively compact chambers sharing a goniometer. However, significant infrastructure, such as elaborate gas handling, chemical exhaust, and engineered safety systems surrounding the goniometer, are typically required to enable these programs.

The requirements for *in situ* studies of bulk materials synthesis techniques (e.g. Bridgman or floating zone crystal growth), and of dynamics of defects in single crystals, also span the range from integrated to shared goniometers. However, for bulk systems, there is a significant advantage in using more penetrating photon energies in the 35-60 keV range.

Table 6.9. Communities served by the CHEX sector and examples of instruments

Research Community *(Coordinators)*	**Example Instruments**	**Goniometer Type**	**Energy Range** *(keV)*	**Need Tunable**	**Potential Locations**
Thin Film Synthesis and Etching *(Bedzyk, Eres, Haile, Hong, Walker)*	Oxide Molecular Beam Epitaxy	Integrated	15-35	Yes	F,G
	Pulsed Laser Deposition	Integrated	15-35	Yes	F,G
	Chemical Vapor / Atomic Layer Deposition	Shared	15-35	No	B,C,D1,D2
	Sputter Deposition and Erosion	Shared	15-35	No	B,C,D1,D2
	Topotactic / Solid-State Reactive Synthesis	Shared	15-35	No	B,C,D1,D2
	Reactive Ion / Atomic Layer	Shared	15-35	No	B,C,D1,D2
Etching					
Bulk Synthesis and Dynamics *(Mitchell, Stephenson)*	Bulk Crystal Growth	Integrated	35-60	No	E1,E2
	Additive Manufacturing / Nanoparticle Growth	Shared	35-60	No	E1,E2
	High Energy Diffuse Speckle	Shared	35-60	No	E1,E2
Electrochemistry and Catalysis *(Fister, Markovic, Zhou)*	Solid-Solid Interfaces	Shared	15-35	No	B,C,D1,D2
	Liquid-Solid Interfaces	Shared	15-35	No	B,C,D1,D2
	Vapor-Solid Interfaces	Shared	15-35	No	B,C,D1,D2
Geochemistry, Environmental Science *(Fenter)*	Combined XRIM and CDI	Integrated	15-35	Yes	F,G
Corrosion and Nuclear Materials *(Highland, Yildiz)*	Environmental Load Frame	Integrated	35-60	No	E1,E2

Electrochemistry and catalysis studies require many different sample environments and cells, with different designs, temperature ranges, and chemistry requirements depending upon whether solid-solid, liquid-solid, or vapor-solid interface dynamics is being probed. We anticipate that standard designs for these cells will allow them to be economically duplicated and customized by different user groups, to minimize issues with cross-contamination. Operation should be possible using a shared goniometer.

The geochemistry and environmental science community has proposed a specialized instrument [61] that combines X-ray reflection interfacial microscopy (XRIM) and BCDI to enable studies of interfaces on multiple length scales, including resonant studies. For *in situ* studies of corrosion and nuclear materials under stress, a mechanical loading system with temperature and environmental control using the 35-60 keV range is envisioned.

We expect some instruments to be in the scope of the CHEX beamline project, while others may be brought by partners and funded separately. Examples in the first category could be goniometer and detector systems shared by several sample environments / chambers that are easily swapped, with some chambers available at the facility, and some brought by user groups. Examples in the second category could be large specialized systems with integrated goniometer, funded, for example, through special DOE or NSF instrumentation grants. For this second category, we will organize user groups interested in carrying out such *in situ* experimental programs at the APS, to propose building the required major equipment. The CHEX facility should provide the infrastructure to optimize research with both types of instruments.

User Access Modes and Instrument Development and Operation

Access to instruments at CHEX will be through the standard APS General User and Partner User programs. Most instruments will be APS owned and operated, such as all of the shared goniometers and sample chambers that use them. These will be accessed through the General User program. For specialized instruments that are funded and developed by partner user groups, access will be according to the Partner User agreement approved by the APS following the standard peer review and Scientific Advisory Committee review of partner programs. These typically involve transitions from an instrument development phase to a general user phase, with details of the timing and fractions depending upon the source of funding (APS or partner) for instrumentation and for effort for continuing user support during operations.

It has been a strength of the APS to have flexible user access modes that allow complex experimental programs to be developed in partnership with user groups for the long-term benefit of the whole community. The CHEX facility will provide the infrastructure and access modes for major experimental programs to attack grand challenges in a flexible way that provides opportunity for competitive program turnover to address new problems. As can be seen from the list of instruments and communities in Table 6.9, we expect each of the CHEX endstations to be oversubscribed. This emphasizes both the need and efficiency of having four simultaneously operating experiments at CHEX.

The CHEX sector is a potential location for the proposed Extreme Materials (XMAT) facility [76], which would enable study of materials under MeV-per-nucleon ion irradiation. This would be a separately funded facility, and if implemented at CHEX would require the ion accelerator to be located on an upper level feeding ion beams into one or more hutches. It has also been proposed that XMAT could instead reside at the High Energy Diffraction Microscopy beamline, in a separate building outside of the APS experimental hall. The XMAT facility is a very exciting opportunity, and an optimum location for it should be decided as part of the APS-U beamline planning process. Facilities at CHEX for high-energy coherent X-ray studies will be of interest to the nuclear materials communities, independent of the location of XMAT.

Because of the strong emphasis on materials synthesis at CHEX and at the Center for Nanoscale Materials (CNM), there is potential for collaboration between APS and CNM to jointly develop and operate some user synthesis instruments. The CHEX beamline layout is designed for Sector 28, adjacent to CNM and its related materials facilities. Some synthesis instruments, e.g. PLD, may be suitable for growth experiments independent of X-ray studies.

The productivity and impact of the CHEX sector will benefit from the ongoing development of a Materials Discovery Institute (MDI) at Argonne that will consolidate, organize, and leverage the laboratory's recent investments in infrastructure and concept development in materials and chemical synthesis. The MDI is envisioned as a crossroads for discovery synthesis, targeting fundamental science as well as focused targeted applied objectives. It will bring together predictive modeling and advanced computational tools with experimental probes of structure and function and link them through *in situ* studies of synthesis. For CHEX users, the MDI will provide a community for exchanging synthesis knowledge and insights. For example, theory and computation collaborations enabled by MDI would provide multi-length and time-scale simulations of atomic scale dynamics to guide the design and analysis of the experimental studies. Additionally, it will provide access to the wealth of Argonne programmatic synthesis experience and tools in materials (bulk and thin film) and in chemical systems (molecular and nano). We anticipate that the MDI will help the APS to provide a nexus to advance U.S. synthesis science and discovery to a new level of sophistication.

6-4.2.3 Need for APS-Characteristics

The CHEX facility is specifically designed to capitalize on the world-leading brightness and coherent flux of APS-U at high photon energies to enable studies not feasible at other facilities. Some of the features of CHEX that will make it a world-leading research facility are:

- *In situ* studies are well matched to penetrating high-energy X-ray techniques (e.g. 15-60 keV).
- Coherence-based scattering and imaging techniques (XPCS, CDI, small beams with diffraction-limited angular resolution) provide powerful new probes, opening up unexplored areas.
- The high coherent flux of APS-U at high photon energies will provide world-leading performance for *in situ* studies of dynamics using these probes.
- Unlike current FEL sources, the large number of simultaneous experiments possible at APS provides the access needed for long-term, complex *in situ* experimental programs to tackle the grand challenges outlined above. The proposed facility will further develop this important distinguishing feature of APS.
- The co-location of APS at a multidisciplinary national laboratory provides a strong research ecosystem for the scientific program, including major computational resources. Such a local ecosystem is critical for sustained progress, and Argonne has a lead in this area over other competing international facilities.
- This will be a worldwide unique dedicated facility for *in situ* X-ray studies, co-located with synergistic Argonne experimental, modeling, and theory programs that will enhance APS user science.

While *in situ* studies and coherent X-ray studies will be carried out at many APS-U beamlines, unique features of this facility will be:

- Beamlines optimized for coherent X-ray techniques at the high energies (15-60 keV) needed

for *in situ* studies, and provided for the first time by APS-U.
- Multiplexed beamlines to efficiently accommodate large complex apparatus for the extended periods needed to address high-impact problems.

Related facilities are under construction at NSLS-II, such as the CHX and ISR beamlines. The coherent flux at photon energies below 10 keV will be excellent at NSLS-II, and these facilities will have outstanding performance for studying processes in transparent environments, such as surfaces in vacuum chambers with beryllium windows. CHEX will instead focus on research requiring higher energies to penetrate inside materials and non-vacuum environments.

CHEX will provide more appropriate facilities for *in situ* coherent X-ray studies than will be available at LCLS. Such experiments at LCLS suffer from issues with undesired beam interaction with the sample (e.g. instantaneous heating) because of the very high pulse energy and low repetition rate. The increased rep rate of the superconducting linac of LCLS-II will allow a greater variety of studies with attenuated pulses, but will not provide penetrating high energy coherent beams. A fundamental issue with FEL sources having few simultaneously operating experiments, as is the case with LCLS, is the lack of beam time availability needed for sustained research programs. The CHEX Sector at the APS will provide more beam time than all of LCLS.

Worldwide, the need for coherent high-energy X-ray beamlines has been recognized at facilities such as ESRF and PETRA-III. The new ESRF ID-1 beamline, described at our May 2016 workshop by Steven Leake, performs *in situ* X-ray studies. It has a single goniometer capable of a variety of coherent X-ray and nanodiffraction techniques, with focal spots as small as 100 nm at a photon energy of 10 keV. Several environmental chambers (for heating in a controlled atmosphere, for example) are available. Coherent diffractive imaging is supported, although the beamline is most heavily used for nanodiffraction by the microelectronics industry. In contrast to ESRF ID-1 or similar beamlines at PETRA-III, CHEX has been designed to focus solely on high-energy coherent techniques, to accommodate specialized chambers, and to provide more user access through simultaneously operating instruments. The co-location of APS at a multidisciplinary national laboratory with other synergistic user facilities such as the Center for Nanoscale Materials and the Advanced Leadership Computing Facility provides an advantage for the users at CHEX.

6-4.2.4 Key Beamline Characteristics

We will optimize the undulator sources, beamline optics, experimental stations and diffractometers, and detectors for coherence-based scattering and imaging techniques (XPCS, CDI, small beams with diffraction-limited angular resolution), at the high X-ray energies (15-60 keV) needed for *in situ* studies. The beamlines will be designed for complex *in situ* experiments to address grand-challenge problems, with features such as,

- Multiple simultaneously operating experiment stations suitable for most CDI and XPCS experiments.
- Space for the siting of major *in situ* chambers provided by beamline partners.
- Infrastructure such as chemical exhaust, gas sources, chemical labs.
- Non-X-ray access to major chambers while other experiments are running.

In order to meet these design goals, we will have multiple fixed energy branches with single-crystal monochromators that will transmit the undiffracted portion of the beam to downstream experiments to allow multiplexing of several simultaneously operating experiments on different branch lines:

- Simultaneous experiments will share a common undulator fundamental energy (K value).
- Judicious choice of mono angles and crystals will give flexibility in energy choices for each branch.

Because the spatial resolution of a chosen area detector determines the necessary hutch size and focal spot size required to resolve speckle features, we will need longer hutches, and smaller focal spots for higher energy coherent X-ray experiments.

Important design features to meet these goals include:

- Canted undulators
  - One feeding a tunable branch with a double-crystal mono, 15-60 keV.
  - One feeding three simultaneously operating fixed energy branches with single-crystal monos for multiplexed, simultaneously operating experiments at various energies from 15-60 keV.
- Focusing optics, diffraction instruments, and hutches with the needed sample-to-detector distance to resolve the speckle from the illuminated volume at photon energies of 15-60 keV.
- Area detectors with the small pixel size and large angular range needed for speckle experiments, and sensitivity at 15-60 keV.
- Tandem hutches that combine a front station housing an instrument that does not require access when other experiments are running (e.g. a diffractometer onto which samples, small environmental cells, or chambers can be mounted), and a back station having space for specialized chambers that do require access while experiments are ongoing in the front station (e.g. large growth chambers).
- Beamline layout that fits on Sector 28, located close to the related materials synthesis and analysis facilities at the Center for Nanoscale Materials.
- Option for pink beam availability, e.g. for polychromatic CDI.

6-4.3 Source & Front End Requirements

6-4.3.1 Insertion Devices

The sector will require canted undulators, optimized for brightness for the 15-60 keV energy range:

- One fully tunable, to provide a single energy in the 15-60 keV range
- One providing a variety of fixed energies in the 15-60 keV range from different harmonics
- 1 mrad cant angle
- Likely use superconducting undulators (SCUs) to achieve high brightness at 15-60 keV (will need 3rd harmonic to reach 15 keV, which implies SCU period 1.9 cm. Will mount both SCUs and the intervening cant magnet inside a single cryostat to maximize undulator length).
- Use of a 1.5 m length undulator will increase the brightness and coherent flux at 15 keV by 37%, and should be considered. The undulator length may be limited by the tolerable heat load on front end components.

6-4.3.2 Other Source Requirements

No special bunch timing requirements.

6-4.3.3 Front End Requirements

Canted undulators, with a high heat load front end to allow for operation of the 3rd harmonic at 15 keV with maximum undulator length.

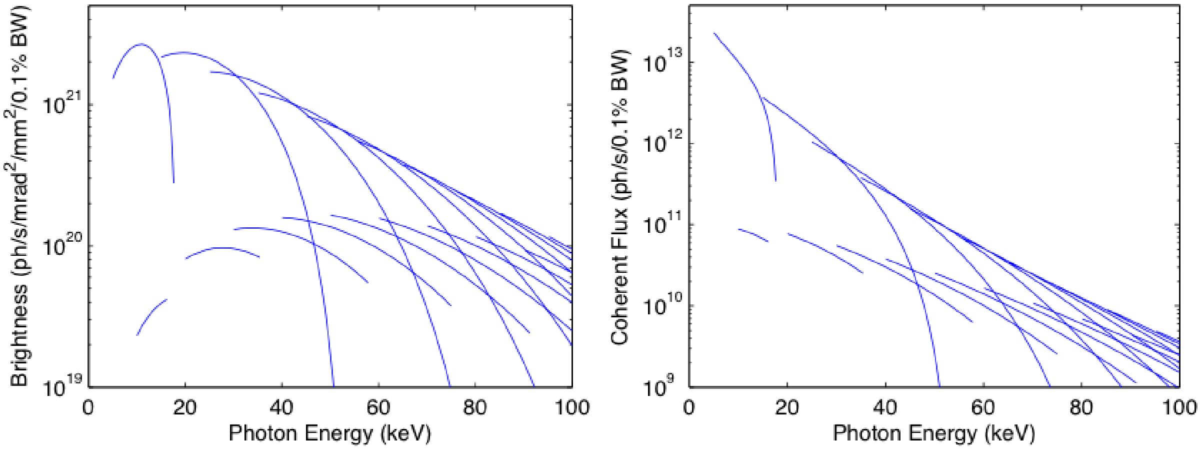

Figure 6.22. Characteristics of a 1.2 m long, 1.9 cm period superconducting undulator as a function of photon energy, showing (left) peak brightness tuning curves and (right) peak coherent flux tuning curves. Both odd and even harmonics are shown. At higher photon energies, the even harmonics are significant.

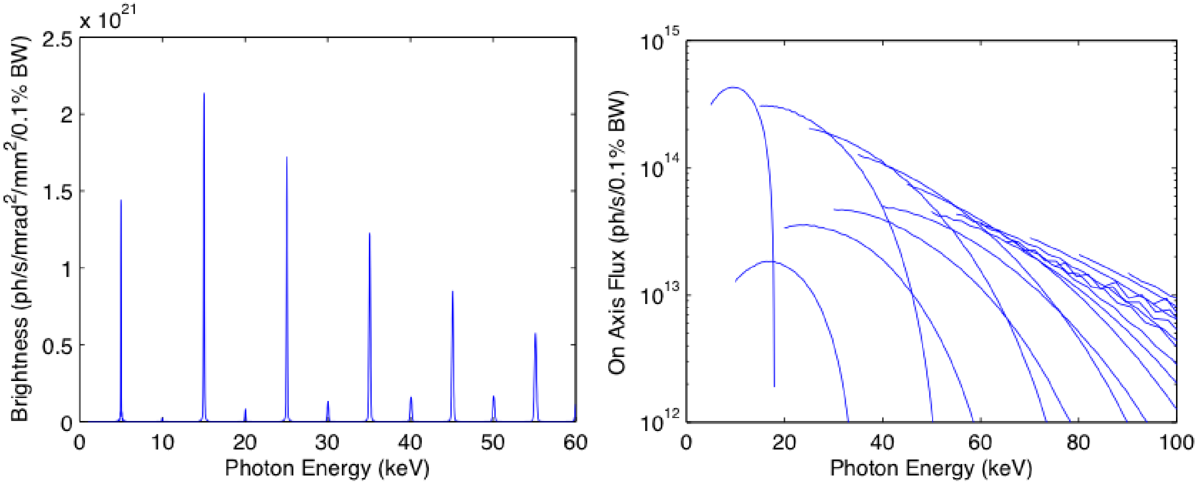

Figure 6.23. Characteristics of a 1.2 m long, 1.9 cm period superconducting undulator as a function of photon energy, showing (left) spectrum for fundamental energy of 5 keV, and (right) peak on-axis flux tuning curves. Both odd and even harmonics are shown.

6-4.4 Beamline Layout

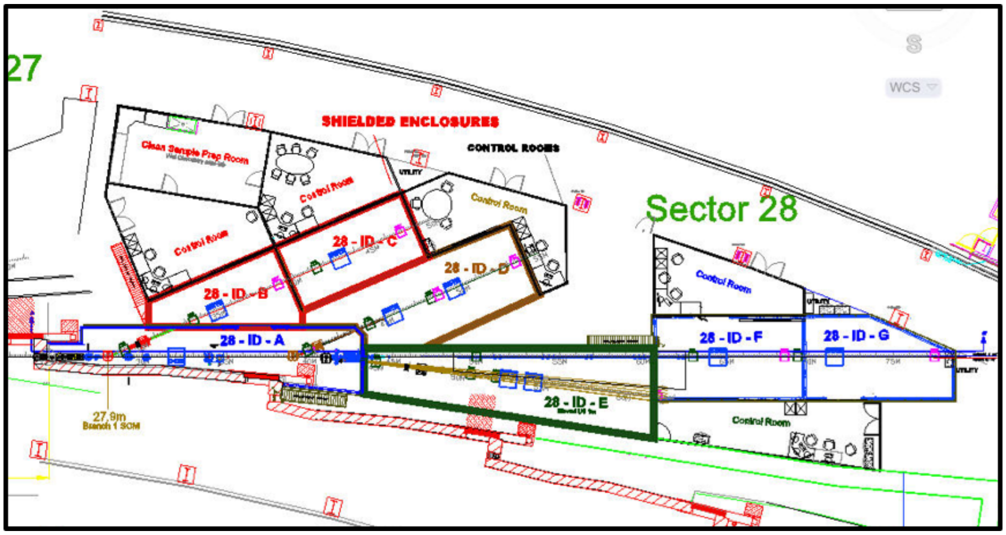

Figure 6.24. Conceptual layout of CHEX sector.

6-4.4.1 X-ray Optical Layout

Overall layout

The CHEX sector optical layout is based on two canted undulators:

- One undulator feeding fixed-energy branches 1, 2, and 3 with single-crystal monochromators for multiplexed, simultaneously operating experiments at various energies from 15 to 60 keV.
- One undulator feeding a tunable-energy branch 4 with a double-crystal monochromator having an energy range of 15-60 keV.

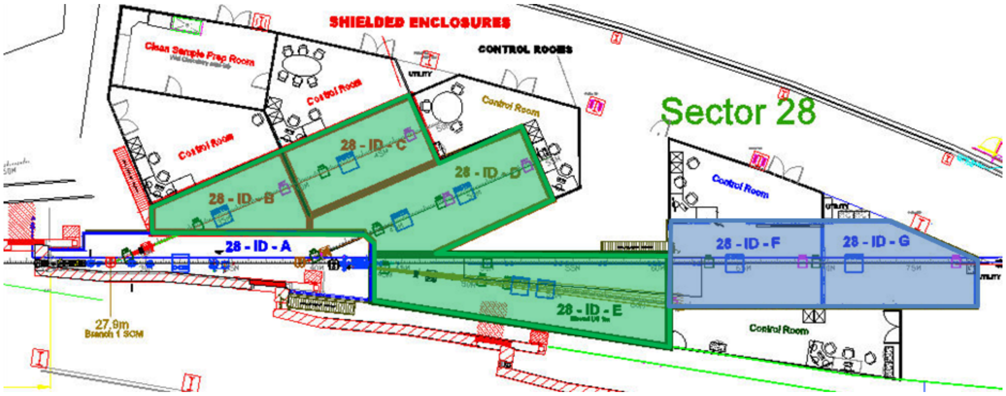

Figure 6.25. Three fixed-energy branch lines indicated in green. One tunable-energy branch line indicated in blue.

Description of optical components: Fixed-energy branches 1, 2, and 3

Three simultaneously operating fixed-energy branch lines will include 4 hutches:

- Branch 1: two tandem hutches, B and C
- Branch 2: one hutch, D, with 2 instrument positions
- Branch 3: one hutch, E, with 2 instrument positions

Monochromators: Single crystal, horizontal deflection at nearly fixed angle, diamond and silicon, various reflections to allow choice of energy at fixed angle.

Heat load: Consider filtering power below 15 keV. Use single-crystal diamond filters to avoid disturbing wavefront

Fixed Energy Branch Angle Choices

Figures 6.26 and 6.27 below show calculated Bragg angles for various monochromator crystal materials (diamond and silicon) and reflections ((111), (220), and (400)), that match odd harmonic energies of an undulator, as a function of the undulator fundamental energy. Potential beamline angles are represented by horizontal lines, and potential operating points for the undulator are represented by vertical lines. The intersections marked by symbols show which beamline choices would match a Bragg condition for each operating point. Note that the (111), (220), and (400) reflections have nearly identical Bragg angles for harmonics having a ratio of 3, 5, and 7, respectively. This can provide flexibility in energy choice for a given beamline simply by switching between its monochromator crystals, keeping the operating point and beamline angle nearly fixed. Figure 6.26 shows the full range of potential beamline angles and operating points, while Figure 6.27 shows the beamline angles and operating points proposed for CHEX.

Tables 6.10 to 6.13 below show the fundamental energy, crystal reflection, undulator harmonic, photon energy, and exact 2θ angle for each of the proposed beamline angles and operating points in Figure 6.27.

Table 6.10. Undulator fundamental energy (keV), crystal reflection, undulator harmonic, photon energy (keV), and exact 2θ angle (degrees) for branches 1 and 2 at a nominal 2θ of 23°.

Operating Point #	Fundamental (keV)	Crystal	Reflection	Harmonic	Photon Energy (keV)	2 Theta (deg)
1	5	C	111	3	15	23.154
		C	220	5	25	22.68
		C	400	7	35	22.913
2	6.93	C	400	5	34.64	23.154
3	8.16	C	220	3	24.49	23.154
4	11.55	C	400	3	34.64	23.154
5	15	C	111	1	15	23.154

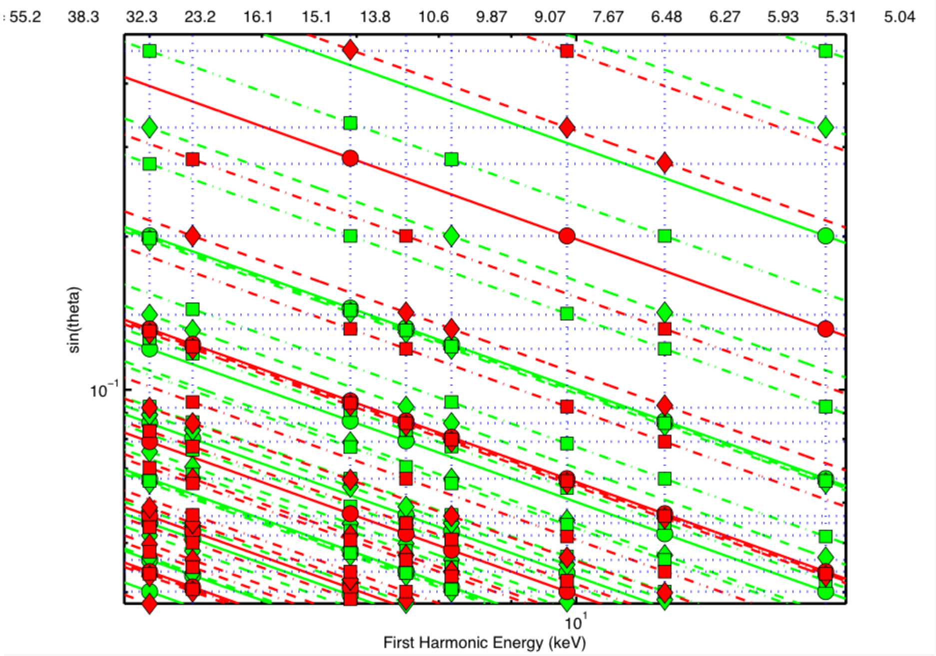

Figure 6.26. Plots of $\sin(\theta)$ *vs. undulator fundamental energy showing Bragg's law lines for diamond (green lines) and silicon (red lines) and odd undulator harmonics. Solid, dashed, and dash-dot lines are for (111), (220), and (400) reflections, respectively. Vertical dotted lines show potential undulator fundamental operating points, and horizontal lines show potential beamline central angles. Title gives central 2θ values in degrees. Intersections of Bragg angles with operating points close to the central angles are marked with symbols (circle, diamond, and square for (111), (220), and (400), respectively).*

Table 6.11. Undulator fundamental energy (keV), crystal reflection, undulator harmonic, photon energy (keV), and exact 2θ angle (degrees) for branch 3 option at a nominal 2θ of 7.6°.

Operating Point #	Fundamental (keV)	Crystal	Reflection	Harmonic	Photon Energy (keV)	2 Theta (deg)
1	5	C	111	9	45	7.671
		C	220	15	75	7.516
		C	400	21	105	7.592
		Si	400	13	65	8.055
2	6.93	C	220	11	76.21	7.397
		C	400	15	103.92	7.671
		Si	220	7	48.5	7.634
3	8.16	C	220	9	73.48	7.671
		C	400	13	106.14	7.51
4	11.55	C	400	9	103.92	7.671
5	15	C	111	3	45	7.671
		C	220	5	75	7.516
		C	400	7	105	7.592

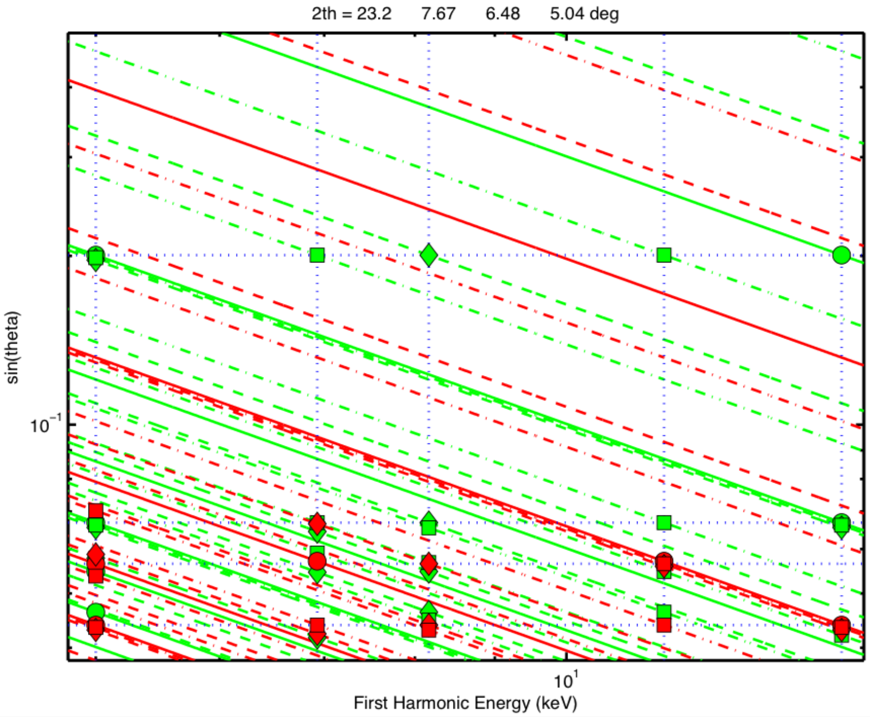

Figure 6.27. Plots of $\sin(\theta)$ *vs. undulator fundamental energy showing Bragg's law lines for diamond (green lines) and silicon (red lines) and odd undulator harmonics. Solid, dashed, and dash-dot lines are for (111), (220), and (400) reflections, respectively. Vertical dotted lines show potential undulator fundamental operating points, and horizontal lines show potential beamline central angles. The central 2θ value proposed for CHEX fixed-energy branches 1 and 2 is 23.2 degrees. Three options for the angle of branch 3 are shown (7.6, 6.4, and 5.0 degrees), all of which are compatible with the proposed layout. Intersections of Bragg angles with operating points close to the central angles are marked with symbols (circle, diamond, and square for (111), (220), and (400), respectively).*

Table 6.12. Undulator fundamental energy (keV), crystal reflection, undulator harmonic, photon energy (keV), and exact 2θ angle (degrees) for branch 3 option at a nominal 2θ of 6.4°.

Operating Point #	Fundamental (keV)	Crystal	Reflection	Harmonic	Photon Energy (keV)	2 Theta (deg)
1	5	C	111	11	55	6.275
		C	220	17	85	6.631
		Si	111	7	35	6.476
		Si	220	11	55	6.73
		Si	400	17	85	6.158
2	6.93	C	220	13	90.07	6.257
		C	400	17	117.78	6.768
		Si	111	5	34.64	6.543
3	8.16	C	220	11	89.81	6.275
		C	400	15	122.47	6.508
		Si	220	7	57.15	6.476
4	11.55	C	400	11	127.02	6.275
		Si	111	3	34.64	6.543
		Si	220	5	57.74	6.411
		Si	400	7	80.83	6.476

Table 6.13. Undulator fundamental energy (keV), crystal reflection, undulator harmonic, photon energy (keV), and exact 2θ angle (degrees) for branch 3 option at a nominal 2θ of 5.0°.

Operating Point #	Fundamental (keV)	Crystal	Reflection	Harmonic	Photon Energy (keV)	2 Theta (deg)
1	5	Si	111	9	45	5.036
		Si	220	15	75	4.934
		Si	400	21	105	4.984
		C	111	13	65	5.309
2	6.93	Si	220	11	76.21	4.856
		Si	400	15	103.92	5.036
		C	220	17	117.78	4.784
3	8.16	Si	220	9	73.48	5.036
		Si	400	13	106.14	4.930
4	11.55	Si	400	9	103.92	5.036
5	15	Si	111	3	45	5.036
		Si	220	5	75	4.934
		Si	400	7	105	4.984

Table 6.14. Summary of energies accessible at each fixed energy branch for each undulator operating point, showing three options for fixed energy branch 3.

Operating Point #	**Fundamental** *(keV)*	**Energies of Branches 1,2** *(keV)*	**Energies of Branch 3 (7.6°Option)** *(keV)*	**Energies of Branch 3 (6.4°Option)** *(keV)*	**Energies of Branch 3 (5.0°Option)** *(keV)*
1	5	15, 25, 35	45, 65, 75, 105	35, 55, 85	45, 65, 75, 105
2	6.93	35	49, 76, 104	35, 90, 118	76, 104, 118
3	8.16	25	73, 106	57, 90, 122	73, 106
4	11.55	35	104	35, 58, 81, 127	104
5	15	15	45, 75, 105	-	45, 75, 105

Fixed-energy branch single-crystal monochromator common design features:

- Use symmetric Bragg reflection geometry to preserve collimation
- Angular stability / vibration < 1 μrad to preserve brightness

Fixed-energy branches 1 (28ID-B/C) and 2 (28ID-D) monochromator design features:

- Use diamond crystals to transmit unused energies
- Use 2 theta of 23 ±0.5 degrees, to give diamond (111), (220), and (400) at 15, 25, and 35 keV, e.g. on 3rd, 5th, and 7th harmonics (see Figure 6.27)
- Monochromators at 27.9 and 39 m from source give ∼4 m offset between branches

Fixed-energy branch 3 (28ID-E) monochromator design features:

- Use silicon or diamond crystals
- Three potential mono 2 thetas (see Figure 6.27):
  - 7.6 ±0.2 degrees, to give diamond (111), (220), and (400) at 45, 75, and 105 keV e.g. on 9th, 15th, and 21st harmonics.
  - 6.4 ±0.3 degrees, to give diamond (111), (220), silicon (111), (220) at 35, 55, 85 keV on various harmonics.
  - 5.0 ±0.2 degrees, to give Si (111), (220), and (400) at 45, 75, and 105 keV e.g. on 9th, 15th, and 21st harmonics.

Fixed Energy Focusing Features Use dual compound refractive lenses (CRLs) to allow a range of focal spot sizes.

- Having two focusing elements in a tandem, "zoom lens" arrangement allows the focal spot size to be varied over a range of values while maintaining its position on the sample.
- Since CRL's do not deflect the beamline axis, alignment of dual focusing elements will be simpler than with KB mirrors.
- Since the source size is reasonably symmetric, we will use two-dimensional (axially symmetric) CRLs to provide equal horizontal and vertical focusing.
- Slits upstream of CRLs will control the coherent fraction.

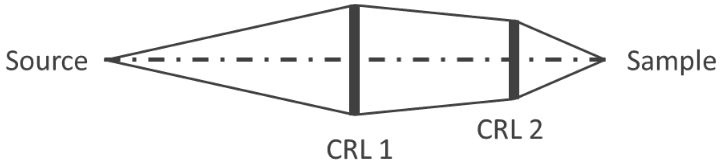

Figure 6.28. Sketch showing the pairing of CRLs to achieve adjustable focal spot sizes without changing the location of the spot on the sample.

Area detectors: pixel array detectors

- For optical design, assume minimum pixel size, p, is 55 μm, based on pixel sizes of current advanced detectors:
    - Pixirad: 52x60 μm
    - Eiger: 75 μm
    - SLAC ePix: 50 μm
    - Medipix/Merlin: 55 μm.
- For weak signals, sub-pixel spatial resolution can be obtained through a droplet analysis.

Table 6.15 gives the focusing geometries for all branches, which meet the goal of resolving speckle up to high energy. Variables used in formulas given below are:

- R = maximum sample-to-detector distance
- p = detector pixel size

where p/R is the detector angular resolution. This determines the maximum focal spot size, $a = 0.886\ \lambda\ R/p$, which varies inversely with photon energy $E = hc/\ \lambda$. Using p = 55 μm, one obtains

$$a \text{ (in } \mu\text{m)} = 20\ R \text{ (in m)} \ /\ E \text{ (in keV)}$$

Since the horizontal source size, e.g. 50 μm FWHM in 324-bunch mode, is typically larger than the vertical source size, the largest focal spot size will be in the horizontal (using axially symmetric CRLs).

Note that 2x oversampling of speckles is typically required for CDI. This will be obtained by:

- Focusing optics designed to go smaller than the limit given above, especially at photon energies less than the design maximum.
- Horizontal sample size or sample aperture smaller than the focal spot size.
- Use of a detector with an effective pixel size less than 55 μm, including the use of "droplet" algorithms that provide sub-pixel spatial resolution.
- using the vertical focus, typically 5 times smaller than the horizontal.

Values for the maximum required focal spot size at the minimum and maximum design energies are given in Table 6.15 for each experimental station. The range of horizontal focal spot sizes achieved by the dual CRL optics is also listed for comparison, using a horizontal source size FWHM of 50 μm.

The designs for CRL 2 (the downstream element of the dual CRL), which produces the smallest focus needed at the highest energy, is most critical. The required number of single Be lenses and the transmission of CRL 2 are shown in Table 6.15, calculated from the CRL calculator at *http://www.rxoptics.de/parameters.html* using typical Be lens parameters of 50 μm radius of curvature and 30 μm thickness at apices. These values are reasonable for all experimental stations.

Dual CRL Focusing Geometries Table 6.15 summarizes the focusing geometries of each branch using dual CRLs to allow the desired range of focal spot sizes to be achieved over the range of operating energies. Figures 6.29 and 6.30 show the number of individual lenses in the CRL stacks and the needed range of translation to maintain the focus for a typical branch line (C) at its minimum and maximum operating energies. Note that for simplicity, these figures assume all lenses have the same radius, given in the caption. It will actually be optimal to use mostly small-radius (50 μm) lenses and make small adjustments to the lens power with a few larger-radius lenses. For example, rather than using 51, 300-μm-radius lenses, one would use eight 50-μm-radius and one 100-μm radius.

The total number of individual lenses will be relatively large. However, lenses can be shared between CRL 1 and CRL 2, between the various endstations, and even with other beamlines. For the baseline design, simple manual changing of lens stacks within the lens housings is envisioned. To run all 4 simultaneously operating endstations at their maximum energy and smallest focal spot (e.g. B, D, E, and G) would require about 335, 50 μm radius lenses. However, a baseline design with about 250 lenses available would be sufficient, since it is highly unlikely that all stations will need to operate at their maximum energy simultaneously. Additional lenses could be part of contingent scope, to allow leaving working setups undisturbed. If other APS beamlines adopt CRL focusing, then a "lens pool" should be considered, similar to the current APS detector pool.

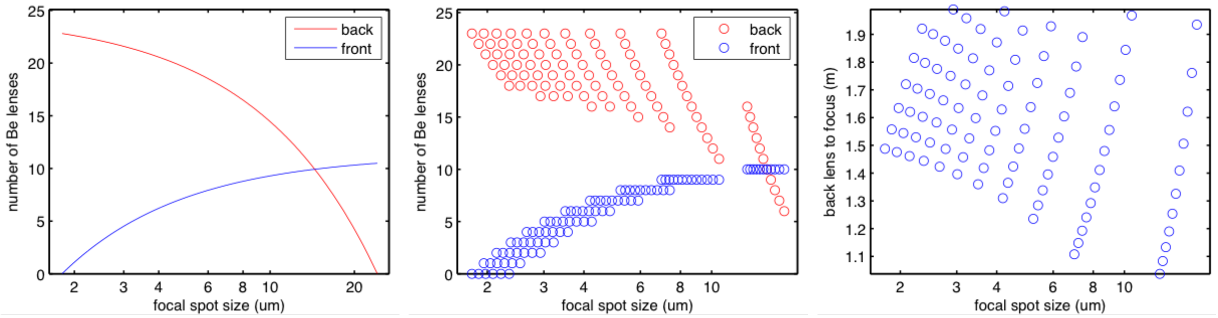

Figure 6.29. Calculated focusing performance of dual CRLs, for branch line C at 15 keV. (left) and (middle) give number of 300 or 100 um radius lenses needed for front or back CRL 1 or 2 to achieve a given spot size, for continuous or discrete variation in lens power. (right) gives change in position of CRL 2 to maintain focus at sample.

Description of optical components: Tunable branch 4

Monochromator:

- Double crystal Bragg geometry, optimized for minimum vibration.
- Energy range 15-60 keV, with option to go down to 5 keV.
- The bandwidth of Si 111 will give the optimal flux/speckle contrast tradeoff for many experiments. Ability to use narrower bandwidth (e.g. Si 220, diamond 111 and/or 220) crystals would be a useful option for some experiments.
- Horizontal diffraction geometry and upstream location to minimize effect of vibration on brightness / focal spot position.
- Need < 1 μrad stability of relative angles.

Table 6.15. Summary of dual compound refractive lens (CRL) focusing geometries for each branch beamline (and instrument location, if applicable). The first five rows give the distances from the center of the ring straight section to the critical beamline optical elements. (Note that the actual X-ray sources from the canted undulators will be at ±1.2 m from the center of the straight section; this has been neglected here.) The next two rows give the range of horizontal focal spot sizes possible by varying the powers of the two CRLs, imaging the 50 μm horizontal source (324 bunch mode) at the instrument position. The next four rows give the minimum design photon energy, and for this energy the required focus size to resolve speckle in a 55 μm detector pixel, the required number of single Be refractive lens sections of 50 μm apex radius in CRL 2, and the transmission of CRL 2. The final four rows give these quantities for the maximum design photon energy.

	Beamline Branch / Instrument							
Item Location:	**B**	**C**	**D/1**	**D/2**	**E/1**	**E/2**	**F**	**G**
Mono (m)	27.9	27.9	39	39	42	42	34	34
CRL 1 (m)	29	29	40	40	45	45	50	50
CRL 2 (m)	33.5	41.5	44	48	50.75	52.25	63	69.25
Instrument (m)	35	43	45.5	49.5	53	54.5	64.5	71.5
Detector (m)	39	47	48.5	53.5	62	62	68.5	77.5
Optical Performance and Requirements:								
hor. focus min. (μm)	2.2	1.8	1.7	1.6	2.2	2.2	1.2	1.6
hor. focus max. (μm)	10.3	24.1	6.9	11.9	8.9	10.6	14.5	21.5
at E min (keV)	15	15	15	15	35	35	15	15
req'd focus (max., μm)	5.3	5.3	4.0	5.3	5.1	4.3	5.3	8.0
CRL 2 N lens max	12	11	11	11	42	42	11	8
CRL 2 transmission	0.72	0.74	0.74	0.74	0.54	0.54	0.74	0.80
at E max (keV)	35	35	35	35	55	55	35	55
req'd focus (max., μm)	2.3	2.3	1.7	2.3	3.3	2.7	2.3	2.2
CRL 2 N lens max	64	63	63	63	105	105	62	103
CRL 2 transmission	0.42	0.43	0.43	0.43	0.31	0.31	0.43	0.32

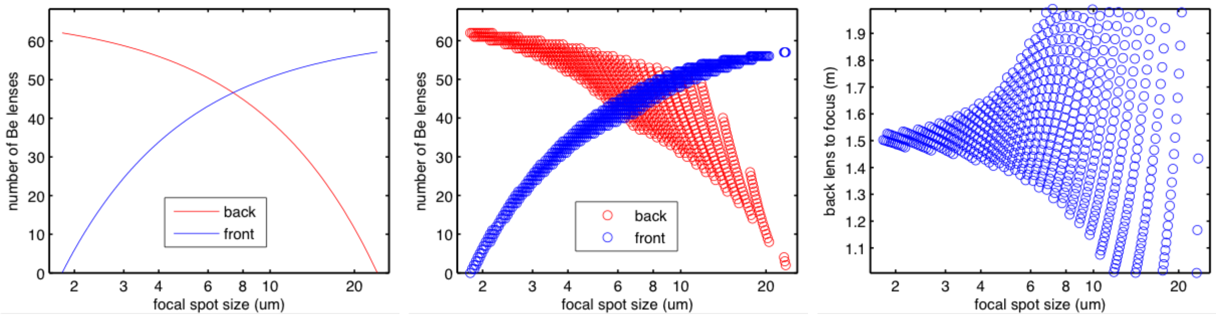

Figure 6.30. Calculated focusing performance of dual CRLs, for branch line C at 35 keV. (left) and (middle) give number of 300 or 50 um radius lenses needed for front or back CRL 1 or 2 to achieve a given spot size, for continuous or discrete variation in lens power. (right) gives change in position of CRL 2 to maintain focus at sample.

- Option for double-multilayer monochromator, and/or direct pink beam.

Focusing:

- Use dual compound refractive lenses to allow a range of focal spot sizes (see description above).
- Compare performance of KB mirrors instead of CRLs for this branch, to allow fast changing of energy.

Table 6.15 gives the focusing geometries for the F and G stations, which meet the goal of resolving speckle up to high energy (analysis given in Section 6-4.4.1 above).

Heat load: Consider filtering power below 15 keV as described above.

Hutches: Two in tandem, F and G, sized to resolve speckle at high energy.

Area detectors: Pixel array detectors as above.

6-4.4.2 Beamline Physical Layout

Overall Beamline

General Description Appendix 2 gives the overall layout, showing three horizontally diffracting single-crystal monochromators on one undulator feeding branches 1, 2, and 3 (stations B/C, D, and E), and a double-crystal monochromator on the other undulator feeding branch 4 (stations F/G). Each station has an enclosed control area. Advantage is taken of space available from sectors 27 and 29 adjacent to sector 28 to provide multiple hutches, four of which can operate simultaneously for high productivity and beam time access. This is possible because of the short beamline at 27-ID and the lack of bending-magnet beamlines at 28-BM and 29-BM. Relatively long hutches are optimized for coherent beam speckle observation.

Radiation Safety Aspects Nothing unusual. To minimize monochromator vibration, the DCM on the tunable branch may have a small offset, with appropriately designed bremsstrahlung shielding downstream.

Vacuum System Because of the highly interconnected nature of the multiple branches, and because of the relatively frequent need to open beamline vacuum to change CRLs, for reliability and risk mitigation we propose to use window(s) to separate the tunable and fixed energy beamlines from the ring vacuum, and potentially from each other. Appropriately polished, high quality Be or diamond windows should preserve the beam collimation. It is desirable to leave sufficient space for installation of differential pumps for windowless operation if needed in the future.

First Optics Enclosure and Infrastructure

Major Components Three single-crystal monochromators (SCMs) and a horizontally deflecting double-crystal monochromator (DCM) (with option for a tandem double-multilayer monochromator (DMM)) will be located in the FOE, as described above.

The upstream CRL 1 housing of the dual-CRL focusing optics for each of the three fixed-energy branches will be located just downstream of each SCM in the FOE. The location of CRL 1 for the tunable-energy branch will be in a separate enclosure downstream of the FOE, to allow access for changing lenses without disturbing operation of the fixed-energy branches.

The baseline scope will include simple CRL housings for manual changing of lenses. As an option in contingent scope, automated 'transfocators' would allow changing CRL 1 lenses in the FOE without disturbing other experiments or opening beamline vacuum. Likewise, transfocators for the tunable branch could allow more rapid changes in energy.

A chemical exhaust system will service the experimental hutches B through G and their associated gas cabinets. The plenums will be sized to minimize vibration at the needed flow. Filtered make-up air will be provided in the hutches so that they are maintained at neutral or positive pressure, to maintain cleanliness.

Windows, Slits, Collimators, Shutters/Stops A polished Be or diamond window will separate the beamline from the ring vacuum, with space to replace it with a differential pump in the future if needed.

- Two power filters to reduce heat load on the monochromators will be located on each undulator beam.
- Two sets of white beam slits will be located on each undulator beam upstream of the first monochromator.
- Four sets of monochromatic beam slits will be located upstream of each CRL 1 to adjust the coherent fraction.
- Four shutters for the three fixed energy branches and the tunable branch will be located in the FOE.

Fixed Energy Branches 1, 2, 3, and Tunable Branch 4

Components Each of the four branches includes two locations for experiments, either in tandem hutches (B and C on fixed energy branch 1, or F and G on the tunable branch 4), or within a single hutch (D on branch 2, E on branch 3). Housings for CRL 2, as well as slit sets to adjust the coherent fraction, will be positioned upstream of all eight experimental locations.

Instruments Four goniometers will be included in the baseline scope, one for each branch line. These will support the instruments using shared goniometers shown in Table 6.9. Sample goniometers will have all six degrees of angular and positional control, stable to sub-microroadian angle and sub-μm position accuracy, and capable of supporting 50 kg chambers. Final slits close to the sample position will be needed to adjust the illumination and provide harmonic rejection. Incident intensity monitors will be needed upstream and downstream of these slits. The goniometer will also include separate detector circles for supporting a pixel array detector at distances up to 1.5 m from the sample. (An example of such an advanced goniometer is the one recently installed at 12-ID-D.) Anti-scatter slits downstream of the sample will prevent background from reaching the detector. Attenuators will allow the detector to record the direct beam and Bragg peaks. For longer detector distances, the detector will be positioned on a separate moving support, with software control of its motion relative to the goniometer.

Outside the funded scope of the project, we anticipate that the community will provide several instruments with integrated goniometers through Partner User agreements. Some of these are also indicated in Table 6.9.

6-4.4.3 Additional

Detectors

Four low-noise, small-pixel pixel, rapid-readout array detectors with good sensitivity to high energy X-rays will be needed for each of the simultaneously operating experiments. Detectors with ∼55 μm or smaller pixels and CdTe sensors are envisioned, similar to those available from Pixirad or Merlin. As contingent scope, additional detectors would allow coverage of multiple regions of reciprocal space (e.g. low angle and high angle), and minimize switching of detectors between operating setups.

Computing

Goniometer control through an advanced scattering software control interface such as SPEC is needed. Online, real-time analysis of XPCS and CDI data flowing from the pixel array detectors will require a dedicated, modest computational facility (e.g. high-performance Linux workstations). The average data rate will be about 1 TB per day for each of the four operating experiments. A facility to store about 1000 TB of data prior to reduction / analysis will be required.

Specific Safety Requirements

Equipment and engineered controls, such as gas cabinets, purifiers, gas sensors, automated flow control systems, and chemical exhaust for hazardous gases (e.g. hydrogen, ammonia, carbon monoxide), will provide needed synthesis sources and chemical environmental control to all of the experimental stations. A coordinated, multiplexed system will allow efficient sharing of gas sources when they are needed by multiple experiments at the CHEX facility.

Specific Conventional Facilities Requirements

Stable ambient temperature, beam position monitoring and feedback, and systems designed to reduce creation and sensitivity to vibration will be required to maintain the position and angle stability of the X-ray beam and sample to the μm and microradian level needed for coherent experiments.

Support facilities

Standard dry and wet laboratories in the adjacent LOM will be required for sample preparation and experimental setup. As part of contingent scope, a clean (e.g. class 100) sample preparation space in the control area adjacent to the beamline would be very useful.

6-4.5 R&D Needs

Here we list some open questions about the design that could be addressed either by further development and comparison of design alternatives, or by more elaborate R&D or prototyping work.

Superconducting undulator and heat load on front end

Increasing the length of each undulator from 1.2 m to 1.5 m would give 37% higher brightness at 15 keV, but would also increase the power and power density on front-end components by 24%. Further design work is needed to determine the best undulator choice, including comparison with revolvers.

Heat load on monochromators

An analysis, and potentially prototyping, should be performed to determine the heat load effects on coherence preservation by the monochromators, and the potential benefits of using an upstream adjustable power filter to remove intensity at energies below the operating energy (e.g. from lower harmonics).

Focusing optics

Currently CRLs are used at coherent X-ray beamlines at LCLS, NSLS-II, and elsewhere. However, improvements may be possible, such as improving the grade of Be used. A study of the effects of CRLs on beam coherence, in collaboration with the manufacturer and users worldwide, would be valuable.

While CRLs offer the simplicity of no displacement of the beamline axis and simple adjustment of focal spot size, the strong photon energy dependence of their focal length may complicate experiments in which the energy is scanned or changed repeatedly. For the tunable beamline, this could be mitigated by employing a “transfocator” that can exchange CRLs by automation to rapidly adjust for energy changes. Alternatively, KB focusing optics that have no energy dependence up to a critical value should be considered.

Harmonic rejection

Because CRLs have a very different focal length for each harmonic, slits close to the focus can effectively reject unwanted harmonics by factors of up to 10^5. For cases in which this is insufficient, a design option for a small harmonic rejection mirror in the hutch should be considered.

Small sphere-of-confusion goniometers

For many experiments, goniometers with one or more axes having sub-μm axis stability would be desirable. Designs for such goniometers should be prototyped and tested.

Manipulation and stability of samples

Methods to manipulate and hold samples stably, such as small particles in reactive environments, should be developed and prototyped.

Pixel Array detectors

Many different pixel array detector systems are available or under development that have characteristics suitable for high-energy XPCS or CDI experiments. Testing of these systems and development of integrated analysis techniques, such as time correlation analysis, droplet algorithms, sub-pixel spatial resolution, etc., should be pursued.

Detector positioner

To position an area detector up to several meters away from the sample, long goniometer arms are impractical. Designs, such as towers mounted on air pads, with laser-based position determination (using commercial systems developed for virtual reality headsets, for example), should be developed and prototyped.

CDI algorithm standardization

On-the-fly analysis of CDI data, as well as subsequent refinement, will be required. This field is ripe for development of standardized algorithms with tested and accepted error and resolution metrics. A cross-facility effort in this area would be useful.

Electronic logbook and metadata system

Like many beamlines, the CHEX sector would benefit from an electronic logbook system that could easily capture experiment status, linked to data files and plots, and provide it in an editable, logbook format documenting the sequence of the experiments. Newly available platforms, such as tablets with good handwriting input, provide an opportunity to create a next-generation electronic logbook.

6-5 Coherent Surface Scattering Imaging (CSSI) Beamline

6-5.1 Executive Summary

At the center stage of the scientific topics, surface/interface phenomena are of great interest to scientists in a variety of fields. Imaging techniques provide ideal tools to directly observe surface/interface structures and monitor their dynamic evolution responding to changes in external conditions. Much progress has been made in the development of hard x-ray sources and tools, including the development of storage-ring and x-ray free-electron-laser (XFEL) sources. Among all, grazing-incidence x-ray scattering and x-ray photon correlation spectroscopy (XPCS) exhibit unique advantages for exploring the surface/interface problems that are challenging to solve using other imaging techniques dynamics probes. The APS Upgrade will increase brightness by a factor of 100 to 1000 – clearly high-brightness and coherence are the cornerstones of the upgraded source. The x-ray beams from the upgraded source possesses a large coherent fraction, which is well suited for measuring the spatiotemporal evolution of structures in complex systems with the highest precision at surfaces and interfaces. A new beamline for coherent surface-scattering imaging (CSSI) takes advantage of the much improved x-ray beam coherence and is ideal for probing and understanding mesoscopic spatial-temporal correlations by integrating the coherence-based surface x-ray probe with state-of-the-art coherence-preserving optics and advanced x-ray detectors.

6-5.2 Scientific Objectives

Surface/interface phenomena are of great interest to scientists in a variety of fields. More specifically, these challenging topics include, but are not limited to: evolution of biological membranes and supramolecules in aqueous environments, thin film and quantum dot growth at surfaces and interfaces, assembly of planner polymer nanocomposites, and structural analysis of three-dimensional (3D) nanoscaled electronic circuits using additive manufacturing. The temporal and spatial resolution promised by the APS low-emittance upgrade ideally matches the challenges of understanding mesoscaled structure and dynamics from nm to mm and ns to s. The experiments at CSSI beamline can provide much needed structural and dynamical information to answer the following questions:

- Hierarchical assembly of functional materials: how physical and chemical processes and dynamics are involved to lead to hierarchical order in mesoscopic structures and the functionalities;
- How to advance nanopatterning using combination of top-down and bottom-up techniques for the controlled fabrication of complex and multicomponent nanomaterials that are needed for advanced functional applications;
- How to control the morphology of thin-film based photovoltaic to optimize the efficiency of the devices; and
- How do the dynamics at every level of the hierarchical structures control the complexity and specific functionalities of mesoscopic systems.

Those questions often need to be addressed in association with processes that involve non-equilibrium temporal evolution of structural complexity at molecular, nanoscopic, and mesoscopic scales [77]. More specifically, the CSSI beamline will be the prime user facility for the research will be include:

- Self-assembly of mesoscale structures at surfaces and interfaces,

- Three-dimensional surface nanopatterning and nanofabrication,
- Three-dimensional morphology of photovoltaic thin films,
- Dynamics at surfaces and Interfaces,
- Capillary instability in confined geometry, and
- At-wavelength and in-situ metrology for x-ray coherence preserving reflective optics.

Coherent surface-scattering imaging (CSSI) [78] will satisfy the needs as a non-destructive in situ structure characterization with three-dimensional high resolution and temporal resolution afforded by the intense coherent x-ray beam from the upgraded APS. In the meantime, grazing-incidence x-ray photon correlation spectroscopy (GIXPCS) is a complementary way to understand the interplay between the dynamics and structure in order to gain the control of the structure evolution in the materials processing. More detailed science cases are described in Chapter 2.

6-5.2.1 Use of APS-U Characteristics

At worldwide synchrotron x-rays sources, coherent diffractive imaging (CDI), coupled with advanced x-ray detectors and computational algorithms, has opened up new research frontiers in structural sciences that are simply not attainable previously [79]. The reconstruction of the images in real spaces requires phase retrieval to complement the x-ray scattering intensity measurement using partially coherent beam. Most CDI methods use transmission geometry, which is not suitable for nanostructures grown on opaque substrates or for objects of interest comprising only surfaces or interfaces, which are highlighted in the Science Section. In order to gain the information in 3rd dimension, namely, in the direction perpendicular to the surfaces/interfaces of interest, CSSI in grazing-incidence geometry takes advantage of enhanced x-ray surface scattering and interference near total external reflection. The concept of CSSI was demonstrated the successful reconstruction of substrate-supported non-periodic surface patterns in three dimensions as shown Figure 6.31[78]. Similar to other CDI methods, one of the unique advantages of CSSI is lensless approach, the theoretical resolution is only limited by the x-ray wavelength.

Coherent beam from the APS Undulator A through a coherence defining slit set was used to reconstructing 3D structures of a silicon-supported Argonne logo (Figure 6.31B). This measurement was made at 8-ID-E beamline of the APS with a monochromatic incident beam (photon energy E= 7.35 keV with $\Delta E/E = 2\times10^{-4}$). The transverse coherence length along the horizontal direction was 7 μm and the beam was fully coherent across the entire vertical direction over the 15 μm beam. The coherent flux was approximately 1 X 10^9 photons/sec. A CCD-based Coolsnap HQ^2 detector was placed 0.7 m away from the sample for collecting scattering patterns. A 5× lens was used, resulting in an effective pixel dimension of 1.29 X 1.29 μm^2 on the detector, to provide the fine reciprocal space resolution for recording speckle patterns with such a short sample-to-detector distance. However, the overall detection efficiency of the detector system suffered, which was estimated to be only 0.13% (i.e. 1 photon detected for about 750 scattered photons). To obtained detectable coherent scattering signal in the demonstration experiment at the APS, the sample size was designed to be very large (400 μm long, 5 μm wide and 40 nm thick). Despite the large sample, the scattering signal was still low. A typical data collected from measurements requiring a few hours of time resulted in 3D imaging reconstruction resolutions of 2.6 μm, 22 nm and 2.7 nm in each of the 3 dimensions. Again, the limitation came from insufficient sample-to-detector distance that renders efficient but large-pixel-size detectors unusable, resulting the poor data collection efficiency.

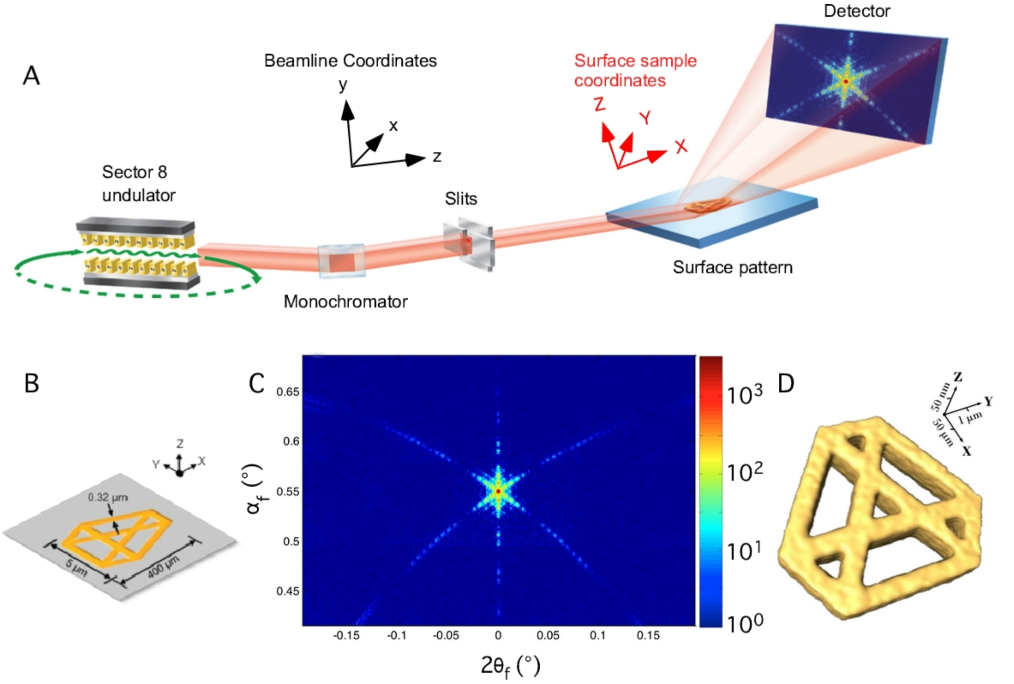

Figure 6.31. CSSI demonstration at the APS Sector 8. (A) Schematics of experiment setup with two specific coordinate systems that used throughout the proposal text. The sample was a lithographically prepared gold pattern at silicon surface. (B) The size of the pattern was 400 μm long (along the x-ray footprint direction) and 5 μm wide with a feature size of 0.32 μm. The coherent surface scattering pattern (C) was taking over a period of a few hours to improve the data statistics with a maximum scattering intensity of 3000 counts. The reconstructed 3D structure (D) has resolutions of 2.6 μm, 22 nm and 2.7 nm in each of the three directions.

Nevertheless, the experiment was highly successful demonstrating the feasibility of CSSI concept as shown in reference[78].

CSSI will benefit directly from the two to three orders of magnitude increase in coherent flux promised by the APS-U, as the current APS beam delivers 0.01% to 0.1% coherent photons over the hard x-ray energy range. To demonstrate the determining impact of coherent flux on CSSI, recently, a similar experiment at the P10 beamline of DESY-PETRA III Source in Hamburg, Germany. Besides having about 10 times more coherent flux than that at Sector 8 of APS, the P10 beamline was designed to optimize coherent experiments such as CDI with beam focusing, large sample-to-detector distance, and efficient detector systems. The preliminary data shows overwhelmingly stronger scattering intensity from a much smaller (1/40) sample over a much larger q range (10 times) and more than 10 times reduction in data collection time. While the data analysis is still ongoing, the data quality indicates that the imaging reconstruction resolution can be improved to 250 nm and 3 nm in the two in-plane dimensions, about an order of magnitude improvement from the APS data. With the short data collection time ($<$ a few seconds for each scattering frame) with a 4-million pixel Eiger detector, we were able to take scattering images at limited azimuthal rotation angles ($\pm 3°$), which will improve the resolution along beam direction by a factor of 10. A CSSI pattern from the much improved measurement at PETRA-III is shown in Figure 6.32A. Therefore, with the APS-U, 1 or more orders of magnitude increase in coherent flux over that at PETR-III, we anticipate that the resolution of the CSSI measurement will reach 10 nm (or 2-5 nm with tomographic measurement) in the beam direction, and around 1-2 nm in the other directions, as shown in Figure 6.32B. The data collection efficiency is improved by at least a factor of 10^5. Again, such resolution values can only be reached when the beamline optics and layout are optimized to preserve the beam coherence and detection efficiency. Conversely, the ultimate reconstruction resolution demonstrates the necessity of the APS-U for CSSI and to make CSSI not only practical but also taking the full advantage of the upgraded low-emittance source at the APS-U in hard x-ray regime up to 30 keV as shown in this beamline Preliminary Design.

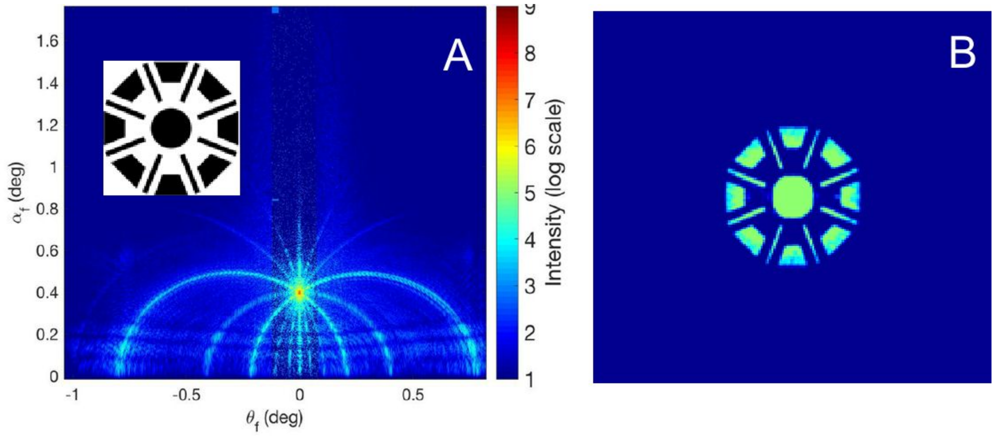

Figure 6.32. CSSI measurement carried out at P10 beamline of PETRA-III: (A) scattering pattern taken within 10 s and (B) reconstructed pattern with spatial resolution 10 times better than what is achievable at current APS. With a more coherent source, optimized optics, instruments, and detectors, the data collection efficiency was improved by a factor of 10^5.

6-5.2.2 Key Beamline Characteristics

The key characteristics of the beam at the sample position at CSSI beamline are summarized in Table 6.16. The coherent flux delivered at the sample position at all beam energies up to 30 keV will be at least 1 order of magnitude higher than any existing beamline worldwide. With all focusing devices imaging the source directly the coherent photon flux is preserved. We anticipate that the beamline will be the world leading beamline that is well suited for coherent scattering for surfaces and interfaces and for understanding mesoscopic spatial-temporal correlations in functional materials and their processing.

Table 6.16. Summary of beam properties at the sample location

Properties	**CSSI**		**GIXPCS**		**GISAXS/WAXS**
Coherent flux (ph/s)	@8 keV $> 5x10^{12}$	@15 keV $> 1x10^{12}$	@10 keV $> 5x10^{12}$	@30 keV $> 5x10^{11}$	Total Flux $> 1x10^{13}$
E Range (keV)	6 - 20		6 - 30		6 - 30
Beam size horizontal (μm)	1-2		15-20		35
Beam size vertical (μm)	0.2 -0.4		3-5		10

6-5.3 Source & Front-End Requirements

6-5.3.1 Insertion Device

There are two figures of merit to consider to choose proper undulator source: coherent flux and x-ray photon energy tunability/tuning range. The efficiency of the CSSI measurement is critically depending on coherent flux, which requires a 4.8-m long undulator that spans the entire straight section of about 5 m. The commonly used x-ray photon energy for CSSI will be between 7 and 8 keV to optimize coherent flux, penetrability of dry film samples, speckle size, detector efficiency and radiation damage. When ultimate coherent flux is needed, the beamline should allow a photon energy as low as 6 keV. The proposed CSSI beamline will also be a world-class facility for studies of liquid-liquid, liquid-vapor, and liquid-solid interfaces. Structure and dynamic studies of those buried interfaces require photon energy tunable to 30 keV, sufficient to penetrate samples of 1 cm thick ionic solutions with metal species such as zinc, copper, cadmium, etc. To accommodate coherence-based experiments on samples at liquid/liquid and liquid/solid interfaces, such high-energy x-rays will be necessary to reduce absorption and background scattering from bulk liquids/solid. Undulators capable of producing 30-keV coherent beam can only be afforded at the APS-U, a hard x-ray coherent source. A revolver type undulator with two magnetic pole periods of 21 and 25 mm would fit the bill: high coherent flux, continuous tunability from 6 to 30 keV as seen in Figure 6.33. Since only the 1st and 3rd harmonics will be used to cover the energy range, there is no appreciable drop in total flux at the high-energy end. The peak brilliance will be over 10^{22} ph/s/mrad^2/mm^2/0.1%bw at 10 keV, a full two orders of magnitude higher than the current Undulator A beam.

6-5.4 Beamline Layout

Given at least 10 times higher coherent flux at APS-U over PETRA-III, the CSSI beamline directly takes advantage of the APS-U source property. Similar to other CDI methods using transmission

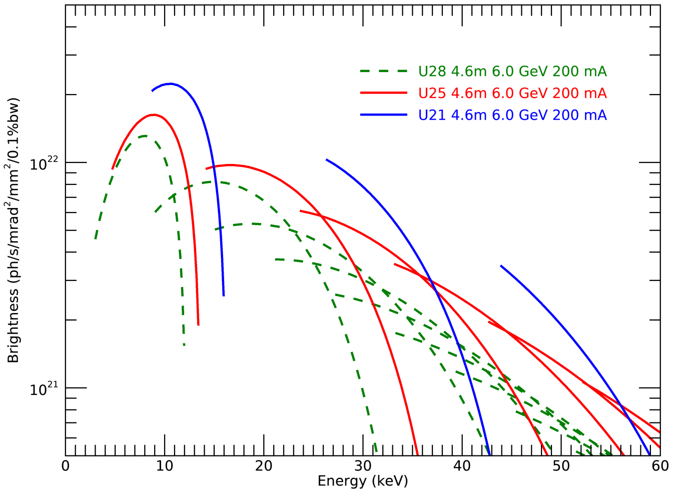

Figure 6.33. Brightness curves of a 4.8-m long revolver type undulator with 21 and 25 mm pole periods that can be tuned continuously from 5 to 30 keV.

geometry, CSSI needs as many coherent photons as possible. The use of maximum number of coherent photons most effectively and efficiently is critical. Also, the wavefront of the x-ray beam should not be distorted by the beamline optics and instrumentation; any distortion should be caused by the samples. Unique to CSSI, special sample handling capability is needed to accommodate the surface grazing-incidence scattering geometry. Therefore, the design of the beamline will take a minimalist approach while the coherence properties and the wave front of the beam will be optimally preserved. This Preliminary Design Report will cover the overview of the beamline, source of the beamline, major optical components and instruments for sample handling, and consideration of the detectors. The beamline will accommodate 3 modes of operations: 1) CSSI using microfocused x-ray beam, 2) GIXPCS using an x-ray beam slight larger than CSSI operation, and 3) conventional GI-SAXS/WAXS using close to 1:1 focused full beam.

6-5.4.1 Overview of the beamline layout

The design of the beamline will take a minimalist approach so the coherence properties and the wave front of the beam will be optimally preserved. Ideally, the only wave front modifying optics will be focusing devices that deliver highest coherent photons to the samples at surfaces and interfaces. The source and optics layout of the beamline will aim to achieve the following goals:

- Brightest possible coherent x-ray photon beam from an undulator source with continuous energy spectrum from 6 to 30 keV suitable for variety of surface and interface samples.
- Highest possible coherent flux on micrometer to sub-millimeter size samples.
- Minimum amount of optics and mechanical motion freedoms to ensure beam and sample stability.
- Sample handling systems having nanometer resolution and stability for grazing incidence geometry.

- Sufficient sample to detector distance to achieve speckle oversampling using efficient but large-pixel detectors.
- Efficient detectors over the entire photon energy range up to 30 keV.

The following source and major optics are planned at the beamline:

- A revolver-type undulator that covers continuous spectrum required for CSSI samples
- A single flat mirror with multiple coating stripes to reject higher-order harmonics in different photon energy ranges
- Multiples sets of monochromators (in the same vacuum chamber) to deliver either narrow bandwidth (10^{-4}) or wide bandwidth (10^{-2}) photon beam to the sample.
- Multiple sets of focusing devices (either sets of CRLs, kinoform lenses, or KB mirrors) in zoom configuration. The focusing device will generate x-ray spot sizes suitable for CSSI (submicrometers to micrometers), GIXPCS (up to 10 micrometers), and GISAXS (10s micrometers) modes.
- Sample positioning and handling need motions, reproducibility and stability of nanometer resolution to satisfy the requirement of grazing incident geometry. A liquid diffractometer will facilitate the study of nanosctructures at air/liquid and liquid/liquid interfaces.
- Probing mesoscaled structures and dynamics requires detecting scattering patterns at both small angles (low-q) and wide angles (high-q) with two detectors. The wide-angle detectors will be close to the sample and the small-angle detector should be at a large distance from the sample to ensure the q-space resolution. A long end station will ensure the large sample to detector distance.
- Most efficient large area detectors are to be used as small-angle detectors. CSSI is a unique method that uses scattering patterns near primary reflection without a beam stop. Therefore, a high-count-rate and high-dynamic-range detector is essential for the complement the large-area commercial detector.

Based on the design concept, Figure 6.34 shows a schematic layout of the beamline with the locations of major beamline components.

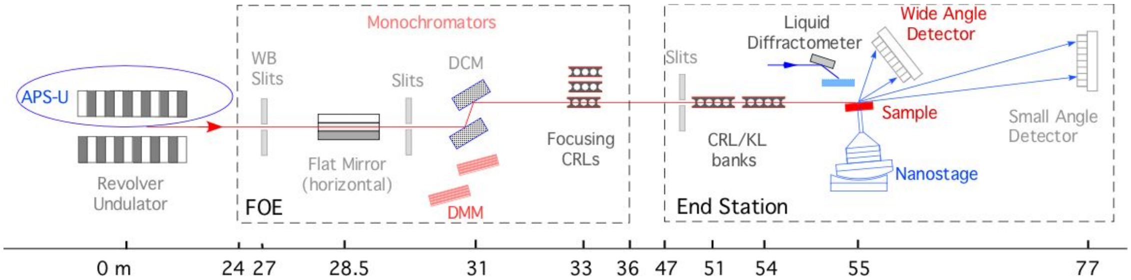

Figure 6.34. Schematic layout of CSSI beamline source, optics, instrument, sample handling apparatus and detectors.

To accommodate the requirements of the beamline layout, Sector 9-ID beamline is chosen to host the proposed CSSI instruments. An engineering drawing is provided in Figure 6.35 to depict the beamline layout at scale, as Table 6.17 includes a list of major beamline components and their approximate locations in the beamline.

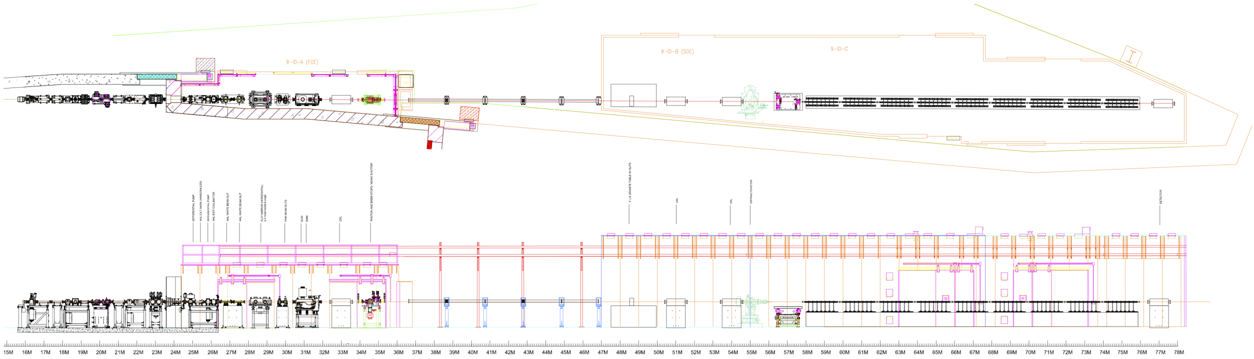

Figure 6.35. Engineering drawing of CSSI beamline to locate at APS Sector 9, including standard APS-U high heat load Front End (FE), First Optics Enclosure (FOE), and End Station (ES).

Table 6.17. Major components of CSSI beamline and their locations at Sector 9-ID of the APS

Location (m from source)	**Component**	**Status**
25.3	FE Exit Mask	HHL Front End
26.1	FE Collimator	HHL Front End
26.8	WB Slits (upstream)	New
27.5	WB Slits (downstream)	New
28.7	Flat mirror – horizontal bounce	New
29.7	Pink Beam Slits (upstream)	New
30.0	Pink Beam Slits (downstream)	New
31.2	Double Crystal Monochromator	New
31.2	Double Multilayer Monochromator	New
33.0	Focusing CRL #1	
34.5	Beam Stops and Mono Shutters	
51.0	Focusing CRL #2	New
54.0	Focusing CRL #3	New
55.0	Sample Chamber, Nanostages, Liquid Diffractometer	New
55.5	Wide-angle Detector	New
77.0	Small-Angle Detectors	New

For synchrotron x-ray beam with a Gaussian intensity distribution at a distance z away from the source point (approximately the center of the undulator), the coherent length can be determined by the source emittance properties (Table 6.18). The transverse or spatial one-sigma coherence lengths ξ in the horizontal (x) or vertical (y) direction is given by the Van Cittert-Zernike theorem, $\xi = \frac{\lambda z}{4\pi\sigma'}$ where λ is the x-ray wavelength, and σ is the one-sigma source size (in x or y direction). For simplicity, with a photon energy at 12.4 keV ($\lambda = 0.1\ nm$), an energy independent $\sigma_x \sim 15\mu m$ and $\sigma_y \sim 4\mu m$ (both RMS) and near the location of the ratchet wall (z ~24 m), this leads to FWHM (=2.35×) spatial coherence lengths of $\xi_x = 45\mu m$ and $\xi_y = 170\mu m$ (FWHM) and corresponding angular sizes of 1.9 μrad and 7.1 μrad respectively. To reduce the unnecessary heat load on the beamline optics and also to achieve a better separation between the x-ray and bremsstrahlung radiation fans further downstream, the maximum size of the beam is limited via a fixed water-cooled beam-defining aperture near the ratchet wall which also serves as the high impedance vacuum section required by the differential pumping scheme. The size of the fixed aperture is 40 X 40 μrad^2 which corresponds to 1 X 1 mm^2. Since the fixed aperture is at least 5 times larger than the coherence length of the beam, it will not affect in any negative way the beamline performance.

Table 6.18. Major brilliance properties of APS-U source for CSSI beamline

Quantity	**Symbol**	**APS-U Range**	**Present-day**	**Units**
Horizontal source size	σ_x	5 - 30	275	μm
Horizontal divergence	σ'_x	2 - 10	11	μrad
Horizontal size-divergence product	$\sigma_x\sigma'_x$	50 - 91	3100	pm
Vertical source size	σ_y	2 -14	10	μm
Vertical divergence	σ'_y	1 -7	3.5	μrad
Vertical size-divergence product	$\sigma_y\sigma'_y$	6 -50	35	pm

The first optical enclosure (FOE) will host the main optical elements – horizontally deflecting mirror, pink beam slits, a double crystal monochromator (DCM) and a double multilayer monochromator (DMM, for pink-beam operations), and monochromatic beam secondary slit. There is a CRL bank (33 m from the source) to focus the x-ray with close to 3:2 demagnification ratio at the sample location.

The CSSI and GIXPCS experiment will be performed in a single experimental station (ES) of about 31 m long and monochromatic and pink beam compatible. In the upstream of the station there will be a long optical table for primary beam conditioning optics such as CRL focusing device, silicon-based kinoform lenses (KLs), or KB mirrors. In addition to slits and beam position monitors, there will be a flat mirror to deflect beam downward 1 to 10 mrad for scattering experiment with air/liquid and liquid/liquid interfaces. The major component inside the station will be a nanostage for sample manipulation tailored for the grazing-incidence geometry required by CSSI. The stage will be fitted onto a versatile sample diffractometer located at around z = 55 m from the source. There will be a 20 m long small-angle scattering (SAXS) table where the area detectors are situated. One of the detectors will be situated close to the sample to collect wide-angle scattering patterns.

Coherent-beam defining slits

In the ES at about 50 m from the source, a pair of slits will have a vertical opening equal to 2 times of the beam vertical coherent length (about 500 μm) and a horizontal opening equal to 3 times of the beam horizontal coherent length (about 300 μm).

Harmonic rejection mirror

There will be a considerable amount of high-order harmonics from the undulator source. The x-ray photons in the harmonics are less coherent than those in the fundamental. A high-quality flat mirror will be used to reject higher order harmonics and to reduce the heat load of the x-ray beam impinging on the first crystal of the monochromator. The mirror will work in horizontal reflection geometry and will be placed 28.5 m from the source. To accommodate the wide x-ray photon energy range from 6 to 30 keV, a flat mirror with three reflection stripes (Figure 6.36), uncoated silicon (or silicon carbide), Pd and Pt coatings, will be used. The substrate of the mirror is either silicon or silicon carbide. The three stripes handle 3 photon energy ranges:

- Uncoated Si: 6 to 11.5 keV, @90% reflectivity
- Pd coating: 11.5 to 23 keV @90% reflectivity
- Pt coating: 23 to 30 keV @80% reflectivity

Reflectivity simulation shows that the optimum incident angles for the photon energy ranges and the mirror coatings is 2.7 mrad (0.154°). With the incident angle, the mirror should be 600 mm long to intercept 1.44 mm x-ray beam in the horizontal direction, or about 1 mm in the middle 70% portion of the mirror, which is considered to be of best quality. To preserve the wave front, the specification of the mirror surface is 0.1 nm rms roughness, 0.05 μrad rms slope error. To handle the high heat-load of the beam, zoned water cooling will be employed to achieve figure correction in real time (similar to those used at high-rep-rate XFEL beamlines).

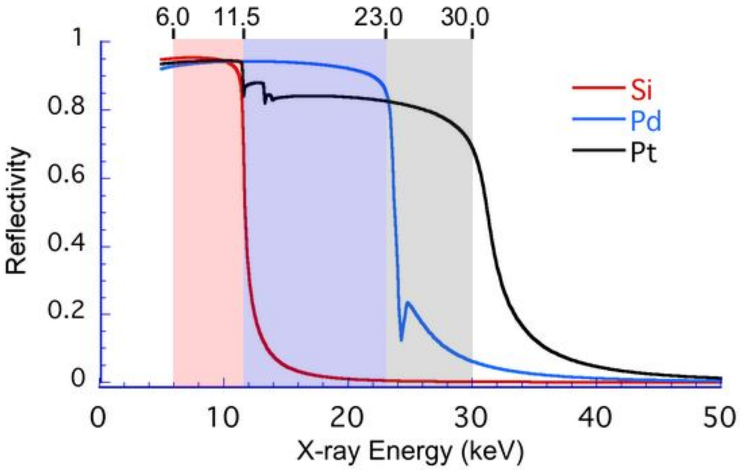

Figure 6.36. Reflectivity curves of three reflection stripes: 1) uncoated Si, 2) Pd coating, and 3) Pt coating. The three stripes will be sufficient for high harmonics rejection in the energy range from 6 to 30 keV.

Monochromators

Monochromators define longitudinal (temporal) coherence of the x-ray beam. In grazing-incidence geometry, the coherent measurement only requires a longitudinal coherent length a fraction of the sample size depending on both incident angle and the scattering angle of the x-rays. In principle, the resolution of the reconstructed images in CSSI is determined by the detectable q range. For CSSI experiments at the current APS beamline, the achievable lateral resolution is about tens of nanometers, and vertical resolution is a few nanometers. In order to further improve the spatial resolutions of CSSI, one must collect data at larger q values (higher than what achievable at PETRA-III). A double-bounce multilayer monochromator with an energy bandwidth of about 1% can improve the coherent flux by a factor 20 to 50 over conventional crystal monochromator ($\Delta E/E=10^{-4}$). Coherence and wave-front preserving multilayer monochromator requires R& D effort. Therefore, we design a monochromator vacuum chamber and stage with a place-holder for the double multilayer monochromator (DMM). A double bounce of crystal monochromator (DCM) setup, using Si (111) and Si (220) in pseudo channel-cut configuration can be also equipped for high-q scattering and diffraction measurement. Also, DCM can be used for samples are sensitive to radiation damage when lower incident x-ray intensity is desirable. To control the beam footprint at the crystal surface, Si (111) will be used for beam energy from 6 to 15 keV and Si (220) from 15 to 30 keV. As shown in Figure 6.37, an offset 1 to 2 mm between the two crystal surfaces will be used to ensure that. Over the x-ray energy coverage by the monochromator from 6 to 30 keV, the beam offset shift is minimal ($< 100\ \mu$m). Given the heat-load value at the current APS beamline with 2 tandem Undulator A's, we anticipate liquid N_2 cryo-cooling of the first crystal will become necessary.

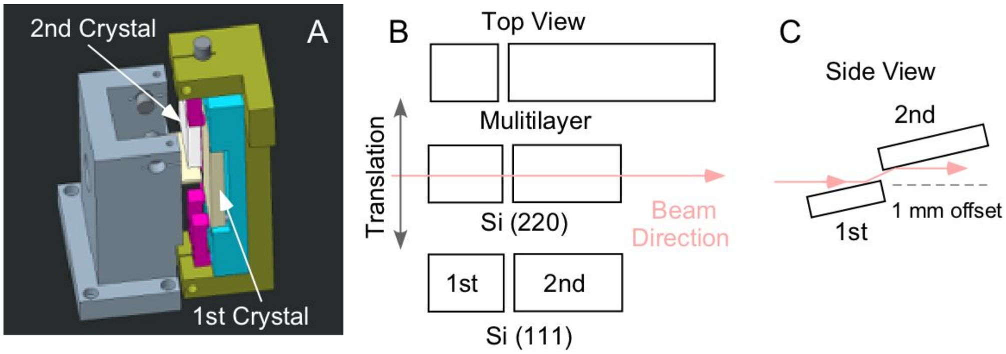

Figure 6.37. Monochromator arrangement at CSSI: (A) Model of a low-offset pseudo channel-cut monochromator, (B) schematic top view of the monochromators with double Si(111) and Si(220) crystals, and double multilayer setup on a translation stage to move in and out of the x-ray beam, and (C) side view of the low offset (ca. 1 mm) arrangement.

Focusing optics

Different to any conventional (transmission) CDI beamlines, CSSI beam shape at the sample location does not have to be square or circular. Rather it is preferred to have an elongated beam along the horizontal direction (x) because the footprint of the beam is greatly magnified at the grazing incidence angles (normally $< 0.5°$). Since the source shape is also elongated, the beamline focusing devices can image the source directly. Three banks of parabolic compound refractive lenses (CRLs), kinoform lenses (KLs) and/or KB mirrors will be the optics for focusing the coherent beam to achieve 3 sets of beam sizes. The beamline will primarily use microfocused beam size of 1 (2) μm (H) x 0.2 (0.4) μm (V), FWHM, representing a demagnification ration of 35 and 25 of the source, respectively, at the sample for CSSI. The setup for GIXPCS measurements will be very similar, except that the beam size at the sample will be about 5× bigger in both vertical and horizontal directions. The speckle size from coherent scattering is inversely proportional to the beam spot size on the sample. The coherent x-ray beam from APS-U has to be focused to generate speckles large enough to be detected by pixelated x-ray detectors. This signifies the importance of implementing a coherence-preserving micro-focusing device so that full coherence flux can be used in order to increase the both signal-to-noise ratio and the reconstruction resolution. For GIXPCS operation, it is desirable to have the speckle size match the size of the detector pixel. Therefore, 5× bigger beam size is achieved by moving the relative distance of the focusing devices and the sample by a few millimeters. The optical layout of the focusing themes for both CSSI and GIXPCS is schematically shown in Figure 6.38. Sub-μm focusing in horizontal direction may not be beneficial for most of samples in CSSI measurement when radiation damage is taken into consideration. The second set of focused beam size is 35 μm (H) x 10 μm (V), below 20 keV, 1:1 imaging of the sources, for general GI-SAXS and WAXS measurements on surfaces and interfaces.

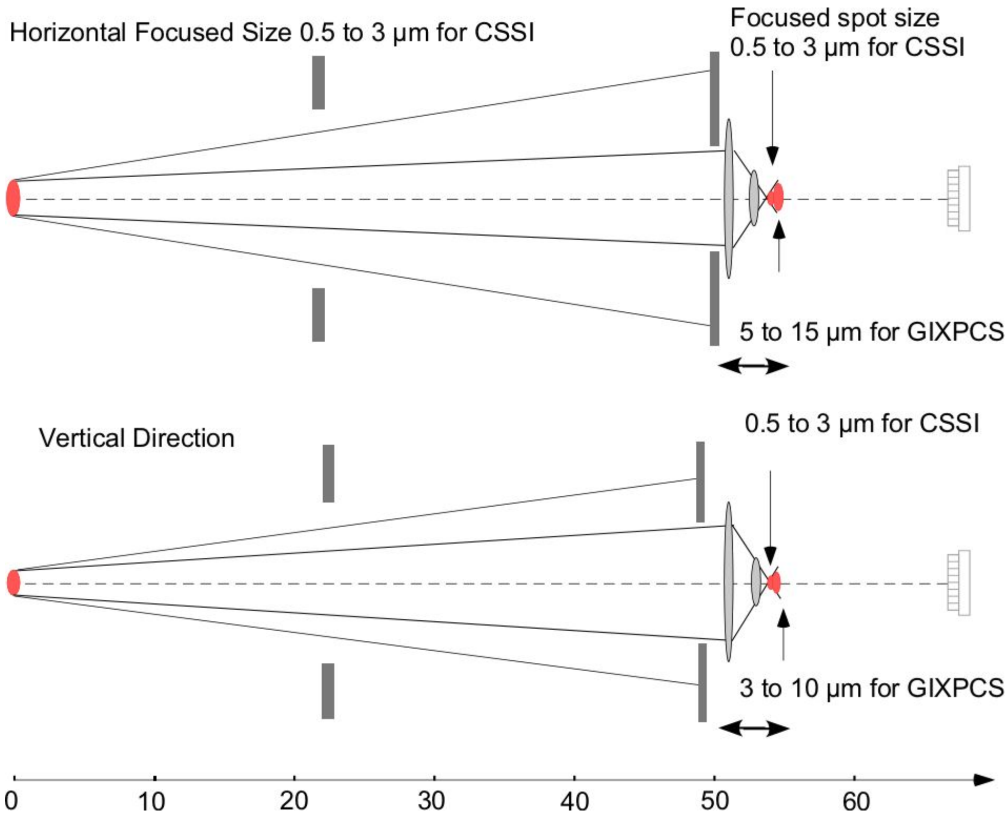

Figure 6.38. Focusing optical layout for CSSI with two sets of different beam size using focusing Banks 2 and 3 located 51 and 54 m from the source, respectively. The change of the beam size is achieved by the zoom mechanism of the two banks. Similarly, Banks 1 and 2 will be used to create the focused beam for GIXPCS and Bank 1 alone for GISAXS/WAXS beam. The focusing elements images the source directly.

Experiment End Station

The challenge issues associated with relatively large detector pixels can be mitigated by allowing a larger sample-to-detector distance (D). With a beam size d at the focal point (sample position), the speckle size, s, at the detector location can be approximated by $s \approx \frac{\lambda D}{d}$. Since the focused x-ray beam has an elongated shape, the speckle size is smaller in the direction in which the beam spot is longer (x direction). In Figure 6.39 we plot the energy dependence of the sample-to-detector distance required to achieve 5 times oversampling in x-direction. The detector parameters used in the calculation are from Eiger (75 μm) and MMPAD (150 μm pixel size) and the horizontal beam size 1 or 2 μm. Therefore, a longer experiment station ($>$ 25 m) starting at about 50 m from the source would be very critical. At the Sector 9, the current B, C, and D stations will be combined and refurbished to create a single long end station spanning from 47 m to 78 m from the source, which will create a long end station that satisfies the need of CSSI small-angle speckle detection requirement.

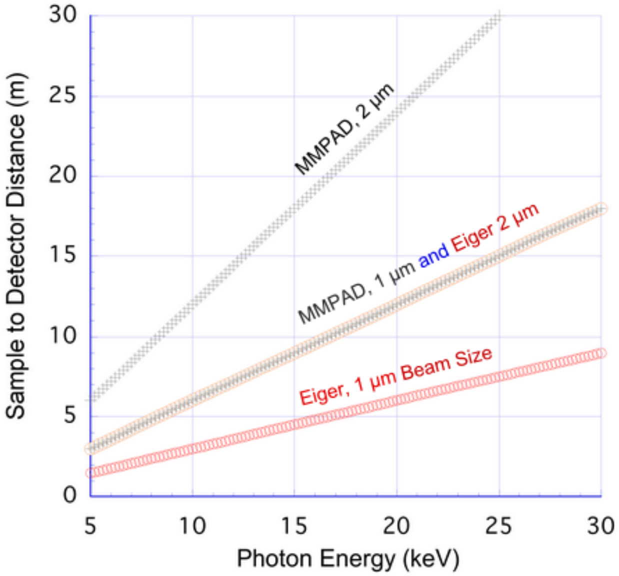

Figure 6.39. Photon energy dependence of sample-to-detector distance in CSSI setup for both Eiger and MMPAD detectors. The calculation is based on 1 or 2 μm beam size in horizontal direction and 5× oversample in the vertical direction. A 20-m sample to detector distance is found critical to facilitate CSSI experiments at APS-U.

Nanostage for surface sample manipulation

There are several coherent scattering beamlines developed worldwide at new low-emittance sources, such as those at PETRA-III and NSLS-II. However, precise control of sample positioning is *many times* more critical in CSSI than that in a conventional CDI experiment from two aspects. First, at a grazing incidence angle, e.g. 20 mrad, or 1°, the beam footprint at the sample surface will displace at a magnified rate of 50 over misalignment of the sample height. In order to perform initial sample alignment and subsequent fine scanning of the reciprocal space, CSSI requires the determination of the surface location and incidence angle with respect to the position of the μm-sized beam with precision of < 50 nm and < 1 μrad, respectively. Second, thermal drift and acoustic/mechanical vibrations, especially for in-situ sample conditions where samples are manipulated in thermal, solvent or in-operando environments, need to be minimized to within tolerance required by the resolution. Leveraged by the resources from a current strategic LDRD project, a prototype high-vacuum compatible sample nano-positioning system (Figure 6.40) has been designed, fabricated, and assembled. It will soon be commissioned at the APS beamline 8-ID-E. The sample position is controlled by close-loop feedback systems with all the motors to achieve a position reproducibility of 50 nm. The specifications are presented in Table 6.19. The design of the stage will be refined to use a laser interferometry system to provide a real-time positional feedback. The iteration of this nanostage will be part of the beamline development tasks.

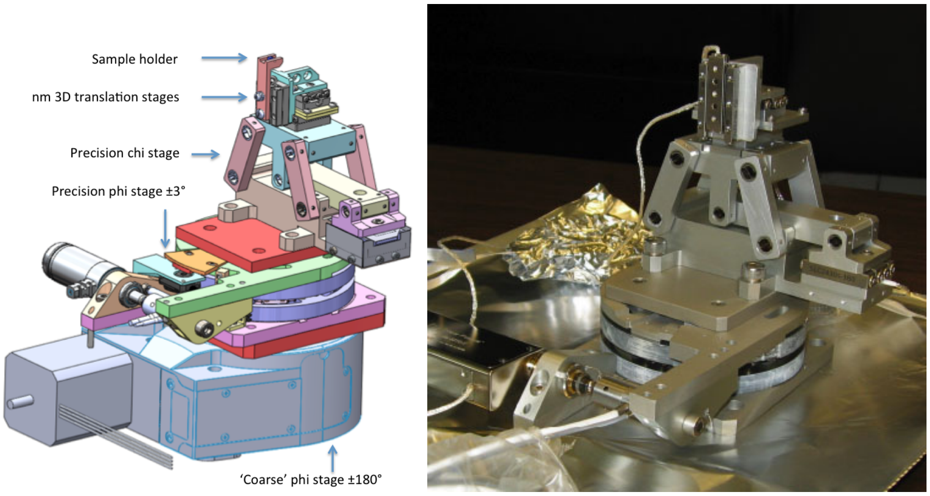

Figure 6.40. Design of prototype CSSI nanostage (left) and assembled vacuum compatible nanostage (right) without the 'coarse' phi stage.

Table 6.19. Design specifications of the APS Z7-4101 compact rotary flexure stage

Z7-4101 compact rotary flexure stage	
Overall dimensions (mm)	144 (L) x 106 (W) x 34 (H) (with open-loop coarse driver)
Overall dimensions (mm)	149 (L) x 149 (W) x 34 (H) (with closed-loop coarse driver)
Normal load capacity (kg)	0.5
Coarse driver type	Picomotor$^{\text{TM}}$ linear actuator
Coarse driver encoder type	Optical grating sensor
Fine driver type	PI 841.10V PZT actuator
Fine driver encoder type	Strain gage sensor
Rotary stage encoder type	Optical grating sensor or Laser interferometer
Coarse angular travel range (degree)	12
Fine angular travel range (degree/mrad)	0.011/200
Coarse min. incremental (nrad)	400
Fine min. incremental (nrad)	2
Laser interferometer resolution (nrad)	10
Vacuum compatibility	UHV Flexure mechanism HV linear actuators

Grazing-incidence XPCS (GIXPCS) measurements

With a large coherent fraction in the incident x-ray beam, the same CSSI beamline optics and instrument can have the same effectiveness for GIXPCS at a grazing-incidence angle. GIXPCS shares the same beamline setup as CSSI. However, the optimized detectors have different requirements. XPCS does not require high dynamic range, rather high time resolution and framing rate (> 1 MHz) for fast dynamics. The specifications required for GIXPCS are identical to those in the Small-Angle XPCS (SAXS-XPCS) beamline PDR.

Instrument for air/liquid and liquid/liquid interface

To accommodate coherent scattering measurement of structure and dynamics of air/liquid and liquid/liquid interfaces, a liquid diffractometer is needed to manipulate x-ray beam direction. The simplest and most robust solution is a double crystal liquid diffractometer [80] as shown in Figure 6.41. The concept has been implemented at both PETRA-III and Diamond Light Source. The setup will be compact and stand alone, so it can be inserted into the beamline when the need of using liquid surface sample environment arises.

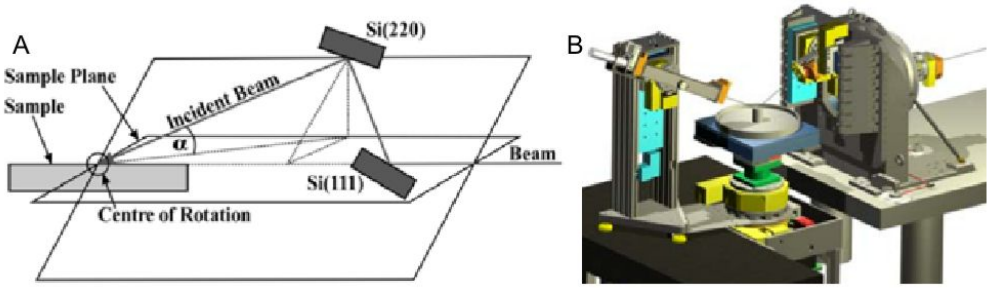

Figure 6.41. Double crystal liquid diffractometer for coherent scattering experiments: (A) concept and crystal reflection geometry, (B) model of an existing instrument at PETRA-III. The advantage of the setup is that the sample position remains to be the same when the beam tilting angle changes, which is ideally suited for the liquid GIXPCS and GISAXS/WAXS experiments at the beamline.

Detectors

Our preliminary work has proven that detectors are an integral part of and have a pivotal role in the success of CSSI experiments. Detectors for CSSI are a challenging issue. First, in coherent scattering with reflection geometry, the ‘specularly’ reflected beam can have an intensity as high as the incident beam, but must be measure to much lower levels as well, spanning 8 to 10 orders magnitude. Near the critical angle of the sample, the intensity can reach 10^{11} counts/s per detector pixel. Unlike transmission CDI, a beam stop should not be used to block the intense reflection because it contains the coherent scattering information that is critical for image reconstruction. More specifically the low-q information serves as the support in the recursive reconstruction process, which is considered to be a major advantage over conventional CDI measurements. Therefore, high-dynamic-range pixel array detectors (PADs) operating in integration mode are needed to handle the count rate higher than the APS-U pulse rate (88 MHz) while retaining single-photon sensitivity. Current commercial

PADs are only available in counting mode, which is not adequate. These detectors include state-of-the-art Eiger by Dectris, Ltd. and LAMBDA (Large Area Medipix-Based Detector Array) by DESY.

Second, a sufficiently small subtended solid angle for each detector pixel is needed in order to meet the oversampling requirement for CSSI, i.e., $\Delta < \lambda L/2d$ (Nyquist frequency), where Δ is the pixel size, λ is the wave length, L is the sample-to-detector distance, and d is the object size.

Third, the maximum spatial resolution is, in practice, defined by the maximum detectable angle, requiring the full detector dimension to extend beyond the scattering angles with intensities comparable to the background noise. Therefore, this beamline will need detectors that provide extraordinarily high dynamic range (10^8-10^{10}), high quantum efficiency (100%), and small pixel size ($<$ 50 μm by 50 μm), to benefit the resolution of the 3D imaging reconstructions in CSSI. This is also related to sample-to-detector distance to be discussed next. Currently we propose to use two types of detectors for CSSI: Eiger 16M [81] and Cornell MMPAD [82]. The present major specifications of both detectors are shown in Table 6.20 for reference. As the only high-dynamic range x-ray detector in the synchrotron and FEL community, the R&D effort MMPAD should be supported.

Table 6.20. Comparison of two promising complimentary detectors that are suited for the CSSI beamline

Properties	**Eiger 16M**	**MMPAD**
Readout type	Counting	Mixed Mode Integrating + counting
Total number of pixels	4150 x 4371 = 18,139,650	256 x 384 = 98,304
Pixel size [μm^2]	75	150
Sensitive area [mm^2]	311 x 328	47 x 49
Frame rate [Hz]	133	1,100
Max. count rate [Hz/pixel]	2.8×10^6	10^{12} (Instantaneous) 10^8 (sustained)
Sensor thickness [μm]	450	500
Top Energy threshold [keV]	18	20
Developer	DECTRIS	Gruner Group (Cornell)
Commercially availability	Yes	No

6-5.5 R&D Needs

6-5.5.1 Coherence and wave front preserving optics

The beamline performance is ultimately determined by the coherence quality of the beamline optics. Although the beamline will be designed using minimum optical elements to preserve the coherence, the properties of mirrors, monochromator crystals and elements, and focusing device will be evaluated with both experiment and numerical simulation. For mirrors, CSSI provides an in situ and at wavelength metrology to evaluate the surface quality (both figure errors and roughness). The choice of focusing optics especially for x-ray energy $>$ 20 keV, will be made in collaboration with the APS optics group. While CRLs and K-B mirrors are widely used at low-emittance synchrotron sources such as PETRA-III and NSLS-II, single-crystal Si based KLs have large numerical apertures and are suitable for high-energy applications. The potential of KLs [83] as wave front preserving optics will be explored.

6-5.5.2 Improving CSSI experiment methods

In grazing-incidence geometry, the transverse coherence length is greatly enlarged as the footprint of the x-ray beam on the sample may reach centimeter scale; however, the detectable q range for the incident direction (X) gets geometrically decreased correspondingly. This results in a much poorer image resolution as compared with the other two directions (Y and Z in Figure 6.42A). The anisotropic spatial resolutions thereby limit the application of CSI technique in studying samples with symmetric dimensions along X and Y directions. In order to solve this problem, we proposed to collect a series of scattering patterns of the sample at different in-plane rotation angles (azimuthal direction, ϕ). In such a way, as shown in Figure 6.42B the combined reciprocal data contains sufficient oversampling rate for reconstructing the fine structure of the sample with high resolutions in all in-plane directions. Even a rotation of several degrees can improve the resolution by an order of magnitude. A systematic scatter simulation has been performed to demonstrate the effect in Figure 6.42C-E, where (simulated) data taken at several rotation angles (6 and 18) were used to reconstruct the surface pattern. The improved resolution is readily seen. Experiments have been designed to prove the ‘tomographic’ concept and to illustrate the effectiveness of the rotation. Again at PETRA-III, we collected the coherent scattering data from a more complex sample (Figure 6.42G inset) at a small angular range (±3°, Figure 6.31G-I). The reconstruction using the data set will be performed to reveal the quantitative effect. In the future experiments, the rotation will be done in a much larger range. Currently, the range is limited by the poor precision of the sample stage, which will be resolved by a nano-positioning and –rotation stage shown in Figure 6.40. The tomographic like experiment will ultimately benefit from the upgraded APS because of much improved data collection efficiency. The result will be a homogenized high-resolution imaging reconstruction in all three dimensions.

6-5.5.3 Developing Advanced Coherent Surface Scattering Reconstruction Method Incorporating Dynamical Scattering Theory

The reconstruction of the images in real space requires phase retrieval to complement the x-ray scattering intensity measurement using partially coherent beam. However, all image-recovery algorithms thus far have used the kinematic theory, assuming that the scattering from the samples is weak (Born approximation). With the assumption, the reconstruction is only a mathematical process involving recursive fast Fourier transform (FFT) and inverse FFT (FFT^{-1}). These algorithms cannot be simply applied to the CSSI cases where the weak scattering assumption is not satisfied at grazing angles. There has not been reconstruction algorithm developed for handling coherent scattering data taken in this unique but powerful way. Therefore, to prepare for the dawn of the new era of CSSI at upgraded APS source while taking advantage of exascale computing capabilities in Argonne, we are in a unique position to develop the computationally intensive and physics-based reconstruction technique for the first time. In grazing-incident condition when CSSI applies, dynamical scattering contain multiple-beam scattering and can be dominating in total external reflection regime. By take full advantage of the dynamical scattering characteristics, the application of distorted wave Born approximation (DWBA) in this regime can revealed enormous

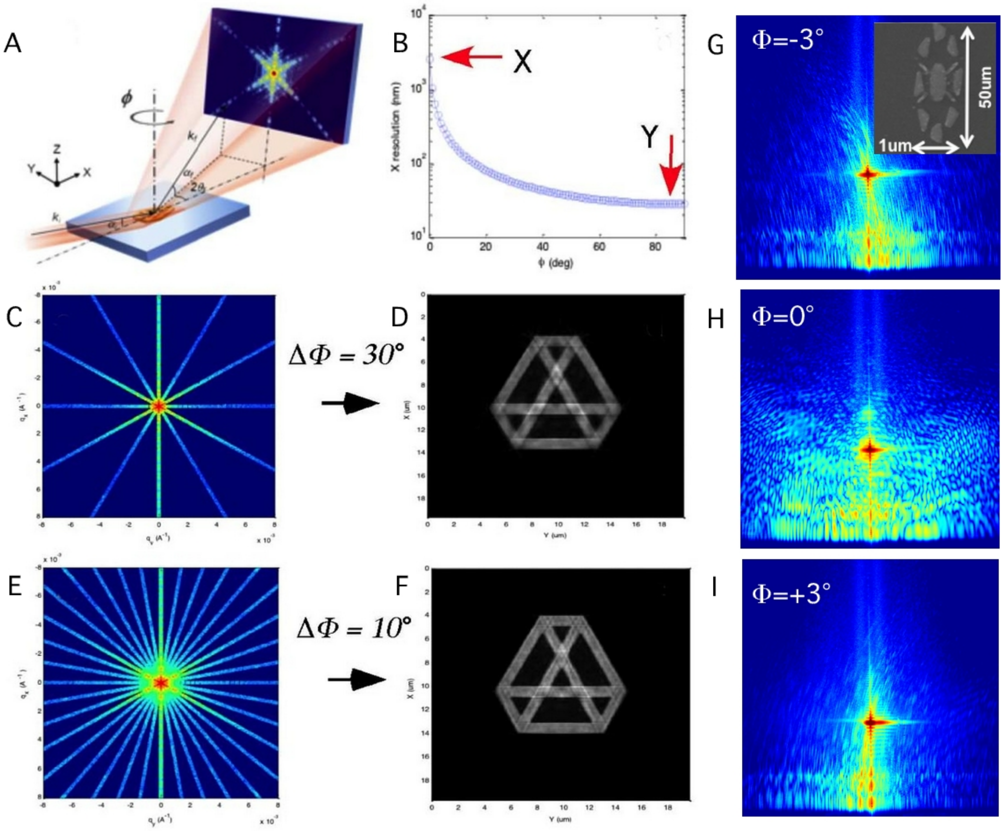

Figure 6.42. Concept and simulation of coherent scattering data collected at different azimuthal angles: A) scattering geometry, B) improvement of spatial resolution along X direction with angular "tomography", C-F) effect of number of viewing angles on reconstruction resolution, G-I) experimental data in a small (±3°) viewing angle range collected at P10 beamline of PETRA-III using a vertically focused x-ray beam (SEM image of the surface pattern is shown in the inset.

amount 3D structural information of the surface/interface patterns with a coherent x-ray beam. Here, we hypothesize that the *dynamical* scattering data collected with *coherent x-rays* can be used for solving surface structures with unprecedented 3D spatial resolution. To test this hypothesis, our specific objectives are to develop a novel reconstruction method (possible genetic algorithm, GA) that incorporates DWBA framework and is far more effective for surface scattering imaging than the conventional reconstruction algorithm illustrated. In the meantime, we predict that the robustness of the reconstruction algorithm will be enhanced due to incorporation of multi-beam dynamical scattering theory in the DWBA framework. Undoubtedly, the implementation of the new reconstruction requires Argonne's HPC power with optimized algorithm through collaboration between x-ray scientists at the APS and HPC experts at ALCF. The reconstruction algorithms require modifying the conventional phase retrieval algorithm. proposed here is a genetic algorithm (GA) that takes advantages of genetic selection of parallel processing to yield fast converging results. As shown in Figure 6.43, the GA algorithm will consist of two nesting loops: (A) iteration loop of processing individual scattering images that is nested inside of (B) GA loop with selections rules to generate real 3D pattern. This type of GA approach may be proven efficient not only for CSSI but also for conventional CDI reconstruction.

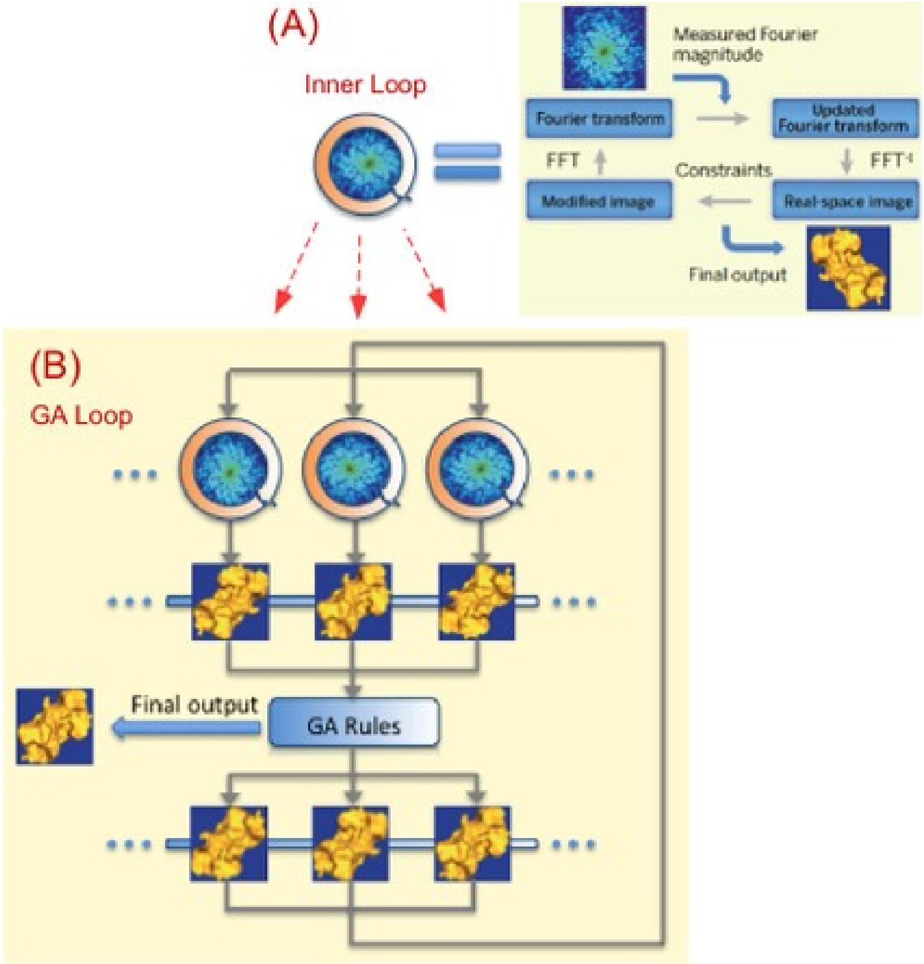

Figure 6.43. Genetic algorithm for reconstructing CSSI data: (A) inner iteration loops that are similar to conventional CDI phase retrieval and reconstruction algorithm to generate complex q_z*-depending complex real-space distribution* $P^j(\mathbf{r})$*. The reconstruction is done by iterative Fourier transform of images in both real and reciprocal spaces. These loops are nested in (B) GA loops with selection rules that optimize the sample pattern* $\rho(\mathbf{r})$ *from a set of* $P^j(\mathbf{r})$ *obtained from* I^j *taken at various incident angles.*

6-6 High-Energy X-Ray Microscope (HEXM) Beamline

The High-Energy X-Ray Microscope (HEXM) will be a long beamline located at APS-20-ID. Operating in the monochromatic 35–120 keV range and also being white-beam capable, it will receive radiation from a superconducting undulator (SCU) source. HEXM will consist of an A station, or first-optics-enclosure (FOE), at 30 m from the source, and two experimental end-stations—a B station at 70 m (within the main experimental floor) and a C station at 180 m (in an external building). The external building will be shared with another long APS-U beamline (In-Situ Nanoprobe [ISN] at 19-ID).

6-6.1 Executive Summary

HEXM will investigate micro-structure and evolution within bulk materials, often in extreme environments, using enhanced high-energy x-ray scattering techniques used today (e.g., at beamline 1-ID) and new coherence techniques, all enabled by the low-emittance APS-U multi-bend-achromat (MBA) lattice. High-energy x-rays interact with matter with low attenuation, small scattering angles (giving large reciprocal space access), and the validity of the single-scattering approximation. These features, when combined with a brilliant source like the APS-U at high energies, make such x-rays the scattering probe of choice for interrogating bulk material structure. Such a combination of penetration capability with high spatial, reciprocal-space, and temporal resolution, enables these x-rays to measure phase, texture, and strain distributions non-destructively under complex sample environments.

These principles will be implemented by combining the low-emittance MBA lattice, an SCU source, and a long beamline with a large end-station, as conceptually shown in Figure 6.44 (to scale in Figure 6.55). The high-energy x-rays (35–120 keV) will be applied through multiple techniques, such as high-energy diffraction microscopy (HEDM), wide- and small-angle scattering (WAXS/SAXS), micro-tomography (μ-CT), scattering tomography (ST), transmission x-ray microscopy (TXM), and Bragg coherent diffraction imaging (BCDI)—available at the same sample location (C station) to probe length scales covering many orders of magnitude. Materials subjected to these techniques would be of relevance to mechanical engineering, biophysics, irradiation/nuclear energy, energy storage, and advanced manufacturing (see HEXM science case in Chapter 3).

The primary experimental station (C) will be 20 m in length, with samples and environments located at 180 m distance from the source. The long beamline will enable:

- Focusing down to small spot sizes at convenient working distances.
- Efficient performance of expansion optics when large beams in one or both dimensions are needed (e.g., near-field-HEDM, μ-CT).
- Producing relatively large, coherent focal spots (tens of μm for BCDI) through low source-demagnification or magnification geometries.

Furthermore, the long end-station enables distances greater than 15 m between the sample and some detectors to optimize direct or reciprocal space resolutions in certain techniques (very-far-field-HEDM, BCDI, SAXS, TXM). Finally, being away from the main APS experimental hall, the external building that houses the C station will be compatible with unique facilities like *in situ* irradiation with an ion source (XMAT initiative, Sections 6-6.2.1 and 6-6.4.8) and activated

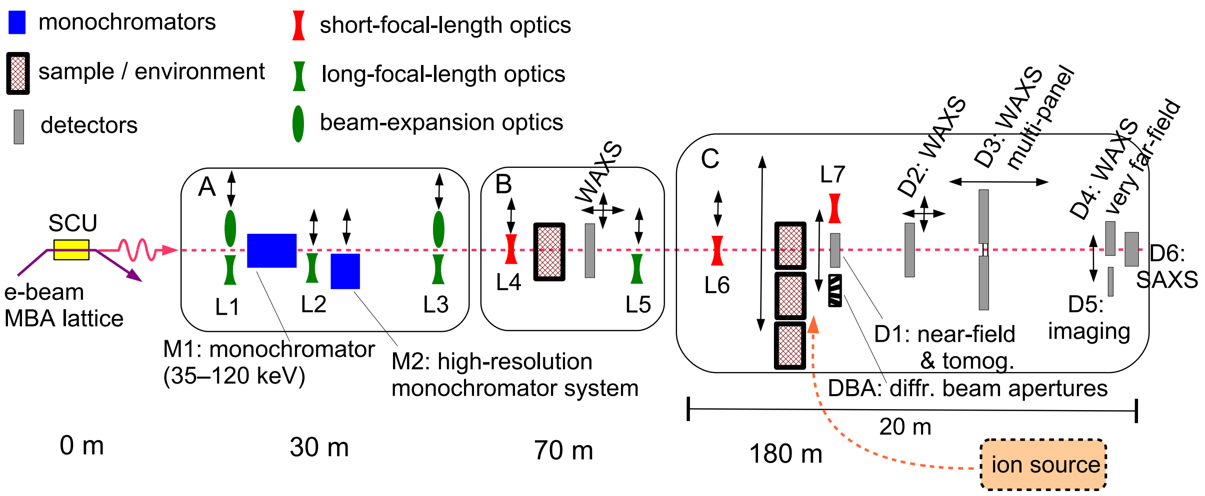

Figure 6.44. Conceptual layout (not to scale) of the HEXM beamline indicating stations, x-ray optics, sample locations, and detectors. See also Fig. 6.55.

materials handling.

6-6.2 Scientific Objectives & Capabilities

HEXM aims to provide unprecedented capabilities to investigate structure and its evolution within bulk materials, as described in Chapter 3 within the overall APS-U science case. Current high-energy x-ray techniques will be refined, and combined with MBA-enabled coherence techniques, to provide multi-modal imaging spanning millimeters to angstroms in single experiments. HEXM requires the source characteristics unique to the MBA-upgraded APS—increased coherence and brilliance at high energies (35–120 keV)—in order to provide non-destructive measurements at the highest spatial and temporal resolutions. New capabilities will benefit a wide suite of materials classes. An end-station external to the APS building will enhance the ability to study extreme material states, including, but not limited to, *in situ* ion-irradiation and additive manufacturing. The coupling of this multi-scale information with modeling efforts promises to revolutionize the ability to accelerate materials development.

6-6.2.1 Community and Stakeholders

The potential HEXM user community is quite large and broad. It is comprised of academic, national laboratory, and industrial researchers in the fields of materials science and engineering, other engineering disciplines (primarily mechanical and biological), physics, and chemistry. Expected demand is reflected at existing APS beamlines utilizing some of the proposed techniques (1-ID, 6-ID, and 11-ID), where over-subscription rates of 5× are common. Interest in science described herein can be expected to increase as these capabilities become better developed and known in the community. HEXM, combined with existing high-energy capabilities at the APS and proposed high-throughput facilities, promises to help meet the expected demand, in particular through the development of multi-disciplinary teams including computational scientists.

The demand for additive manufacturing and related advanced processing techniques is expected to grow steadily over the next decade. In real-world manufacturing processes, local variations in the microstructure exist throughout components. Many models exist to predict these variations, but need validation, and thus there are almost unlimited opportunities for using HEXM experiments to validate new classes of models that address *in situ* processing. The non-destructive strain and micro-structural mapping capabilities can also be used to verify post-manufacturing processes (e.g., peening, case hardening) often applied industrially, but typically measured using layer-removal techniques. Existing partners using APS in this area include Pratt & Whitney, Rolls-Royce, GE, GM, John Deere, and Caterpillar.

Grain mapping will be enhanced through HEXM and remain the premier non-destructive method for this purpose. Currently, there are over 1500 electron backscatter diffraction (EBSD) systems in the world that provide 2D grain mapping at surfaces. EBSD can be extended to 3D through serial sectioning (polishing or focused ion beams) which, however, is time consuming and destructive, making *in situ* measurements impossible. A significant fraction of EBSD users are possible users of HEXM. Thus there will be a high demand for emphex situ HEDM alone, particularly given the increase in spatial resolutions which will approach those of EBSD. These increased resolutions will allow systems with finer grain sizes and more complex microstructures to be investigated, including those related to energy storage, (nano-)electronics and bio-materials, in addition to the larger grained metals and ceramics mapped today. The ability to perform 4D (3D + *in situ* response) characterization will remain unique and be a large portion of expected demand in this area.

The interest and demand of the nuclear materials community to use synchrotron x-rays to advance these goals has grown rapidly in recent years. Opportunities are well documented in the *Basic Research Needs for Advanced Nuclear Energy Systems* (DOE-BES 2006), and addressed in a series of workshops including *Research Needs and Opportunities for Characterization of Activated Samples at Neutron and X-Ray User Facilities* (LANL 2009), *Role of Synchrotron Radiation in Solving Scientific Challenges in Advanced Nuclear Energy Systems* (ANL 2010), and *Synchrotron X-Ray Studies of Advanced Nuclear Energy Systems at NSLS-II* (BNL 2011). The Argonne workshop concluded that "there is unanimous agreement that synchrotron studies hold enormous potential to answer questions central to all aspects of nuclear energy production, from simulation validation, to quantifying materials problems, to environmental remediation."

HEXM is in a position to deliver goals of the XMAT concept/initiative (eXtreme MATerials beamline) [84], a strategic initiative within Argonne, to be a leader in developing next-generation radiation-tolerant materials and predictive capabilities, by integrating an ion source into an x-ray beamline. Funding for the ion source is being sought from three different agencies—NNSA, DOE-FES, and DOE-NE. Each agency has an important interest in the issues in radiation damage that HEXM can address. Even without the ion source a significant number of issues can be addressed by performing HEXM techniques on post-irradiated (at ATLAS or other national facilities including the Advanced Test Reactor) samples. Interest by the NNSA in particular extends beyond the ion source. Over the next few decades, the challenges implicit in remanufacturing and aging of the nuclear stockpile demand insight beyond the historical approach. Most notably, diagnostics are needed at the length scales at which mechanisms of response occur, in addition to greater reliance on physical simulations at lower length scales. This work must also be directly coupled to the questions raised at the device level. The NNSA has a compelling interest in collections of experiments with direct observation of physical mechanisms over a wide variation of length scales and thus has a strong interest in the success and development of the HEXM beamline.

6-6.2.2 HEXM Worldwide Context

With regard to beamlines having similar technical and/or scientific scope as HEXM, other high-energy storage rings (especially ESRF and PETRA-III/IV) are heavily investing in this area, and either recently constructed or plan to construct long high-energy x-ray beamlines. In the multi-phase ESRF upgrade, for example, high-energy beamlines have been constructed just prior to and during Phase-I, while another beamline of similar scope to HEXM is being considered in Phase-II of the upgrade. At the APS, beamlines 6-ID, 11-ID, and in particular 1-ID, will provide some scope overlap with HEXM, albeit at lower achievable resolutions due to their < 70 m maximum lengths, allowing efficient sharing of common resources (e.g., detectors, *in situ* set-ups, optics, software). These advantages, spearheaded by the unique HEXM characteristics, will create a world-leading suite of high-energy x-ray beamlines at the APS for decades to come. CHESS, Diamond, and NSLS-II have, or are developing, similar techniques, but will not be competitive for high-energy x-ray brilliance and coherence.

6-6.2.3 Use of APS-U Characteristics

In order to provide world-leading, high-energy x-ray capabilities which take best advantage of APS-U characteristics, HEXM requires a long beamline and a large end-station C shown in Figures 6.51 and 6.54). These features are considered from the standpoints of focusing, beam-expansion options, coherent focusing, and the implementation of multi-modal zoom-in/out techniques as described below and summarized in Tables 6.21 and 6.22.

Table 6.21. High-energy x-ray benefits from low emittance and a long beamline

Consideration	High-energy (HE) x-ray benefits from: **low MBA emittance**	**long beamline**
Focusing	small spots / high demags at long focal (working) lengths	
	σ_y , $\sigma_{y'}$ reductions (not just σ_x , $\sigma_{x'}$) discernible at HE, enhancing gains	
Coherence	higher coherent fraction	enables low-demag or magnification geometries for large, coherent focal spots
Beam-expanding refractive optics	efficient due to small initial beam size, aperture	efficient due to low refractive power needed over long distance

Table 6.22. HEXM techniques' benefits from a long end-station

Technique	Long end-station provides: more distance to achieve far-field at small λ	improved Q-resolution or imaging magnification on detector pixels	increased imaging depth of field
BCDI fringes	✓	✓	
Very-far-field HEDM	✓	✓	
SAXS		✓	
TXM		✓	✓

Long Beamline with Low Emittance: High-Energy Focusing Optics

The emittance reduction from the MBA lattice is most dramatic in the horizontal plane, enhancing focused beam production at all photon energies. However, the emittance reduction in the vertical plane is also substantial in the brightness mode (low-coupling, 324-bunch), having $\epsilon_y = 4.2$ pm versus today's $\epsilon_y = 40$ pm. High x-ray energies can benefit from vertical emittance reduction to a more significant degree than do lower energy x-rays. For the latter, the vertical beam divergence can be dominated by an undulator's intrinsic radiation divergence $\sigma_{r'} \propto \sqrt{\lambda}$, so the reduction of electron source divergence $\sigma_{y'}$ doesn't fully translate into more flux intercepted vertically by focusing optics apertures. Vertical source size σ_y reduction also yields diminishing returns at low energies due to vertical focusing already being optics diffraction limited. For high energies, the situation is very different. The smaller $\sigma_{r'}$ broadening enhances photon capture within small focusing optics apertures in both directions (assuming appropriate reductions are made in particle beam energy spread). Due to increased challenges of optics fabrication at high energies, focal lengths are relatively long and vertical spot sizes are still source size limited. Therefore, high-energy focusing benefits from a smaller vertical source size as well. The APS-U brightness mode is most attractive in terms of pushing the limits of vertical focusing of high-energy x-rays. Also, the lower vertical divergence at high energies combined with emittance reduction improves the efficiency of narrow-angular-acceptance high-energy-resolution crystal monochromator systems to be employed.

The ability to obtain smaller spots at longer focal distances from the MBA emittance is further facilitated by a long beamline, providing benefits from various standpoints: optics fabrication, depth of focus, large working distance for complex sample environments and nearby hardware, and reduced beam divergence contribution to diffraction resolution. With a focal length of 2 m at 180 m distance, assuming a 150 μm refractive lens aperture and $\Delta E/E = 10^{-3}$ energy spread at 70 keV, the FWHM contributions to the vertical spot size are 100 nm, 150 nm, and 100 nm, from source demagnification, chromatic aberration, and diffraction limit, respectively, which add in quadrature to 210 nm. With a combination of reduced focal length (e.g., 1 m), higher energy resolution (1.4×10^{-4} bandwidth), and larger aperture lenses (400 μm using kinoforms), sub-100 nm vertical focusing is achievable at such high energies, with respective contributions 50 nm, 60 nm, and 20 nm. KB mirrors, being achromatic, obviate the need for reducing bandwidth and could offer similar focal spot sizes with higher flux, but at the expense of short working distances (< 0.3 m) to permit slope errors of 0.05–0.1 rad (rms). For the reasons of sufficient working distances to accommodate complex sample environments and in-line focusing optics to facilitate multi-modal techniques, HEXM places more emphasis on the refractive lens approach.

Long Beamline with Low Emittance: Expansion Optics

Although the low emittance offers higher spatial resolution capabilities, certain high-energy techniques benefit from larger beams, in one or both directions. Standard tomography (μ-CT) is one example where a several-mm-wide beam is desired to match mm-level penetration depths for true bulk studies. Another example, the near-field(nf)-HEDM method, uses a long line-focus beam profile—focused to a (sub-)micron size vertically, but (ideally) as large as 3–4 mm horizontally—to diffract from a large number of grains within a polycrystalline material, one thin slice at a time. From large data sets of diffraction exposures taken (by detector D1, Fig. 6.44) under sample rotation and fine vertical translation at multiple close detector distances (1–2 cm), one can reconstruct a 3D grain map with orientation (Fig. 6.45). A low-coupling MBA lattice, with a long beamline, would clearly help the vertical focusing to 100 nm levels. However, even at 180 m distance, the horizontal beam size is only $\sim$ 2 mm FWHM (brightness mode), driving consideration of beam-expanding optics. Simulation shows that refractive lens beam expanders work best on long beamlines where the beam starts out very small. Closer to the source where the refractive expander is placed, the small starting beam size requires a small lens aperture. This, combined with the low refraction needed in propagation over a long beamline, helps transmission efficiency. Calculations show that in the case of diamond refractive optics placed at 34 m (lenses L3), where the beam's horizontal size is 480 μm FWHM at 70 keV, one can easily expand it to 3–4 mm at 180 m with high efficiency.

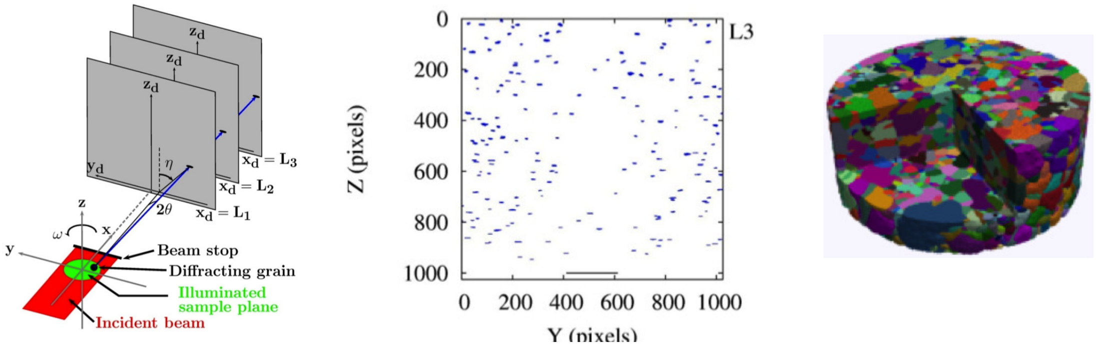

Figure 6.45. The nf-HEDM method collects diffraction spots (center) from grains illuminated by a line-focused beam under sample translations/rotations and at multiple distances (left). Significant computation reconstructs grain maps with crystallographic orientation (right).

Multi-Scale Direct-Space Imaging at HEXM

In direct-space imaging, standard tomography with millimeters of field of view would be facilitated by a long beamline coupled with beam expansion optics (L3) as discussed above, with a broad bandpass beam expansion optics (L1) option giving the highest flux and temporal resolution. This will permit tomographic data-sets at 1 μm resolution to be collected on the order of fractions of seconds. Zoomed-in imaging would be achievable with a high-energy transmission x-ray microscope (TXM). Such a full-field TXM, based on a refractive lens objective after the sample (L7 in Figure 6.44), has already been demonstrated at 45 keV having 500 nm resolution, with the specimen, objective, and detector all fitting within a 6 m length in the current APS 1-ID-E end-station [85]. Having more sample-detector length ($\sim$ 15 m to detector D5) in a new end-station would enable a TXM system with higher magnification, larger sample depth of field, and detector pixel oversampling to achieve 100 nm imaging resolution at high energies, with samples being positioned at the same location/environment for interrogation by other techniques in the C station. For samples in the B station, the interesting possibility of a very high-magnification TXM arises by using an x-ray objective in the B station to image onto detector D5, with >100 m separation between them.

Multi-Scale Scattering-Based Imaging at HEXM

Although shorter wavelengths are always disadvantaged relative to longer wavelengths in terms of coherence, the APS-U source size reduction improves transverse coherence at all energies. A long beamline would exploit the increased coherence at high energies to pursue BCDI, currently conducted at low energies [86], to obtain a highly zoomed-in measurement of the internal strain fields and shapes of single grains buried within a bulk polycrystalline specimen, complementing the relatively zoomed-out HEDM measurements. Aside from the already discussed facilitation of high source demagnification geometries, a long beamline also enables very low demagnification (or even source magnification, geometries (e.g., by focusing with L5) needed to create relatively large focused spots of tens of μm that can be made highly coherent by aperture selection at the focusing optics (more in Section 6-6.4.2). The low emittance on a long beamline facilitates the transverse coherence at high energies for BCDI, and also the high-aspect-ratio line-focus for nf-HEDM due to good vertical focusing and refractive beam expansion in the two orthogonal directions. Finally, increased end-station length also allows detector D4 pixel oversampling of fine, far-field BCDI fringes at high energies and permits new approaches for placing refractive optics in diffracted beams from single grains (L7 in Figure 6.44). One approach can provide very high-resolution imaging by implementing the concept of TXM in diffracted beams [87]. Another approach could help reciprocal-space imaging by adjusting the lensing not to image the grain, but instead to bring far-field diffraction patterns to the D4 detector plane (e.g., for very-far-field(vff)-HEDM [88] or BCDI).

In addition, the large sample-detector (D6) distance enabled by the long end-station, coupled with focusing optics, allows access to smaller Q_{min} (larger d_{max}) using SAXS than possible today. In particular, at a minimum radius from the direct beam of 0.5 mm (achievable using long-length focusing optics and a set of C station slits upstream of the sample for parasitic scattering) and 14 m distance, we can access $Q_{min} = 0.0007$ [0.0014] Å^{-1} at 40 [80] keV with corresponding maximum observable feature sizes of $d_{max} = 868$ [434] nm, representing a 6× higher range than possible today at 1-ID-E. Of particular interest is that this range will, for the first time, overlap with the direct space imaging from the TXM, allowing the same features (e.g., voids, nanoparticles) to be detected in both reciprocal and direct space.

Choice of HEXM Beamline Length

The beamline length (source to C station sample location) was revised from 150 m to 180 m. The original length of 150 m, proposed in the HEXM white-paper and full-proposal documents, is about twice the maximum possible distance for an end-station within the regular APS experimental hall, and would permit sub-100 nm vertical focusing at 1-m working distances (in APS-U brightness mode) due to source demagnification. Increasing the distance from the source yields diminishing returns due to the spot size contributions from chromatic aberration and the optics diffraction limit (although it would help in the case of the APS-U timing-mode lattice [high coupling, 48-bunch], having a larger vertical source size). Lengthening the beamline would also reduce the x-ray flux captured within the distant focusing optics aperture, more so in the less optimal timing mode, with its larger vertical beam size. The 150-m length was adequate to enable magnifying (in a focusing geometry, e.g, using lenses L3 or L5) the small vertical source size (9 μm FWHM) to a few tens of μm for BCDI. A distance of 150 m is also enough for a beam-expander (nf-HEDM application) to enlarge the horizontal beam size to 3–4 mm, although allowing more propagation distance would improve upon the expander efficiency. The reason for slightly increasing the planned distance from 150 m to 180 m was to enable a single external building to house the distance end-stations of both the long beamlines HEXM (20-ID) and ISN (19-ID), the latter desiring a length in the 220–250 m range.

6-6.3 Source and Front-End

6-6.3.1 Superconducting Undulator

The HEXM beamline's techniques and tunable x-ray energy range require a high-brilliance source capable of covering the spectrum from 35 keV to beyond 100 keV. Optimal source performance at these energies drives the selection of SCU device technology, which enables the achievement of high fields at short device periods, to provide full coverage of the desired energy range with the odd harmonics. An SCU candidate for this purpose would be a 1.65-cm-period device of approximately 3.5 m magnetic length, operating at a fixed 8.0-mm gap, with a maximum deflection parameter $K_{max} = 1.63$, corresponding to a 1.06-T peak field. Due to the added cryostat space requirements of SCUs, a magnetic length of 3.5 m would be the most possible in the 5-m-long straight section. Furthermore, it would most likely be segmented, e.g., as 2 × 1.75 m, requiring an adjustable delay for keeping the segments properly phased. The spectral brilliance tuning curves of this proposed SCU-HEXM is shown in Figure 6.46 along with the current SCU1 and past permanent magnet undulators used at the 1-ID high-energy beamline. The SCU-HEXM (brightness mode) would outperform the current SCU1 device by a factor of 530 in brilliance and a factor of 4.5 in total flux within the central cone. In flux density at the same distance it outperforms by about an order of magnitude. Accounting for the distance change to 180 m (HEXM) from today's 70 m (1-ID), SCU-HEXM outperforms SCU1 by 1.5 in flux density.

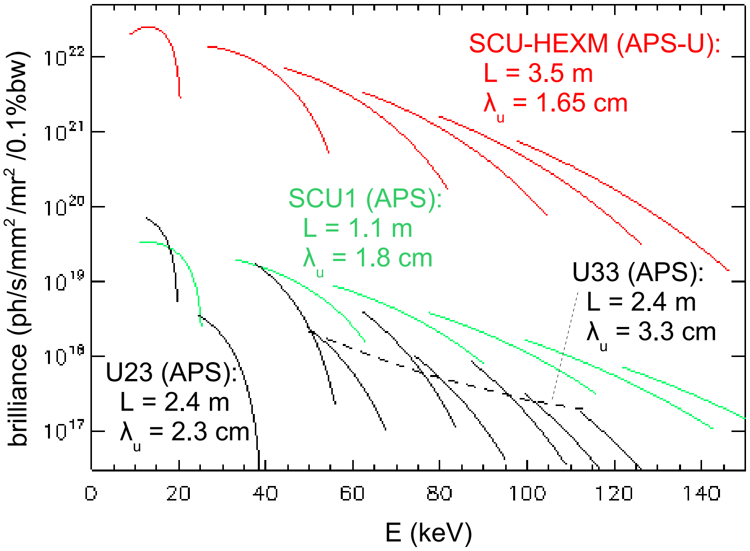

Figure 6.46. Brilliance tuning curves of the proposed SCU-HEXM source (APS-U brightness mode, 200 mA) compared to various insertion devices (SCU1, U33, U23) that are/have been used at APS 1-ID (100 mA). Device magnetic lengths and periods are given.

6-6.3.2 Front-End

The SCU-HEXM insertion device with parameters given here imposes a thermal load of 17.9 kW (total power) and 616 kW/mrad^2 (power density) at the maximum field. This is within the design limits of the high-heat-load front-end.

6-6.4 Beamline Layout

The conceptual layout of HEXM already shown in Fig. 6.44 (not drawn to scale) displays x-ray optics, sample environments, and detectors. Figure 6.55 is a scale drawing of the entire beamline. Separate layouts of the stations are also shown below. Table 6.23 lists components in order of distance from the source.

Table 6.23. HEXM beam-handling components after the front-end, including optics and experimental instruments. Bremsstrahlung shielding is not listed.

Component	Location (station)	Distance from source (m)	Comments
white beam filters	A	26.5	
white beam slits	A	27.5	
L1 optics	A	28	white beam focusing/expanding
M1 high-energy monochromator	A	29	bent double-Laue, horiz offset
L2 optics	A	30	collimation into M2
M2 high-resolution monochromator	A	31	vertical, 4-reflection $(+--+)$
L3 optics	A	34	monochromatic focusing/expanding
transport	A–B	36–67	
beam conditioning system-B	B	68	includes L4 focusing optics
instruments-B	B	69–75	sample env, WAXS det
L5 optics	B	76	focusing optics
movable stop	B	77	white and monochromatic
transport	B–C	77–177	
beam conditioning system-C	C	178	includes L6 focusing optics
instruments-C	C	180–196	sample envs, L7 optics, dets D1–D6
fixed stop	C	197	white and monochromatic

6-6.4.1 X-Ray Optics—Monochromators

Two monochromator systems will be located in the FOE/A station (6.47). The monochromator M1 in the A station will consist of a cryogenically cooled (in vacuum), bent double-Laue crystal system in sequential Rowland conditions (like one that has been in use at APS 1-ID for seventeen years [89]) to deliver a high-flux, fully tunable over 35–120 keV, fixed-exit beam with preserved source brilliance, i.e., size and divergence (Fig. 6.48). Bent Laue crystals are known to distort the x-ray phase-space in the diffraction plane. However, in propagation through the two-crystal configuration shown here, there is a compensation effect that restores the phase-space upon double-reflection. So in the current 1-ID configuration, the source's vertical emittance is confirmed to be preserved, despite the crystals diffracting vertically, thermal load, and cooling. In the APS-U MBA lattices, the horizontal emittance ϵ_x will be comparable to the present vertical emittance ($\epsilon_y = 40$ pm). HEXM will adopt a horizontal diffraction/offset geometry instead, which should not only preserve the horizontal emittance via the compensation effect, but also preserve the orthogonal vertical emittance, which would be significantly reduced in the brightness-mode ($\epsilon_y = 4.2$ pm). The horizontal offset would be 25–35 mm outboard.

The $\Delta E/E \sim 10^{-3}$ bandwidth delivered by the bent-crystal optics described would be adequate for many techniques. However, higher energy resolutions are required for certain techniques including BCDI and high-resolution reciprocal-space vff-HEDM measurements, as well as for limiting

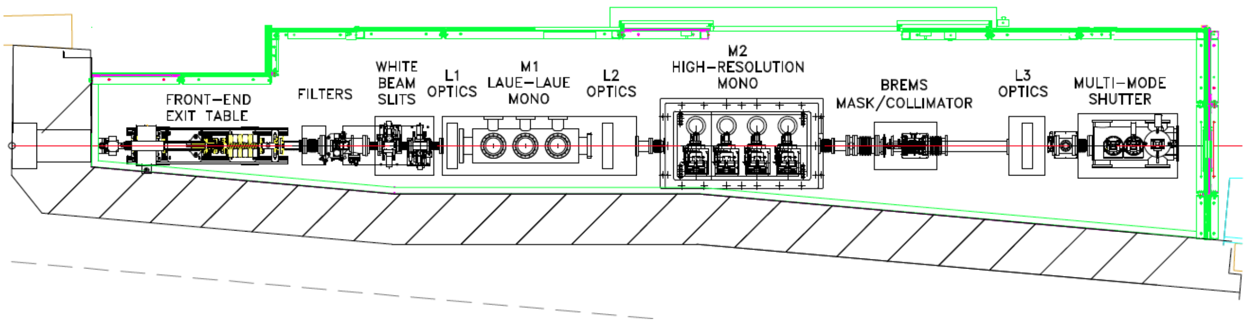

Figure 6.47. HEXM-FOE/A station

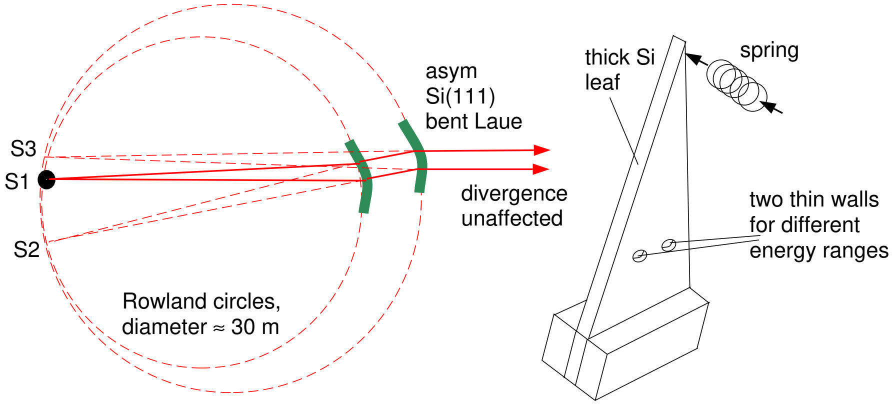

Figure 6.48. Tunable, fixed-exit monochromator (denoted as M1 in other layout sketches) consisting of two bent Laue crystals in nested Rowland conditions. Crystals are shown with small thinned regions that diffract the x-rays.

chromatic aberration in nanofocusing. To meet such conditions, a high-resolution monochromator system M2 in the A station, operating in air, would be available to optionally further reduce the energy bandwidth down to 10^{-4}–10^{-6} levels (Fig. 6.49). Such a system, whose performance improves with lower source emittance, has already been developed and utilized at 1-ID for many years and consists of four flat Bragg Si crystal reflections in a vertically diffracting $(+--+)$ dispersive configuration [90]. Different crystal reflections would be used, depending on the resolution required. Si(111) reflections would provide $\Delta E/E \sim 10^{-4}$. The highest energy resolution (10^{-5}–10^{-6}, from Si reflections in the (444)–(660) range) would meet stringent longitudinal coherence requirements for conducting BCDI on reasonably large sized 10 μm crystal grains. A vertically collimating lens L2 placed in between the monochromators M1 and M2 would enhance the throughput of the narrow-angular-acceptance M2 system. If focusing is also required along with the narrower bandwidth, downstream focusing optics (L3–L6) located in the A, B, or C stations could be used as well.

6-6.4.2 X-Ray Optics—Focusing and Beam-Expansion

Cooled refractive focusing lenses (L1) immediately upstream of the monochromator (in white beam) would deliver a focused high-flux pink beam (e.g., a full undulator harmonic of 0.6% bandwidth at 70 keV) into the end-stations for low-Q-resolution (e.g., PDF/SAXS) experiments at the highest

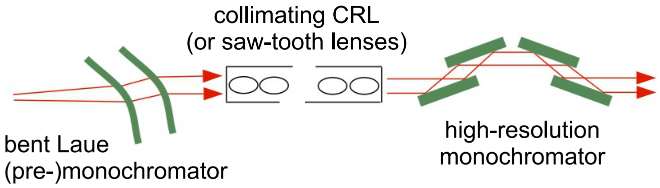

Figure 6.49. The beam from the bent Laue monochromator undergoing further bandwidth reduction using a four-reflection high-energy-resolution monochromator (M2 in layouts). Refractive lenses (L2) positioned in between the monochromators collimate the x-rays.

flux. In the brightness mode, the FWHM spot sizes would be $50 \times 15\,\mu\text{m}^2$ and $180 \times 50\,\mu\text{m}^2$ in the B and C stations, respectively, with 4–5 times more flux than would be obtained with the monochromator. A separate set of lenses (also part of L1) could be alternatively used as white beam expansion optics, to deliver beams on the order of several mm to the end-stations for direct-beam imaging applications. Recently there has been notable progress in single-crystal diamond compound refractive lens (CRL) fabrication, making them suitable candidates for such purposes, particularly in view of the thermal load.

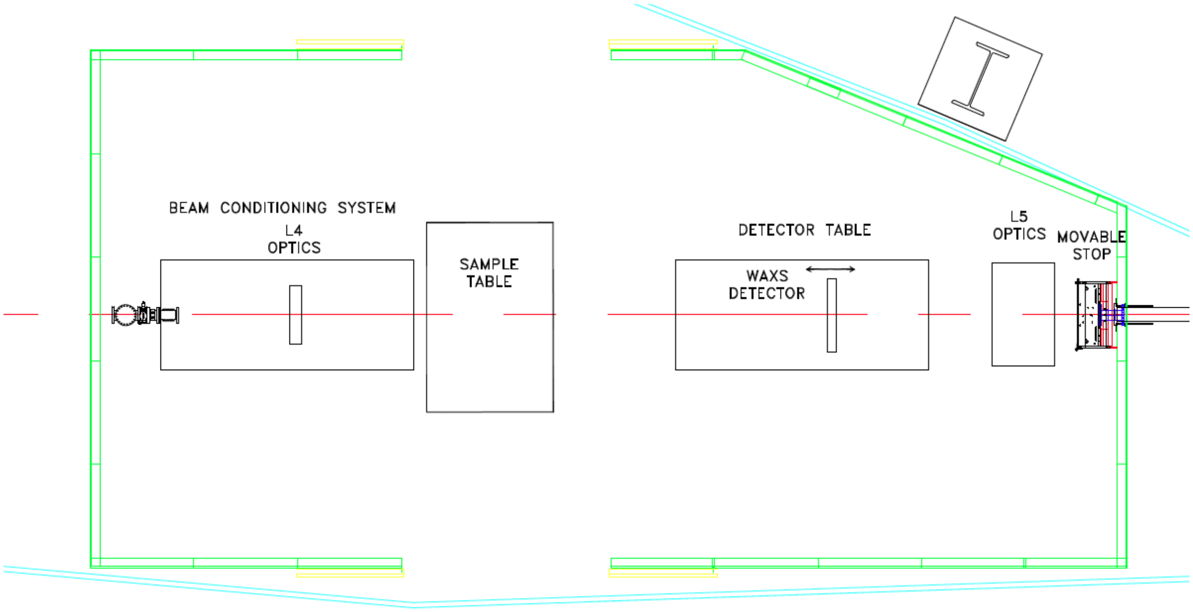

Figure 6.50. HEXM-B station.

Additional refractive lenses would also be placed in the A station. As already mentioned, one set (L2) placed between the primary and high-resolution monochromators would be used to collimate the beam vertically into the narrow angular acceptance of the high-resolution flat crystal reflections. Another set (L3) at the downstream end of the FOE would provide long-focal-length focusing into the B and C end-stations, or serve as beam expansion optics to deliver larger monochromatic beams (similar to the broadband case with L1) for imaging applications. On beam conditioning system (BCS) tables positioned at the upstream ends of both end-stations (Figs. 6.50, 6.51), short-focal-length focusing optics (L4, L6) would be available to focus x-rays to micron and sub-micron sizes, with sub-100 nm achievable vertically in the distant C station. The BCS tables in B and C stations would also support slits, ionization chambers, and fast-shutters controlling detector exposure times.

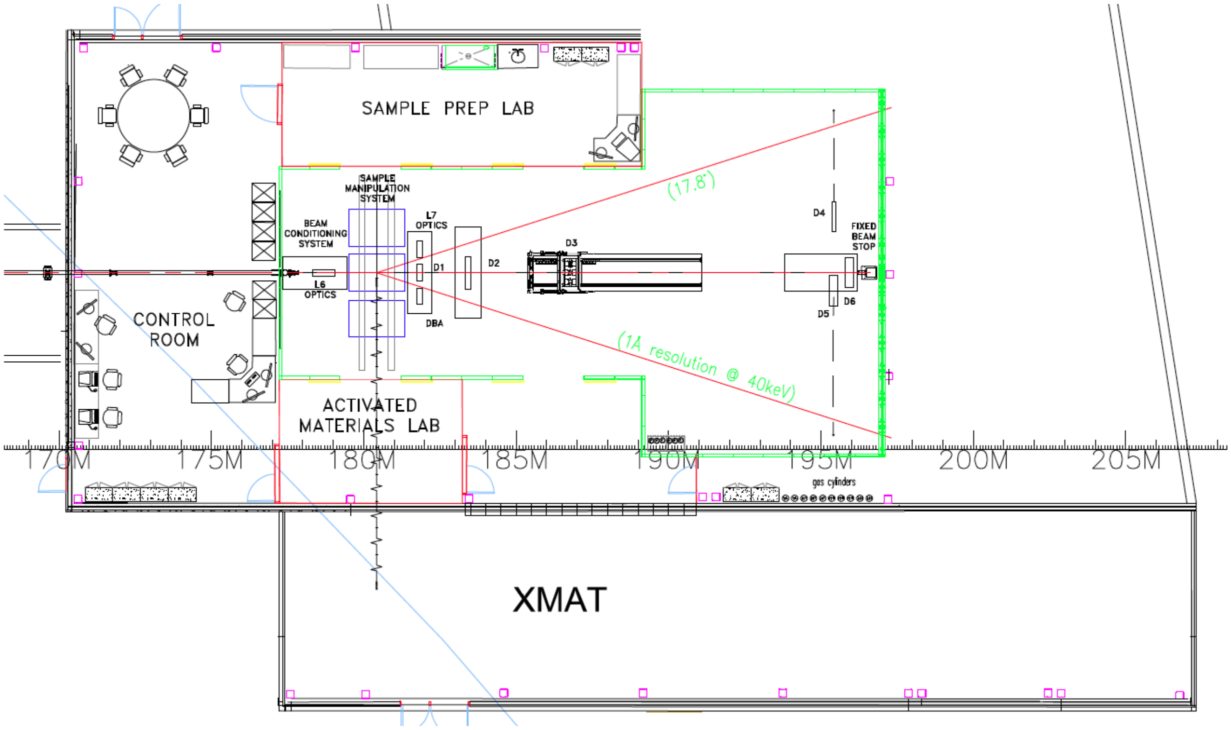

Figure 6.51. HEXM-C station plan view. See Fig. 6.54 for elevation view.

APS 1-ID researchers have over a decade of experience focusing up to 100 keV x-rays to micron and sub-micron spot sizes with CRLs, kinoforms, and especially saw-tooth refractive lenses [91, 92]. The perhaps lesser-known saw-tooth and kinoform lenses are depicted in Fig. 6.52. The last is based on the principle that a triangular saw-tooth structure, when tilted with respect to a beam, presents an effectively parabolic thickness profile, as required for aberration-free performance. A full parabolic profile is obtained by placing two such structures face-to-face, tapered symmetrically about the beam axis. In addition to being in-line, saw-tooth lenses have the great advantage of continuous tunability in focal length or energy by a straightforward symmetric adjustment of the taper angles of the two pieces, which alters the extremal curvature radius of the effective parabola. In addition, the device has no attenuation on-axis, unlike the case of CRLs, for which even the on-axis ray passes through all the elements' walls. Based on the equation in Fig. 6.52(a), tooth heights v and periods of 0.1–0.2 mm in Si with grazing angles α of tenths to hundredths of a degree correspond to focal lengths f of 1–10 m for 50–100 keV x-rays. Kinoforms, Fig. 6.52(b), can be viewed as perfectly profiled (i.e., "blazed," in the diffraction grating sense) zone plates. They can also be viewed as single, plano-concave parabolic lenses, from which one has absent, to the extent possible by fabrication, refractively inert material thicknesses corresponding to integer-2π phase shifts. Consequently, unlike conventional zone plates, they do not produce other orders, and direct all the intercepted radiation into a single, first order focus. Unlike saw-tooth lenses, they are similar to zone plates in that they are not tunable. However, kinoforms, at present, appear to provide the smallest spot sizes at high energies, e.g., 230 nm FWHM demonstrated at 51 keV [91] and 660 nm at 102 keV, at 1-ID.

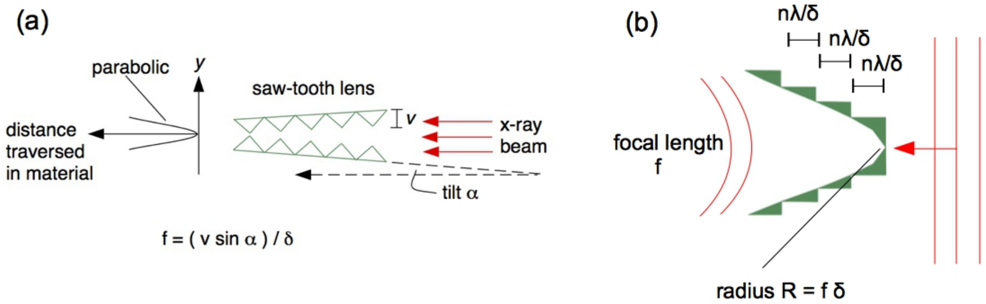

Figure 6.52. Focusing by (a) saw-tooth and (b) kinoform refractive lenses.

The presence of focusing optics at numerous locations along the long HEXM beamline provides flexible possibilities for obtaining variable spot sizes, either with one optic or a compound combination. Focusing into the C station (at 180 m) using lenses L2 and L5 combined in the vertical and only lenses L5 in the horizontal (in the brightness mode) will produce a fairly round focal spot of a few tens of microns (Fig. 6.53). By adjusting apertures at the focusing optics to select a transversely coherent region of the beam (with 500 [150]× gains in coherent flux [fraction] expected at 40 keV over today at 1-ID), one can make this focus highly coherent, and suitable for BCDI measurements on grains up to 10–20 μm in size. To obtain more coherent flux onto a smaller grain, one can increase this defining aperture to keep the focal spot size unchanged, while decreasing coherent fraction, thereby directing more coherent radiation into a smaller transverse coherent region within the focus. If one desires to explore a ptychographic approach to BCDI by illuminating the grain with a smaller, intermediate-sized beam (of 1–2 μm, but not sub-micron), an adjustable focal spot can be obtained by having the L3 lenses define a real, secondary source that can be refocused by the L6 optics.

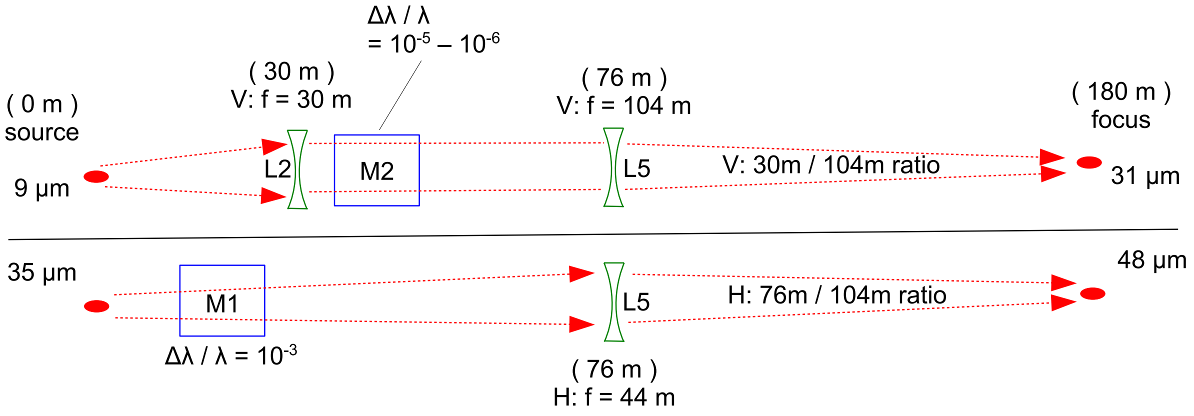

Figure 6.53. Optics operational configuration for obtaining large focal spots (FWHM) for BCDI.

6-6.4.3 Filters and White Beam Slits

Emerging from the front-end, the beam will go though filters and white beam slits, in that order. The cooled filters will provide thermal load alleviation for the white beam slits, lenses L1 (when used), and the monochromator M1.

6-6.4.4 Shutters and Stops

The front-end shutter will be capable of blocking the beam from entering the beamline, including the A station.

A multi-mode shutter/stop would be present at the downstream end of A. This component's status could be in one of two modes, "white" or "monochromatic," with remote shuttering capability in either mode. In "white beam mode" it shutters the white beam. In "monochromatic mode" it serves a white beam stop while shuttering the monochromatic beam.

A compact, cooled, movable stop would be integrated into monochromator M1 after the first crystal to block the transmitted white beam. This stop is intended for downstream equipment protection during monochromatic operation, and would not be part of the radiation safety system (RSS) for personnel protection. The multi-mode shutter/stop in A would meet that purpose. However, if the white beam stop as part of the monochromator is designed to meet RSS standards with white beam shuttering capability, then the component at the downstream end of A would only need to be a monochromatic shutter. Another possibility is to relocate the multimode shutter/stop to place it just after monochromator M1, dispensing with the need for the additional compact white beam stop.

A cooled, movable stop would be present at the downstream end of B. When "open," it would let white and monochromatic beams pass. When "closed," it would stop both beams. This arrangement permits white and monochromatic beam experiments in either B or C, with personnel access to C when any experiments with beam are ongoing in B. The previously discussed situation of focusing a full undulator harmonic using lenses L1 would require white beam operation of an end-station. One could also have the possibility of broadband short-focal-length focusing, e.g., using elliptically bent multilayers.

At the downstream end of C, the final component would be a cooled, fixed stop for white and monochromatic beams.

6-6.4.5 Transports, Windows, and Vacuum

Both experimental stations and evacuated beam transports (A-to-B and B-to-C) would have to be white beam compatible. The long transport from B to C would be unsheltered. However, the ISN beamline's long transport would be built on a fully enclosed/sheltered corridor for enabling personnel and equipment to transit between the main APS experimental hall and the external building.

Aside from the front-end, the HEXM beamline would consist of three vacuum sections. The first would extend from the font-end exit window up to and including the monochromator M1. The second would include the multi-mode shutter/stop in A and the A-to-B transport. The third consists of the B-to-C transport. All these segments would terminate in cooled, flanged windows for x-ray entry/exit. Optional evacuated flight-tube hardware will be available to couple to the appropriate flanged windows to eliminate air gaps in A, B, and C, particularly for white beam operation. In that case, an extra cooled window will be available to create a final evacuated path from the upstream end of the station used right up to the experimental set-up.

6-6.4.6 Bremsstrahlung Shielding

During white beam operations in an end-station, a direct line of sight exists from the electron source in the storage ring all the way down the beamline. The very-high-energy bremsstrahlung radiation (up to 6 GeV) cone emitted around this line of sight must not escape into areas accessible to personnel. This is achieved by having collimator/mask pairs placed at spatial intervals down the line to ratchet down the bremsstrahlung cone. Their number and positioning is yet to be determined.

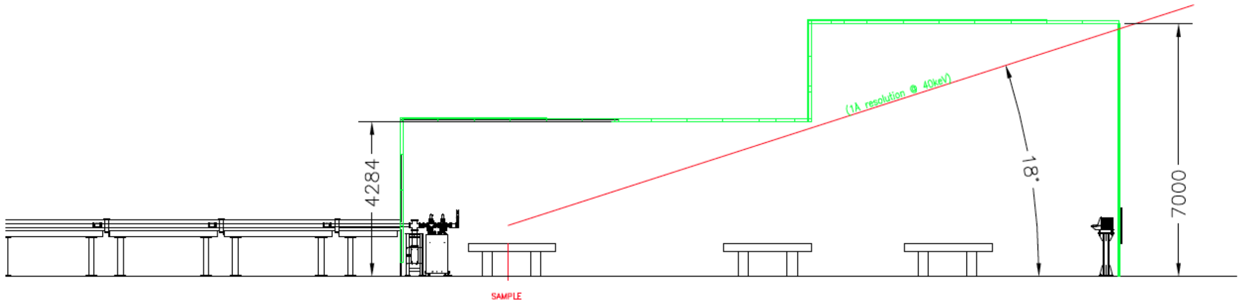

Figure 6.54. HEXM-C station elevation view. See Fig. 6.51 for plan view.

6-6.4.7 HEXM C Station Instruments

The C station instruments are shown in Figures 6.51 and 6.54. Numerous components in this station have already been introduced in previous sections. At the upstream ends of the C station, there will be a BCS table to support short-focal-length ($f < 2$ m) focusing optics (L6), beam apertures, flux-monitoring ionization chambers (including some having beam position sensitivity), and compact fast-shutters for precise detector exposure.

The C station will be the primary end-station, with a sufficiently large size (20 m along beam) to house several imaging techniques. Upper-half-cone, sample-diffracted beams from 1 Å d-spacings ($Q = 6.3$ Å^{-1}) at 40 keV would be able to propagate all the way to the downstream end to be recorded by the BCDI/vff-HEDM detector D4. The station will be designed to allow the user to seamlessly switch between modes during beam-time. A single sample position will be used so that all of the detectors downstream can be utilized in a calibrated fashion, with different sample manipulation systems (SMS) accessed by a floor-mounted rail system. Several (2–4) SMSs will be developed to allow mounting of a variety of sample environments including (thermo-mechanical) deformation, *in situ* additive manufacturing, and electro-chemical cycling. *In situ* studies of activated samples can also be conducted in this station, potentially including *in situ* ion irradiation. Aspects of the detectors placed after the sample are discussed in Section **??**. Besides detectors, diffracted-beam apertures (DBA) are optionally placed after the sample, i.e., conical and/or spiral slits for defining the sample spatial resolution along the beam. The L7 lens system after the sample serves as a TXM objective in the direct or diffracted beams.

6-6.4.8 HEXM B Station Instruments

The B station arrangement is shown in Figure 6.50. It will be located as far downstream as possible ($\sim$ 70 m) within the main APS experimental floor and be used for a variety of scattering experiments. These include a standardized, high-throughput HEDM set-up and complex *in situ* environments which cannot fit within the C station.

At the upstream ends of the B station, there will be a BCS table to support short-focal-length ($f <$ 2 m) focusing optics (L4), beam apertures, flux-monitoring ionization chambers (including some having beam position sensitivity), and compact fast-shutters for precise WAXS detector exposure.

High-energy x-ray experiments that can be conducted in the nearer B station, which do not require the C station's distance from the source (e.g., the latter for high-demagnification focusing, beam size), will benefit from a significant enhancement in photon flux density over that currently delivered to station 1-ID-E, which is at the same distance as HEXM-B. The SCU-HEXM, combined with the brightness mode, will provide an order of magnitude more flux density than that currently delivered by SCU1 to 1-ID-E.

The L5 focusing optics in the downstream end of the B station will allow long-focal-length focusing into C in an approximately 1:1 geometry, e.g., for BCDI experiments (Figure 6.53). Lenses just after the B station sample could be used to implement a very high-magnification TXM set-up, imaging all the way to the D5 detector in the C station, exploiting the distance separation of more than 100 m.

The external building that will contain the distant HEXM C station (and also the ISN beamline's end-station) offers opportunities to provide facilities including *in situ* ion irradiation and handling of hazardous materials. These possibilities will be discussed next.

Activated Materials Laboratory: An Activated Materials Laboratory (AML) is proposed to provide safe handling of activated materials for studies at both HEXM and around the APS. It is motivated by the strong and growing interest in access to the most advanced synchrotron x-ray techniques for activated samples, which is currently largely limited by the challenges in sample transfer and handling. Because of the HEXM's long beamline configuration, the AML would be separated from the APS main building, providing better control from a radiological safety standpoint. This design would also provide good sample accessibility, flexible operation, and minimize the time exchanging samples, which would enhance scientific productivity.

The AML will be designed and funded in collaboration with other national or international facilities, including the Nuclear Science User Facilities (NSUF) and Idaho National Laboratory. Planned features include shielded glove boxes, laboratory fume hoods with HEPA filters, an equipment storage area, a specimen storage area, and an area for shipping and receiving. The design will be guided by the As-Low-As-Reasonably-Achievable (ALARA) principle, and implement various safety measures and engineering controls. The AML will allow sample handling and preparation in a fume hood or shielded glove boxes, e.g., mounting and remounting samples into sample holders, sample loading into environmental chambers, and simple sample modification. Optical microscopy, thermal treatment, experimental chamber pre-pumping, and fabrication of small-scale samples by SEM/FIB for *in situ* ion irradiation experiments may also be conducted in the AML. A staging area will be designed to assist sample transfer to other beamlines around the APS. The specimen storage area will provide users short-term storage options before and after the experiment. The proposed facility will work in conjunction with other radiological facilities at the laboratory for receiving, shipping, and more involved preparation work (e.g., cutting, polishing, etc.).

XMAT Ion Source: An MeV-per-nucleon ion accelerator (similar to the recently upgraded Argonne-ATLAS front end) would provide a unique radiation damage source whose damage depth is well matched to HEXM characterization depths. Ions would be steered into the C station using apertures and focusing lenses to impinge on the sample with a variable size down to $10\,\mu\text{m}^2$ in the vicinity of the x-ray beam. The design would also allow hundreds to thousands of samples to receive preliminary doses before being moved into the C station for analysis. Thus even multi-year dose rates can be accommodated, with users moving samples to the AML and/or HEXM station for periodic examinations. The ion source itself would require approximately 20–30 m of space and a preliminary design has been produced by the ATLAS staff [84]. The configuration of the HEXM beamline provides flexibility for siting this source with respect to the C station, as shown in Figure 6.51.

6-6.4.9 HEXM Beamline Stability

The APS-U electron beam stability specifications are approximately one-tenth of the emittance sizes and divergences. In addition to this x-ray source contribution, other instability influences are mechanical and thermal in nature, depending on various elements in the beamline, including optics, samples, and detectors. As already mentioned, the current APS 1-ID bent double-Laue monochromator (cryogenically cooled) preserves the APS vertical emittance, even while operating in the vertical diffraction geometry. This performance holds true in view of concerns from cryogenic cooling vibrations, as well as diffraction effects in bent Laue crystals. Rotating the monochromator to operate in the horizontal geometry in APS-U should therefore preserve the comparable horizontal emittance, and also the out-of-diffraction-plane vertical emittance, from the standpoint of stability.

Experiments in the distant end-station C that employ a short focal distance are, in principle, not affected by overall rigid translations that impart the same displacement to both the focusing optics and sample. However, thermal and vibrational effects on different sub-structures (separated by 1–2 m working distances) may not be equal or in phase. For this reason, achieving 100 nm focusing would require floor vibration below 20 nm (rms). A separate foundation of sufficient thickness for the external building housing the C station should help achieve such requirements, with additional results possible from an isolation-joint perimeter separating the C station floor from the rest of the building. Temperature stability is also a concern, and could be addressed through nested zones of tighter tolerances, e.g., 0.5 °C (peak-to-peak) in the building, and appropriately narrower margins in the C station and a possible enclosure surrounding the BCS table and sample.

Beam position stability in long focal length configurations where the focusing optics and sample are in separated stations (e.g., A-to-C or B-to-C focusing) can pose a challenge due to the long lever arm from the focusing optics to sample and the lower demagnification in suppressing source and monochromator perturbations. In this proposal, long focal lengths are proposed for providing large focal spots for BCDI experiments and other diffraction experiments. These concerns drive the need for appropriate temperature stabilization of the A and B stations as well, to preserve source-optics-sample collinearity. However, temperature stabilization of different stations does not address relative floor motions among them, especially in view of separated foundations. Real-time diagnostics from position-sensitive split-plate ionization chambers (e.g., on BCS tables) would be used for feedback control using small active displacements of focusing lenses or rotations of monochromator crystals (of M1 or M2). Much could be learned from installing a hydrostatic leveling diagnostics system, probing relative vertical floor displacements along the entire HEXM beamline all the way from the source point in the storage ring to the distant C station. Such a system can also detect net rigid rotations of the C station floor, which, over a 1–2 m focal distance, might move the focus by an appreciable amount on the sample.

HEXM requires a variety of area detectors, as summarized in Table 6.24. Hard x-ray area detectors have undergone rapid development in the past 20 years, as the significance of the high-energy x-ray applications has motivated both detector research groups and companies. The advantage of the high penetration power of the high-energy x-rays is also the main obstacle for obtaining both efficient and high-resolution detectors. Current high-energy x-ray detectors can be grouped into:

- **Scintillator-based optical detectors** which can achieve micron resolution, based on thin (10–25 μm) single-crystal scintillators. These detectors have relatively low efficiencies, with current scintillators having $< 10\%$ stopping power above 40 keV and the emitted visible photons collected in a small solid angle (with 3% efficiency) by a high-resolution, magnifying optical system and a CCD or CMOS camera. For these detectors, R&D efforts are ongoing to find new scintillator materials and forms (especially structured scintillators) for improved efficiency.
- **Flat panel detectors** can achieve very high detection efficiency due to their thick scintillation layers (up to mm) in front of a sensor chip. These integrating detectors can be made as large panels, with sensors of amorphous-Si (e.g., GE-41RT, Perkin Elmer XRD1621) or CMOS (e.g., Dexela 2923). New sensor materials (e.g., amorphous-Se) may be of interest for future detectors of this type. The disadvantage of these detectors is the relatively large pixel size (75–200 μm) and the limited read-out speed ($<$ 30 fps).
- **Direct detection detectors** function by directly transforming x-ray photons to electrons, with the most viable today being CdTe-based (e.g., Pilatus3 CdTe, Pixirad) or GaAs-based (e.g., ASI-Medipix). These detectors also have some energy sensitivity, which can be efficiently used for filtering unwanted Compton scattering, undulator harmonics and/or fluorescence. These detectors have no read-out noise and high dynamic ranges of 15–20 bits coupled with high frame rate read-out (100–1000 fps). The disadvantage of these detectors is the large pixel size (50–175 μm) and relatively high price.

The most challenging detectors for HEXM are D1/D4/D5, all of which require high spatial resolution and detection efficiency. While some of the detectors (with R&D) listed above may be appropriate in this context, hybrid pixel detectors also offer great promise. The detection principle is that an incoming individual photon generates charges which are shared between neighboring pixels, and that with analogue read-out and interpolation the hit location can be determined to sub-pixel precision. The first prototype detector MÖNCH03, recently developed by the PSI/SLS Detector

Table 6.24. Current and anticipated detector performance parameters relevant to HEXM techniques

Detector	Technique	Current	Anticipated
D1, **D5**	μ-CT, nf-HEDM, TXM	LuAG:Ce scintillator + mirror + microscope (in-house design)	R&D needed for $\leq 1\mu$m resolution at higher efficiency
D2, **D3**	WAXS/ff-HEDM	Dexela 2923, 4× GE-41RT	Pilatus 6M, Dexela/GE equivalents, high dynamic range
D4	BCDI/vff-HEDM	none	R&D needed for $\leq 5\mu$m resolution at high efficiency, high dynamic range
D6	SAXS	Pixirad	Pixirad or equivalent

Group, has achieved $\sim 1\mu$m resolution with 25-μm-size pixels in an 400×400 array and was tested up to 55 keV, thus being of great interest for HEXM applications. Another new type of detector is the so-called mixed-mode pixel array detector (MM-PAD), developed by Cornell University, which is combining the analog integration with counter-based detection in each pixel, and is also available in a CdTe-based version. This detector is unique with its high frame-rate (1000 Hz) that does not sacrifice dynamic range (a trade-off disadvantage of other detectors), making it very valuable for dynamic, time-resolved studies. A prototype has been tested at APS-1-ID and commercialization of this detector is ongoing. In summary, considering the APS-U timeline, these detectors currently under development have a very good chance of being commercially available by the start of the upgrade implementation phase.

6-6.4.10 Computing

Several computing requirements need to be addressed to make best use of the high-volume data generated by HEXM. Data rates are expected to be about 100 times higher than the current rates at 1-ID due to the enhanced brilliance and expected gains in detector technology. In addition, users increasingly wish to attain real-time data analysis, such that experimenters can better steer experimental strategy, such as modifying the level of applied load prior to crack initiation. Key elements to meet these challenges include stable data acquisition systems, reliable software, and appropriate storage, network, and computing resources. For some existing experimental techniques such as WAXS/SAXS and μ-CT imaging, 1-ID is at the cusp of real-time data analysis today. For HEDM, the infrastructure necessary for real-time data analysis is being built in collaboration with internal and external partners. In the case of ff-HEDM, for example, interrogating a 3D slice of a polycrystalline aggregate takes approximately 10 minutes and yields approximately 15–60 GB of data today. The analysis of this dataset typically takes approximately five minutes to several tens of minutes on the moderately sized APS cluster Orthros, depending on the micro-mechanical state of the aggregate and the resulting diffraction patterns. While this is an acceptable time frame for a more static process such as monotonic loading, improvement is necessary to study dynamic processes such as crack initiation during cyclic loading of a structural alloy or material degradation due to electro-chemical cycling of batteries.

Simply deploying a larger cluster will not necessarily resolve the computational needs. Real-time data analysis means that large network and computing resources are utilized in bursts—these resources are idle when the dataset is being collected but the full capacity is needed once the data collection is completed. To meet the computational requirements in a more economically sound way, several avenues will be considered. The first is taking advantage of computational capabilities of graphical processing units, which can deliver large computational resources without a huge investment. The second is working with computational workflow experts to optimize the analysis procedures so that computing resources like the Argonne Leadership Computing Facility can be utilized effectively.

To best utilize the zoomed-in modes of TXM and BCDI, data-sets from the complementary zoom-out modes (standard μ-CT and HEDM, respectively) need to be rapidly analyzed and visualized so that an "interesting" sub-volume can be chosen more intelligently. Tools utilizing general-purpose visualization packages like ParaView or VisIt, as well as specialized packages like Dream3D, will be developed in collaboration with both Argonne and external partners.

Finally, data storage and archiving must be adequately addressed. For example, a full, *in situ* ff-HEDM dataset is typically on the order of several tens of TB today. As mentioned earlier in the section, this is expected to be at least two orders of magnitude larger after the APS-U. Multi-modal, zoomed-in/out capabilities will make these datasets even larger. Efficient and secure data storage solutions that can be accessed by computing resources for analysis and discovery, while maintaining the integrity and provenance of the data, are vital. One promising avenue towards this goal is the data management pilot program (run by Scientific Software Engineering and Data Management Group within the APS X-Ray Science Division) which has been deployed at the 1-ID beamline.

6-6.5 R&D Needs

Previous sections listed key infrastructure components for the HEXM beamline, several of which (detectors, stability, and computing) will benefit from R&D efforts. Below, two additional areas are pointed out, focusing optics and BCDI approaches, for which R&D is warranted so that they can have the highest impact.

6-6.5.1 High-Energy X-Ray Focusing

For reasons of larger working distances and operating in an in-line geometry, HEXM considerations lean more towards refractive lenses, mainly saw-tooth lenses and kinoforms for the short focal distances (1–2 m in B and C stations). Saw-tooth lenses offer straightforward, continuous tunability, whereas kinoforms appear to offer the smallest focal spot sizes. Efforts in improving the performance of both these types of lenses are intended to realize the full capabilities of the low-emittance APS-U source and long beamline.

Currently, saw-tooth lenses routinely used at 1-ID focus vertically down to slightly over 1 μm in the 50–90 keV range. Simulations show that improvements in the periodic saw-tooth profile quality should achieve 700 nm focusing. Pushing the focusing down to a few 100 nm would likely require correcting for a so-called length aberration by imposing bending or having a tooth period gradient. These high-energy focusing efforts are being supported by funding from the DOE-BES Accelerator and Detector Research (ADR) Program, whose scope was expanded to include x-ray optics.

Kinoforms have already demonstrated sub-micron focusing at 1-ID in collaboration with NSLS-II and LANL. Further kinoform development efforts will be directed towards improved fabrication for achieving larger spatial apertures and smaller spot sizes. This further development is also supported by ADR funding.

There are efforts by a few researchers worldwide on diamond CRL fabrication. This is of interest to HEXM in implementing efficient beam expansion optics (L3) and white beam focusing (L1).

6-6.5.2 Bragg Coherent Diffraction Imaging

Currently available HEDM techniques are capable of mapping intra-granular crystallographic orientation changes with approximately $1\,\mu$m spatial resolution and 0.01° in angular resolution. However, intragranular strain tensor fields cannot be retrieved—only the grain-average strain tensor can be determined. The coherent diffraction imaging program at the APS has demonstrated (at lower energies with nano-sized grains) that with appropriate data collection strategies and reconstruction algorithms, the intra-granular orientation changes and strain tensor field, as well as the shape of a crystal of interest, can be determined [86]. With the APS-U and the long HEXM beamline that can deliver stable and coherent beams at higher energies, BCDI is a natural avenue that can deliver additional information at smaller length scales (down to tens of nm).

HEXM aims to have the capability to conduct BCDI measurements on crystal grains of $\sim 10\,\mu$m in bulk by making such measurements at 40 keV. Challenges in achieving this in the combined parameter space of large grains and high energy include: high-resolution monochromatization ($\Delta E/E \sim 10^{-4}$–10^{-6}) to meet longitudinal coherence requirements, and the angular compression of reciprocal space features with respect to the diffracted wave-vector. The latter entails two effects—the increased Ewald sphere radius and the reduction in crystal-size interference fringes, thereby driving the need for a long end-station and high-spatial resolution detectors with high efficiency and dynamic range. Several groups have demonstrated that undersampled 3D diffraction profiles can be treated by providing additional constraints on the reconstruction algorithms [93, 94]. Overcoming diffraction profile undersampling can be addressed by denser sampling in angular (or energy) stepping, interrogation of multiple reflections for the same grain, sub-pixel detector displacements, ptychographic approaches to generate larger fringe spacings, and use of nf-HEDM-provided grain shape as a constraint for the BCDI reconstruction. All these considerations are the subject of a high-energy x-ray BCDI feasibility study being pursued by a collaboration among Argonne-XSD, MSD, and MCS researchers, funded by an Argonne Laboratory-Directed Research and Development (LDRD) Program.

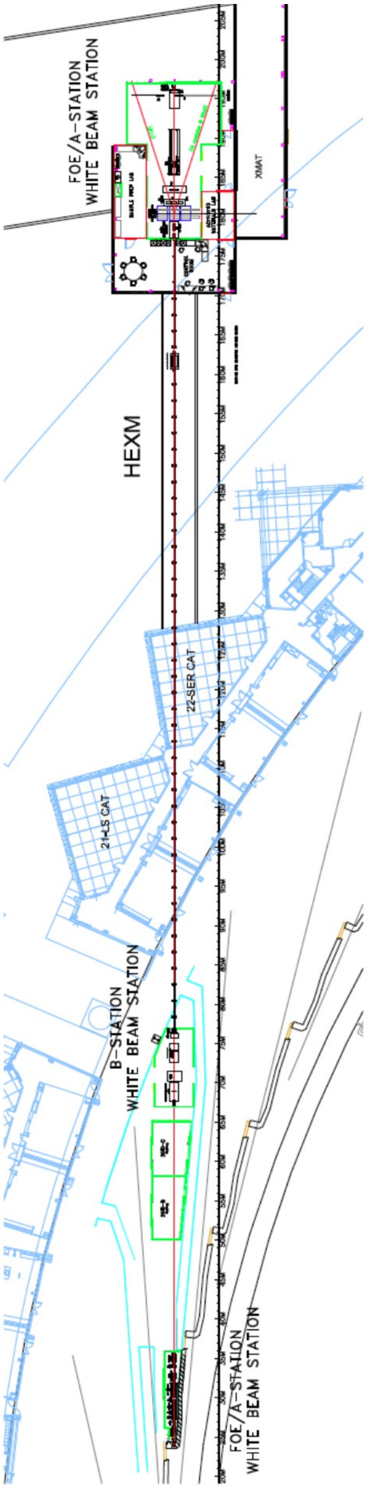

Figure 6.55. HEXM layout. Two currently existing 20-ID stations are still shown here, just before the HEXM-B station.

6-7 *In Situ* Nanoprobe Beamline

6-7.1 Executive Summary

The In Situ Nanoprobe (ISN) will utilize the massive increase in coherent flux in the hard x-ray range at APS-U to provide transformative imaging and spectroscopy capabilities for *in situ* studies of complex multiscale materials and systems in varying environments, at very high spatial resolution, and with close to atomic sensitivity. This capability will enable entirely new microscopic studies of materials as diverse as catalysts, batteries, photovoltaic systems, nano-electronics, and earth and environmental systems, under a broad range of conditions, such as during synthesis and during operation. These systems have in common heterogeneity at length scales from nanometers to macroscopic scales, complex compositional, chemical and structural features, functional units and sites, and high sensitivity to often multiple external environments such as temperature, gaseous environment, acidity, and external fields. The ISN will focus the coherent flux provided by the MBA lattice into a focal spot of 20 nm, enabling rapid, multidimensional imaging across many length scales, and combining x-ray fluorescence imaging and spectroscopy with coherent methods to achieve sub-10 nm spatial resolution and close to atomic sensitivity. The combination of brilliance increase and instrument design enables an increase in focused flux by 3 to 5 orders of magnitude compared to current nanofocusing capabilities, enabling very fast data acquisition across many length scales, and fast imaging of responses to changes in environmental parameters. Coupled with broad *in situ* capabilities and long working distance, this enables paradigm-shifting new understanding of functional materials and systems, and contributes to inspiring and conceiving new materials, materials systems, and approaches required to address some of the current and future challenges in energy and sustainability.

6-7.2 Scientific Objectives & Capabilities

6-7.2.1 Science Case for the Beamline

The Upgrade of the Advanced Photon Source with an MBA magnetic lattice, APS-U, will provide massively increased coherent x-ray flux in the hard x-ray range, and 20x reduced source size in the horizontal dimension, making it ideally suited to bring to bear coherent methods to a broad range of questions from materials and condensed matter science to chemical science and environmental science. Both nanofocusing approaches and coherence-based techniques benefit directly from the high brilliance and new source geometry, by (i) achieving diffraction limited spot sizes of 20 nm and below, (ii) massively increased speed of data acquisition, which in turn enables multiscale imaging of complex systems, and (iii) enabling high time resolution for the study of dynamic processes, such as defect formation and growth, and fluctuations. At the same time, the brilliance gain at high photon energies significantly enhances the essential capabilities of hard x-rays to penetrate gases, fluids, windows, and matrices, enabling very high spatial resolution imaging and nanospectroscopy under *in situ* conditions, and access to K and L absorption edges of most elements in the periodic system.

The In Situ Nanoprobe (ISN) exploits the transformative capabilities of APS-U by focusing coherent hard x-rays into a focal spot 20 nm in size, and uses coherent techniques to achieve a spatial resolution down to a few nanometers. The ISN allows probing of structure, composition, and chemistry of complex, multi-scale materials in 2D and 3D, with close to atomic sensitivity. The high coherent flux allows imaging of heterogeneous samples with nanoscale features across many length scales, enabling, for example, study of the evolution of an individual defect inside a material with macroscopic dimensions. The ISN uses x-rays with photon energies between 4.8 and 30 keV, enabling quantitative nano-spectroscopy at the K and L edges of transition metals and rare Earth metals, as well as penetration through environments and windows, and into materials to sites where active processes are taking place. To enable the study of materials under actual synthesis and operating conditions, the ISN will provide a very large working distance of 55 mm. This enables deployment of a large range of *in situ* environments, namely low, high, and variable temperatures, flow of gases and fluids, varying pH, high pressure, and application of external fields. It also provides added flexibility to integrate advanced detectors, such as emission spectrometers. The scientific focus of the ISN beamline is the investigation of complex, functional materials, and materials systems, such as catalysts, batteries, photovoltaic systems, nanoscale earth and environmental samples during synthesis, operation, and under actual environmental conditions. The ISN is designed to study these systems across many lengths scales, under *in situ* conditions, using x-ray fluorescence (XRF) for composition and trace contaminants, XRF nano-spectroscopy for local composition and chemical state, X-ray induced current[95] and voltage (XBIC/XBIV)[96], and X-ray excited optical luminescence (XEOL)[97] for electronic properties, and coherent methods such as ptychography for structural imaging and coherent diffraction to study slow dynamics.

A typical example of the kind of science the ISN will perform is the characterization of defects and their evolution under changing external conditions in photovoltaic materials. In these systems, as well as in many other materials, small local defects, such as contaminants or structural defects, can affect the macroscopic materials and systems response and properties. Examples include organic [98] and inorganic PV materials [99], and advanced thin-film materials with tunable properties. Defects and inhomogeneities that affect overall device efficiency can occur at grain boundaries, inside of grains, or at interfaces, and can be distributed over macroscopic dimensions. The ISN will be able to quantitatively characterize the composition and chemical state of individual defects, and map their distribution across macroscopic scales, with close to atomic sensitivity. These studies will be performed under change of temperature and/or flow of gases, to understand the evolution of individual defects and their distribution. Compositional/structural measurements will be coupled with measurements of local electronic properties, providing pixel-by-pixel correlation between local materials properties and the local electronic response. Very fast mapping in 2D and 3D enables several qualitatively new scientific problems to be addressed: (1) Some of the most exciting novel materials in photovoltaics, hybrid organic-inorganic perovskites, are also very susceptible to beam damage [100]; fast and efficient scanning, with total radiation dose comparable or even lower than with current approaches, will enable synchrotron-based compositional studies of these materials at the nanoscale. (2) Fast scanning with varying spatial resolution enables correlative microscopy, bridging the length scales of nano-XRF to lab-scale mapping and imaging techniques with micrometer to millimeter sizes. (3) Fast scanning enables multi modal studies to be conducted under non-repeatable conditions, such as *in situ* conditions.

The ISN will be capable of elucidating defect formation and evolution in energy materials in response to heating, cooling, electrical stimulation, light bias, and interaction with various gases. This can lead to new insights into defect engineering to improve process parameters or performance. For example, synthesis of chalcogenides thin films such as Cu(In, Ga)Se2 (CIGS) can be studied under flow of H2Se over CIG under temperature change, or under flow of H2S over a CIG thin film covered with a capping thin selenium layer, allowing direct observation of the formation of CIGS

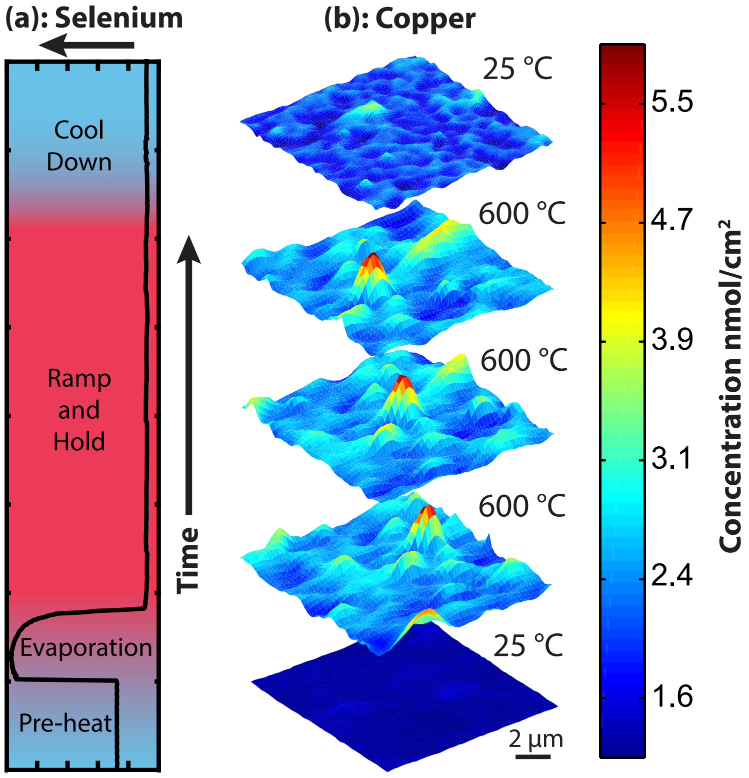

Figure 6.56. In situ study of the formation of the solar cell absorber layer CuInxGa1-xSe2 (CIGS). This study was performed using an in situ heating stage at 600°C, via diffusion of Se into metallic CuInxGa1-x in inert atmosphere to form the semiconductor CIGS. Left: the Se concentration peaks in the beginning when Se evaporates. Right: the Cu is homogeneously distributed in the beginning and goes through intermediate phases until it stabilizes. The map size is 10 µm x 10 µm, the acquisition of an individual map took about 7 min. Courtesy M. Bertoni, B. West, M. Stuckelberger.

and associated defect evolution (Figure 6.56)[101, 102]. Knowledge of defect reactions can serve as inputs and validation of kinetic process simulations, accelerating the pace of materials optimization and industrial scale-up.[103] The intrinsic multimodal approach to imaging with the ISN will provide qualitatively new understanding of local materials properties, by combining composition (XRF), structure (XRD), local defects (coherent scattering), time performance (XBIC) and bandgap (XEOL), with correlation of local properties at the individual pixel level.

6-7.2.2 Description of user community/stakeholders

The ISN scientific community encompasses both existing users of synchrotron x-ray imaging capabilities at the APS and other laboratories, as well as new communities. Many existing users have taken advantage of APS microprobes and nanoprobes, and, in the process, have communicated a variety of needs to better understand their materials systems, and to reduce the often long data acquisition times. Specifically, they require much faster data acquisition, significantly increased elemental sensitivity, smaller spot sizes to access smaller sample regions, and, in particular, *in situ* capabilities such as heating/cooling and/or flow of gases, applied fields, and high pressure. As important as a wide variety and combination of *in situ* environments there is an ever-increasing need for fast data acquisition in 2D and 3D, and in particular fast acquisition under changing *in situ* conditions. Enabling collection of 3D data with very high resolution and elemental sensitivity while changing several independent experimental parameters, such as temperature *and* process gas, has been a continuously rising but yet unmet demand. New users, such as users of electron microscopy, optical microscopy or of non-focusing x-ray beamlines, are used to a broad variety of *in situ* capabilities, often commercially available, and take them for granted. As such, providing broad *in-situ* capabilities with nanoscale resolution and sensitivity at the APS will open new user communities.

The Buonassisi and the Bertoni groups have for many years performed x-ray characterization on inorganic solar materials, using microprobe, nanoprobe and microspectroscopy capabilities, in an effort to understand and manipulate performance-limiting defects at ever smaller lengths scales to achieve improved solar materials efficiency. Both groups have invested in initial *in situ* capabilities at 2-ID-D. The range of *in situ* capabilities at high spatial resolution will enable the study of defects under realistic growth and processing conditions, enabling the development of strategies to improve performance of low-cost and/or high-performance materials. Users studying polymeric solar materials have, to a significant degree, used nanospectroscopy in the soft x-ray range to obtain the chemical state of block-copolymers and other materials; study of the effect of metal impurities in a polymer matrix at small length scales has to date rarely been performed, and will open up a new community. New users or users with new programs of interest, such as David Fenning, bring in new materials or materials systems. Nanoelectronics require a multitude of characterization techniques. Conal Murry represents a broader community of industrial researchers that study approaches to enhance future technology nodes, and develop materials capable of handling some of the fundamental materials issues related to the very small scale of next-generation transistors. With increasing 3D characteristics of future electronics devices and relevant lengths scales of 20 nm and below, with CDI providing a path towards nanometer resolution, the ISN facility is expected to serve both existing users from industry and academia, and attract new users from the community. The theme of Chemistry and Catalysis taps into a new user community that has, to date, used mostly incoherent techniques and microprobe-based spectroscopy. There is significant experience using scattering and diffraction-based methods to study catalysts or chemistry. The potential to perform spectroscopy at length scales below 50 nm is unique and powerful, and the combination of spectroscopy with high-resolution structural imaging via ptychography and auxiliary XRD contrast opens new ways to look, in particular, at catalysts. Both Argonne staff scientists, such as Randy Winans (XSD) and David Tiede (CSE), and experienced external users, such as Simon Bare, represent large communities of academic and industrial scientists that could become major users of the ISN facility. The E^3 community has traditionally relied on microprobe studies, particularly spectroscopy. Opening a new length scale, as exemplified by Tony Lanzirotti, for example will attract a community that is interested in micro- and nanoscale complex systems, such as marine and terrestrial microorganisms and microbes at interfaces with soil and gases. Aside from fundamental interest in understanding marine and terrestrial microorganisms in their complex environment, there is the opportunity to develop technologies for use of subsurface reservoirs as primary targets for carbon capture and sequestration, and for new energy production technologies. At the same time, there is potential to reduce impacts related to unintentional release of contaminants to the environment, and in understanding the global cycling of elements that are drivers for climatic change. With nanoscale 3D imaging, and spectroscopy under established *in situ* conditions established, we anticipate significant growth of this community.

6-7.2.3 Use of APS-U characteristics

The ISN beamline will make use of two aspects of the MBA Upgrade: the coherence gain and the reduced horizontal emittance of the x-ray source. The coherence gain allows both diffraction-limited focusing to a very small spot, and use of coherent techniques.

Use of coherence: nanofocusing and gain in focused flux

1) The ISN depends on diffraction-limited focusing to achieve the smallest possible focal spot size. Given that only the coherent part of the undulator beam will be used for diffraction-limited focusing, the massive increase in coherent flux delivered by the MBA lattice will directly increase the focused flux of the ISN.
2) The ISN requires high photon energy to penetrate environments and windows to access buried materials structures and interfaces. Therefore, the ISN takes particular advantage of the increase of coherent flux for higher photon energies. The design of the ISN source calls for a revolver undulator with two different magnetic structures, one of which (with period 2.3 cm) is aimed at further increasing the coherent flux at high photon energies.
3) By virtue of using non-chromatic nanofocusing mirrors as high-resolution optics, the ISN will be able to use the full undulator bandwidth of 1% for elemental mapping, yielding another factor of approximately 25x in focused flux.
4) The high reflectivity of mirrors provides 10x increase in focusing efficiency over diffractive optics at 10 keV, and of 100x at 30 keV.
5) Overall, the ISN design maximizes the coherent flux that can be obtained from the MBA lattice. It yields a focused flux gain of 10^3 x to 10^4 x over existing nanoprobes for spectroscopy applications with a bandwidth of 0.01%, and a total flux gain of 10^4x to 10^5 x for elemental mapping and ptychography, with a bandwidth of 1%.

Use of coherence: coherent techniques

The diffraction-limited nanofocus is intrinsically coherent. Therefore, coherent techniques such as ptychography can be performed. Ptychography will be done on a routine basis with every transparent sample. This will yield a factor of 5x to 10x improvement in spatial resolution beyond the spot size, enabling sensitivity to nanoscale structures. Ptychography yields both the aperture function of the nanofocusing optic and the sample amplitude and phase. As such, measured XRF maps can be deconvolved with the aperture function of the optics, providing an increase of $\sim$ 2x in the spatial resolution of elemental maps, to $\sim$ 10 nm.

Status of ISN beamline, domestically and internationally

The ISN beamline will be the leading hard x-ray nanoprobe in the U.S., based on the small spot size in the hard x-ray range (only surpassed by the HXN beamline at NSLSL-II), the massive focused flux, which is superior to other US facilities by orders of magnitude, and, in particular, by the long working distance it provides for *in situ* x-ray microscopy. The combination of working distance, focused flux, and spatial resolution is unmatched in the US, and positions the ISN as one of the leading or possibly the leading hard x-ray nanoprobe beamline worldwide. International competitors are at the ESRF, SOLEIL, DIAMOND, PETRA III, and MAXLAB. The NI branch of NINA at the ESRF achieves $\sim$15 nm spatial resolution at two select energies (17 keV, 33.6 keV) via use of nanofocusing multilayer mirrors. The NA branch achieves 50 nm resolution, at photon energies between 5 and 70 keV. NANOSCOPIUM at SOLEIL delivers a spatial resolution of 50 nm and is limited by the brilliance of a 3rd generation synchrotron, and the low electron energy of the storage ring. The HX Nanoprobe at the 3rd generation DIAMOND ring aims at 10 nm resolution. NanoMAX, which aims at a spot size of 10 nm, and is powered by a 4th generation SR source, will be a main competitor in regard to spatial resolution (10 nm), and in the lower part of the energy range (5 – 30 keV). It will not provide the working distance and *in situ* capabilities of the ISN, and is limited in brilliance at high photon energy. It is worth noting that all of these beamlines are longer than 90 m, with NI at ESRF and HX at DIAMOND being 185 m long, NanoMAX being 94 m long, and ESRF-NA as well as NANOSCOPIUM being 165 m and 160 m long, respectively.

6-7.2.4 Key beamline characteristics

The ISN beamline will use hard x-rays with photon energies between 4.8 keV and 30 keV. This will provide access to absorption edges of most elements in the periodic system, including the Ti K_α edge at the lower end of the energy range, I K_α at the high end of the energy range, and the L edges of the rare earth elements and heavy elements such as Pb and Bi. In addition, the penetration of x-rays into matter increases with photon energy, allowing study of samples in environmental cells with windows, and in gases and fluids.

The design of the ISN beamline is based on a *spatial filter*, with intermediate focusing on a beam defining aperture (BDA), which in turn defines a secondary x-ray source. All beamline optics, namely two focusing mirrors, a crystal monochromator and a multilayer monochromator, are positioned upstream of the BDA. Thus, any wavefront deterioration or instability caused by the beamline optics will be filtered out at the BDA, which in turn defines a coherent source that enables diffraction-limited focusing by the nanofocusing optics.

The ISN instrument will be positioned at a distance of approximately 220 m from the source. This provides a lateral coherence length sufficiently large to match the acceptance of the nanofocusing mirrors, namely 305 μm in the horizontal direction and 1 mm in the vertical direction, and thereby enables a large working distance of 55 mm. The final length of the beamline will be chosen to enable the HEXT beamline at 20-ID and the ISN beamline at 19-ID to share one satellite building.

The ISN instrument will provide a nanofocus of 20 nm (25 keV), with numerical aperture of 1.7 mrad in both directions.It will enable 3D XRF mapping, nanospectroscopy, and ptychography with a resolution of 20 nm to well below 10 nm (with ptychography). Based on strong user demand, the ISN will also provide limited Bragg diffraction capabilities to provide crystallographic information on the sample. The ISN instrument will provide cooling to 10 K, variable temperature up to 1000 ℃, gas flow (under variable temperature conditions), flow of fluids, pressure, and applied electric fields.

6-7.3 Source & Front End Requirements

6-7.3.1 Insertion Device

The ISN beamline requires the full brilliance of the MBA lattice to perform multimodal studies of materials under *in situ* and *operando* conditions at diffraction-limited resolution. The high scanning speed enabled by high coherent flux is required to probe the properties of the samples across many length scales; high speed will also minimize drifts and therefore allow operation at the diffraction limit. The high speed will furthermore enable capturing of the time-evolution of processes, such as change of local composition and chemistry and defect migration in complex systems under conditions such as variation of temperature, flow of process gases, change of acidity, or in response to applied currents and voltages.

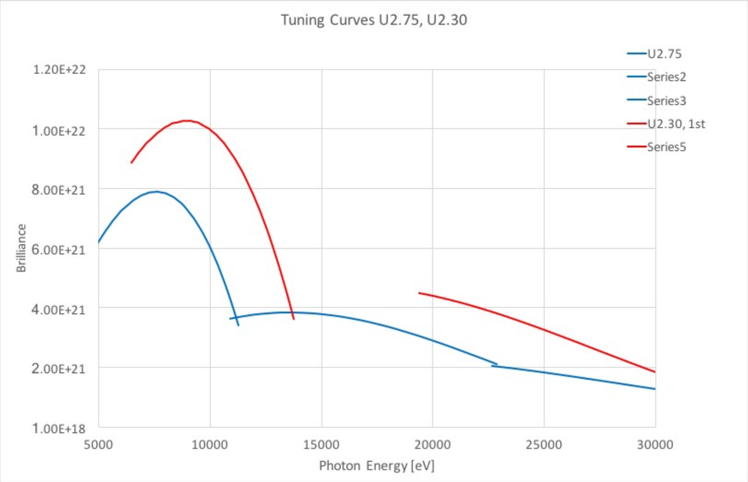

Figure 6.57. Tuning curve for 4.6m long revolver undulator with periods of 2.5cm and 2.1cm, respectively.

To maximize the brilliance in the relevant range of photon energies, a revolver undulator with a length of the magnetic structure of 4.6 m will be used. A magnetic structure with periodicity of 2.5 cm will provide continuous coverage across the full range of photon energies, providing access to all elemental absorption edges situated in the 4.8 – 30 keV range of photon energies. A magnetic structure with periodicity of 2.1 cm provides higher brilliance at higher photon energies in particular, fully exploiting the strength of the upgraded APS for high photon energies. The device must allow tapering for nanospectroscopy. A final decision on insertion devices will be made during the final design stage.

6-7.3.2 Other Source Requirements

Source stability is vital to avoid loss of flux and intensity variations during data acquisition. 10% variation in source position and angle will be acceptable.

We desire accurate information on source positions and angles (e.g. EPICS PV's) to allow us to follow potential source changes. We wish to explore a hardware-link with source position/angle information, to potentially integrate with a feedback system.

6-7.3.3 Front End Requirements

To preserve the brilliance of the source, a windowless front end with differential pumping section is required. Two Si_3N_4 windows will be used as exit windows in the experimental endstation.

A small front end exit mask is desired to minimize total power into the First Optical Enclosure, and reduce scattering at beamline optics. The aperture needs to be sufficiently large to allow for optics alignment and to accommodate potential beam motions. We currently anticipate an exit aperture with a size of 2 x 2 mm, but a smaller size with improved power reduction might be feasible as well.

6-7.4 Beamline Layout

The ISN beamline is designed for the highest-resolution 2D and 3D imaging, fluorescence mapping and nanospectroscopy of energy materials, and other complex, hierarchical systems under *in situ* conditions. The ISN will use nanofocusing mirrors in Kirkpatrick-Baez (K-B) geometry to focus hard x-rays to a diffraction-limited focal spot of 20 nm size. To achieve a long working distance of 55 mm, the ISN will use long mirrors with correspondingly large acceptance and long focal length. The beamline is designed to provide the large lateral coherence lengths required to illuminate the full length of the mirrors. The resulting focused x-rays will be spatially coherent, enabling the use of coherent methods, such as ptychography, to achieve sub-10 nm resolution in transmission imaging, and sub-20 nm resolution in fluorescence mapping.

The ISN beamline is designed along two guiding principles:

(i) Use of a spatial filter to allow adjustment of the lateral coherence length with minimum loss of brilliance to guard against brilliance deterioration by upstream beamline optics, and prevent potential positional or angular instabilities of these optics to affect the focal position.
(ii) Enable the large lateral coherence length required for diffraction-limited focusing with a nanofocusing K-B system with large working distance. The beamline must provide sufficient positional and angular stability to enable 2D and 3D mapping at a spatial resolution of 20 nm.

These principles lead to the the following beamline layout:

A *high-heatload mirror* and a *pink beam mirror, M2*, are used to focus x-rays from the undulator on a *Beam Defining Aperture (BDA)*. M1, which focuses the white undulator beam in the vertical direction, is placed as close to the source as possible, to allow a secondary focus as far upstream as possible, without reducing the size of the secondary source below the original source size. M2 is positioned such that the horizontal source is demagnified by a factor of two and positioned downstream of the secondary source in the vertical direction, thus matching the lateral coherence length to the horizontally focusing nanofocusing K-B. This astigmatic design reflects the astigmatic nanofocusing setup and leads to a symmetrical focal point. The *BDA* will consist of two separate slits, one horizontally aperturing (H-BDA) and the second one vertically aperturing (V-BDA), each positioned on the focal plane of the respective focusing mirror.

A *Double Crystal Monochromator (DCM)* and a *Double Multilayer Monochromator (DMM)* are positioned directly downstream of M1, where the power density is lowest. The BDA positions for vertical and horizontal directions at 55 m (V-BDA) and 64 m (H-BDA), respectively.

A set of *white beam* slits is required upstream of M1 to define the area that is illuminated; a set of *pink beam* slits is required upstream of M2. A set of *pink beam* slits is required upstream of the monochromators. A removable x-ray flag and beam intensity sensor are required downstream of each monochromator. A mono beam slit designed to handle the power density of a two-dimensionally focused pink beam with a bandwidth of $10^{-2}$is required in front of M2. A removable beam flag is required downstream of the last BDA. Beam position monitors are required after each BDA.

6-7.4.1 X-ray Optical Layout

The ISN beamline will provide very high spatial resolution of 20 nm, and very high photon flux and flux density using Kirkpatrick-Baez (K-B) mirrors in a diffraction-limited configuration as nanofocusing optics. The ISN beamline will provide a range of photon energies between 4.8 keV and 30 keV, select a spatially coherent x-ray beam, and provide control of the lateral coherence length in horizontal and vertical directions at the ISN instrument station. The ISN beamline is designed around a spatial filter (SF) consisting of a two-dimensionally focusing mirror system and a two-component beam-defining aperture (BDA). This setup provides a clean secondary source in the horizontal and vertical directions. To maintain reasonable minimum sizes for the BDA close to 5 μm, the BDA components are placed at a position of 55 m (V-BDA) and 64 m (H-BDA) from the source, respectively. The undulator beam is focused horizontally and vertically on these positions via high heatload mirrors placed at 27.5 m and 43 m from the source, respectively, yielding a secondary source with a size of 16.4 μm FWHM x 4.4 μm FWHM (elliptical beam mode). All beamline optics are positioned upstream of the BDA, such as to remove any effects of source motion, optics motion, or wavefront deterioration from affecting the focused beam in the ISN instrument. By positioning the beamline optics as such, only monochromatic beam is focused on the BDA, which in turn can be designed to be highly stable and move with high accuracy, without engineering constraints imposed by high heatload design. In addition, further reduction of secondary source size by closing the BDA for manipulation of the lateral coherence length of the beam at the ISN position. Figure 6.58 shows the optical concept of the ISN beamline. The ISN beamline will deploy a crystal monochromator (DCM) with a bandpass ΔE/E of 10^{-4} for spectroscopy, and a double multilayer monochromator (DMM) with ΔE/E of 10^{-2} for high-speed imaging. Use of the DMM in combination with the non-chromatic K-B mirrors will provide a factor 25 x in flux and flux density gain for all applications where chemical state information is not required.

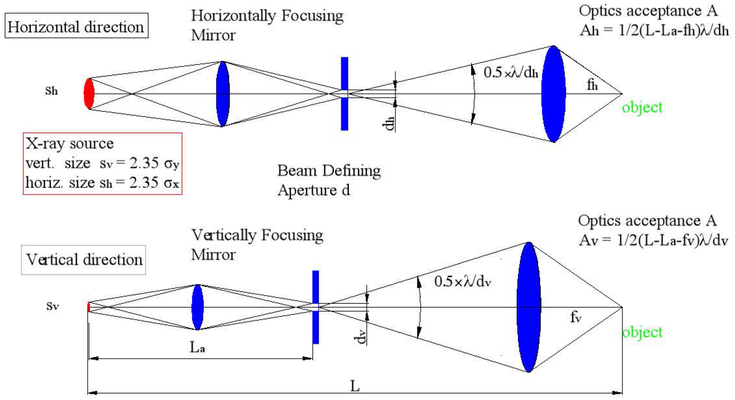

Figure 6.58. Optical layout of the ISN beamline. S_h *and* S_v *are the horizontal and vertical source sizes, respectively. L is the distance of the sample from the source, and La is the distance of the beam defining aperture from the source. dh and dv are the sizes of the beam defining aperture in the horizontal and vertical directions. A is the acceptance of nanofocusing mirrors.*

To achieve sufficient working distance to deploy a wide variety of *in situ* environments, while providing a spatial resolution of 20 nm, K-B optics with large acceptance and long focal length have to be used. To coherently illuminate such long mirrors without sacrificing working distance, the ISN instrument has to be placed at a sufficient distance from the secondary source, at 220 m from the primary x-ray source. The vertically focusing NF mirror has a length of 400 mm and a focal length of 400 mm. The horizontally focusing NF mirror has a length of 125 mm and a focal length of 122 mm. The vertically defining BDA is placed at 55 m, the horizontally defining BDA at 64 m. With a BDA setting of 19 μm in the horizontal direction and a setting of 6 μm in the vertical direction a spot size of 19.6 nm (h) x 19.8 nm (v) is obtained at a photon energy of 25 keV. Further reducing the BDA sizes will yield yet smaller focal spot size and increase of the degree of coherence, but a reduction of focused flux. Opening the BDA to larger sizes will yield larger spot sizes and increased focused flux, as well as reduced degree of coherence. The size of the secondary source at the respective BDA positions is 18 μm (h) and 6.6 μm (v). Opening the BDA beyond the size of the secondary source will not lead to an increase in flux or spot size, but reduce the effectiveness of the spatial filter to correct wavefront imperfections and beam drifts from the upstream beamline optics. The slope errors required to achieve a spot size of the 20 x 20 nm^2 are 3 x 10^{-8} rad, a challenging but feasible specification. The length in particular of the 400 mm long vertically focusing K-B element is challenging, but has, at the time of this writing, been accomplished by a commercial vendor.

6-7.4.2 Description of Optical Components

The first optical component is a vertically focusing high heatload mirror. It will have a length of 400 mm or less to accept most of the undulator beam. The mirror will be illuminated along most of its length, thus minimizing thermally induced slope errors in the area that is used for coherent imaging.

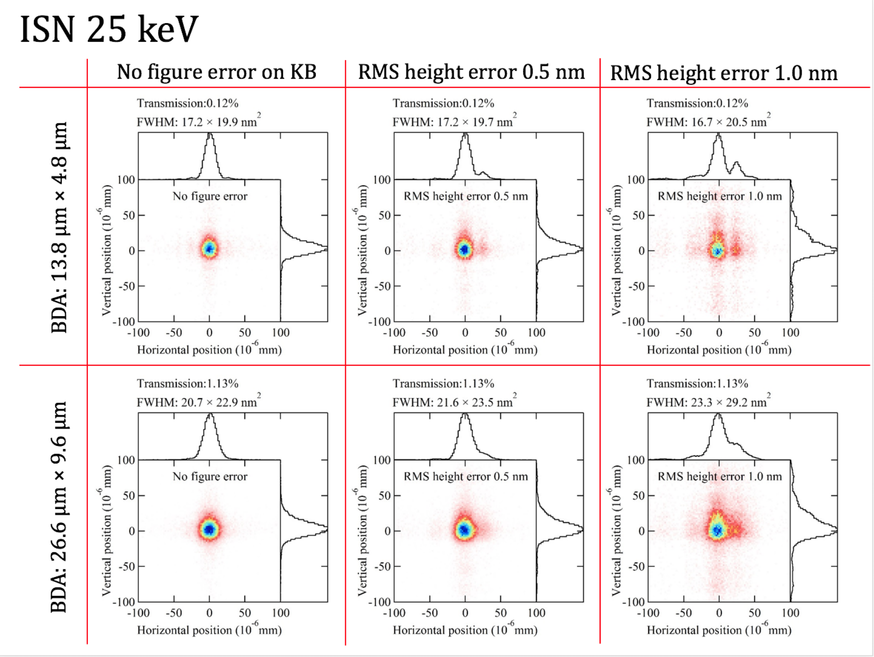

Figure 6.59. Focal intensity distribution for a photon Energy of 25 keV. Results for BDA sizes of both 13.8 x 4.8 μm^2 (fully coherent illumination) and 26.6 x 9.6 8 μm^2 (partially coherent illumination) are shown in the upper and lower panel, respectively. The effect of surface figure errors on the final spot size are shown, with perfect mirror figure in the panels on the left side, and RMS height errors of 1 nm shown in the right panel.

Monochromators are required to select the photon energy and to define an energy bandwidth. They are positioned downstream of M1 and consequently experience only pink beam thermal load. Being positioned close to M1 minimizes the power density on the monochromator optics. A double-crystal monochromator (DCM) using Si <111> crystals is required to provide the small bandwidth needed to achieve diffraction-limited resolution with nanofocusing diffractive optics and to allow spectroscopic studies. A double-multilayer monochromator (DMM) is required to provide a flux of roughly 25 times more at increased bandwidth for operation with reflective optics. To minimize any effects the mirror optics or monochromator optics have on the uniformity of the wavefront in the vertical direction, horizontally deflecting geometry as opposed to vertically deflecting geometry will be used. Wavefront aberrations caused by the monochromators will be corrected by spatial filtering using a BDA at approx. 60 m. In horizontally deflecting geometry, some intensity will be lost due to reduced reflectivity of the π polarized component of the incident x-ray beam. The reflectivity of the π component is 83% for a photon energy of 5 keV ($\theta_{\mathrm{Si}\,<111>} = 23°$). Given that the coherent flux increases inversely with the photon energy, this small reduction of brilliance at the low photon energies has a minimal effect on the beamline throughput.

M2 is positioned downstream of the monochromators and, as such, experiences pink beam thermal conditions (10^{-2} - 10^{-4} bandwidths). However, M2 is placed into the vertically convergent beam downstream of M1, and, as such, experiences increased power density.

High positional stability of the focused spot in the end station requires high angular stability of the beam accepted by the focusing optics. This requires high relative angular stability of the 1st with regard to the 2nd crystal of the DCM, estimated at $\sim 0.1\ \mu$rad. Similar stability is required for the DMM to provide diffraction-limited resolution and positional stability of the focal spot obtained with reflective mirror optics.

Pink beam with high total power at closed gap will impinge on the DMM and the DCM. To allow operation at 20 nm spot size, the local thermal expansion (thermal bump) of the monochromator optics needs to be minimized. This is typically achieved by cooling with liquid nitrogen (LN2). Therefore, LN2 cooled monochromators and the requisite LN2 pump is required.

6-7.4.3 Beamline Physical Layout

The ISN beamline has a length of 220, measured from the center of the straight section. It will extend well beyond the APS floor, with the ISN instrument located in a satellite station. The satellite station will be shared with the HEXM program; therefore, the final length of the ISN beamline and of the HEXM program are being determined with shared occupancy of the satellite station in mind.

Overall Beamline General Description

The scheme of the physical layout of the ISN beamline is shown in Figure 6.60. All beamline components other than the BDAs are positioned in the First Optical Enclosure (FOE) (current 19-ID-A and 19-ID-B enclosures). The FOE contains a differential pumping section to enable windowless operation, a set of white beam slits, a vertically focusing HHL mirror (M1), a double crystal monochromator and a double multilayer monochromator, and a horizontally focusing mirror (M2). The second optical enclosure (SOE) (current 19-ID-C and 19-ID-D enclosures) contain the

BDAs and the related beam diagnostics. A list of the positions of the optical elements is shown in Table 6.25.

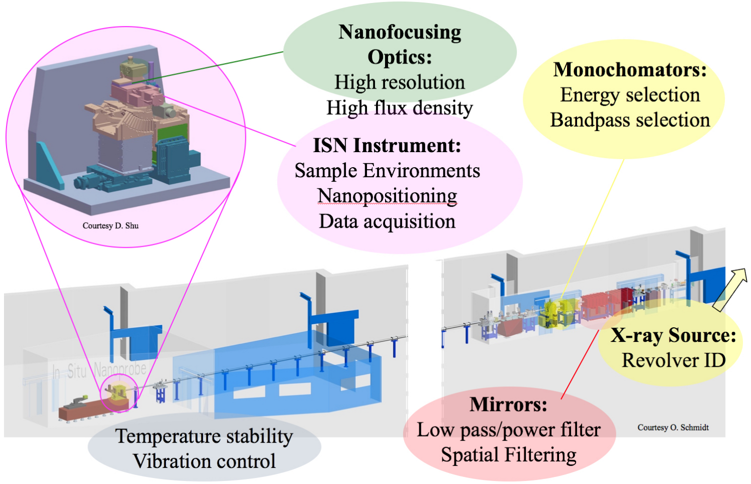

Figure 6.60. Sketch of beamline physical layout.

The FOE will be followed by a long propagation path, with the ISN instrument positioned at a distance of approximately 220 m from the source. The ISN Enclosure will be positioned as a satellite station outside the APS floor. We anticipate a length of the enclosure of approximately 10 m, to provide sufficient propagation distance between the sample and detectors used for ptychography. The satellite station must be sufficiently stable in position to angle to reduce virtual source motions caused by relative motions between BDA and ISN instruments to below 10 nm. It needs to be designed with sufficiently small vibration background. Detailed specifications will be developed with the APS engineering team.

General Description of Radiation Safety Aspects, Vacuum System

The beamline will follow all APS and APS-U radiation standards. There are not exceptional radiation requirements for the beamline.

First Optical Enclosure

The first optical enclosure corresponds to the current 19-ID-A and 19-ID-B stations. It contains a differential pumping section, a set of white beam slits, a vertically focusing high heatload mirror, a set of pink beam slits, a horizontally focusing double crystal monochromator and a horizontally focusing double multilayer monochromator, a horizontally focusing mirror, and a white beam stop.

Second Optical Enclosure

The second optical enclosure corresponds to the current 19-ID-C and 19-ID-D stations. They house the vertically aperturing and the horizontally aperturing beam defining apertures.

Table 6.25. Beamline components location

Component	**Distance to center of straight section (m)**	**Notes**
Front end exit window	N/A	Windowless front end.
Differential pumping section	25.5	
White beam slit, WBS	26.7	Define beam size and total power for mirror system.
Mirror M1	27.5	Up- or down-deflecting high-heat-load mirror. Focuses vertically on beam-defining aperture at 55 m.
Pink beam slit PBS	29	Limits beam size and total power to monochromators (DCM, DMM).
Double-crystal monochromator DCM	30	Energy selection between 4.8 keV and 30 keV, with bandwidth of 10^{-4}. Angular stability of $\sim$ 0.1 μrad between 1st and 2nd crystal.
Double-multilayer monochromator, DMM	32	Energy selection between 4.8 keV and 30 keV, with bandwidth of 10^{-2}. Angular stability of $\sim$0.1 μrad between 1st and 2nd multilayer optic.
Access to ratchet wall door	36-37.8	Access to ratchet wall door.
Mono Beam slit	41	Define beam size on M2
Mirror M2	43	Inboard or outboard deflecting high-heat-load mirror. Focuses horizontally on beam-defining aperture at 64 m.
White beam stop	43	
Beam-defining aperture, vertically aperturing, V-BDA	55	Define the vertical size of intermediate x-ray source.
Beam-defining aperture, horizontally aperturing, H-BDA	64	Define the horizontal size of intermediate x-ray source.
Exit window assembly	216	Filter boxes, shutter, exit window for ISN branch
ISN control room	TBD. Controls room must be adjacent to ISN enclosure and provide direct access.	Control room will be temperature stabilized to match enclosure temperature. Must include an anteroom to provide enclosure access. Control room must provide user access to end station.
ISN enclosure	215-225.	Enclosure must accommodate monochromatic beam. Enclosure must provide HVAC system with temperature stability of $\sim$0.1 °Cand low air flow speeds.
ISN instrument	220	ISN instrument with high-resolution focusing optics, *in situ* environment, energy dispersive detector, area detectors

Endstation

The endstation houses an exit window assembly, the ISN instrument, detectors and related electronics, and the instrument controls. The exit window assembly contains a fast shutter, absorbers, beam diagnostics, and a double Si3N4 window It further houses *in situ* equipment, including a gas handling system for reactive gases.

As part of the construction of the satellite building for the HEXM and ISN instruments, the floor of the endstation must be constructed to be positionally and vibrationally stable. Initial meetings pointed to a thickened floor underneath the ISN hutch as a promising approach. All components positioned inside the endstation must be specified/designed such that they minimize sources of vibration or heating. The HVAC system required for temperature stabilization must provide laminar flow of temperature-stabilized air. Passive cooling for all components inside the endstation is highly desired. No fans, pumps, or similar equipment should be positioned inside the endstation, or on the floor surrounding the station. In cases where that is not feasible, damping and vibrational decoupling of the equipment in question must be designed and implemented.

Instrument

The ISN instrument will use elliptically figured mirror optics to focus x-rays with large bandpass to a spot size of 20 nm. Mirrors have reflectivities between 80% and 90% across the full energy range, and therefore propagate most incident coherent photons onto the samples. Mirrors are non-chromatic, which enables spectroscopy at very high speeds, without the need to adjust optics or sample position. Mirrors also serve as low-pass filters, which allows improvement of higher-harmonics rejection—and thereby improves the detection limit—provided by upstream beamline optics. The ISN instrument will further integrate components designed to provide *in situ* environments: a heating/cooling stage to provide temperatures between 40 K and ∼500℃, a high temperature stage to provide temperatures of 1000℃or above, sample cells that accommodate flow of gases and fluids, cells optimized for high pressure, and cells optimized for application of electric fields. The ISN will be optimized for x-ray fluorescence detection. Complementary to fluorescence detection, the ISN will provide phase contrast as well as coherent diffractive imaging capabilities to allow simultaneous mapping of low-Z matrices using hard x-rays, as well as enable super resolution by deconvolving XRF maps via ptychography. The ISN will deploy “fly scanning techniques,” i.e. data acquisition while the sample moves, in XRF mode. This will allow acquisition of high-resolution maps with a large number of pixels in 2D and 3D.

To fully exploit the opportunity on non-chromatic focusing with nanofocusing mirrors, the ISN beamline is conceived as a long beamline, with a length of approximately 220 m. This allows for the achievement of a very small focal spot of 20 nm and, *at the same time*, yields very large working distances of 55 mm, which is vital to enable the wide variety of *in situ* environments required to pursue the proposed science program.

Detectors

The ISN requires energy dispersive detectors for x-ray fluorescence imaging and spectroscopy, and area detectors for diffraction and coherent diffraction/ptychography.

Energy dispersive detectors

The workhorse detector for XRF mapping and spectroscopy will be an energy dispersive, thermoelectrically cooled multi-element detector with a typical energy resolution of 125 eV at Mn K_a. To process the high incident count rate, detectors and electronics capable of processing 10^8 Photons/s or more, with minimum loss of energy resolution, are required. While the large working distance of the ISN instrument eases constraints for capturing a significant solid angle of emitted x-rays, it is still anticipated that the detector must have a “snout” that allows for positioning of the sensor close to the specimen, thereby maximizing the solid angle of detection. It is important that the detector minimize coupling of vibrations into the ISN instrument, in order to not degrade the spatial resolution achieved in scanning.

He-cooled detectors for emission spectroscopy, with an energy resolution on the order of a few eV, but very low count rate capability, are under development. These would be very suitable for emission spectroscopy if the count rate is significantly improved.

Area detectors

For ptychography, area detectors with high dynamic range and single-photon counting capability, positioned on-axis on the transmitted beam, are required. Fast scanning requires the detector to work with a very high frame rate, on the order of tens of microseconds. Therefore, multi-Kilohertz frame rates with duty cycle $> 99\%$ will be a critical parameter for the detector used in the ISN. In addition, a large dynamic range with pixel counter depth of more than 20 bits is needed for high-resolution ($\sim$nm) ptychography imaging with the new upgraded source. A large dynamic range for the pixel counter can be obtained through on-board image summation, a technique that is employed in an EIGER detector that extends the data depth from 12 bits to 32 bits. Based on the above discussion, example detectors, such as EIGER characterized by a small pixel size (75x75 μm^2), a frame rate up to 22 kHz and a small dead time between frames (4 μs) and its developing generations, can be considered in the In Situ Nanoprobe.

An auxiliary area detector on a detector arm will be used to detect diffracted x-rays from the sample and help identify the local crystallographic phase of the sample and its evolution under the change of *in situ* conditions. The detector will be positioned in one of the upper quadrants downstream of the ISN sample, either inboard or outboard. The detector will be able to capture diffracted x-rays from small angles of a few degrees to large angles of 80 degrees in the horizontal direction, and to angles of 45-60 degrees in the vertical direction. Single-photon counting is required to capture small signals from nanocrystals. The detector will be particular useful in conjunction with the broad bandpass delivered by the DMM, and, as such, must be able to process high data rates. Single-photon counting capability is not a requirement, given that Bragg peaks as opposed to scattering around Bragg peaks will be recorded.

Computing

A standard EPICS-based beamline controls system will be sufficient for the purposes of beamline controls.

For data acquisition at high speed, we anticipate the need for a dedicated controller and related controls software implementation. Fly-scanning in 2D and 3D is anticipated to require large buffer sizes, with acquisition rates of 1GB/s for XRF imaging, and 20 GB/s for ptychography. In addition, the DAQ controller must monitor sample and optics positions and correct for beam drifts. Fly scan control hardware and software will be specified in close interaction with the APS detector group and the BCDA groups. We will work closely with the Ptychoprobe beamline and the ATOMIC beamline, as well as other relevant beamlines, such as 2-ID, to arrive at solutions that have broader utility and can be efficiently supported by APS controls engineers.

Specific Safety Requirements

The ISN instrument will use fluids and gases that may pose hazards. Gases may include toxic gases. Fluids may be acidic or basic. As such, a gas cabinet and related venting system is required.

The ISN may deploy LHe-cooled beamline devices such as monochromators, which will be connected to the APS distributed LN2 system.

Specific Conventional Facilities Requirements

The ISN enclosure must be temperature stabilized, with laminar flow to minimize acoustic vibrations.

A temperature-controlled controls room is required to minimize thermal gradients. An anteroom between the controls room and hutch is required to prevent air flows when opening the hutch door.

The ISN enclosure should be positioned in an area that has very low vibration background.

Support Facilities Requirements

The anteroom to the ISN enclosure will be used for specimen mounting. Laboratory space for limited specimen preparation should be in close proximity. Lab space should also provide areas to stage and store nanofocusing optics and sensitive beamline equipment such as crystals, monochromators, detectors, environmental sample holders, and related equipment.

6-7.5 R&D Needs

The ISN beamline represents a next-generation nanoprobe, with advanced capabilities that require significant development to implement. While the ISN does not aim to achieve the smallest-possible focal spot size, the requirements of achieving 20 nm resolution at a very long working distance and under *in situ* conditions are very demanding. The challenges that need to be addressed can be classified into three topics:

(i) Provide sufficient accuracy and stability for the nanopositioning system to maintain a specimen-optics registration of 10 nm or below.
(ii) Maintain positioning accuracy under *in situ* conditions, in particular during variable temperature experiments.
(iii) Maintain registration between the ISN instrument, at ~ 180 m, and the Beam Defining Aper-

ture, at $\sim$ 60 m to prevent virtual motions of the source.

(iv) An added area of study is approaches to minimize radiation dose to the sample to the minimum number required to achieve the desired spatial resolution and elemental sensitivity. Approaches include fast shutters that open and close in synchronization with the specimen scan, prepositioning/fiducialization of the sample, and precharacterization of the sample using non-ionizing radiation.

The first challenge requires development of a nanopositioner that holds and positions a 122 mm long and 400 mm long nanofocusing mirror, and has sufficient angular and positional stability to maintain registration with the specimen to 10 nm or better. A prototype for such a system was developed by Wenjun Liu and Deming Shu, in collaboration with Barry Lai and Jörg Maser, and has been tested and implemented at APS sector 34-ID. The nanopositioning system with the JTEC mirrors system has demonstrated a spatial resolution on the order of 50 nm. R&D aimed at the ISN instrument needs to provide better than 0.1 micro-radian angular stability over extended periods.

The second challenge involves developing specimen environments that provide high positional stability under heating and cooling conditions, in particular. Barry Lai and Jörg Maser pursued development of a heating stage with gas flow under a DOE BRIDGE grant, in collaboration with Mariana Bertoni at ASU and Tonio Buonassisi from MIT. The stage demonstrated high positional stability under heating to 600 ℃, under flow of H_2S. The system was aimed at operation at the 2-ID-D beamline, which operates with a spot size of 150 nm. R&D would be focused on implementing the approaches used at MIT to develop a system capable of stability at the sub-20 nm level. Contact has also been made with Natana Inc. and Hummingbird concerning the development of both heating stages and variable temperature stages with the lowest temperatures of 10 K. Natana has developed a variable temperature stage for x-ray microscopy in the past, aimed at a spatial resolution of below 50 nm resolution, and has developed concepts for cooling to below 10 K.

The third challenge of registration the nanofocus to the BDA requires development of a concept for sensing the position of the BDA from a reference point at the ISN instrument. We consider such an approach to be relevant if the satellite station shows insufficient stability with respect to the APS experimental floor, both in regard to slow drifts or cycles, and with regard to vibrations. The sensitivity of the position of the focal spot depends on the size of the BDA, with larger BDA openings being less sensitive than smaller BDA. Before setting out on such a development we will study existing long beamlines to understand the actual displacements encountered.

Other challenges, such as development of approaches to minimize the radiation dose to the sample, are not currently anticipated to require specific R&D funding.

6-8 PtychoProbe

6-8.1 Executive Summary

The race is on for chemical x-ray imaging with nanoscale resolution. There currently are substantial efforts underway at hard x-ray synchrotron facilities worldwide that aim to improve the spatial resolution and chemical sensitivity of x-ray microscopes. The excitement of the scientific community regarding the development of these techniques is clearly evident in the ever-growing number of research teams working toward this aim. The PtychoProbe project we propose here is unique, because it will enable the world's first general user program for 5-nm focusing with ultra-fast scanning, facilitated through the APS upgrade. It will give nanoscientists unprecedented capabilities to accelerate the discovery of complex materials and establish the APS as the go-to place for hard x-ray high-resolution microscopy. There is a lot at stake in this competitive landscape. Nevertheless, the PtychoProbe beamline will guarantee U.S. leadership for years to come.

The goal of the PtychoProbe (Ptychography + Nanoprobe) beamline is to realize the highest possible spatial resolution x-ray microscopy both for structural and chemical information. The unprecedented brightness of the APS MBA lattice will be exploited to produce a nm beam of focused hard x-rays to achieve the highest possible sensitivity to trace elements. Ptychography will be used to further improve the spatial resolution for structural components to its ultimate limit. The beamline will enable high-resolution, two- and three-dimensional imaging of thick objects, bridging the resolution gap between contemporary x-ray and electron microscopy. Pushing x-ray microscopy into the nanoscale is crucial for understanding complex hierarchical systems on length scales from atomic up to meso- and macroscales, so as to be applicable to scientific questions ranging from biology, earth and environmental materials science, electrochemistry, catalysis and corrosion, and more.

6-8.2 Scientific Objectives & Capabilities

6-8.2.1 Science case for beamline

The PtychoProbe will take significant advantage of the enhancements of the APS-U source parameters. Needle-like x-ray beams with a diameter down to 5 nm will enable high-resolution, two- and three-dimensional imaging of thick objects, bridging the resolution gap between contemporary x-ray and electron microscopy. Pushing x-ray microscopy into the nanoscale is crucial for understanding complex hierarchical systems on length scales from close atomic up to meso- and macroscales.

The scientific applications of the PtychoProbe will range from biology, earth and environmental materials science, electrochemistry, catalysis and corrosion, and more. For example, the understanding and control of energy capture, conversion, and storage constitutes one of the grand challenges of society. Nano-architectured structures are expected to provide powerful solutions. However, advanced x-ray microscopes such as the PtychoProbe are needed in order to visualize related nanoscale structures, and consequently guide and improve their design. Likewise, the drive to miniaturize electronics also calls for microscopes with high-spatial resolution. The current roadmap of the semiconductor industry plans for lateral structures sizes of 5 nm in 2021. In addition to the shrinking structures sizes, controlled doping and low impurity concentrations will become very important to enhance the properties of nanoelectronics. The PtychoProbe will not only deliver the desired spatial resolution, it will also offer the required trace-element sensitivity.

6-8.2.2 Description of user community/stakeholders

The unique advantage of hard x-ray microscopy compared to other techniques is that it can provide not only chemical and structural information, at high spatial resolution, but also do so in 'thick' samples. These can be buried interfaces, complex multicomponent structures, samples in a reactor under realistic *operando* conditions, etc. The information volume accessible via x-ray microscopy is unmatched by other microscopies, and crucially important for many 'needle-in-the-haystack'-type problems. These kinds of problems typically require the highest spatial resolution, but combined with the ability to visualize a large field of view (to see the whole haystack in a reasonable amount of time). To find the needle, sufficient contrast, *i.e.*, flux density, is needed. If it is possible to approach 3D resolutions at 10 nm or below in a sample of 100s of microns and above, then the only way to access this is via hard x-ray microscopy techniques, and the PtychoProbe will push this boundary as far forward as possible. It will be the instrument to deliver the highest possible spatial resolution in complex, amorphous systems, for 'thick' objects and will bridge the resolution gap between contemporary x-ray and electron microscopy. The high penetration power of x-rays, in particular, will provide scientists a valuable and complementary tool to overcome the limitations of high-resolution electron microscopy.

The PtychoProbe will build on vast expertise developed through existing capabilities at the APS, namely the Nanoprobe beamline (sector 26), the Bionanoprobe (currently at sector 9), and the Velociprobe project (2-ID, in commissioning). It will also benefit from what has been learned at the Hard H-ray Nanoprobe (HXN) at the NSLS II, to combine instrumentational advances in x-ray microscopy with the ultimate hard x-ray source for scanning probe microscopies.

At the upgraded APS, the PytchoProbe will not exist in isolation, but in the context of other x-ray microscopy instrumentation. It will be the instrument to deliver the highest attainable 2D and 3D resolution, but will sacrifice working distance (2 mm) and therefore sample flexibility. In the context of other proposals to the APS-U, it will be complemented by the In Situ Nanoprobe (ISN), an instrument that will deliver down to 20 nm spatial resolution, but at a much increased working distance, accommodating a far wider range of *in situ* sample environments, fast scanning, and 'classical', *i.e.*, monochromator-based nanospectroscopy. On the more biological side, it would be complemented by the Bionanoprobe II, an instrument focused on mapping trace elements in biological systems, cryogenically preserved, down to 10 nm spatial resolution (as determined by radiation damage limitations). It would also be complemented by Bragg-type Coherent Diffractive Imaging, which will push the spatial resolution towards atomic length scales, but focusing on structural information (as opposed to chemical), and supporting the Bragg geometry to visualize crystal-based systems. It will be further complemented by existing micro- and nanoprobes, at spatial resolutions of about 100 nm to microns, that can address scientific questions that do not require the highest possible spatial resolution, but may have more stringent requirements on sample throughput, complex environments, or spectroscopic precision.

The PtychoProbe will be applied in fields ranging from biology to earth and environmental science, materials science, chemistry, composite materials, and well beyond. It will focus on comparatively 'radiation hard' samples and scientific questions, as outlined above. The co-authors of the proposal represent only a small fraction of the overall community, which will draw naturally upon the user base of existing micro- and nanoprobes, who wish to extend their experiments towards higher spatial resolution and improved sensitivity. At the APS, we anticipate a significant fraction of current users of 2-ID-D, 2-ID-E, 9-ID, 13-ID, 20-ID, 21-ID-D, and 26-ID to want to extend their experiments correspondingly (there will still be a very significant demand on these types of beamlines, a demand probably only limited by the available overall beam time; the PtychoProbe will simply provide an avenue through which those types of experiments can be extended to new resolution regimes). Similarly, we expect users of HXN and SRX beamlines at NSLS II that have hit the limits of those respective beamlines to want to extend their experiments by using the PtychoProbe. Furthermore, we expect that the PtychoProbe will draw numerous users from analytical electron microscopy who thus far have been unable to make use of x-ray microscopy due to limits in the spatial resolution of existing hard x-ray micro- and nanoprobes, but require the increased sensitivity of x-ray excitation and penetration depth to extend their experiments to the next level. The PtychoProbe will be the instrument of choice in both the U.S. and internationally to carry out the highest resolution hard x-ray nanoprobe experiments with both elemental as well as structural contrast.

6-8.2.3 Use of APS-U characteristics

Hard x-ray nanoprobes are purely brightness driven instruments. Therefore, the PtychoProbe will be a well-matched instrument for the APS upgrade. The source is imaged onto the sample, while the sample raster scanned through the focused beam. The spot size, s, on the sample is given by the convolution of the diffraction limited spot size s_{diff} of the optics combined with the demagnified source size s_{demag}.

$$s = \left(s^2_{\text{demag}} + s^2_{\text{diff}}\right)^{\frac{1}{2}}$$

In order to achieve diffraction-limited spatial resolution, the source therefore needs to either be sufficiently small to be indistinguishable from a point source, or fully coherent. In practice, this is achieved by using slits to spatially filter out incoherent modes, but at the cost of much reduced focused flux. For example, to achieve high spatial resolution at 2-ID-D today, typically horizontal slit settings of 80 microns are used, sacrificing 90% of the total flux of the APS in order to achieve high spatial resolution. Even if we had optics capable of 5-nm focusing today, the losses due to spatial filtering would be so large that experiments would not be feasible. Today's slow data acquisition makes it impossible to scan sufficiently large sample areas with drift between scan points for which corrections are necessary. In contrast, as the coherent flux increases by more than two orders of magnitude after the upgrade, the focused flux increases correspondingly. The extreme flux density and nanometer focused beam of the PtychoProbe will offer exquisite sensitivity to low elemental concentrations (see also Figure 6.61). In samples that are a few microns thick, it should be possible to detect concentrations as low as a few zinc atoms via x-ray fluorescence.

The second thrust for the drive toward achieving high spatial resolution is using the ptychography technique. Ptychography is a form of coherent diffractive imaging that is able to image beyond the resolution limit of a microscope's focusing optics. The sample is scanned through a focused beam of x-rays and a detector in the far-field of the sample records a coherent diffraction pattern. By ensuring that there is an overlap in the illuminated region between adjacent scan positions, it is possible to recover the complex transmission function (phase and absorption image) of the sample. The spatial resolution, given by the numerical aperture subtended by the far-field area detector, is theoretically only limited by the x-ray wavelength and can easily exceed the best focusing optics. The latter makes it an attractive candidate for pushing the frontiers of spatial resolution in x-ray

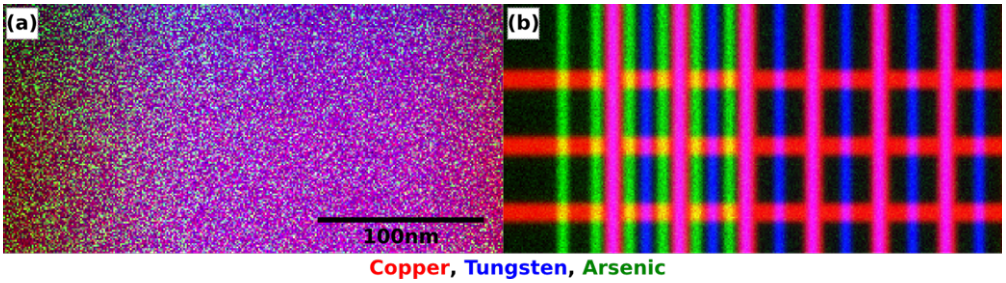

Figure 6.61. PtychoProbe Elemental Sensitivity. Simulated elemental maps of an integrated circuit with copper and tungsten wires with arsenic-doped regions. (a) Contemporary scanning nanoprobe at the APS, (b) the PtychoProbe at APS-U with 5 nm spatial resolution[10].

microscopy and is the principal reason ptychography has attracted significant development effort over the past decade. Since ptychography requires a coherent beam of x-rays, it takes full advantage of the extreme brightness of the MBA lattice. The spatial resolution of ptychography is limited in practice by the numerical aperture of the far-field diffraction pattern and the maximum tolerable dose of the sample. In this section, we assume a radiation hard sample that can withstand doses up to 10^{13} Gy. Porod's Law, well known in the small angle x-ray scattering community, states that the far-field x-ray intensity decreases as $I \propto Q^{-4}$ where I is intensity and Q is the scattering vector. Put simply, this means that an order of magnitude improvement in the spatial resolution required four orders of magnitude increase in the incident intensity. A number of authors [26, 104, 105] have developed models for the spatial resolution of coherent diffractive imaging experiments. These models agree that atomic resolution can be achieved on radiation hard samples with sufficient incident flux density. For example, in order to resolve a single Gold atom ptychographically a flux density of 3-5x10^8 ph/nm^2 is required [26, 105], by comparison we estimate focused flux densities today of 10^5-10^6 ph/s/0.01%BW/nm^2 (50 nm spot size) compared to 10^8-10^9 ph/s/0.01%BW/nm^2 (5 nm spot size) after the APS upgrade [106].

There are several efforts underway at hard x-ray synchrotron facilities both domestically and internationally that aim for chemical imaging with nanoscale spatial resolution with high chemical sensitivity. For example, in 2017, beamline ID16A at the ESRF put a high-energy beam with about 13 nm spot size at about 20 keV [107] into operation. However, nanofocusing at the 5-nm level with fast scanning would require much higher brightness only be accessible through an MBA upgrade of the source. NanoMAX in Sweden is powered by a 4th generation synchrotron source and will be a main competitor in the energy range 5-30 keV. However, NanoMAX aims for a spot size of 10 nm. Domestically, the PtychoProbe will be unique and give U.S. scientists unprecedented capabilities to accelerate the discovery and understanding of materials. There is much at stake, internationally. MBA-type upgrades at other facilities will result in a competitive landscape in which scientists and engineers will try to push the limits of ultra-fast high-resolution x-ray microscopes.

6-8.2.4 Key beamline characteristics

The PtychoProbe will operate at energies from 5-30 keV. This enables quantitative spectroscopy at the K and L edges of most transition metals and rare earth metals. Additionally, this energy range allows penetration through *in situ* and *operando* environments. In order for the PtychoProbe to realize the highest possible spatial resolution, the key requirement is to maximize the number of coherent photons on the sample per unit time. At the same time, it is necessary to maximize stability of the beamline, in order to achieve the desired spatial resolution. To achieve the latter, it is paramount to utilize a horizontally deflecting monochromator. This minimizes the degrading influence of floor vibrations, whose amplitude is always much smaller in the horizontal versus the vertical direction. The monochromator will be equipped with Si<111> and Si<311> crystals to enable the required bandwidth for 5-nm focusing over the whole photon energy range of 5-30 keV.

6-8.3 Source & Front End Requirements

6-8.3.1 Insertion Device

The PtychoProbe will directly depend on maximized coherent flux to achieve its goal of 5-nm spatial resolution (or better, using ptychographic approaches). The PtychoProbe depends on maximized focused flux so as to be able to scan samples as rapidly as possible to minimize loss of spatial resolution and sample distortions due to sample drift. An insertion device that provides maximum brilliance across energies between 5 keV and 30 keV is required. It has to deliver an overall tuning curve that should be close to continuous in order to access all relevant elemental edges.

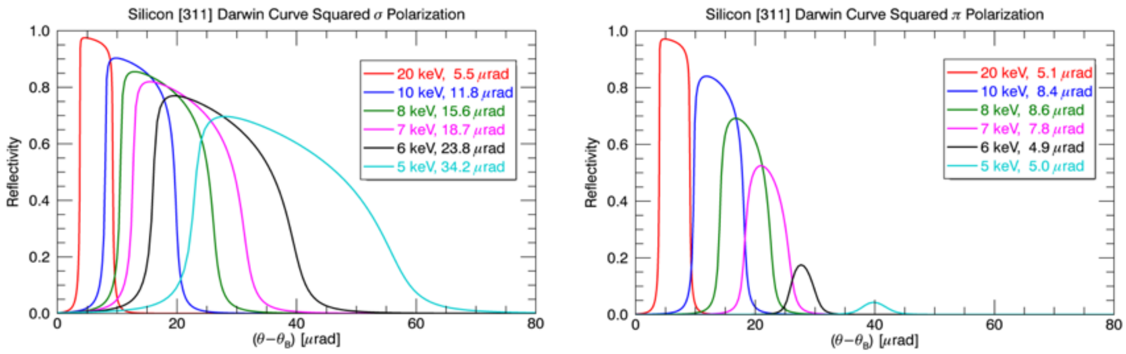

Figure 6.62. Darwin curves for silicon <311> with sigma (left) and pi (right) polarization demonstrate that only a horizontal ID is suitable for the PtychoProbe, because of the drastic polarization losses otherwise caused for low photon energies[11].

Due to the use of a stable horizontally deflecting monochromator (required for beamline stability), the PtychoProbe beamline demands a horizontal ID to achieve the required polarization that allows nanofocusing. The monochromator provides the required bandwidth for nanofocusing using the Si<311> reflection for low photon energies. Only the sigma polarization provides a suitable reflectivity for <311>, while the pi polarization would lead to drastic polarization losses (Figure 6.62). Consequently, nanofocusing with the anticipated working distance of 2 mm would be rendered impossible without a horizontal ID.

6-8.3.2 Front End Requirements

The PtychoProbe requires a windowless standard high-heat-load front end to maintain the brilliance of the beam even at low photon energies. Since the PtychoProbe utilizes the coherent part of the beam for most of its operation, the front end exit window should be as small as possible, to minimize the power load on the first optical elements in the beam path. Assuming that steering is highly stable, the exit window could be as small as 1 x 1 mm^2, corresponding to about 16 coherence lengths at a photon energy of 5 keV, or 100 coherence length at a photon energy of 30 keV.

6-8.4 Beamline Layout

6-8.4.1 Overall layout

The main goal of the PtychoProbe is to realize the highest possible spatial resolution x-ray microscopy of samples, both with structural and chemical information. In order to reach this goal, working distance between the optics and sample will be sacrificed, and the beamline will therefore only support a limited set of *in situ* and *operando* environments. Nevertheless, based on comparable working distances present in electron microscopy or soft x-ray microscopy, the PtychoProbe is expected to be able to address important high impact questions as laid out in the science case. The PtychoProbe focuses primarily on attaining the highest spatial resolution for chemical information, *i.e.*, using x-ray fluorescence contrast. This is achieved by using diffractive optics such as either Multilayer-Laue-Lenses (MLLs) or Fresnel zone plates (ZP). This information is supplemented by adding phase and absorption contrast information at spatial resolution beyond the diffraction limit via ptychography. In addition, the instrument will support ‘ptychography-poly’ mode where much larger sample areas can be scanned rapidly with a comparatively large beam (100 nm - micron sized) and ptychography is used to recover structural detail down to the nm level. Ptychography decouples the microscope’s spatial resolution from the focused beam size and extends it to the diffraction limit. Spatial resolution below 10 nm has already been demonstrated using ptychography [108, 109, 110, 111]. With the flux density that is achievable assuming even modest focusing, it may be possible to achieve atomic resolution for radiation hard samples [26, 42, 104, 105]. X-ray fluorescence (XRF) offers exquisite sensitivity for measuring elemental concentration. Collecting the photon stimulated secondary fluorescence signal with an energy resolving detector will add elemental contrast complemented by structural contrast from ptychography. When combined with ptychography, additional improvements in spatial resolution beyond the native XRF elemental maps can be achieved using deconvolution techniques [112]. In addition, the microscope can be operated in spectroscopic mode to yield chemical state contrast (chemical state mapping, by scanning a sample at well defined incident energies). Assuming the technology matures sufficiently, as seems plausible based on recent results [113], the PtychoProbe plans to incorporate superconducting spectrometers for emission spectroscopy. The ‘holy grail’ would be to combine elemental mapping with emission spectroscopy, to fully characterize chemically (elements and speciation) the sample at the 5-nm spatial resolution level.

Both diffraction-limited nanofocusing and ptychography require a high degree of coherence [114] of the x-ray beam. For the beamline design, there are two important contributions to the coherence of the beam: the source properties (size, divergence, energy, and bandwidth) and the properties and stability of the beamline optics (roughness, slope errors, heat effects, vibrations, and drift). The photon beam source properties are set by the undulator and electron beam and are not generally modified for each experiment. However, by re-imaging the source onto a secondary-source aperture (SSA), or beam-defining aperture (BDA), the spatial coherence of the transmitted beam can be manipulated. As a matter of fact, even the best optics have some imperfection and unwanted motions, but these can be mitigated by the SSA because it acts as a spatial filter to produce a stable wavefront. Vibrations in the optics upstream of the SSA therefore only affect focused flux (i.e., they lead to intensity fluctuations), as opposed to apparent source motions (i.e., a smeared-out focus spot size).

With these goals in mind, a preliminary design has been developed (Figure 6.63) that offers the flexibility to image a broad range of samples with the highest possible simplicity for ease of alignment and use. The PtychoProbe beamline employs a simple but ultra-stable design that combines the flexibility of a single endstation to accommodate both the highest spatial resolution (∼5-nm) focusing optics as well as high flux optics that can be used for fast overview scans to determine target areas for high-resolution scanning. A ptychography-only mode will be used when only structural information is desired. The energy range of 5–30 keV was chosen to cover a broad range of spectroscopic edges from elements of interest and make use of the increased coherent beam fraction at lower energies. The upgraded APS will be able to run in two different modes. The beamline design will be optimized for the high brilliance mode. In high brightness mode, the beam will essentially be elliptic, in timing mode, much closer to round. In order to perform well in both modes of operation, be able to potentially accommodate future possibly different operational modes, and be able to accommodate different set of optics that permit one to trade spatial resolution vs. focused flux, the beamline will be capable of re-imaging the source onto a SSA at two different locations using bendable mirrors. The two SSAs will be located at 40 m and 60 m from the source, but only one will be used at a time. The 60 m SSA was chosen to maximize stability and achieve the highest resolution nanofocusing, whereas the 40 m SSA was chosen to maximize the working distance. The longer working distance can be used to accommodate *in situ* environments as well as larger samples for ptychography-only mode. There will be no optical elements between the SSA and nanofocusing optic so as not to disturb the wavefront or introduce instability.

The beamline front end will be designed for windowless operation capable of handling the heat load from the undulator(s). An exit mask will limit the total power entering the first optical enclosure. The exit mask will be followed by a pair of crossed white beam slits designed to further limit the power on the first optical component. A pair of dynamically bendable mirrors, M1 and M2, will be used to focus the beam onto either of the two SSA positions. Following the horizontally focusing mirror M1, the beam will pass through a horizontally deflecting monochromator with LN2 side-cooled Si crystals with small offset for optimal angular stability. The monochromator will house a pair of Si<111> and Si<311> crystals to fulfill the required bandwidth needs of the PtychoProbe. The horizontally deflecting geometry is used to minimize vibrations. Based on previous experience, e.g. at NSLS II, horizontally deflecting monochromators are significantly more stable than those that offer vertical deflection. The monochromator is used to select the monochromaticity required by the nanofocusing optic and to match the longitudinal coherence length of the beam to the sample. The monochromator bandwidth is adjusted by choosing either the <111> or <311> reflections, which provide $dE/E \sim 10^{-4}$ and $dE/E \sim 10^{-5}$, respectively. In addition to the double-crystal monochromator (DCM), a double-multilayer monochromator (DMM) is used to provide a relatively wide-energy bandpass beam. This supports many ptychography experiments in which higher flux is preferred to speed up data collection and improve the signal to noise ratio. The combination of two monochromators (DCM/DMM) provides rapid switching between high resolution and high flux modes. The first secondary-source aperture (SSA1) is mounted on a stable granite block at 40 m from the source. It will be actively water-cooled to maintain a constant temperature and to minimize drifts. During operation, M1 and M2 will project an image of the source demagnified by 3:1. The SSA1 aperture will be approximately 3x3 mm^2. A feedback system involving a diagnostic measurement (BPM1) on the upstream side of SSA1 will be used to keep the beam focused on the aperture. The feedback will dynamically adjust the angle and curvature of M1 and M2. When not being used, the SSA1 aperture, as well as BPM1, will be opened and the beam will pass through without modulation.

The nanofocusing optic (NFO) in the PtychoProbe endstation will be located approximately 70 m from the source. The endstation enclosure will be approximately 20 m in length. The alternative secondary-source aperture (SSA2) will be located 60 m from the source. This is 10 m upstream of the NFO, but installed on the same granite block (or other solid support with similar stability properties). Having SSA2 and NFO on the same granite support will reduce the relative motion, greatly increasing stability of the experiment. When SSA2 is being used, the mirrors M1 and M2 will re-image the source 1:1 (no demagnification), requiring an aperture of 10x10 μm^2. A diagnostic measurement (BPM2) upstream of SSA2 is used to operate an active feedback that controls angles and curvatures of M1 and M2. The relative positions of SSA2 and NFO are also measured in order to develop an additional feedback that can minimize the influence of long-term drifts. Such long-term drifts have to be anticipated, even when SSA2 and NFO are housed on the same granite support. The PtychoProbe endstation instrument will utilize a vacuum chamber containing the optics and sample. Operation in vacuum will increase the longevity of all NFOs and also minimize the influence of acoustic noise. Further, it will enhance the quality of XRF measurements through background reduction. Nevertheless, the vacuum chamber still allows operation under atmospheric pressure and in gas environments that do not harm the components of the microscope (Ar, He, N_2, etc.). A modular 5 m-long vacuum flight tube will connect the endstation to a direct detection photon counting pixel array detector that will record the coherent diffraction patterns required for ptychography. The modular flight tube will allow camera distances between 1 and 5 m.

The expected coherent flux of the PtychoProbe is shown in Figure 6.64. The calculations assume a 4.8 m insertion device using the 1st (2.3 cm) and 3rd (2.7 cm) harmonic. The reflectivity of the beamline mirrors is included in the calculations. The Si <111> reflection will provide a coherent flux onto the nanofocusing optics that ranges from about 2x10^{13} ph/s at 5 keV to 1x10^{11} ph/s at 30 keV. Likewise, <311> will yield about 5x10^{12} ph/s to 2x10^{10} ph/s. Obviously, the flux obtained by the <311> reflection is significantly smaller, but for low photon energies up to about 10 keV, it is mandatory to use the much smaller bandwidth of this reflection to obtain diffraction limited focusing. Note that the flux on the sample has to be adjusted using the actual efficiency of the NFO that will be used.

Description of optical components

The use of stable and precise x-ray optics is vital for a full utilization of the high coherence and brightness of the upgraded APS. A horizontally focusing mirror (M1) and vertically focusing mirror (M2) will be utilized to focus the beam onto either SSA1 or SSA2. The mirrors need to be supported such that vibrations and drift are minimized. Vibrations of beamline optics can severely affect the path of x-rays. Mitigation of vibrations are therefore vital for beamline design and development. The PtychoProbe aims for spatial mirror stability on the order of micrometers. The first mirror, M1, will accommodate high heat load using LN2 cooling. Any potential heat-related issue will thus not significantly impact the vertical beam direction, in which the source size is smaller. Additionally, a mirror system is less complex than a monochromator, which also supports its location as the first optical component under high heat load. This approach increases the overall beamline stability. Following M1, the beam will pass through a horizontally deflecting monochromator with LN_2 side-cooled Si crystals with small offset for optimal angular stability. Side-cooling is sufficient since M1

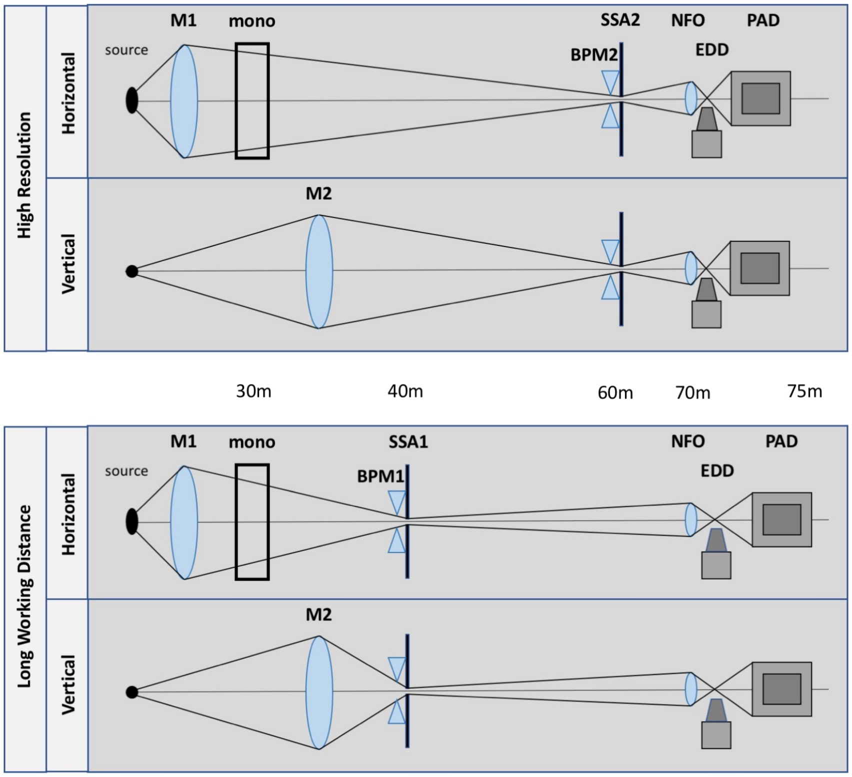

Figure 6.63. Optical layout of the PtychoProbe Beamline. In High Resolution mode (top) x-rays from the source pass through a horizontal monochromator and are focused by mirrors M1 and M2 (∼30m) onto a secondary-source aperture SSA2 (60m) from which point the beam propagates to the nanofocusing optic NFO (70m) and finally to a movable pixel-array detector PAD (71-75m). In Long Working Distance mode (bottom) SSA2 is removed from the beam path. Mirrors M1 and M2 refocus the beam onto SSA1 (40m). Energy dispersive detectors EDDs are utilized for the detection of x-ray fluorescence from the sample (EDD in backscattering geometry not shown). Beam position monitors (BPM1,2) are used as diagnostic tools to keep the optics focused onto the SSA1 or SSA2.

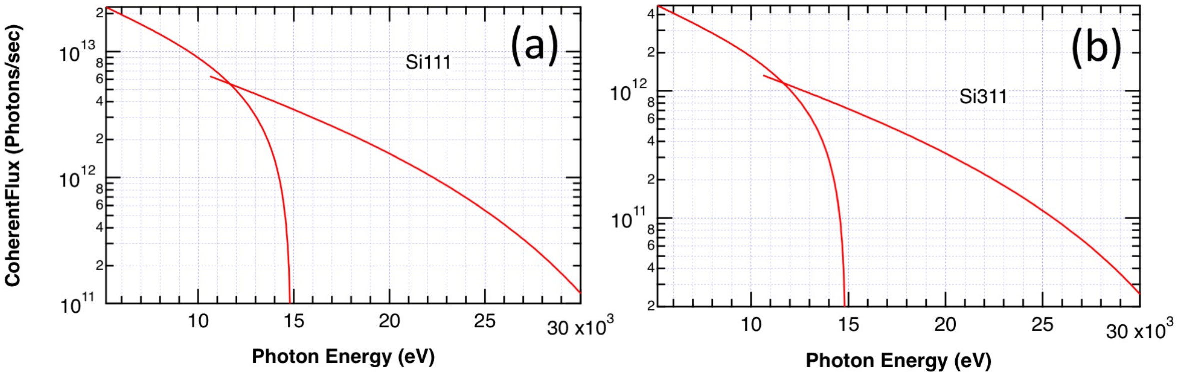

Figure 6.64. Calculations of the coherent flux of the PtychoProbe beamline. (a) The Si<111> reflection will provide the highest flux. (b) The Si<311> reflection will reduce the beamline flux, but it will offer the small band width necessary for 5-nm focusing at low photon energies. Note that the actual flux on the sample has to be adjusted by including the efficiency of the nanofocusing optics.

has removed substantial heat load already. The monochromator is used to select the monochromaticity required by the nanofocusing optic and to match the longitudinal coherence length of the beam to the sample. The monochromator bandwidth is adjusted by choosing either the <111> or <311> reflection which provide approximately $dE/E=10^{-4}$ and $dE/E=10^{-5}$, respectively. Using multiple crystals in the monochromator could potentially influence the stability. Therefore, care has to be taken to develop a stable platform. It should also be noted that the flux will scale with the bandwidth, i.e., the flux will be significantly smaller for <311> as shown in Figure 6.64.

A detailed calculation of the bandwidth (natural and bandwidth broadening due to the horizontal divergence with a 1:1 demagnification horizontal focusing mirror) is shown in Table 6.26. For low photon energies, up to about 10 keV, the <311> will be utilized to fulfill the bandwidth requirements of the nanofocusing optics. For larger energies, the band width of <111> will be sufficient. Generally, the broadening increases for high energies. However, since diffractive optics for higher photon energies have fewer zones, this will not impact the performance of the PtychoProbe.

While in the high-resolution mode of the PtychoProbe, strict bandwidth requirements have to be fulfilled to achieve a 5-nm focused spot. The bandwidth of the <111> reflection is suitable for the entire energy range in the long working distance mode (3:1 demagnification). Here, nanofocusing optics with a focal spot size of about 20 nm will be utilized. In this mode, the increased working distance will provide the opportunity for more flexible *in situ* and operando measurements. The calculated resulting bandwidth for a source image demagnified by 3:1 is shown in Table 6.27.

The nanofocusing optic in the PtychoProbe endstation will be located approximately 70 m from the source. We anticipate that diffractive optics such as either Multilayer-Laue-Lenses (MLLs) or Fresnel zone plates (ZP) will be able to provide the goal focus spot size of about 5 nm (or about 20 nm in long working distance mode). In high resolution mode, the working distance has to be at least 2 mm or larger to accommodate a limited set of *in situ* and operando capabilities. Based on previous R&D carried out through an SBIR by Hummingbird Inc. and Rose et al., a working distance smaller than 2 mm would not be possible in an x-ray microscope using ZP or MLL optics.

Table 6.26. Calculation of the natural bandwidth and the broadening due to the horizontal divergence for Si<111> and Si<311>. Results for the two expected operational synchrotron modes are presented. The <311> reflection provides the required bandwidth for the nanofocusing optics in the high-resolution mode at low energies

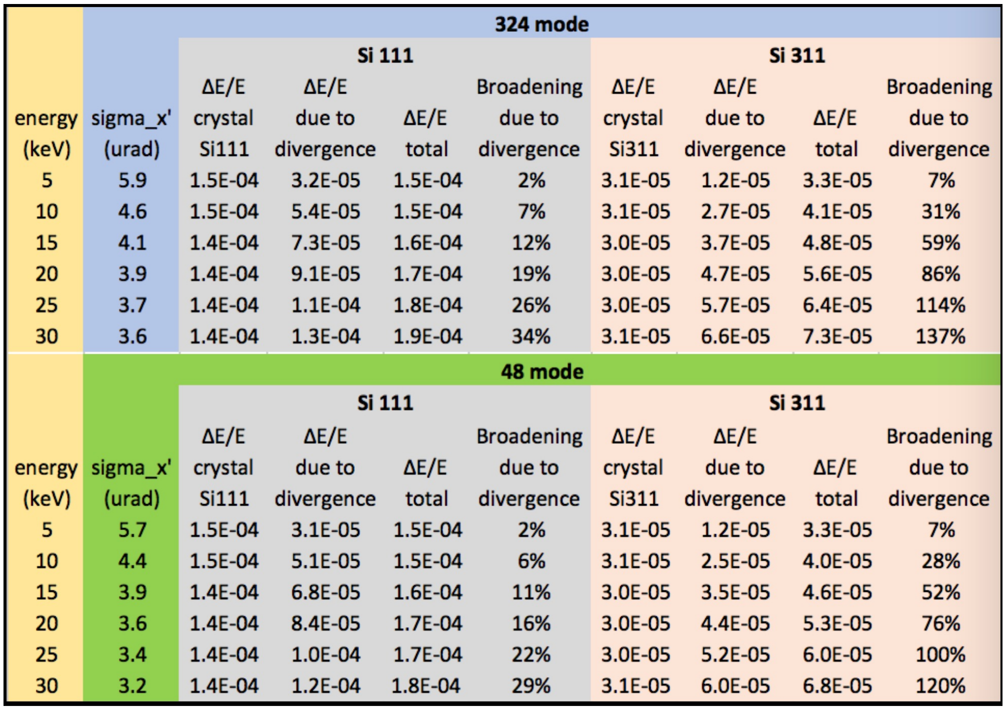

		324 mode							
		Si 111				**Si 311**			
energy (keV)	sigma_x' (urad)	ΔE/E crystal Si111	ΔE/E due to divergence	ΔE/E total	Broadening due to divergence	ΔE/E crystal Si311	ΔE/E due to divergence	ΔE/E total	Broadening due to divergence
5	5.9	1.5E-04	3.2E-05	1.5E-04	2%	3.1E-05	1.2E-05	3.3E-05	7%
10	4.6	1.5E-04	5.4E-05	1.5E-04	7%	3.1E-05	2.7E-05	4.1E-05	31%
15	4.1	1.4E-04	7.3E-05	1.6E-04	12%	3.0E-05	3.7E-05	4.8E-05	59%
20	3.9	1.4E-04	9.1E-05	1.7E-04	19%	3.0E-05	4.7E-05	5.6E-05	86%
25	3.7	1.4E-04	1.1E-04	1.8E-04	26%	3.0E-05	5.7E-05	6.4E-05	114%
30	3.6	1.4E-04	1.3E-04	1.9E-04	34%	3.1E-05	6.6E-05	7.3E-05	137%
		48 mode							
		Si 111				**Si 311**			
energy (keV)	sigma_x' (urad)	ΔE/E crystal Si111	ΔE/E due to divergence	ΔE/E total	Broadening due to divergence	ΔE/E crystal Si311	ΔE/E due to divergence	ΔE/E total	Broadening due to divergence
5	5.7	1.5E-04	3.1E-05	1.5E-04	2%	3.1E-05	1.2E-05	3.3E-05	7%
10	4.4	1.5E-04	5.1E-05	1.5E-04	6%	3.1E-05	2.5E-05	4.0E-05	28%
15	3.9	1.4E-04	6.8E-05	1.6E-04	11%	3.0E-05	3.5E-05	4.6E-05	52%
20	3.6	1.4E-04	8.4E-05	1.7E-04	16%	3.0E-05	4.4E-05	5.3E-05	76%
25	3.4	1.4E-04	1.0E-04	1.7E-04	22%	3.0E-05	5.2E-05	6.0E-05	100%
30	3.2	1.4E-04	1.2E-04	1.8E-04	29%	3.1E-05	6.0E-05	6.8E-05	120%

Table 6.27. Calculation of the bandwidth and the broadening due to the horizontal divergence for a demagnification of 3:1 as used in the long working distance mode of the PtychoProbe. Here, the <111> reflection provides the required bandwidth

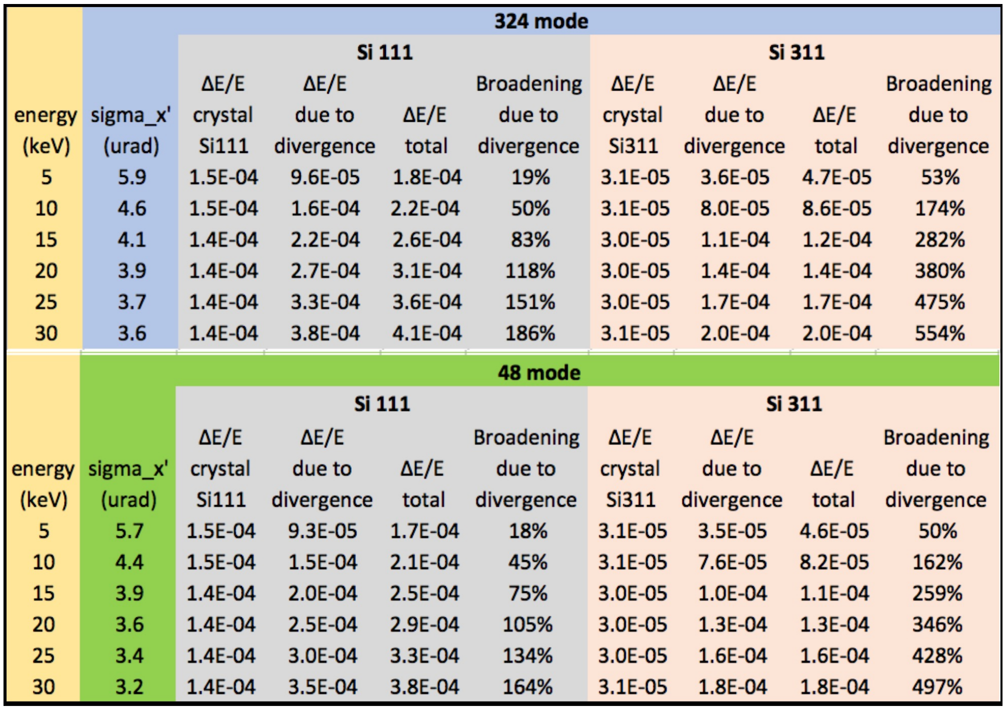

		324 mode							
		Si 111				Si 311			
energy (keV)	sigma_x' (urad)	ΔE/E crystal Si111	ΔE/E due to divergence	ΔE/E total	Broadening due to divergence	ΔE/E crystal Si311	ΔE/E due to divergence	ΔE/E total	Broadening due to divergence
5	5.9	1.5E-04	9.6E-05	1.8E-04	19%	3.1E-05	3.6E-05	4.7E-05	53%
10	4.6	1.5E-04	1.6E-04	2.2E-04	50%	3.1E-05	8.0E-05	8.6E-05	174%
15	4.1	1.4E-04	2.2E-04	2.6E-04	83%	3.0E-05	1.1E-04	1.2E-04	282%
20	3.9	1.4E-04	2.7E-04	3.1E-04	118%	3.0E-05	1.4E-04	1.4E-04	380%
25	3.7	1.4E-04	3.3E-04	3.6E-04	151%	3.0E-05	1.7E-04	1.7E-04	475%
30	3.6	1.4E-04	3.8E-04	4.1E-04	186%	3.1E-05	2.0E-04	2.0E-04	554%

		48 mode							
		Si 111				Si 311			
energy (keV)	sigma_x' (urad)	ΔE/E crystal Si111	ΔE/E due to divergence	ΔE/E total	Broadening due to divergence	ΔE/E crystal Si311	ΔE/E due to divergence	ΔE/E total	Broadening due to divergence
5	5.7	1.5E-04	9.3E-05	1.7E-04	18%	3.1E-05	3.5E-05	4.6E-05	50%
10	4.4	1.5E-04	1.5E-04	2.1E-04	45%	3.1E-05	7.6E-05	8.2E-05	162%
15	3.9	1.4E-04	2.0E-04	2.5E-04	75%	3.0E-05	1.0E-04	1.1E-04	259%
20	3.6	1.4E-04	2.5E-04	2.9E-04	105%	3.0E-05	1.3E-04	1.3E-04	346%
25	3.4	1.4E-04	3.0E-04	3.3E-04	134%	3.0E-05	1.6E-04	1.6E-04	428%
30	3.2	1.4E-04	3.5E-04	3.8E-04	164%	3.1E-05	1.8E-04	1.8E-04	497%

An example for suitable zone plate parameters that might be utilized at the PtychoProbe is shown in Table 6.28. The ZP is illuminated by a source with intrinsic bandwidth. Since ZPs are based on diffraction, the performance is sensitive to the source bandwidth. In order to achieve diffraction-limited performance and obtain the desired small spot size at low energies, the narrow bandwidth of the <311> monochromator reflection will be used.

6-8.4.2 Beamline Physical Layout

Overall Beamline

The beamline consists of two long experimental enclosures. The First Optical Enclosure (FOE) will house a pair of slits to reduce the beam power, two mirrors that will focus the beam on either of the two secondary-source apertures, a horizontal deflecting DCM for optimal vibrational stability, photon and bremsstrahlung stops, a monochromatic shutter, and finally, a beam position monitor together with the first secondary-source aperture. The secondary-source aperture will be mounted on a granite table for additional stability.

The experimental station in the second enclosure will house a large 10-m long granite base (or similar stable support), where a beam position monitor and the second secondary-source aperture will be mounted, as well as the PtychoProbe endstation instrument. A detector for ptychography will be located downstream of the endstation instrument, connected to a variable-length evacuated flight pass. Fluorescence detectors will be located perpendicular to the beam in the sample plane.

Table 6.28. Zone plate parameters for optics with 5 nm resolution limit (drN = 4 nm) maintaining the minimal working distance of 2 mm

	5 keV	10 keV	30 keV
ZP diameter	300	150	50
Focal length/Working distance	6 mm/2 mm	6 mm/2 mm	6 mm/2 mm
Number of zones	11,250	7,500	2,500
Depth of focus [microns]	0.25	0.5	1.4
Bandwidth requirement	3×10^{-5} (requires monochromaticity of <311>)	6×10^{-5} (ok for Si <111>, but better with <311>)	2×10^{-4} (ok for Si <111>)

Likewise, a superconducting spectrometer for emission spectroscopy will be installed. The large granite base will minimize the relative motion between all components, again increasing stability. In addition, stringent environmental controls on the order of variations of less than 0.1 degree per a 24 h period, should be maintained in the enclosure areas to prevent thermal expansions of components. This is roughly equivalent to the linear expansion of a 10-cm stainless steel support by 4 nm per hour. The type of each primary component with location is shown in Table 6.29.

Table 6.29. Component Reference Table. The source point is given by the center of the ID straight section

Location (m from source)	Component
25.4	FE Exit Mask
26.2	FE Collimator
26.8	WB Slits (upstream)
27.5	WB Slits (downstream)
28.8	Focusing Mirror
30.4	Photon Mask
31.2	W Collimator
32.3	Horizontal-bounce DCM
33.9	Focusing Mirror
37.6	White Beam Stop
37.8	Bremsstrahlung Stop
38.3	Mono Shutters
40.0	Beam Position Monitor
40.0	Secondary Source Aperture
60.0	Beam Position Monitor
60.0	Secondary Source Aperture

First Optics Enclosure and Infrastructure

Due to the operational requirements of this beamline, the number of beryllium windows will be minimized to achieve adequate flux and reduce the influence of potential phase objects caused by windows. As stated earlier, the PtychoProbe will utilize a windowless differential pumping exit table. APS requirements state that for a windowless beamline, a residual gas analyzer must be installed and monitored in the FOE to prevent accidental contamination of the front end and/or storage ring. The front end exit table will be supplied with a standard tungsten collimator; however, in order to achieve the low monochromator offset required (25 mm or below), another tungsten collimator will likely need to be added just upstream of the monochromator. Detailed bremsstrahlung ray tracing will be done to determine exact specifications.

A high-heat-load slit design will be used for this application. It is capable of withstanding the heat loads generated by the horizontal undulator. The beamline will utilize two secondary-source apertures (SSA1 and SSA2) with beam position monitors (BPM1 and BPM2) as secondary sources that are imaged onto the sample. The SSAs will consist of a pair of water-cooled slits in both horizontal and vertical directions. Any mirror and monochromator vibrations then become intensity fluctuations, as opposed to position movements. Changes in intensity can be corrected via a M1 (M2) feedback system using BPM1 (BPM2) to overcome long-term thermal drifts. Vibrations or drifts of the slits itself have to be controlled as well. These would lead to a position movement of the focused beam on the sample. A shift of an SAA by the amount of the slit size would translate the focused beam by the equivalent of the focused spot size. Thus, the horizontal and vertical vibrational stability of the slits should be better than 10% of the slit size, i.e., 300 nm for SSA1 and 1000 nm (peak to peak) for SSA2. SSA1 will be located in the FOE, while SSA2 will be located in the endstation hutch.

A horizontally focusing mirror will be the first optical component. In order to accommodate the high heat load, cryogenic cooling is required. The mirror has to enable stable focusing into the two secondary-source apertures. Vibration of the mirror as well as thermal drifts have to be minimized. In order to achieve the highest possible stability, a horizontal monochromator will be utilized. It will house two cryo-cooled crystal pairs next to each other with <111> and <311> cut. This will provide the required bandwidth for the nanofocusing optics in the endstation instrument (Si<111> for 10^{-4} bandwidth, and Si<311> for 10^{-5} bandwidth). A vertically focusing mirror located downstream of the monochromator will focus the beam into the two secondary-source apertures. Water cooling of the mirrors is anticipated. Vibration of the mirror as well as thermal drifts have to be minimized. The movable segmented beam-position monitors will be located upstream of the secondary-source apertures in order to characterize vertical, horizontal, and angular displacements of the beam. An active feedback control of the focusing mirrors will be implemented to correct for temperature drifts. This allows for maximization and stabilization of the amount of coherent flux passing through the SSAs. Movable fluorescence screens will be located behind the mirrors and the monochromator as well as upstream of the secondary-source apertures. These will serve alignment procedures. The locations of SSA1 as well as SSA2 relative to the NFO will be monitored, e.g., using laser interferometry. These diagnostics enable a feedback between the SSAs and the focusing optics to control slow thermal drifts.

The PtychoProbe will not utilize monochromatic beam alone, therefore a photon and bremsstrahlung stop will be installed in the FOE downstream of the monochromator and mirrors.

Endstation Components

The secondary-source aperture SSA2 and the movable beam position monitor (BPM2) will be located in the endstation hutch. There will be one Be window necessary at the exit of the end station prior to the detector flight pass. This will be a monochromatic window and will not see excessive heat loads.

Instruments

The PtychoProbe's goal of achieving the highest possible spatial resolution coupled with the APS-U photon flux puts significant constraints on the instrumental design. The high spatial resolution necessitates an extremely stable instrument, minimizing the effect of environmental disturbances. At the same time, the drastically increased flux necessitates a fast and efficient instrument to minimize on-sample dosage, preventing radiation damage. As a significant benefit, the resulting fast scanning reduces overall measurement time and minimizes the effects of instrument drift.

In order to address these criteria, four main areas will be considered during the design: 1) a stable instrument platform, 2) an advanced control system, 3) fast scanning mechanics, and 4) stable optics-to-secondary-source positioning. It is critical that the fast scanning mechanics and control system be considered together at the point of design. This is to avoid bandwidth- and stability-limiting constraints that can be imposed on the system. In addition, the stability of the secondary-source apertures will be directly linked to the instrument to minimize relative motion. Some of these approaches are already under development as part of the Velociprobe LDRD project. Some concepts will require additional R&D beyond the Velociprobe.

Current scanning x-ray microscopes are based on, fine-motion piezo stages mounted on stacks of coarse-motion stepper motor stages. Feedback is provided by fiber-coupled interferometry. Scanning control is typically done with a Delta-Tau (or similar) controller. These systems are limited in scanning rate and disturbance rejection by low frequency resonances; they have low mechanical bandwidth. The low frequency resonances make the instruments sensitive to environmental vibrations while the low bandwidth renders disturbance rejection from the control loop effective only at very low frequencies ($\sim$10 Hz). If we are to take full advantage of the APS-U, a new type of instrument will be required.

For the first area, the stable instrument platform will be comprised of coarse motion stages constructed from granite or other engineering material with low thermal expansion. These mm-travel-range stages form the instrument base, align the instrument to the beam, align the optics to the sample axis, position the area of interest in the beam, and provide for focal length change across the 5-30 keV energy range. A novel integrated air bearing design allows the stages to have granite-to-granite contact when in position, providing the most stable instrument platform. Figure 6.65 shows recent measurements of the relative motion between the x-ray optic position and the sample position on the Velociprobe instrument. The relative motion transverse to the beam is extremely low, with the vertical motion being less than 1 nm rms and the horizontal motion being 1.4 nm rms on a 5-100 Hz bandwidth. This result is despite being less than 2 m from a mezzanine support column, a known transmitter of utility system vibration.

In the second area, the control system will use both advanced feedback and feed-forward techniques.

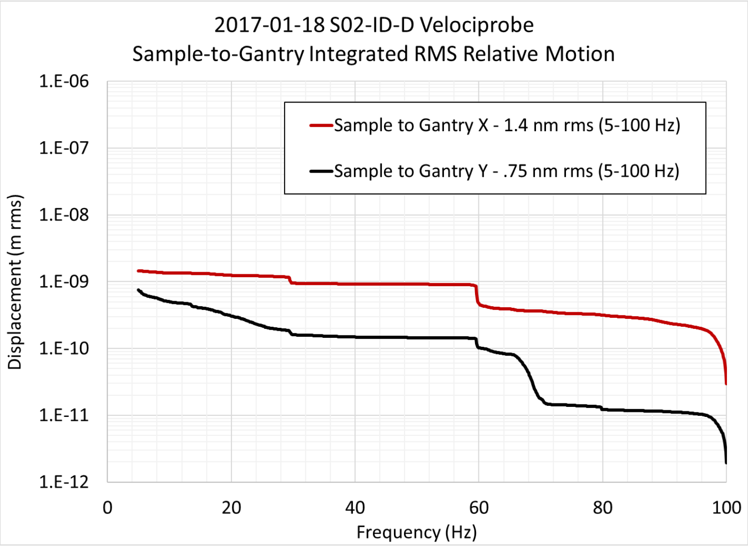

Figure 6.65. Chart showing the relative motion between the Velociprobe sample position and the optics gantry. This level of relative motion in a stage system is very low, in a range typically associated with very short distances on rigid structure.

State of the art fiber-coupled interferometry will be used to accurately measure the sample, zone plate, and secondary-source position feedback. Robust feedback control techniques will maximize the ability of the system to reject external disturbance, mitigate system vibrations, and control system dynamics. The feedforward control will increase system bandwidth. The resulting system performance and accurate position metrology will enable more efficient scanning techniques such as Lissajous trajectories. The scanning controller(s) will be implemented on a field-programmable gate array (FPGA), such as those available from National Instruments or other manufacturers. All other motion control can be handled with a conventional motion controller, an example of which is a Delta Tau controller like those used by the Bionanoprobe and Velociprobe.

The scanning control and mechanics need to be considered as a system and designed together. Recent work on the Velociprobe scanning control show that significant gains in bandwidth, stability, and resolution can be achieved with an FPGA-based H-infinity control algorithm design. Figure 6.66 shows measured results from a positioning resolution experiment on the Velociprobe scanning stage. Sub-nanometer positioning resolution can be achieved with this scanning stage and controller, and a similar performance can be expected for systems used in the PtychoProbe. In addition, the controller also increased in the bandwidth at which a particular scan trajectory can be tracked for a given amount of error. Furthermore, the scanning controller design process allows the bandwidth, noise rejection, and tracking error to be quantified *a priori*. For the PtychoProbe, integrated design of the scanning system and controller will ensure the best possible performance.

Finally, special attention should be paid to the relative stability of the sample, zone plate optics, and SSA. The SSA for the high-resolution mode will be located 15 m upstream of the sample. The relative motion between these two points will influence the resolution of the instrument. Figure 6.67 shows the floor motions in the X and Y directions, both the absolute, and the relative motion between two points 18 m apart.

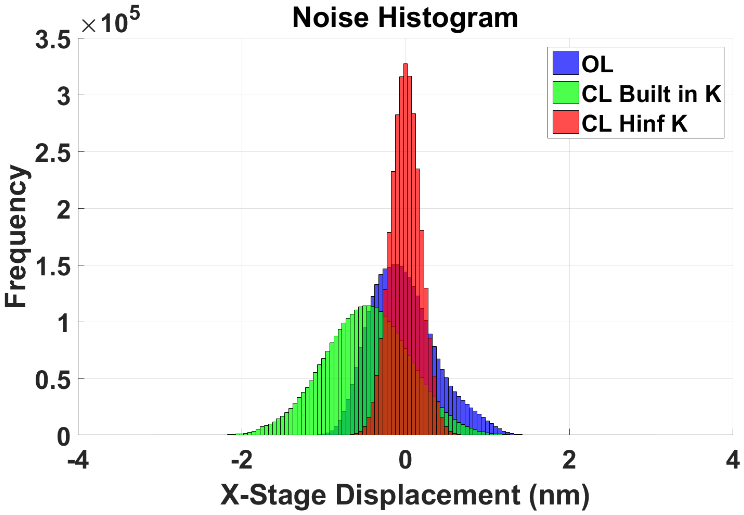

Figure 6.66. Comparison of the resolution of the Velociprobe nanopositioning scanning stage for three different types of control algorithms. The data were acquired with zero input to the system, and the resulting measured output is attributed solely to system and environmental noise. The histograms are: blue – the open loop system, green – closed loop system using the manufacturer supplied controller, and red – a FPGA-based H-infinity controller. The positioning resolution is defined as 3σ. The open loop, built-in, and H-infinity algorithms resulted in 1.6 nm, 1.2 nm, and 0.5 nm resolution, respectively. This shows that sub-nanometer resolutions are achievable.

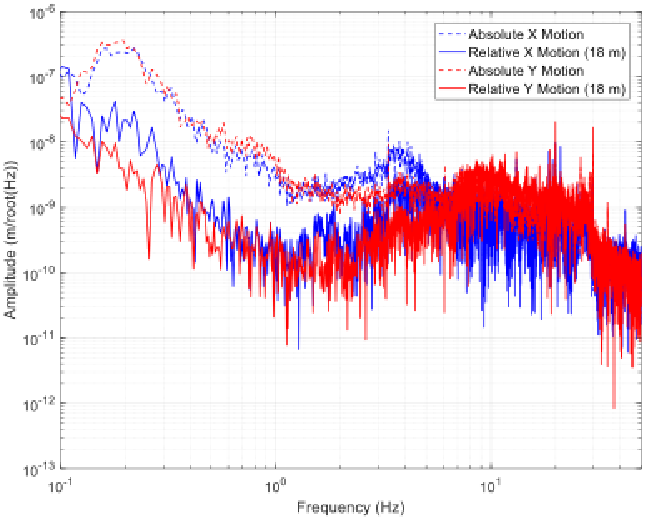

Figure 6.67. Chart showing both the absolute floor motion in the X and Y directions and the relative floor motion between two points separated by 18 m (slightly longer than the SSA to sample distance in the PtychoProbe) in the APS storage ring tunnel. From .1 to about 8 Hz, the relative motion is much less (∼10x) than the absolute motion. This is very good, as the absolute floor motion is quite large in this same range. On the other hand, above 10 Hz, the relative motion is the same or larger than the absolute motion.

These numbers vary somewhat around the facility and the data shown are from the storage ring tunnel, which likely behaves somewhat better than the experimental hall floor. Measurement at the final beamline location and compensation of these relative motions are necessary to achieve the required instrument performance.

6-8.4.3 Additional

Detectors

Area detector. The performance of detectors plays an important role in ptychography. Parameters like single-photon precision, single-pixel point-spread function, no readout noise, and high dynamic range are critically important to high precision ptychography with few nanometers resolution. In order for the PtychoProbe to realize the highest possible spatial resolution, single-photon-counting detectors will be employed for ptychography experiments. The resultant focused flux density will be increased by five orders of magnitude through increased coherent flux by the APS Upgrade, improved optic efficiency, and smaller spot size (down to 5 nm), and therefore the exposure time per diffraction frame can be greatly reduced. Using fast scanning, this requires the detector to work with a high frame rate. With 10^8-10^9 ph/s /nm^2 after the APS upgrade, the exposure time can be reduced to tens of microseconds. Therefore, multi-Kilohertz frame rates with duty cycle $>$ 99% will be a critical parameter for the detector used in the PtychoProbe. In addition, large dynamic range with pixel counter depth of more than 20 bits is needed for high-resolution ($\sim$nm) ptychography imaging with the new upgraded source. Two types of pixelated area detector can be considered for the PtychoProbe: one is a photon counting detector which has good dynamic range but has its performance limited by the count range. Based on the data from current and future beam source, a count rate better than 10^9 ph/s is needed for ptychography using the upgraded beam source. The other is a photon integrating detector which does not have a count rate limit, but has limited dynamic range. The limited dynamic range issue needs to be solved if a photon integrating detector is considered for the PtychoProbe. For example, a semi-transparent beam stop can be added in front of the photon integrating detector so as to increase the dynamic range. A large dynamic range for the pixel counter can be obtained through on-board image summation, a technique that is already employed today in some detectors that extends the data depth from 12 bits to 32 bits.

Based on the above discussion, detectors with a frame rate of 3 kHz and a small dead time between frames (3 μs or better) can be considered for the PtychoProbe. In addition to the dynamic range and the frame rate, the detector has to offer a suitable pixel number, pixel size, and distance from the sample. For example, with a probe size of 5 nm and a resolution pixel size in the reconstruction of 0.5 nm, a detector with a pixel size of 75x75 μm^2 and 512 pixels has to be located only 155 mm downstream of the sample at 10 keV. This arrangement would provide a suitable oversampling ratio of 51; simulations without noise show that a reconstruction converges when the oversampling is 10 or larger. Thus, for a small beam the oversampling requirement for ptychography reconstructions is easy to meet. In the long working distance mode, the PtychoProbe will utilize a probe size of about 20 nm. This will increase the detector distance up to about 5 m. The respective detector distances for a 5-nm and 20-nm probe size are shown in Figure 6.68. Depending on the NFO and desired resolution, the distance ranges between a few centimeters and 5 meters. Therefore, the detector will be connected to an adjustable-length flight pass.

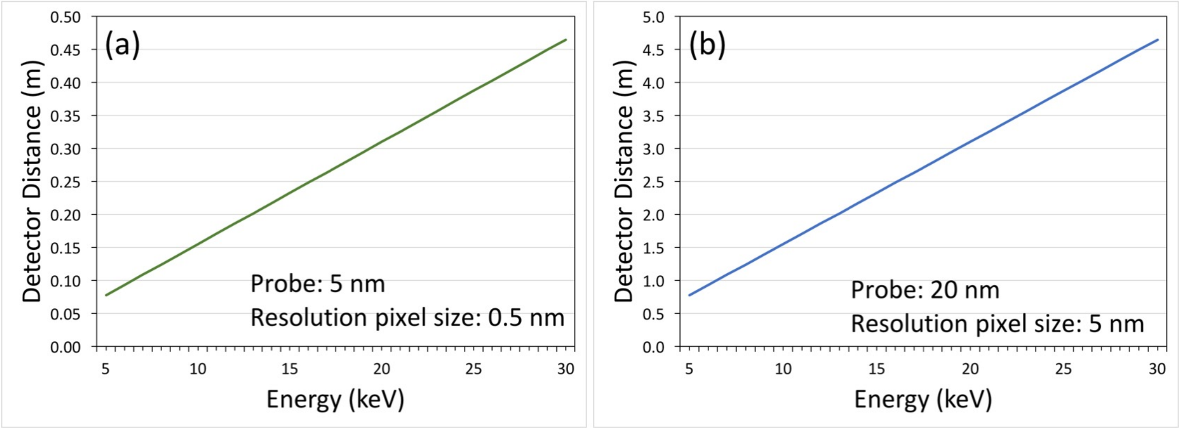

Figure 6.68. Distance between the sample and the detector for ptychography (pixel size: 75 μm; pixel number: 512). (a) 5-nm probe with 0.5 nm resolution pixel size in the reconstruction. (b) 20-nm probe with 5 nm resolution pixel size.

Energy dispersive detectors. In scanning probe mode, the energy-dispersive detectors are the heart of the system. However, the depth of field of the NFO rapidly starts to become an issue. For example, at 10 keV incident energy, the depth of field for 5-nm spatial resolution is only ±0.3 μm. This will be partly mitigated with two different XRF detector systems. There will be a detector in backscatter geometry, optimized for total subtended solid angle. It can provide high detected flux rates, and enables very large 2D samples to be imaged effectively. However, it will have non-optimized sensitivity (due to the increased scattering background and larger detected volume in this geometry), and the disadvantage that out-of-focus XRF signal is still detected, and if not mitigated by imaging filters, appears as a 'haze' of out of focus information reducing the contrast for the structures of interest. This detector is complemented by a detector at 90 degrees with regards to the incident x-ray beam, which is equipped with a capillary optic that serves as a collimator. With this detector system, the overall count rates are lower, but in particular, the capillary optics are capable of restricting the sensitive volume of the sample to $\sim$ 1 μm in the focus direction. In turn, this enables optical sectioning, or, where higher z-resolution is required, XRF tomography in 'stitched' tomograms – 1 Îijm at a time. Both detector systems will need to be able to deal with extremely fast data acquisition rates, and large volumes. Based on current routine per-pixel-dwell times of 10s of ms, and given the advances in methods such as tomographic reconstruction and dose fractionation, it is expected that dwell times of 1 ms will become a necessity. Taking advantage of ultrafast scanning techniques, such as those based on Lissajous figures, will require detectors capable of dwell times on the order of 250 ns or below. This appears feasible given today's advanced energy-dispersive detector electronics (e.g., Xpress3). Given the high focused flux rates anticipated with APS-U, it will be necessary to use heavily multiplexed detectors, and given the need to mitigate potential radiation damage issues, large solid-angle detectors become a must. Both should be addressable with advanced energy dispersive detector arrays such as the HEXID being developed by P. Siddons et al.

Spectroscopic detector. The development of superconducting x-ray fluorescence detectors is also an extremely exciting development. It seems feasible that an energy resolution of $\sim$1 eV can be reached, which would enable x-ray emission spectroscopy. If this could be combined with substantial multiplexing to achieve large subtended solid angles and high overall count rates, such a detector would be an incredible boon for the PtychoProbe. It would make it potentially possible to acquire a full chemical state map of elements of interest by simple XRF mapping, and in one shot at each pixel acquire (presumably complimentary) chemical information (for example, if both Fe and Co are co-localized in pixel, one might be able to get both oxidation states, and thus a far more superior handle for understanding in detail the localized chemistry occurring in the sample). While the scientific program of the PtychoProbe does not depend on this development, it would benefit hugely.

Computing

A number of research and development challenges must be addressed for the PtychoProbe. The increased brightness of the source relative to 3rd generation storage rings will enable rapid data acquisition with per pixel dwell times approaching one microsecond. A rapid-scanning, precise-motion, ultra-stable imaging platform requires significant advancement in motion control and data acquisition systems. In addition to the mechanics and control challenges, such an instrument could produce several TB's of data per second that need to be reduced in real time. This beamline positions the APS at the leading edge in optics, coherent imaging, big data, motion and control to open up new frontiers in x-ray microscopy.

We will require the ability to directly stream the acquired data to 'local' data storage space, and then the ability to analyze the acquired data in close-to-real time, so as to steer ongoing experiments. For the analysis, high performance computing resources will be required, in particular for ptychography. For scanning probe mode, a (raw) data throughput on the order of 1 GB / min is achievable, for ptychography mode, 2-3 orders of magnitude higher data rates will need to be accomplished. Some of these data volumes may be mitigated by the development of methods that make effective use of compressed sensing approaches to only store relevant data. Also, in order to reconstruct acquired data for XRF tomography or ptychography, vast volumes of data need to be processed. Consider the example of connectomics: it seems feasible to acquire the necessary data to reconstruct a full 3D dataset of a $(1\ \mathrm{mm})^3$ volume at a resolution of $(10\ \mathrm{nm})^3$ voxels, in about 1 day of beam time. If each voxel is represented as a single byte grey scale value, the dataset volume is 1 petabyte. Today's approaches are not able to handle such data, yet work like the collaboration between XSD and MCS is underway to develop methods that will enable exactly this kind of data analysis.

6-8.4.4 Specific Safety Requirements

All safety aspects are within the normal beamline safety envelope, and all APS and APS-U safety guidelines will be observed.

6-8.4.5 Specific Conventional Facilities Requirements

Conventional facilities are a critical enabling aspect of the PtychoProbe system. As previously stated, the PtychoProbe will be designed to achieve the highest spatial resolution (toward 5 nm). Ideally, any environmentally-driven disturbances should have a maximum amplitude of no more than 2 nm. While the PtychoProbe system will be designed to be as insensitive as possible to environmental disturbance, performance is always enhanced with a thermally and vibrationally stable environment. This is still the conceptual stage and the engineering specifications are still being determined, but it is reasonable to expect a hutch temperature stability of 0.1 ℃ for a 24 h period (recent work in the APS storage ring has shown that .03 ℃ variation is possible) and a vibration background of less than 20 nm rms on a 2-100 Hz bandwidth.

To highlight the importance of long-term stability, we consider two engineering materials that could be used in the construction of the PtychoProbe: a 10-cm length of aluminum or a 10-cm length of granite. If each material undergoes a 0.1 ℃ temperature cycle over a 24 hour period, this results in 230 nm and 60 nm length changes, respectively. Or put another way, a drift rate of 9.6 and 2.5 nm per hour, respectively. Providing the best achievable hutch temperature stability will help mitigate temperature-driven instabilities.

Likewise, for vibrational stability, minimizing the relative motion between the nanofocusing optics and sample is very important. This relative motion should be at the nanometer level. The ambient vibration environment and the air flow in the hutch are the main sources of mechanical disturbance to the instrument. Providing the best achievable ambient vibration environment will help mitigate vibrational instabilities.

The PtychoProbe team plans on working with the APS engineering staff to ensure that the instrument is installed in the best achievable environment. Vibration and temperature surveys will be conducted at the beamline. The known vibration sources of deionized water pumps, experimental hall air handlers, and hutch-mounted water piping can be address as needed. Working with the APS and FMS, low-risk and relatively low-cost changes can be made on an as-needed basis to mitigate the effects of these sources. In addition, air distribution to the hutch will be done in a manner that minimizes turbulence (similar to S26 and S32). On the temperature control side, recent experience shows that 0.1 ℃ temperature control should be achievable with standard modifications to the air handling system. Carefully addressing these conventional facilities aspects will ensure the best environment for the siting of the PtychoProbe.

6-8.4.6 Support facilities

We require ‘standard’ support facilities, such as a drylab for various instrument development and maintenance tasks, as well as a wet lab for sample preparation, mounting, and sample preview using complimentary methods (e.g., state of the art light microscopy or table-top electron microscopy).

6-8.5 R&D Needs

A number of research and development challenges must be addressed for the PtychoProbe. Some of these research needs are already actively being addressed to a certain degree, such as the LDRD project to develop the Velociprobe. This project aims for the development of a stable microscope platform that enables ultra-fast scanning for ptychography.

Area: Continued work on scanning control design and implementation – There is synergy here (by design) with the Velociprobe. Continued work is necessary on both the algorithm and the control hardware. The best algorithm approach for the PtychoProbe may be slightly different than the VP due to possibly scanning the sample rather than the zone plate. Less expensive, APS-supported

hardware should be explored for algorithm implementation.
Work needed: Explore fast scanning of larger systems, e.g. sample with environment. Explore best hardware to implement H-infinity or similar algorithms.

Area: Scanning mechanics development (in parallel with controller) – Off-the-shelf motion systems may not meet the instrument requirements. Likewise, choosing a fast scanning system without considering the control of the system may result in unintended constraints on performance. An example of this could be stages stacked to achieve three axis motion. This configuration is one way (not the only way) through which the feedback control phenomena of non-minimum phase zeros (NMPZ) can arise. Without much explanation, these NMPZs can put constraints on bandwidth and cause system instability. Current x-ray microscopes at the APS exhibit this behavior.
Work needed: Simulation and design efforts are necessary to determine what is required for the scanning stages. These simulations can help determine if an off-the-shelf system exists. If not, an appropriate system will be designed.

Area: Secondary-source aperture-to-optics stability – There may be some synergy here with the APS-U beam/beamline stability work. The APS-U accelerator side is working on using water levels to measure relative positions of components widely separated (∼20 m). For the PtychoProbe high-resolution mode, sub-micron relative position stability may be needed.
Work needed: Quantify expected relative motions between optics and SSA. Determine feasible way to measure the vertical and transverse relative positions of the zone plate optics, sample, and SSA. Develop approach for feedback control of relative position.

Area: Quantification (and remediation) of environmental noise at beamline location. Environmental vibration environment can greatly influence the instrument performance. The current environment should be known before the instrument is designed and installed. Any significant environmental vibration issues should be addressed.
Work needed: A vibration survey should be conducted at the proposed beamline location. Any large sources of vibrational noise should be addressed. The work done at S26 may be viewed as a model for this work.

Area: Development of zone plate (ZP) optics for 5-nm focusing. The primary technical milestone to achieve the desired focus spot with ZPs is to fabricate the desired zone width. Currently, there are limitations in the lithography that complicate fabricating structures with a size below 10 nm. High resolution lithography, in addition to pattern thinning via etching, can reduce feature size to sub-10 nm reliably, but this technique would have to be developed for the grating-like structure of zone plates. The resulting structure can be combined with zone doubling and interlacing the pattern to achieve the desired zone width. This indicates that most likely, to achieve the required specifications, no single technical development can achieve the desired focus spot size, and a combination of technologies would be required.
Work needed: A dedicated R&D effort needs to be established at Argonne to achieve the specifications for the optics desired. In addition to the technologies described in the previous section, new concepts should be explored, such as developing sputter slice zone plates to maximize the chance of success. In general, the tools required for R&D are available at Argonne today, though collaborations with groups at BNL or SLAC would provide access to more advanced tools than those available now. Additional R&D is required for integrating any fabricated optics into the beamline.

Area: Development of multilayer Laue lenses (MLL) for 5-nm focusing. Multilayer Laue lenses (MLLs) are a realistic candidate for focusing down to 5 nm. Although they are more difficult to align (2 MLLs are needed for point focusing), they might provide higher efficiencies. The optics group is world-leading in the fabrication of MLLs. As a risk mitigation strategy, we expect to design the PtychoProbe endstation instrumentation such that MLLs could be accommodated if the development of appropriate ZPs does not lead to the expected success.
Work needed: Existing equipment at Argonne needs to be optimized to be able to grow the required large number of layers for a 5-nm MLL. Additionally, materials R&D has to be conducted to grow such structures.

Area: Data management for an instrument that delivers high data volumes at fast speed. To take full advantage of APS-U, an ultra-fast detector with short exposure times and frame rates in the kilohertz range will be utilized. Today's EIGER detector already acquires up to 180,000 frames and about 360 gigabytes per minute. The goal is to not only stream and save these large data volumes, but to make them available to analysis tools in close-to real-time. Scientists should be able to obtain a rough analysis of the measurements on-the-fly.
Work needed: Today's data infrastructure is not capable of dealing with the high data volume. Thoughtful R&D in hard- and software is paramount for the success and efficient operation of the PtychoProbe.

Area: The beamline design of the PtychoProbe requires a horizontal insertion device to meet its specification of focusing down to 5 nm with high stability. Otherwise, polarization losses would not allow for a horizontal monochromator that is required for beam stability. Currently, a horizontal gap vertically polarized undulator (HGVPU) of 29 mm period is under consideration. In case a horizontal ID is not available, the PtychoProbe beamline design would be adjusted; most importantly, a vertical-reflecting monochromator would be employed. However, this would negatively influence the beam stability, one of the most important qualities for achieving 5-nm focusing. Therefore, R&D for a horizontal ID is critical.
Work needed: R&D needs to be initiated based on feasibility studies that are ongoing.

6-9 POLAR: Polarization Modulation Spectroscopy

6-9.1 Executive Summary

Electronic inhomogeneity is a hallmark of correlated electron systems with competing interactions. These inhomogeneous quantum states underlie some of the most exciting phenomena of current interest in condensed matter physics including nematic charge/spin stripe order as a possible mediator of high T_c superconductivity in copper-oxide "cuprates", and spin liquids where bond directional anisotropy or geometrical frustration leads to complex magnetic textures. We leverage two key properties of APS-U, namely, brilliant x-ray beams and round insertion device vacuum chambers to enable studies of mesoscale electronic/magnetic inhomogeneity by means of tuning/controlling competing ground states under extreme high-pressure conditions (Mbar range). A novel scheme for rapid polarization switching (both linear and circular) using dual superconducting undulators, coupled with $\sim$ 200 nm focused beams, results in ×500 average polarized flux density gains at currently accessible electronic resonances below 13 keV, and opens up access to new resonances in the 14-27 keV range. These brilliant, polarized beams enable a tenfold increase in pressure range opening remarkable opportunities for discovery of new phases and furthering our understanding of quantum matter, allowing x-ray probes of electronic matter at extreme pressure conditions to enter a new era of search and discovery.

6-9.2 Scientific Objectives & Capabilities

6-9.2.1 Science Case for Beamline

Competing interactions in correlated electron systems lead to degenerate ground states resulting in quantum critical points or spontaneous electronic phase separation at low temperatures. [115, 116] These complex ground states are highly responsive to external stimuli allowing manipulation, and ultimately controlling, complex electronic matter. While proximity to electronic degeneracy can be achieved with chemical doping, i.e., changing charge density via chemical pressure or via electron/hole doping, extrinsic doping leads to chemical inhomogeneity affecting electronic texture and preventing a thorough understanding of the driving forces behind intrinsic electronic heterogeneity. Advances in high-pressure generation now allow reaching multi-Mbar pressures and large changes in energy density $\sim$ eV/Å^3 [117, 118], bringing pure, undoped compounds to the regime of quantum degeneracy/criticality via tuning of Coulomb interactions, electronic bandwidth, hybridization, and crystal fields triggering electronic order (magnetic, ferroelectric, superconducting, Kondo lattice), electronic disorder (mixed/fluctuating valence, Kondo screening, magnetic frustration), or competing/segregated phases at the nano/meso-scale. [119, 120, 121] Polarization dependent x-ray probes such as x-ray magnetic circular/linear dichroism (XMCD/XMLD) and x-ray resonant magnetic scattering (XRMS), coupled with high-flux nm-to-μm sized beams and extreme conditions, provide a unique route to unraveling the nature of electronic heterogeneity and drive discovery of novel phases of electronic matter. Hard x-rays enable studies in extreme environments where penetrating radiation is required. In the case of extreme pressures (Mbar regime), polarized x-rays are a unique probe of electronic matter providing element-specific information on valence state, orbital occupancies, hybridization, charge transfer, and electronic/magnetic ordering. [122, 123, 124] The ability to probe most types of electronic/magnetic order, including inhomogeneity with polarized $\sim$ 200 nm x-ray beams at extreme pressure conditions (Mbar range) at low temperature ($\sim$ 1 K) in high magnetic field (10 T), is unique to high-brilliance synchrotron radiation and will remain so for the foreseeable future.

The new capability will provide much needed insight into critical problems in condensed matter physics. In the area of interplay between mixed valence, Kondo instabilities, magnetic order and crystal structure in 4f (rare-earth) and 5f (actinide) heavy fermion systems, resonant scattering will provide rich information on the nature of magnetic ordering while polarized spectroscopy will probe mixed valency, f-conduction electron hybridization, and magnetic order. Combined, these techniques allow imaging the inhomogeneous magnetic state expected to arise in the intermediate regime between onset of Kondo screening and collapse of magnetic ordering. In 5f systems, long-standing questions such as the nature of hidden order in URu_2Si_2 [125] and unusual magnetism in Pu [126, 127] can be addressed with polarization modulation experiments at ambient- and high-pressure conditions in the 16-27 keV range which spans the $L_{2,3}$ edges of actinides, a capability currently unavailable. Large flux gains at the $M_{4,5}$ edges of actinides in the 3.4-4.5 keV range will allow probing 5f electronic states directly. Insight will also be provided into the unique properties of transition metal (TM) oxides which display a wide variety of exotic phenomena including high-T_c superconductivity, charge-orbital order, colossal magneto-resistance, and multiferroicity, as well as related electronic inhomogeneity associated with these competing ground states. [128, 129] Pressure tuned electronic bandwidth thus provides a unique tool to drive I-M transitions and help understand the underlying physics of Mott insulators. This beamline will allow the probing of electronic order and inhomogeneity in TM oxides with low compressibility (high bulk modulus 150-300 GPa) across their I-M transitions, helping clarify the role of magnetic correlations in gap formation. The discovery of conventional high T_c superconductivity at 203 K in a sulfur hydride in the 1-2 Mbar pressure range generated renewed interest in the electronic properties of hydrides. [119] Since BCS has no theoretical upper bound for T_c, prospects for room-temperature superconductivity are not unrealistic. Compounds with light hydrogen atoms displaying hydrogen bonding with high-frequency phonon modes are natural candidates, with iron hydrides synthesized under pressure recently coming to the forefront.[130] A strong interplay between magnetism, dimensionality, proton zero-point energy, and superconductivity is at play, providing a fertile ground for discovery of new electronic phenomena. Finally, the ability to tune interatomic distances and bond angles with external pressure is unique in engineering frustrated magnetic states via tuning of (competing) exchange pathways and interactions. The new capabilities will allow studies of spin melting/freezing with resonant scattering and spectroscopic probes including mapping spin liquid/solid mixtures and their evolution across first-order transitions. Stabilization of long sought-after novel quantum states such as the Kitaev quantum spin liquid [131] may be possible. High-pressure studies of these phenomena necessitate the highest possible brilliance, particularly when measuring weak diffuse x-ray resonant magnetic scattering from regions with short-range magnetic order. A full scientific case for this beamline is described in Chapter 3.

6-9.2.2 Description of User Community/Stakeholders

This beamline upgrade builds on $\sim$ 10 years experience at beamline 4-ID-D of the APS developing x-ray instrumentation and a robust and productive user program for condensed matter physics studies at intermediate pressure conditions using XMCD (APS lead, $\sim$ 0.5 Mbar) and XRMS (U. Chicago and APS leads, $\sim$ 0.2 Mbar). These programs are unique in the US and are generally regarded as world leading. The information provided by these probes is by and large not accessible with any other probe (neutrons, electrons, nuclear; with minor exceptions) so these capabilities are essential. Despite only $\sim$ 30% of beam time at 4-ID-D allocated to high-pressure studies since the program inception ∼ 10 years ago (4-ID-D is the only hard x-ray XMCD beamline in the US and is oversubscribed by ×3-4), over 25 unique user groups generated 4 Nature/Nature-flavored, 5 PNAS, 7 PRL, 28 PRB amongst a total of about 60 papers. This beamline upgrade plan expands the pressure range tenfold opening a remarkable opportunity for discovery of new phases and for understanding the role of electronic inhomogeneity in a wide range of phenomena. The existing user community for these programs, ∼ 25 unique user groups, serves as a solid foundation for the new developments. These users come from institutions with established high-pressure programs such as Washington U. (Schilling), Caltech (Rosenbaum, Feng), LANL (Bauer), LLNL (Jeffries), Carnegie Institution (Struzkin), UNLV (Kumar, Cornelius), U. Colorado (Cao), and HPSTAR (Mao, Ding) to name a few.

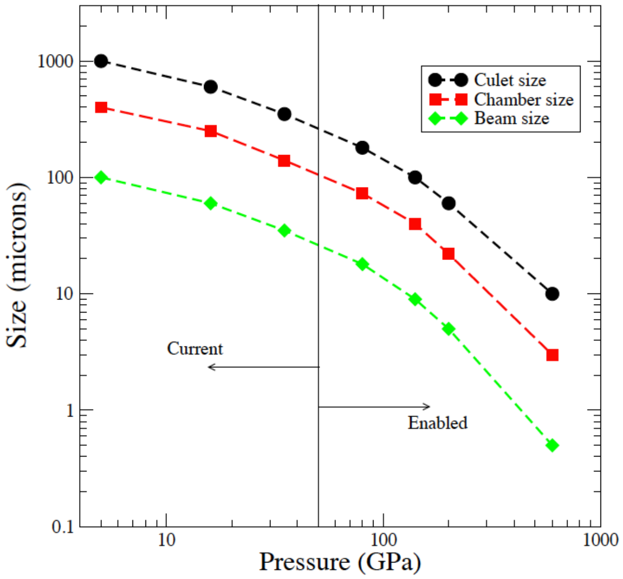

Figure 6.69. X-ray beam size requirements for high- pressure measurements into the multiple Mbar regime (100 GPa=1 Mbar). The x-ray resonant conditions often require use of perforated (weakened) diamond anvils, hence ∼ 2× smaller culet size relative to regular anvils to reach the same final pressure. Long working distances associated with simultaneous low-temperature/high- magnetic field/high-pressure sample environments limit demagnification ratios and focused beam size relative to sample environments with short working distances. APS-U brilliant beams extend the pressure range tenfold and allow for mapping of electronic inhomogeneity with ∼ 200 nm resolution.

The MSD division at Argonne (Mitchell, Rosenkranz, Norman) plays an important role through its excellent platform for materials synthesis and expertise/programs in x-ray probes and theoretical studies of correlated electron systems. This proposal also thrives from its synergy with HP-CAT and GSE-CARS, two centers of excellence for high-pressure research at APS. The probes of electronic matter described in this proposal are not available at HP-CAT and GSE-CARS beamlines. It is quite common for condensed matter physics/materials/quantum chemistry/geosciences users of 4-ID-D to use complementary high-pressure techniques at HP-CAT (XRD, XES) and at XSD-S3 (Mössbauer spectroscopy in the time domain), and vice versa. Access to user facilities at HP-CAT and GSE-CARS, e.g. gas loading and laser drilling systems, has been an important contributor to the success of S4 programs. The existing high-pressure program at 4-ID-D already involves collaborations with several of the major high-pressure centers in the US and abroad (CDAC, Carnegie, UNLV, HP-CAT, HPSTAR, etc). Expanding the US capabilities in the area of x-ray probes of electronic matter at high pressures will benefit a significant fraction of the high pressure community both in the US and abroad.

Since 4-ID-D is the only hard x-ray XMCD beamline in the US, it enjoys a healthy user base for polarization dependent, dichroic spectroscopy/scattering measurements other than at high-pressure conditions. The beamline design detailed in this document results in large polarized flux gains at all resonant energies currently accessible, access to new resonances in the 14-27 keV range, and smaller focused beams with increased stability. It therefore benefits all current and future users of 4-ID-D, not just users of its high pressure programs.

6-9.2.3 Use of APS-U Characteristics

Two properties of APS-U are key for this beamline upgrade: x-ray brilliance and round ID vacuum chambers. The enhanced brilliance of APS-U enables focused beams in the ~ 200 nm range with $\times 50$ average flux density gains relative to the current APS source (Section 6-9.4.2), despite the rather long working distances 100-400 mm associated with the two main instruments at this beamline. These brilliant beams are required for XMCD/XMLD/XRMS experiments at high pressures in the hard x-rays, particularly in the multiple Mbar regime where small diamond culet/sample size is needed and where low dichroic contrast/resonant scattering amplitudes require the highest x-ray flux. Typical beam sizes for pressures in the 3-4 Mbar are ~ 1 micron (see Figure 6.69). In addition, these small focused beams from APS-U are critical to enable mapping of electronic/magnetic inhomogeneity at the mesoscale with ~ 200 nm resolution. Other advances enabled by sub-micron beams include use of small samples to reduce effects of pressure gradients, placement of multiple samples in the same gasket hole so that they can be measured under identical experimental conditions, and extending experiments through x-ray transparent Be gaskets to higher pressures where gasket indentations reach the micron size.

The round ID vacuum chambers enabled by APS-U as a result of on-axis injection allows implementation of polarizing superconducting insertion devices. This includes helical superconducting undulators and the novel "universal" Superconducting Arbitrarily Polarized Emitter "SCAPE" undulator (Figure 6.70), the latter capable of generating LCP, RCP, L-H, and L-V polarization states. SCAPE undulators will replace phase plates currently used at 4-ID-D in the 3-14 keV range. This will (1) result in $\times$5-20 polarized flux gains, (2) provide access to currently inaccessible resonances in the 14-27 keV range where Bragg-transmission phase plates are either inefficient or impractical, and (3) will allow polarization modulation spectroscopy and scattering experiments (1-10 Hz). The scheme planned for implementation in this beamline is further discussed in Section 6-9.3.1. The sizable increase in polarized flux over the entire energy range covering all resonances of interest, coupled with polarization modulation capabilities, is key for optimal detection of weak XMCD/XMLD/XRMS signals.

The high-pressure instruments at 4-ID-D are unique in the US and are generally regarded as world-class/world leading capabilities. While the APS will remain, for the foreseeable future, the only light source in the US offering x-ray instrumentation for probing electronic properties of condensed matter under simultaneous high-pressure, low temperature and high magnetic field conditions, other light sources outside the US have developed similar capabilities, particularly for XMCD measurements

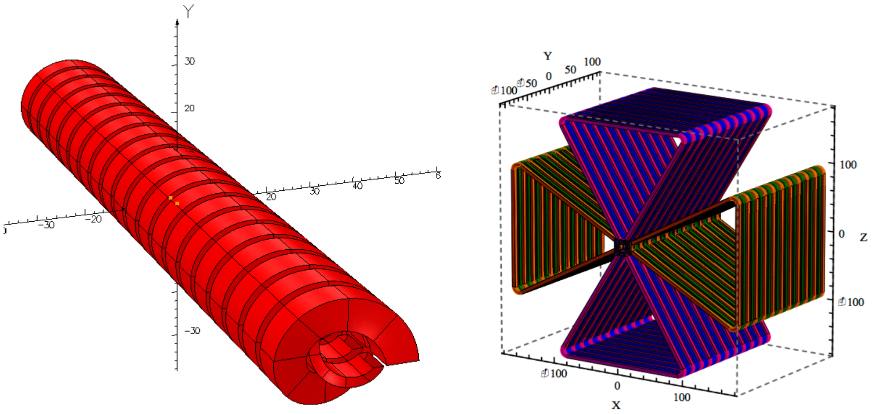

Figure 6.70. Helical (left) and "SCAPE" (right) SC undulators enabled by round ID vacuum chambers [12].

(ESRF ID-24, Spring-8 BL39XU). New efforts have started at PETRA III (P09), ESRF (ID12), and SIRIUS (Extreme Conditions beamline) aimed at mostly replicating current capabilities at 4-ID-D. Thus, the proposed upgrade extending pressure range tenfold, expanding polarization tunability into the 14-27 keV range with polarization modulation capabilities, increasing polarized flux across all resonances of interest, and enabling probes of electronic inhomogeneity in the diamond anvil cell with $\sim$ 200 nm resolution, will ensure world leading status for this beamline.

6-9.2.4 Key Beamline Characteristics

Three key ingredients are needed to meet the requirements of the scientific case: (i) polarizing insertion device(s) producing fully tunable, rapidly switchable (modulated) polarization states across a wide energy range covering all resonances of interest; (ii) $\sim$ 200 nm focused beams with high polarized flux and high spatial stability; (iii) unique instrumentation for dichroic and resonant/magnetic scattering experiments at simultaneous extremes of pressure (Mbar range), high magnetic fields ($\sim$ 10 Tesla), and low temperature ($\sim$ 1 K).

Specifically, this beamline will deliver the highest flux in sub-micron beams with tunable polarization states (LCP, RCP, L-H, L-V) covering electronic resonances in the 2.75-27 keV range including K, L, M edges of 3d, 4d, 5d, 4f, 5f elements. Additionally, rapid polarization switching between LCP/RCP or L-H/L-V polarization states, enabled by a novel implementation of tandem SCAPE superconducting undulators (see Section 6-9.3.1), allows measurements of weak XMCD/XMLD signals (down to 10 ppm of absorption edge jump) and weak XRMS signals (down to 1 ppb of lattice Bragg peaks). The rather long working distances required to implement high pressure sample environments under simultaneous low temperature and high magnetic field conditions, coupled with flux requirements, results in optimized spot sizes of about 100 (250) nm for the proposed instruments with 100 (400) mm working distance (Section 6-9.4.2). These sub-micron spot sizes are sufficient to achieve a ten-fold increase in pressure relative to today's capabilities, matching the limit of static high-pressure generation technology (6-7 Mbar). This beamline delivers a ×500 increase in polarized flux density in $\sim$ 200 nm beams relative to today's source (×10 average gains from novel SC undulator x-ray source and ×50 average gains from reduced source emittance). The new source also

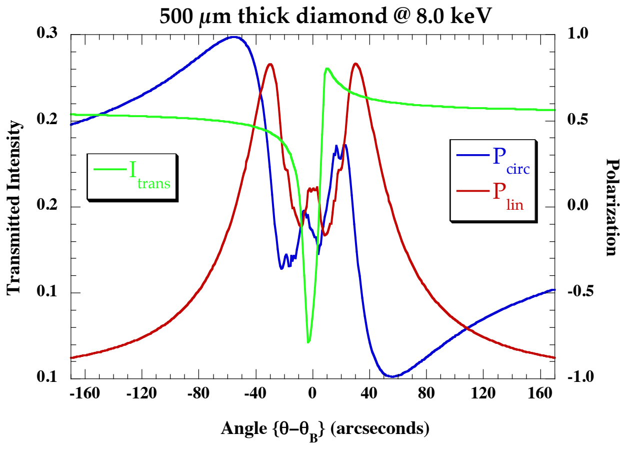

Figure 6.71. Phase retarding optics operated in Bragg transmission geometry allow fast polarization switching but strongly attenuate x-ray beams, deliver LCP and RCP beams with different intensity, and produce incomplete L-V polarization [13, 14, 15].

enables dichroic studies at resonances in the 14-27 keV range, currently unavailable. The beamline will be equipped with unique instruments for resonant scattering and absorption experiments at extreme high-pressure conditions under simultaneous low T and high magnetic field conditions.

6-9.3 Source & Front End Requirements

6-9.3.1 Insertion Devices

Variable polarization in the hard x-rays can be achieved with either phase retarding optics or Apple-II type (PM) undulators. Phase plates, typically diamond crystals used in Bragg transmission geometry, allow for fast polarization switching [13], but due to finite thickness and small footprint they significantly reduce x-ray flux (×5-20 in the 3-14 keV range is typical) [14, 15]. Additionally, phase plates produce LCP and RCP beams with significantly different intensities (5-30%) which is problematic for detection of weak dichroic signals as it relies on perfectly linear detector response (Figure 6.71). Finally, a single phase plate produces incomplete L-V polarization (80%) which is detrimental for XMLD experiments. Apple-II type undulators produce variable polarization states directly at the source but polarization switching requires slow mechanical movement of permanent magnet arrays resulting in low switching times. This impedes polarization switching at every energy point in a resonant scan, which is needed to minimize systematic errors (e.g. it prevents implementation of lock-in detection methods for high S/N ratio measurements of small dichroic signals). Furthermore, unlike implementations at soft x-ray beamlines, the short undulator periods $\sim$ 3 cm required in the hard x-ray range present a big challenge for achieving the necessary peak magnetic fields with the complex magnet pole structures of Apple-II type undulators.

The round ID vacuum chambers enabled by the on-axis electron injection of APS-U allow implementation of novel polarizing superconducting (SC) undulators (Figure 6.70). Helical SC undulators using bifilar windings produce circular (LCP, RCP) polarization states needed for XMCD-type experiments (Figure 6.70, left). However, lack of on-axis higher harmonic radiation limits their energy range to fundamental radiation only ($\sim$ 2.75-10 keV) and linearly polarized radiation needed for

XMLD and XRMS probes is not available (the latter are ideal probes of antiferromagnetic order). The SCAPE design proposed by Efim Gluskin and Yury Ivanyushenkov (Figure 6.70, right), which can be thought of as cross-planar undulators with 90° phasing between vertical and horizontal magnetic fields, produces LCP, RCP, L-H, and L-V polarization states by energizing coil pairs separately or simultaneously. Magnetic modeling of SCAPE devices confirms that necessary peak field (K) values [12] and appropriate tuning curves [132] can be achieved with realistic parameters of winding bores (Figure 6.72). The device can deliver circular, elliptical, or linear (H,V) polarization in first harmonic, and linear (H,V) or elliptical with tunable degree of circular polarization, P_c, in higher harmonics (P_c can be tuned in the 75-90 % range with trade off in flux [132]; see Figure 6.72 ("4-jaw uSCU" is equivalent notation for "SCAPE").

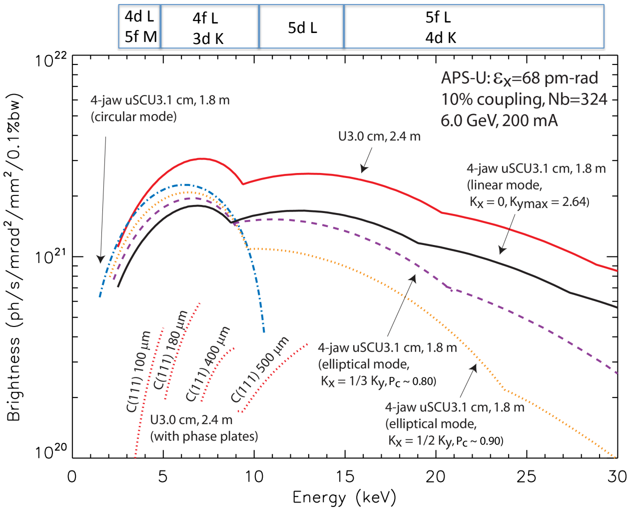

Figure 6.72. Tuning curves for "4-jaw uSCU" (SCAPE) device in circular, elliptical, and linear modes and comparison with phase plates. Resonances/edges of interest are shown at the top.

While a single SC undulator is incompatible with fast polarization switching (ramp down/up of large currents in the 100-400 Amps range would be needed), this beamline will use instead dual, in-line SCAPE undulators collocated in the ID straight section to achieve rapid polarization switching. The concept involves presetting each of the undulator sources to generate opposite x-ray polarization (LCP and RCP, respectively, or L-H and L-V, respectively) and providing a mechanism for the source of radiation delivered to the end user to alternate between these two undulators. We are exploring two different approaches to fast polarization switching involving dual SCAPE undulators.

The first approach is illustrated in Figure 6.73 and is based on a previous implementation at a Spring-8 soft x-ray XMCD beamline using tandem Apple-II undulators.[16, 133] Electron orbit bumps are used to alternately steer the electron beam orbit so that, at any given time except during the short transition period when the fast steering corrector magnets (kicker magnets) are active, radiation from one undulator is delivered off-axis while that from the other undulator is delivered on-axis to the end user. The electron orbit bump angles required to prevent unwanted radiation from the "bypassed" device from reaching the end user are rather small, on the order of 30 μrad. This is nearly an order of magnitude smaller than the 200 μrad bumps used in the original implementation of this concept at a soft x-ray XMCD beamline in SPring-8.[16] The smaller x-ray beam divergence in the hard x-rays relative to soft x-rays ($\sim \sqrt{\lambda}$) primarily explains the reduced orbit bump angle although power considerations also contribute to enabling a smaller orbit bump in the hard x-rays.

The smaller orbit bumps require ∼ × 7 lower fields in the fast steering corrector magnets, which translates into reduced perturbation of the electron beam orbit and may lead to higher switching frequencies. In order to achieve polarization modulation at 10 Hz with a duty cycle of 80% or higher, the synced, transient current ramp times in the fast steering corrector magnets producing the orbit bumps would need to be 10 msec or faster. Higher polarization switching frequencies above 10 Hz may be achievable with this method. Calculations used to derive the size of the required orbit bumps, including power considerations and polarization purity, are described below in Section 6-9.3.2.

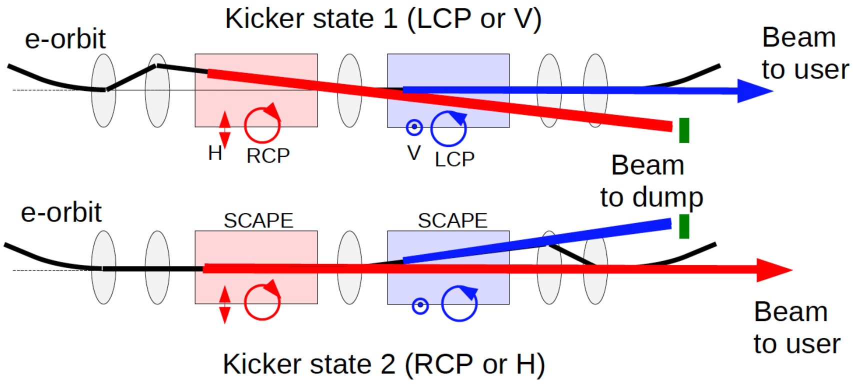

Figure 6.73. Fast polarization switching using two in-line SCAPE undulators and electron orbit bumps to provide an alternating source of polarized x-rays with opposite polarization. Orbit bumps are in the horizontal plane. The ellipses in the figure are steering corrector magnets. The steering corrector magnet between the two IDs is a DC magnet providing a static ∼ 30 µrad bump while the other four are fast correctors. The implementation of this scheme in the hard x-rays enables smaller orbit bumps of ∼ 30 µrad relative to the 200 µrad bumps implemented previously at a Spring-8 soft x-ray beamline[16].

An alternative scheme for polarization switching, currently under development, involves applying a small ∼ 6 Amps undulator current bump that alternates between the insertion devices in order to shift undulator harmonic energy by an amount comparable to its bandwidth (Figure 6.74). The monochromator downstream effectively becomes a selector of polarization since flux from the "detuned" device is reduced by ∼ × 100 (see Figure 6.74 right [134]). Polarization modulation in the 1-10 Hz range may be achieved in this scheme with use of secondary coils wrapped around the primary NbTi coils in the SCAPE devices. These secondary coils would use small filament NbTi wire specifically designed for fast current ramps with lower AC (hysteresis) losses than those in regular NbTi wire.

While the "undulator current bump" approach has an advantage over the "electron orbit bump" approach in that it does not directly perturb the electron orbit, an off-project R&D is still required to bring this concept into reality. The "electron orbit bump" approach can be implemented with current technology and is therefore a lower risk approach. It also carries the potential to enable faster polarization switching, perhaps even at kHz rates. Therefore, we currently plan to implement the "electron orbit bump" approach at the beamline. If the off-project R&D work on the "undulator current bump" were to lead to a practical solution in the near future, we will evaluate its possible implementation at that time.

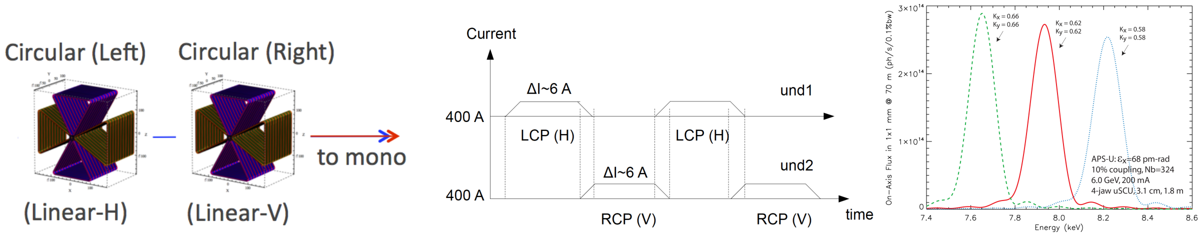

Figure 6.74. (left) Scheme for rapid polarization switching utilizing dual 4-jaw "SCAPE" SC undulators (Middle) Time-dependent current bumps used for polarization modulation (LCP/RCP or L-H/L-V) and (right) harmonic energy shift with 6.4% change in K (∼ 6 A current) value.

The wide energy range and polarization tunability of the SCAPE devices enables XMCD, XMLD, and XRMS measurements in the 2.75-27 keV energy range covering all resonances of interest (see top bar of Figure 6.72). These insertion devices are revolutionary in many respects: 1) they provide large polarized flux gains in the 3-14 keV range by replacing phase retarding optics, 2) they enable XMCD/XMLD measurements at higher energies (14-27 keV) where Bragg transmission phase plates are either impractical or very inefficient, and 3) when two devices are used in tandem they enable polarization modulation in the 1-10 Hz range (and possibly higher) while delivering on-axis beams with alternating polarization (in contrast with approaches that use different optical paths for beams with opposite polarization emanating from canted undulators where polarization selection is done with a chopper).[135]

6-9.3.2 Orbit Bump Angle with Dual SCAPE Undulators

A successful implementation of the electron orbit bump scheme requires accepting most of the central cone from the undulator delivering on-axis radiation while minimizing radiation "leakage" from the bypassed, off-axis, undulator. Figure 6.75 shows angular flux density distribution (ph/s/mrad^2/0.1% BW) for a 3.0 cm, 1.5 m long SCAPE device at selected energies, with APS-U operated in brightness mode. Similar results are expected for timing mode since the beam divergence is dominated by the single electron photon divergence. A 0.5×0.5 mm^2 white beam aperture placed at 25 m from the center of the ID straight accepts 20 μrad and is shown superimposed on the plots. This aperture is sufficient to accept nearly all of the central cone radiation at 8 and 17 keV, and most of it even at a low energy of 2.7 keV (note that the relative change in flux density with angle is the same for linear and circular polarization modes). The total flux for circular (linear) polarization through this aperture at 8 keV is 3.1×10^{14} (2.6×10^{14}) ph/s/0.1% BW. At 2.7 keV the corresponding numbers are 3.9×10^{14} (2.4×10^{14}) ph/s/0.1% BW. At 17 keV (third harmonic) the total flux for elliptical (linear) polarization is 1.3×10^{14} (1.4×10^{14}). The undulator settings in elliptical mode are $K_x=1/3\ K_y$.

The amount of on-axis radiation leakage from the "bypassed" device can be quantified as a function of the horizontal orbit bump angle by integrating the flux density in Figure 6.75 through the 0.5×0.5 mm^2 aperture at 25 m, as this aperture is shifted in the horizontal direction. The results are summarized in Figure 6.76. By selecting a horizontal electron orbit bump of 30 μrad, the leaked on-axis flux through the aperture from the bypassed undulator is 0.5% or less of the flux from the "active" undulator at 8 and 17 keV keV. This leaked fraction increases at lower energies but does not reach 5% even at 2.7 keV. The leaked radiation, which adds incoherently to the radiation from the "active" undulator and has opposite polarization, effectively reduces the degree of polarization seen

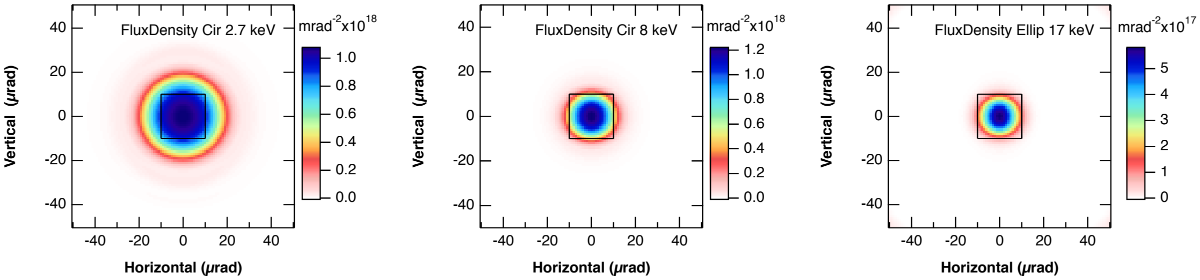

Figure 6.75. Angular flux density (ph/s/mrad^2/0.1% BW) circularly polarized radiation at 2.7, 8, and 17 keV. The black square represents a white beam aperture 20 µrad on a side corresponding to 0.5×0.5 mm^2 at 25 m.

by the sample. The angular distribution of the polarization content from a single undulator is also shown in Figure 6.76. For example, at 8 keV in circular mode, the degree of circular polarization remains at 100% to at least 40 µrad. At 17 keV in elliptical mode (third harmonic), the degree of circular polarization shows significant angular dependence but the leaked radiation fraction at this energy is below 0.5%. Polarization purity in both circular and linear (H,V) modes obtained with this method is equal or better than that obtained with phase retarding optics with the added advantage of significantly higher flux in the 3-14 keV range where phase retarders are currently in use, and extension of the energy range where elliptical/linear-V polarization can be generated efficiently to the 14-27 keV range.

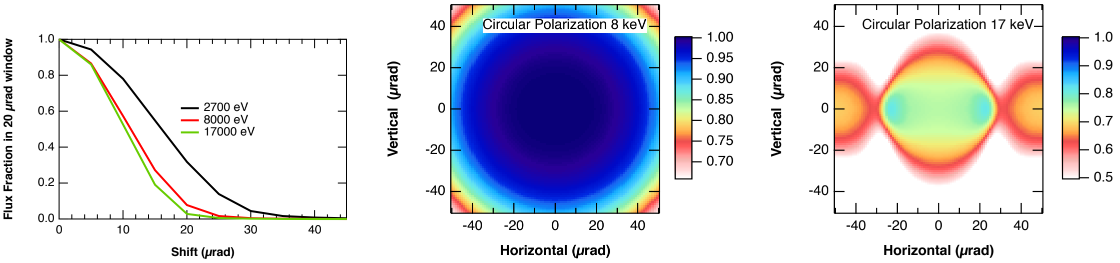

Figure 6.76. (Left) Fraction of leaked radiation from bypassed SCAPE undulator tuned to 2.7 and 8 keV in circular mode (first harmonic) and 17 keV in elliptical mode (third harmonic). The results are practically the same for linear polarization modes. (Right) Angular profile of degree of circular polarization at 8 keV (first harmonic, circular mode) and 17 keV (third harmonic, elliptical mode K_x=1/3 K_y).

An additional aspect that ought to be considered is the total power delivered to the monochromator through the 20 µrad aperture from both "bypassed" and "active" undulators. Figure 6.77 shows angular profiles of power density for a SCAPE undulator tuned to 2.7 and 8 keV in circular mode first harmonic, and 17 keV in elliptical mode third harmonic. In circular/elliptical mode the power density does not change significantly with horizontal angle out to at least 30 µrad. The same holds for linear-H mode. The largest changes in power seen by the monochromator upon beam deflection would take place when switching between undulators preset to linear-H and linear-V modes, but even then, changes are below 20% at all energies. These results are summarized in Figure 6.78. The total power through the aperture from the "active" SCAPE device at 8 keV in circular (linear) mode is 13 (17) Watts. The corresponding numbers at 2.7 keV are 4 (49) Watts. When "leakage" power from the bypassed device is included, the maximum change in power seen by the monochromator is from 90 W to 100 W at 2.7 keV when switching between L-H and L-V modes with 30μrad electron orbit bumps. Note that in this worst-case scenario, the monochromator would see a time-averaged power of 95 W due to the high frequency switching. At higher energies when switching between linear modes, or at all energies when switching between circular/elliptical modes, the absolute power drops significantly and the changes in power seen by the monochromator during polarization switching become quite small.

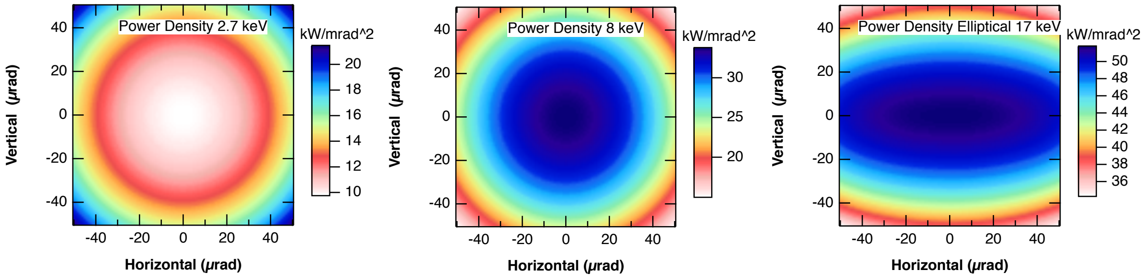

Figure 6.77. Angular profile of power density for a 3.0 cm period, 1.5 m long SCAPE undulator tuned to 2.7 and 8 keV in circular mode (first harmonic) and 17 keV in elliptical mode (third harmonic, K_x=1/3 K_y).

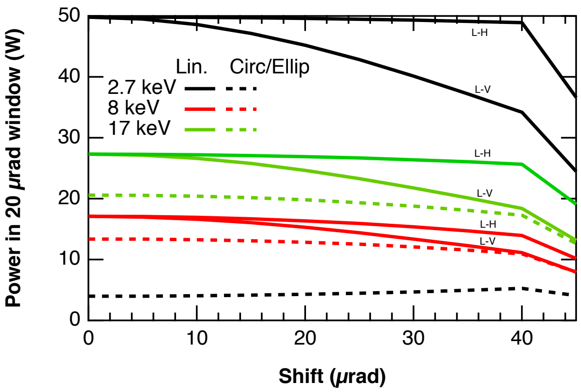

Figure 6.78. Power through 0.5×0.5 mm^2 aperture at 25 mm incident on monochromator from a single SCAPE device as a function of horizontal angle steering for selected energies in different polarization modes. Change in power during dynamic orbit bumps are always below 5% of time-average values. The latter range from 10 W to 95 W across the entire energy range and different polarization modes.

6-9.3.3 Other Source Requirements

The implementation of fast polarization switching with dual ∼ 1.5 m SCAPE undulators requires the entire length of a 5 m straight section. The two undulators can be built into a single ∼ 4.5 m long cryostat including steering and corrector magnets, as illustrated in Figure 6.79. Timing signals associated with switching of the fast steering magnets or undulator coils during polarization switching would need to be available to beamline controls for synchronization with data acquisition.

Source(s) positional stability should be better than 3 microns, which translates into about 10-15

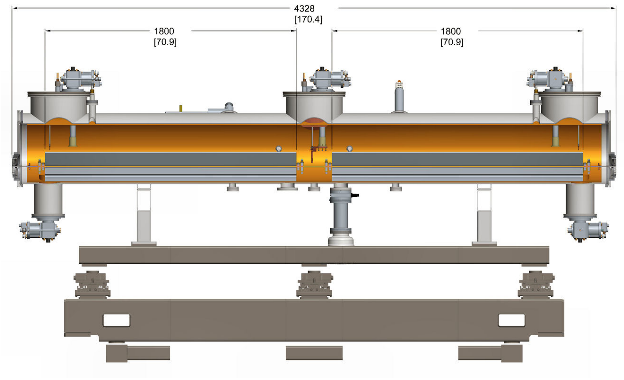

Figure 6.79. Model of tandem SCAPE superconducting undulators located in a single cryostat.

nm positional stability at the sample position for focusing optics with demagnification ratio in the 200-500 range planned for this beamline. Angular stability of x-ray source(s), in steady state and during polarization modulation, should be about 0.1 μrad, which translates into 7 microns at the position of the furthest downstream instrument (72 m) or about 35 nm for a demagnification ratio of about 200 in the focusing optics for this instrument. This angular stability is also required to ensure absence of sizable energy shifts in monochromatic radiation when switching between polarization states (0.1 μrad corresponds to about 3 meV shift for Si(111) monochromator at 8 keV. This should be compared with about 1 eV intrinsic bandwidth, and a few eV typical core-hole lifetime broadening at K, L, M electronic resonances). The precision of front end XBPM of about 0.1 μrad is sufficient to prevent dichroic artifacts as a result of energy differences between two beam sources. One notes that these artifacts are not uncommon at beamlines where polarization cannot be switched at every energy point in a resonant scan and where instead scans for different polarizations are collected independently at very different times. This is not the case here.

6-9.3.4 Front End Requirements

A high heat load (HHL) front end will be required to handle the emitted power and power density from the two collinear undulators. For 1.5 m long undulators with 3.0 cm period and pole gap of 13 mm, the resulting peak field is 0.896 T (K_{max}=2.51, E_{min}=2.75 keV in linear mode). The maximum total power at "closed gap" (maximum current) is calculated at 5.5 kW for a single device so two devices will be at 11 kW, well below the 21 kW limit. On-axis power density is also calculated to be well within the 590 kW/mrad^2 limit of a HHL front end.

6-9.4 Beamline Layout

6-9.4.1 X-ray Optical Layout

Overall layout

The x-ray optical layout is schematically represented in Figure 6.80. A XBPM in the front end provides positional and angular source stability. White beam slit aperture of approx. 0.5×0.5 mm^2 limits heat load on the monochromator by blocking undulator radiation outside central cone. A Si(111) monochromator covers the 2.75-27 keV energy range. While a horizontally-diffracting monochromator may present an advantage in terms of vibrations (better tolerated in the horizontal plane due to the larger source size), power restrictions on the linear-vertical mode may force a vertically-diffracting geometry which preserves intensity of linear-horizontal polarized beams. Second crystal PZT stages for fine control of both pitch and roll angular motions are needed for dynamic control (feedback) of horizontal and vertical beam position using XBPMs located in the end stations (0.1 micro-rad accuracy). Vertically-reflecting, toroidal and cylindrical mirrors provide near full ID flux into focused beams in the 10-40 micron range at two end stations, in addition to harmonic rejection. These mirrors are used for experiments that do not require spot sizes below 20 microns (e.g. XMCD/XMLD experiments at ambient or low pressures) or experiments that cannot use a strongly convergent beam (e.g. high Q resolution x-ray resonant magnetic scattering experiments at high pressure). An in-vacuum polarimeter is used to measure the polarization content of the beam. Diamond XBPMs are used for active feedback stabilization of beam position utilizing monochromator second crystal PZT stages. An in-vacuum chopper operating at approximately 1 kHz is used in double lock-in measurements where signals from photodiodes undergo beam on/off modulation (for dark current subtraction) in addition to polarization modulation (dichroic effect measurement). K-B mirrors with fixed curvature are used to deliver high flux (approx. 25-40% of ID beam) into ∼ 150 (250) nm focused beams at short (long) working distance instruments at two end stations.

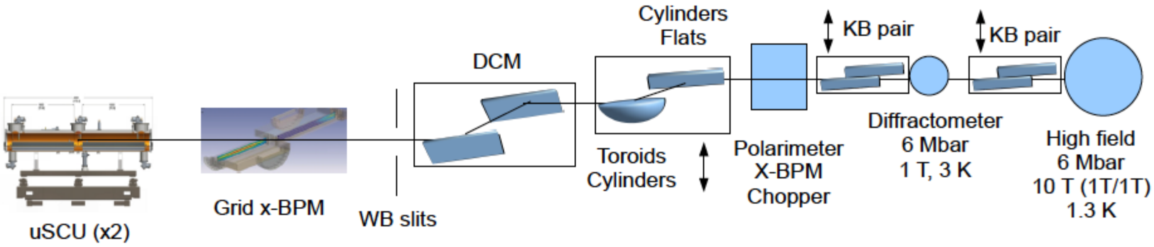

Figure 6.80. Simplified version/schematic of x-ray optical layout of POLAR beamline.

Description of optical components

Universal SCU (×2) (New): Two identical "SCAPE" superconducting undulators placed in a single cryostat with steering and corrector magnets provide tunable polarization states (LCP, RCP, L-H, L-V) in the 2.75-27 keV energy range with ability to rapidly modulate polarization using electron orbit bumps or undulator current bumps.

Double Crystal Monochromator (∼ 29 m): LN2 Internally-cooled, low vibration (< 0.1 micro-rad) diffracting DCM with provision for two sets of crystals. Second crystal stage equipped with pitch and roll PZT stages for dynamic feedback of beam position using diamond x-ray beam position monitors in end stations (0.1 micro-rad stability). Si(111) crystals are used for the entire 2.75-27 keV range with the exception of a narrow energy range around 2.8 keV when operating in circular or L-V polarization modes (θ_{Bragg}=45°). A second set of 6H-SiC crystals can potentially preserve polarization/intensity at these energies (L-edges of 4d metals Ru, Rh, Pd are in the 2.8-3.3 keV range). The (0006) reflection of 6H-SiC crystals is at θ_{Bragg}=61.5°at 2.8 keV and thermal conductivity, peak reflectivity, and energy resolution are similar to Si (Section 6-9.4.2). In addition, SCAPE undulators can generate elliptical polarization at these energies to preserve the degree of circular polarization after the mono.

Double toroid, double cylinder mirror ($\sim$ 48 m) (Existing tank, new mirror/bender): Vertically-reflecting (upwards), bendable mirror about 0.6 m long provides near full ID flux into 10-40 micron-size beams at two end stations, as well as harmonic rejection. These beams are needed for experiments that do not benefit from smaller spot size and related flux reduction, or strong beam convergence. These include XMCD/XMLD experiments at ambient or low pressures and high Q resolution XRMS experiments. The mirror has Pd and Si toroids with sagittal radii of 86 mm designed to focus horizontally @ 60m (72m) at 4.5 (2.7) mrad in the 2.7-14 (6-23) keV range with sufficient harmonic rejection. The mirror also has Pd and Si stripes for vertical focusing and harmonic rejection when used in combination with a second mirror downstream (see Section 6-9.4.2 for details). The Pd cylindrical stripe provides vertical focusing @ 60 m (@72 m) at 2.2 (1.2) mrad in the 14-27 (23-27) keV range. The Si cylindrical stripe provides vertical focusing @ 72 m at 5 mrad in the 2.7-6 keV range (see Section 6-9.4.2). Slope errors below about 0.3 x 10 μrad^2 are sufficient for the required spot sizes in the 10-40 microns range. The mirror is retractable. Ray tracing calculations for a representative case are included in Section 6-9.4.2.

Double cylinder, double flat mirror ($\sim$ 50 m) (Existing tank, new mirror): Vertically reflecting (downwards), non-bendable mirror about 0.6 m long, returns beam to horizontal plane and provides near full ID flux into 10-40 micron-size beams at two end stations as well as harmonic rejection. Mirror has cylindrical Pd (Si) stripes with sagittal radii of 37 (153) mm designed to focus horizontally @60m (72m) at 2.2 (5.0) mrad in the 14-27 (2.7-6) keV range with sufficient harmonic rejection. The mirror also has Si and Pd "flat" stripes for harmonic rejection when used in combination with a second mirror upstream (see Section 6-9.4.2 for details). The two mirrors combined provide focusing and harmonic rejection at both instruments across the entire energy range. Slope errors below about 0.3 x 10 μrad^2 are sufficient for the required spot sizes in the 10-50 microns range. The two mirrors are separated by $\sim$ 2.0 m, resulting in a vertical beam offset of 4 mm/mrad incidence angle. The mirror is retractable.

Polarimeter ($\sim$ 53.5 m) (New): In-vacuum polarimeter to measure polarization components of incident beam consists of (retractable) 90°scatterer, collimator, and two photodiodes all rotating in unison azimuthally around the incident beam direction.

XBPM ($\sim$ 53.6 m) (New): In-vacuum (retractable) diamond x-ray beam position monitor used for active feedback stabilization of beam position in both vertical and horizontal using mono's second crystal pitch and roll PZT stages (0.1 μrad stability).

Chopper ($\sim$ 54 m) (New): In vacuum chopper operates at $\sim$ 1 kHz to subtract dark current in photodiode detectors. This is used in double lock-in measurements where dark-current-subtracted signals undergo polarization modulation.

K-B Pair ($\sim$ 59 m) (New): Fixed curvature K-B mirrors deliver $\sim$ 150 nm beams at diffractometer position (6 Mbar, 1 T, 3 K instrument with WD=10 cm). Optimal mirror lengths of 350 and 122 mm for vertical and horizontal focusing, respectively, are designed to optimize transmission (T) and spot size area (S) (figure of merit T/S^2). Analytical calculations yield beam size of 142(83) nm (V) x 97(107) nm (H) with transmission of 24%(25%) for timing (brilliance) modes, respectively (E=10 keV). Full analysis is given in Section 6-9.4.2. Slope errors ∼ 0.1 μrad and surface height fluctuations of about 1 nm would be needed, both achievable for such short mirrors with today's technology. Mirrors have Si, Pd and Pt stripes to cover the entire energy range at 3 mrad incidence angle. Mirrors are retractable. Ray tracings, including the effect of two sources on spot size, are included in Section 6-9.4.2.

K-B Pair (∼ 72 m) (New): Fixed curvature K-B mirrors deliver ∼ 250 nm beams at high field magnet position (6 Mbar, 10 T, 1.3 K, WD=40 cm). Optimal mirror lengths of 535 and 243 mm for vertical and horizontal focusing, respectively, are designed to optimize transmission (T) and spot size area (S) (figure of merit T/S^2). Analytical calculations yield beam size of 261(147) nm (V) x 237(267) nm (H) with transmission of 41%(42%) for timing (brilliance) modes, respectively (E=10 keV). Full analysis is given in Section 6-9.4.2. Slope errors ∼ 0.1 μrad and surface height fluctuations of about 1 nm would be needed, both achievable for such short mirrors with today's technology. Mirrors have Si, Pd, and Pt stripes to cover the entire energy range at 3 mrad incidence angle. The mirrors are retractable. Ray tracings are included in Section 6-9.4.2.

6-9.4.2 Optical Simulations

ZP versus K-B mirrors; Optimization of K-B mirrors

Analytical calculations were carried out for both zone plate (ZP) and K-B mirror focusing at the locations of primary beamline instruments [134]. These are a high pressure/low field instrument at ∼ 59 m with a working distance (WD) of 100 mm and a high pressure/high field instrument at ∼ 72 m with WD=400 mm. The results of this analysis are summarized in Table 6.30. K-B mirrors generally lead to smaller spot size and significantly higher transmission (over ×2) relative to zone plates. A further advantage of K-B mirrors is their achromaticity, which greatly simplifies implementation in spectroscopic studies. Therefore K-B mirrors were chosen over zone plates as the optics of choice for delivering the required ∼ 200 nm beams at beamline instruments.

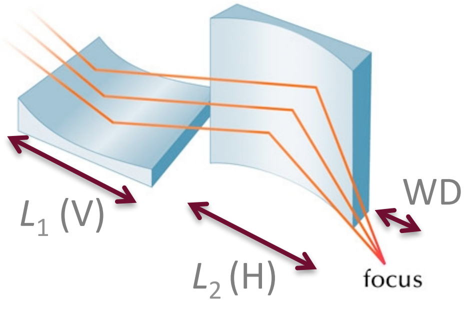

Figure 6.81. Transmission and focused spot size were parameterized in terms of mirror length L1, L2 to balance polarized flux and focused spot size.

Optimization of K-B mirrors involved a careful analysis of the trade-off between polarized flux and spot size. Analytical calculations of mirror transmission and focused spot size were parameterized

Table 6.30. Analytical calculations of x-ray focal size and transmission (at 10 keV) obtained with zone plate and K-B mirror focusing optics for two different instruments with working distances (100 mm and 400 mm). Source-to- image distance is 59 m (100 mm WD) and 72 m (400 mm WD). K-B mirrors are separated by 10 mm. Spot sizes and transmission are given for timing 48 bunch (brilliance 324 bunch) modes, respectively, using 42 pm-rad lattice parameters. K-B mirror lengths are averaged of optimized lengths for timing and brilliance modes. K-B mirror length is obtained by optimizing figure of merit T/S^2 as described elsewhere in this section. K-B transmission includes mirrors' reflectivity (0.81)

	Transmission *48b(324b)*	**Focal size FWHM (H)** *48b(324b)*	**Focal size FWHM (V)** *48b(324b)*
100 mm WD			
Zone Plate Δr (out. zone)= 50 nm D = 750 μm 3720 zones	9(10)%	167(188) nm	117(80) nm
KB pair 122 (H) x 350 (V) mm^2 3 mrad incidence	24(25)%	97(107) nm	142(83) nm
400 mm WD			
Zone Plate Δr (out. zone)= 100 nm D = 1500 μm 3720 zones	17(18)%	525(596) nm	348(210) nm
KB pair 243 (H) x 535 (V) mm^2 3 mrad incidence	41 (42)%	237(267) nm	261(147) nm

in terms of the length of KB mirrors (see Figure 6.81) [134]. Geometrical constraints account for location and WD for the two instruments and a 10 mm separation between mirrors (vertical focusing mirror placed upstream of horizontal focusing mirror). Undulator length of 1.8 m was used to calculate source size and divergence. Calculations of spot size include contributions from diffraction and demagnification (slope errors, neglected in the analytical calculations, would need to be about 0.1 micro-rad). Mirror incidence angle is 3 mrad. Calculations were done using source size and divergence values for the 42 pm-rad APS-U lattice in 48 (timing) and 324 (brilliance) bunch modes, as well as for current APS values. We define (S_1, T_1) and (S_2, T_2) as the spot sizes and transmissions for V and H mirrors, respectively. We also define a "compounded" spot size and transmission for both mirrors, $S=S_1 \times S_2$ and $T=T_1 \times T_2$.

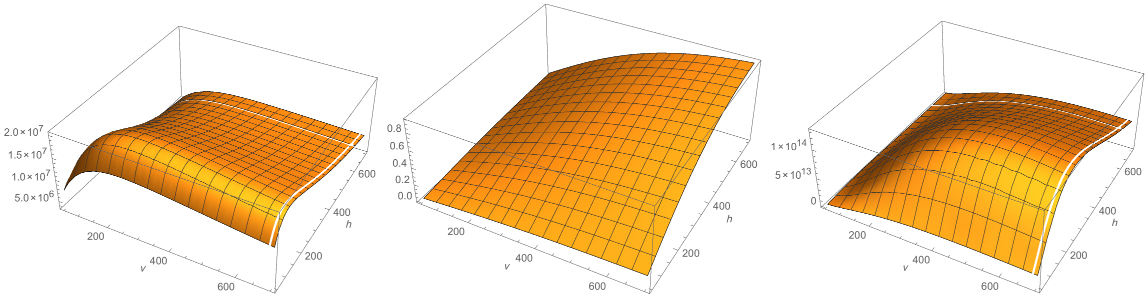

Figure 6.82. Inverse of compounded spot-size 1/S (left), compounded transmission T (middle) and figure of merit T/S^2 (right) as function of V, H mirror lengths for APS-U 48 bunch mode (E=10 keV). Units for left and right plots are mm^2 and mm^4, respectively. Data is for instrument at 72 m (WD=400 mm).

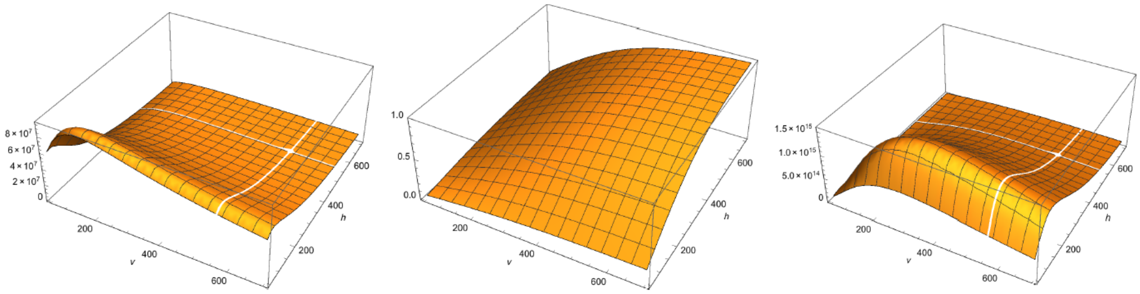

Figure 6.83. Inverse of compounded spot-size 1/S (left), compounded transmission T (middle) and figure of merit T/S^2 (right) as function of V, H mirror lengths for APS-U 48 bunch mode (E=10 keV). Units for left and right plots are mm^2 and mm^4, respectively. Data is for instrument at 59 m (WD=100 mm).

Figure 6.82 (left) shows a plot of 1/S (inverse compounded spot size) for the 72 m instrument (WD=400 mm) as a function of V, H mirror lengths. Results for 48 bunch/timing mode are shown (E=10 keV). Spot size first decreases with a decrease in mirror length due to increased demagnification, only to increase again at short mirror lengths due to diffraction. Figure 6.82 (middle) shows compounded transmission T which increases with mirror length until full illumination is achieved. In order to balance transmitted flux and spot size, a "figure of merit" is defined as T/S^2 and plotted in Figure 6.82 (right) as function of mirror length. The maximum in this 3D plot corresponds to 516 (246) mm V(H) mirror lengths, and 259(237) nm V(H) spot size with a combined transmission of 0.41 (including 0.81 reflectivity from double bounce). Other figures of merit were also explored.

For example, optimization using a T/S^3 figure of merit only provided a marginal reduction in spot size ($< 7\%$) at the expense of a larger decrease in flux density ($\sim 15\%$) hence deemed inferior to the power=2 optimization. Optimized V(H) mirror length is slightly different for 324 bunch mode at 554(241) mm. Mirror length values shown in Table 6.30 are averages of optimized values for 48 and 324 bunch modes. Table 6.30 shows spot sizes and transmission corresponding to these final mirror lengths in both timing and brilliance modes.

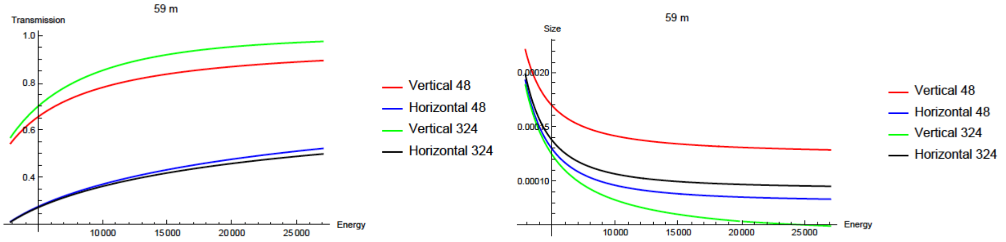

Figure 6.84. Energy-dependence of compounded K-B mirror transmission and spot size in both timing and brilliance modes. Data are for short WD instrument located at 59 m. Beam size units are mm.

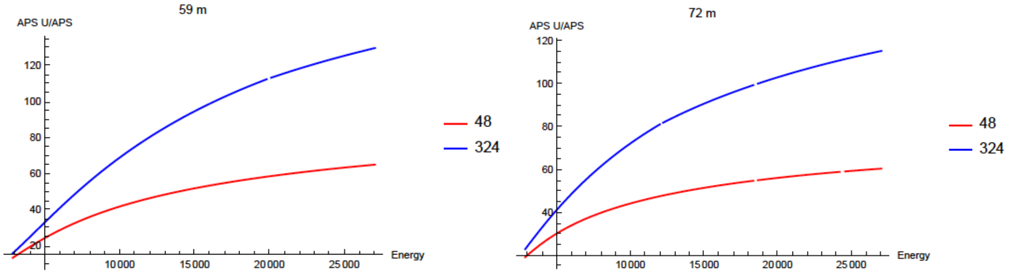

Figure 6.85. Brilliance gain relative to current APS defined as (SAPS/SAPS-U)(TAPS-U/TAPS) where S and T are compounded spot size and transmission, respectively. Top (right) plots are for short(long) WD instruments at 59(72) m, respectively. Average gains are $\sim \times 50$ at 10 keV with roughly $\times 20$ coming from reduced horizontal source size and the additional $\times 2.5$ from reduced horizontal source divergence. Average gains are $\sim \times 80$ at 20 keV.*

Calculations were repeated for the instrument at 59 m (WD=100 mm). Figure 6.84 shows 1/S, T, and T/S^2 contours. The maximum in T/S^2 for 48 bunch mode (10 keV) is obtained for 327 (125) mm V(H) mirror lengths, and 140 (97) nm spot sizes with a combined transmission of 0.23. Mirror length is slightly different for 324 bunch mode, 371(121) mm V(H). Averaged mirror length was used in final calculations leading to spot sizes and transmission values listed in Table 6.30. We note that both spot size and mirror transmission display significant energy dependence as a result of decreasing source size and divergence with increasing energy. For example, compounded mirror transmission becomes ~ 60 (42)% at 27 keV for long (short) WD instruments in 48 bunch mode. Spot size area decreases slightly in the 10-27 keV range, by up to 25(5)% in 324(48) bunch mode, respectively, but a significant increase in spot size takes place below 5 keV. For the instrument at 59 m (WD=100 mm), V(H) spot size increases by 57(90)% at 3 keV in 48 bunch mode. The corresponding numbers for the instrument at 72 m (WD=400 mm) are 42(50)% (this is due to increase in source size at low energies). Mirror transmission drops at low energy due to increased source divergence. Energy dependence of transmission and compounded spot sizes are shown in Figure 6.85 for the short WD instrument (both 48 and 324 bunch modes).

It is instructive to compare gains in brilliance for the optimized focused beams in APS-U relative to the current APS source. Figure 6.90 shows the figure of merit for brilliance gains $[(S_{APS}/S_{APS\text{-}U})\times(T_{APS\text{-}U}/T_{APS})]$ for both instruments. The gains average to ×50 at 10 keV (transmission contributes $\sim\times2.5$, a result of reduced beam divergence, and spot size $\sim\times20$, a result of reduced beam size).

Ray tracing calculations for Toroidal mirror

Ray tracing calculations were carried out for a double toroid mirror located at $\sim$ 49 m from the source using APS-U source parameters corresponding to 48 bunch mode. The active area of the mirror is 600 mm. Meridional and sagittal slope errors are 0.3 μrad x 10 μrad, respectively. These specs are standard even with today's mirror technology. In these calculations, each toroid is designed to focus at the location of a primary instrument (diffractometer @ $\sim$ 59 m and high-field magnet @ $\sim$ 73 m) at 3 mrad incidence angle. Sagittal radii Rs=50(95) mm and meridional radii 5.5(10.5) km were used for 59(73) m instruments, respectively (mirror is bendable). Figure 6.86 shows spot sizes of 10×20 μm (HxV) and 20×40 μm for the instruments at 59 and 73 m, respectively (E= 8 keV). All rays are intercepted so transmission is only limited by reflectivity of mirror (0.9). Using a 1.8 m long, SCAPE undulator as source and Si(111) bandwidth, the calculated flux in focused beams is 4.5×10^{13} ph/sec.

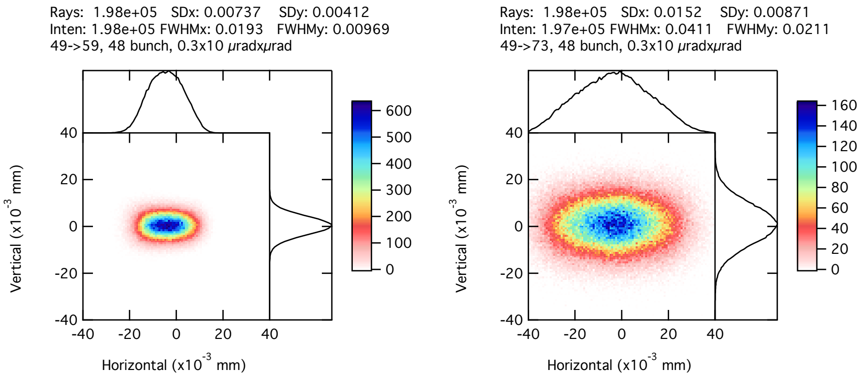

Figure 6.86. Ray tracing calculations of focused beams at diffractometer (59 m) and high field magnet (73 m) positions obtained with double toroid mirror located at 49 m from the source.

Ray tracing/Hybrid calculations for K-B mirrors

The analytical calculations used to optimize K-B mirror length and T/S^2 figure of merit described in Section 6-9.4.2 placed the x-ray source at the center of the straight section. Ray tracing/hybrid calculations were carried out separately for each one of the two undulator sources envisioned for this beamline (1.8 m undulators, sources separated by 2 m). Calculations are for E=8 keV in brilliance (324 bunch) mode, and flux estimates are for a single insertion device in circular polarization mode. Figure 6.87 shows ray tracing/hybrid calculations of focused beams using the downstream SCAPE undulator as the source (hence distances to instruments are 58 m and 71 m, respectively) and mirror lengths obtained from T/S^2 optimization (given in Table 6.30, Section 6-9.4.2).

The effect of K-B mirrors not imaging a source at the center of the ID, but rather two sources displaced by ± 1 m, was evaluated in more detail. Figure 6.88 shows ray tracing/hybrid calculations

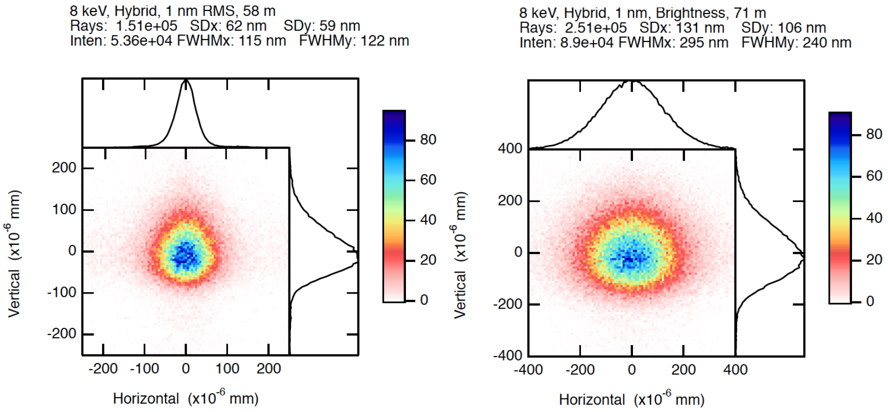

Figure 6.87. Ray tracing/hybrid calculations of focused beams for short WD=100 mm instrument at 59 m (left) and long WD=400 mm instrument at 72 m (right) using the upstream insertion device as the source. Calculated flux is 5.4×10^{12} ph/sec and 1.3×10^{13} ph/sec, respectively. Spot sizes of 115×122 nm^2 (295×240 nm^2) and transmission values of 35% are obtained. These calculations use wave propagation [17] and 1 nm RMS figure error. Calculations are at 8 keV using the brilliance mode (324 bunch) of the 42 pm-rad source.

for focusing at 59 m using the K-B mirror length listed in Table 6.30 of Section 6-9.4.2. Since the elliptical figure of the K-B mirrors is optimized to focus at the center of the ID, it is not surprising that the calculation for a single source at the center of the ID gives a rather symmetric beam (top left panel). However, clear asymmetries are observed when the actual source position is accounted for (top middle, right panels). The integrated intensities of focused beams from the two devices differs by about 5%. The spot sizes are very similar. The shape asymmetry is a concern when beams from different devices are used in spatially-resolved dichroic measurements of electronic inhomogeneity when domain size is comparable to beam size.

Since the asymmetry in focused beams is related to improper elliptical mirror shape (optimized for a source at the center of the straight) it can be minimized by limiting the illuminated area of the mirrors (primarily the vertical focusing mirrors which are twice as long as the horizontal focusing mirrors; see Table 6.30). Figure 6.89 shows that, for the instrument at 59 m, reducing the illuminated area to 100×160 mm^2 (from 122×350 mm^2) removes most of the asymmetry, albeit with a reduction in flux by ×2.2. The shape-corrected beams display a 6% difference in their integrated intensity. Therefore, defining slits located before the K-B mirrors can be used to remove beam asymmetry for experiments where this is an issue (dichroic imaging where domain size is comparable to beam size). Note that focused spot size is slightly larger ($\sim$ 15%) due to diffraction effects. The required slit size for the 59 m instrument discussed here is 0.48 x 0.3 mm^2 (VxH).

Characterization of 6H-SiC crystals for potential use as polarization/intensity preserving monochromator in the vicinity of 2.8 keV

The Si(111) monochromator is not suitable for dichroic measurements in the vicinity of 2.8 keV ($\theta_{\mathrm{Bragg}} \sim 45°$) when polarization is varied at the source. Circular polarization is converted to linear polarization and the intensity of linear-vertical polarization is strongly suppressed in the vertical diffraction geometry. 6H-SiC crystals are a good candidate to preserve polarization and intensity

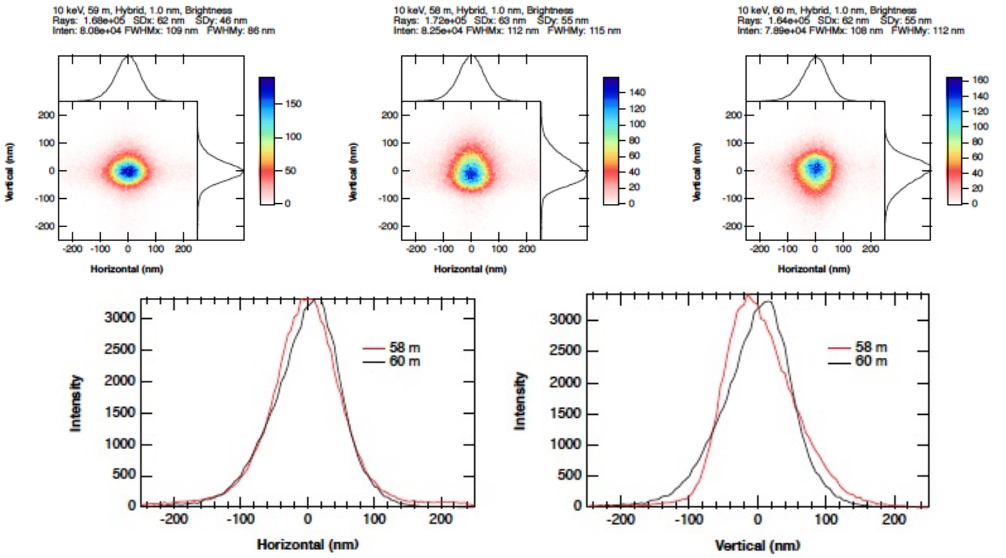

Figure 6.88. Ray tracings/hybrid calculations of focused beams at 59 m (short WD instrument) at E=10 keV in brightness (324 bunch) mode. A 1 nm RMS figure error is used. The focused beams are images of an undulator source in the middle of the straight section (top left) and sources displaced by 1 m (top middle) and -1 m (top right). Since the asymmetry is due to improper elliptical mirror shape when the source is displaced, the effect is more significant in the vertical direction (mirror length for vertical focusing is more than double the length of horizontal focusing mirrors, see Table 6.30 of Section 6-9.4.2).

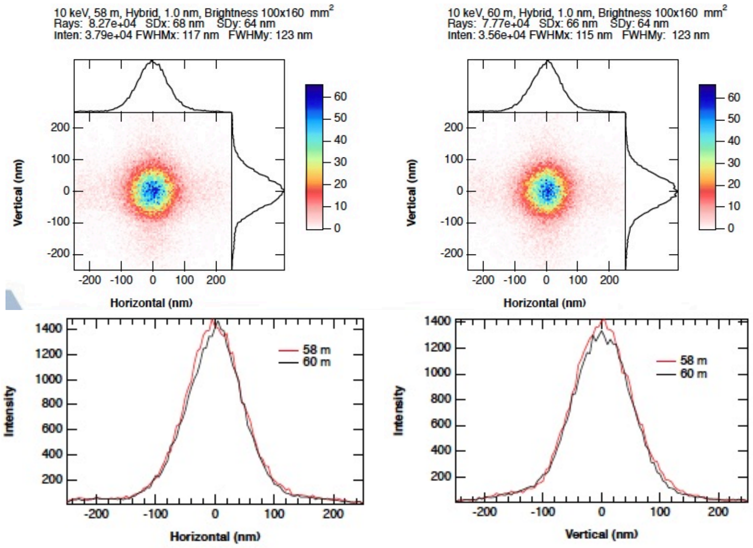

Figure 6.89. Focusing at 59 m from undulator sources at + 1 m (top left) and -1 m (top right) from the center of the straight section. The asymmetry in spot size is largely removed by limiting the illuminated area of the mirror with a defining slit, with a reduction in flux by ∼ × 2.2.

in this narrow energy range. The (0006) reflection of 6H-SiC crystals is at θ_{Bragg}=61.5°at 2.8 keV and thermal conductivity, peak reflectivity, and energy resolution are similar to Si. Theoretically, Darwin width of lowest order (0006) reflection is 0.294 eV at 2.8 keV, and single bounce peak reflectivity 74% (average reflectivity 60%), very comparable to Si (111). 6H-SiC crystals in hand have been characterized with white beam topography and double-crystal rocking curve topography measurements at 1-BM [18]. These measurements, summarized below, show near perfect crystalline quality in two out of three crystals, which is preserved after mounting/clamping. Figure 6.90 shows the three crystals used in the studies. Figure 6.91 shows white beam topographs for the three crystals, indicating that, while crystal #3 is plagued by a high density of dislocations and is therefore unsuitable, crystal #1, #2 are of relative high quality. Double crystal rocking curve topography measurements at E=8 keV used a symmetrically cut Si(331) crystal as collimator to probe the well matched (00012) reflection of 6H-SiC in a double crystal setup. The theoretical Darwin width of this reflection at 8 keV is 12 micro-rad. The measurements, shown in Figure 6.92, show rocking curve values in the 13-15 micro-rad range and 5-6 micro-rad COM rms when the whole crystal dimension is proved. Over a smaller 4×4 mm^2 low strain area, the rocking curves are 13 micro-rad with less than 1 micro-rad COM rms deviation. For comparison, the Darwin width of the (00012) reflection at 2.9 keV is 170 micro-rad. The 4×4 mm^2 area is more than sufficient for this application (beam footprint at this energy would be under 1 mm^2).

Figure 6.90. Three single crystals of 6H-SiC used in white beam topography and mono beam double crystal rocking curve topography [18].

Crystal #2 was mounted on a Ni-plated Cu block with a GaIn eutectic for thermal contact and clamped for mechanical stability to simulate conditions necessary for cooling. The rocking curve topographs show negligible strain associated with the mounting/clamping (Figure 6.93). The low on-axis power emitted from a SCAPE undulator in circular mode, of about 4 W at closed gap through a 0.5×0.5 mm^2 aperture at 25 m, may enable use of water-cooled crystals in this polarization mode although power in linear-vertical mode is much larger at closed gap (50 W). Simulations of heat transport in SiC-In-Si and SiC-GaIn-Si configurations will be undertaken to explore feasibility of mounting the 6H-SiC crystals onto Si crystals cooled at 120 K. Alternatively they will be mounted and independently cooled on the second crystal bank of the monochromator.

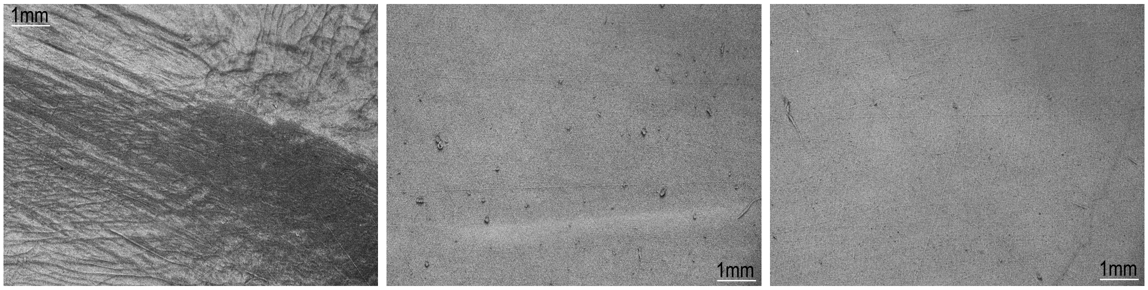

Figure 6.91. White beam topographs for crystals #3 (left), #2 (middle) and #1 (right). Crystal #3 is plagued with dislocations and is therefore unsuitable. Crystal #2 is of high quality although some superscrew dislocations (micropipes) are observed. Crystal #3 is of highest quality with a much lower density of micropipes (courtesy of XiangRong Huang [18]).

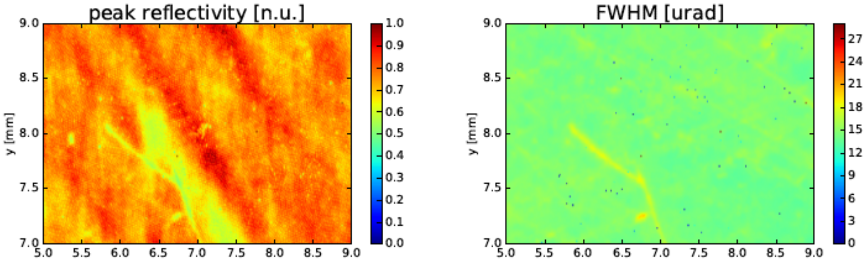

Figure 6.92. Rocking curve topographs of (00012) reflection of 6H-SiC crystal #2 (8 keV) over a 2×4 mm^2 area showing peak reflectivity and Darwin width near theoretical values (courtesy T. Kolodziej [18]).

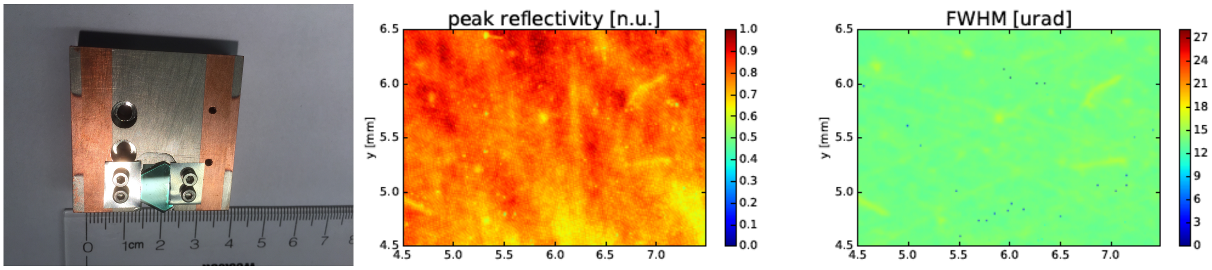

Figure 6.93. 6H-SiC crystal mounted on Ni-plated Cu block with GaIn eutectic for thermal contact (left) and corresponding rocking curve topographs (middle/right). The mounting/clamping did not introduce significant strain in the crystal (courtesy T. Kolodziej [18]).

Details of toroidal, cylindrical, and flat mirrors used for moderate focusing at two end stations

Two mirrors are used to provide moderate focusing in the 10-40 microns range at the two end stations and to provide the necessary harmonic rejection for all energies in the 2.75-27 keV range. The mirrors are used in a DCM geometry reflecting in the vertical plane. Mirror 1 at ∼ 48 m reflects up, while Mirror 2 at ∼ 50 m reflects down. A schematic of the mirror stripe layouts is shown in Figure 6.94. The first mirror is bendable and features Si and Pd toroids (denoted as Si1-T and Pd1-T, respectively) and Si and Pd stripes (which become cylinders under bending, denoted as Si1-C and Pd1-C). The second mirror is not bendable and features Si and Pd cylinders for horizontal focusing (denoted as Si2-C and Pd2-C) and two flat stripes (denoted as Si2-F and Pd2-F). Table 6.31 shows mirror parameters for operation spanning the entire energy range.

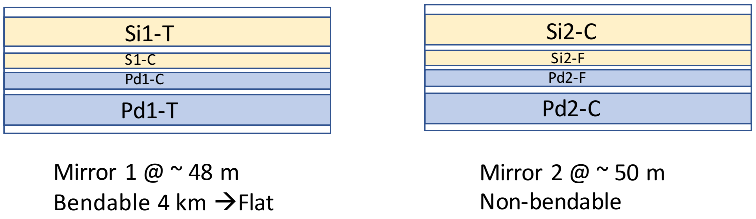

Figure 6.94. Stripe configuration for moderate focusing mirrors. T, C, and F stand for toroid, cylinder, and flat, respectively.

Table 6.31. Mirror configuration for moderate focusing and harmonic rejection across the 2.75-27 keV range. Emphasis is placed on large harmonic rejection below 10 keV as well as preserving focused spot size

	Focus @ 60m			
Energy (keV)	2.7-6.6	6.6-14	14-27	
Mirrors	Si1-T+Si2-F	Pd1-T+Pd2-F	Pd2-C+Pd1-C	
Angle (mrad)	4.5	4.5	2.2	
R_s (mm)	86	86	37	
R^m (km)	4.3	4.3	7.5	
Critical Energy	∼ 6.6	∼ 14	∼ 27	
Harmonic rej.	x8000 @ 4keV	x8000 @ 8keV		
Focus (μm^2) (HxV)	∼ 10×20	∼ 10×20	∼ 10×20	
	Focus @ 72m			
Energy (keV)	2.7-6	6-11	11-23	23-27
Mirrors	Si2-C+Si1-C	Si1-T+Si2-F	Pd1-T+Pd2-F	Pd2-C+Pd1C
Angle (mrad)	5.0	2.7	2.7	1.2
R_s (mm)	153	86	86	37
R_m (km)	6.1	11.9	11.9	27
Critical Energy	∼ 6	∼ 11	∼ 23	>27
Harmonic rej.	×2e^5@4keV	×6e^4 @8keV	×210 @10 keV	
Focus (μm^2) (HxV)	∼ 20×40	∼ 20×40	∼ 20×40	∼ 20×40

6-9.4.3 Beamline Physical Layout

Overall Beamline

A physical layout of the beamline is shown in Figure 6.95. The beamline remains in its current location at sector 4. The most significant changes needed to sector infrastructure are:

1. Replace SmCo3.5 planar undulator with two SCAPE undulators;
2. Upgrade front end to HHL version to handle power from dual undulators;
3. Expansion of existing mini-hutch (MH) before 4-ID-B enclosure by ∼ 4 m upstream and ∼ 1 m outboard, with door addition, to accommodate toroidal/cylindrical/flat mirrors;
4. Add outboard doors to 4-ID-B enclosure for instrumentation maintenance and user access;
5. Expand 4-ID-D enclosure by 2 m upstream, 1 m inboard/outboard and raise ceiling to 6 m, to accommodate high field (10 T) magnet and platform/crane for vertical sample loading; add outboard door for user access;
6. Add control room between B and D enclosures (outboard side).

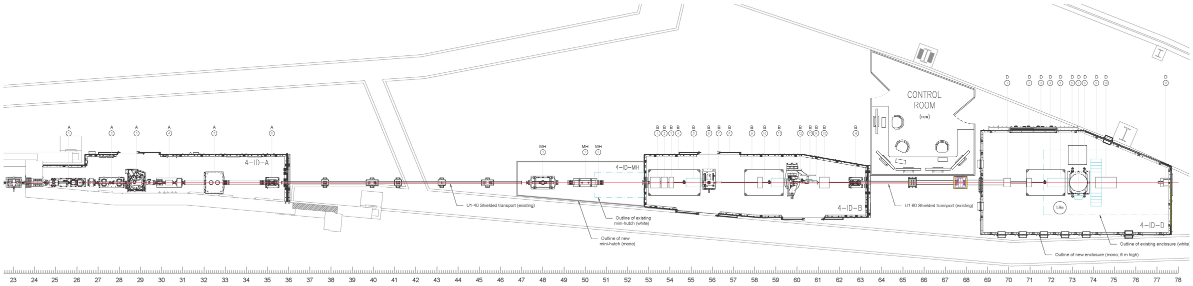

Figure 6.95. Overall physical layout assuming location at S4. Expanded views of the enclosures are shown later in this document.

First Optics Enclosure (FOE) and Infrastructure

A physical layout of the FOE is shown in Figure 6.96. Key components in the FOE are HHL white beam slits, internally cooled DCM, Mask and Collimator, white beam stop, collimator and photon shutter. Figure 6.95 shows the location of these components as well as whether these components are already available (Existing), ought to be secured (New), or ought to be modified (Modified). While a horizontally-diffracting monochromator may present an advantage to mitigate the effect of vibrations on focused spot size, power limitations in linear-vertical polarization mode at low energies may force a vertically diffracting geometry. The existing phase retarder tank currently in use at 4-ID will be placed and remain in the FOE until the polarization modulation scheme using tandem universal SCAPE superconducting undulators is fully commissioned and operational.

4-ID-B (with mini-hutch) endstation

Components 4-ID-B (with mini-hutch) endstation A physical layout of the first experimental station including its upstream mini-hutch is shown in Figure 6.97 and Figure 6.98. The existing mini-hutch will be expanded by ∼ 4 m upstream and ∼ 1 m outboard to accommodate two toroidal/cylindrical/flat mirrors; see Figure 6.97. The function and specs for these mirrors are de-

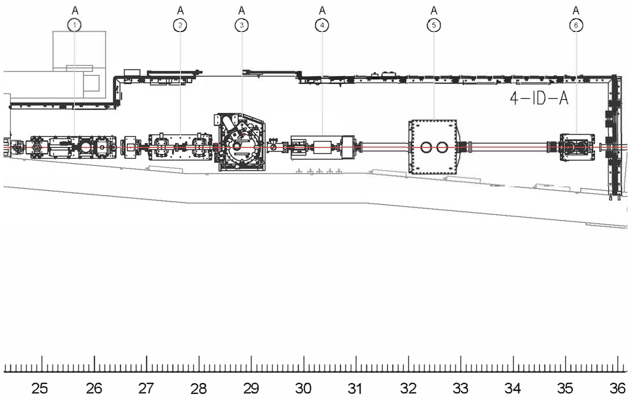

4-ID-A COMPONENTS

No.	Name	Status
1	HHLFE Exit Table	New
2	HHL White Beam Slits (H + V)	New
3	Double Crystal Monochromator	New
4	WB Stop & Collimator	New
5	Phase Retarder Tank	Existing
6	Mono Shutter	New

Figure 6.96. Physical layout of first optical enclosure denoting component locations and descriptions.

scribed in Section 6-9.4.1 and Section 6-9.4.2. The single Be (or diamond) window in the beamline, after the second mirror, preserves flux at low energies and protects the mirrors from poor vacuum in the downstream experimental stations.

Beam diagnostics components at the entrance of the 4-ID-B station include in-situ polarimeter, diamond XBPM, and in-vacuum chopper (all NEW). Their functions were described in Section 6-9.4.1. Other components include bendable K-B mirrors (MODIFIED) @ $\sim$ 55.2 m, fixed curvature K-B mirrors (NEW) @ $\sim$ 59.5 m, polarization analyzer (NEW), and photon shutter (see Figure 19b for a complete list of components). Doors will be added in the outboard side of this station for user access from the (new) work area.

Instruments 4-ID-B endstation The first instrument located @ $\sim$56 m is an (EXISTING) "2 T" electromagnet equipped with a flow cryostat and Ruby fluorescence setup for in-situ pressure calibration. Tunable x-ray spot size down to ~ 10 μm is provided by bendable (MODIFIED) K-B mirrors (bender exists, new 200 mm long mirrors; WD $\sim$ 0.4 m). This instrument is used for polarization-modulated XMCD experiments requiring $P < 1$ Mbar, $T > 10$ K, $H \sim 0.8$ T (a sizable magnet pole gap is needed to accommodate the diamond anvil cell). XMCD experiments at LN$_2$ temperature or above can be carried out with this instrument at no cost to the user (electromagnet is water cooled; no LHe usage). This instrument also allows fast ramping/switching of magnetic field, an advantage over high field superconducting magnets for field-dependent measurements. A schematic of this instrument is shown in Figure 6.99.

A second instrument in this station is built on a (MODIFIED) psi-diffractometer located @ $\sim$ 60 m. This is used for polarization-modulation and polarization-dependent measurements in the scattering channel (see Figure 6.100). Dichroic experiments in the absorption channel requiring precise sample

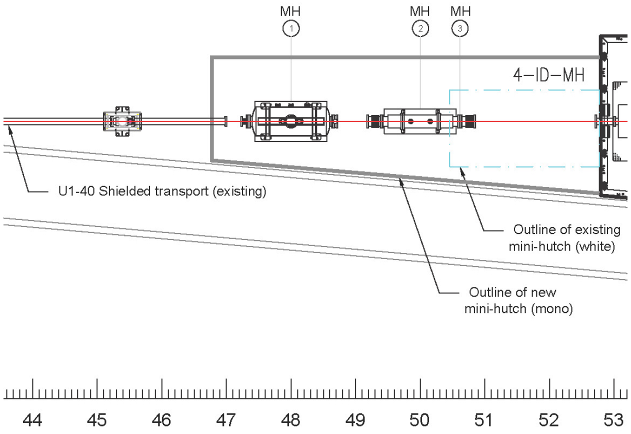

4-ID-MH COMPONENTS		
No.	Name	Status
1	Vertical (Double Toroid + Bender) Mirror	Modified: new mirror, holder, bender
2	Vertical Flat Mirror	Modified: new mirror, holder
3	Be or (Diamond) Window	Existing (new)

Figure 6.97. Mini-hutch enclosure with list and status of components.

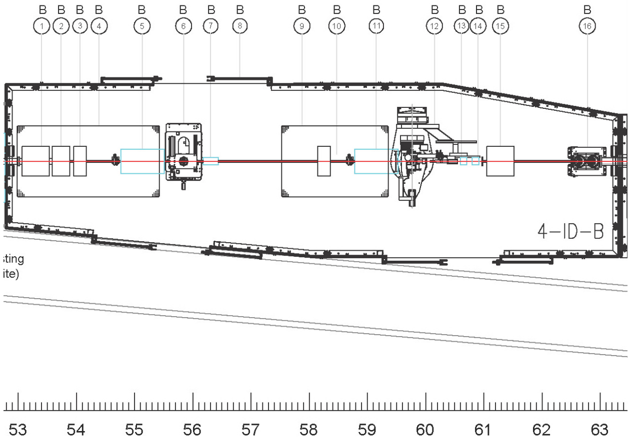

4-ID-B COMPONENTS		
No.	Name	Status
1	In-Situ Polarimeter	New
2	Beam conditioning / Detection *	New
3	In-vacuum Chopper	New
4	Optical Table: 8' x 4', X (2 motors) & Y (1 motor)	New
5	KB Mirrors - Bendable & I0 Detector	Modified: new mirrors
6	2T Electromagnet	Existing
7	Detector (I) Photodiode	New
8	Enclosure Door, 2 m	New
9	Optical Table: 6' x 4', X (2 motors) & Y (1 motor)	New
10	Mono Slits, Attenuators	Existing
11	KB Mirrors - Fixed Curvature & I0 Detector	New
12	Difractometer & 1 T Magnet	Modified or New
13	Attenuators, Pixel Array Detector	New
14	Polarization Analyzer	New
15	Detector Table / Flight Tube Mount	New
16	Mono Shutter	New

* In-Vacuum Mono Slits, Diamond XBPM, Attenuators

Figure 6.98. First experimental station 4-ID-B with list and status of components.

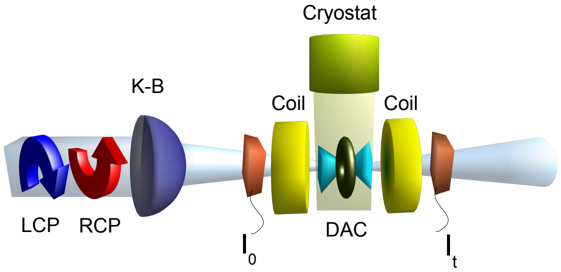

Figure 6.99. Schematic of XMCD instrument in first experimental enclosure (P <1 Mbar, T > 10 K, H < 0.8 T).

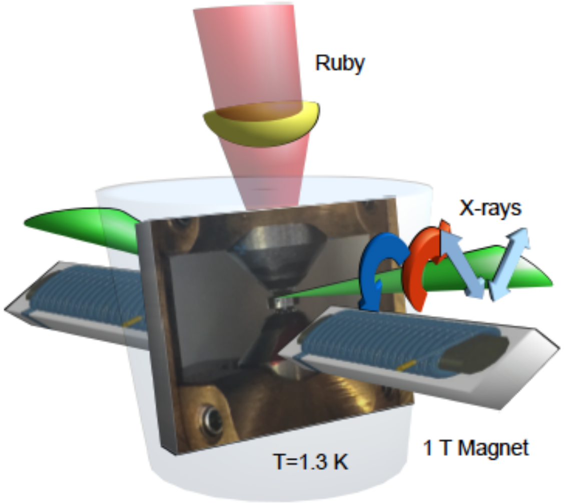

Figure 6.100. Schematic of resonant scattering instrument in first experimental enclosure (P= 6 Mbar, T=1.3 K, H=1 T). This setup is mounted on a six-circle diffractometer.

alignment or highest spatial resolution can also be done in this instrument. X-ray focusing for this instrument ~ 100 x 100 nm^2 is provided by fixed-curvature K-B mirrors described in Section 6-9.4.1 and Section 6-9.4.2 (WD=0.1 m). This allows for mapping of electronic inhomogeneity as well as reaching extreme pressures of up to 6 Mbar. Panoramic DACs made out of high thermal conductivity material CuBe are used to access large swaths of reciprocal space and reach low temperatures. An online Ruby fluorescence system is used for in-situ pressure calibration. Magnetic field is limited to ~ 1 T in order to enable short WD (highest spatial resolution) and preserve angular access (limited with high field SC magnets). Flow cryostats are used to avoid vibrations, and mapping is done by scanning the DAC with high resolution stages compatible with operation at low T in magnetic fields. A schematic of this instrument is shown in Figure 6.100 (diffractometer not shown). Modified diffractometer will have an Eulerian cradle with an open top to access high Bragg angles at low resonant energies and a robust 2-theta arm to support in-vacuum polarization/energy analyzers.

4-ID-D endstation

Components 4-ID-D A physical layout of the second experimental station 4-ID-D is shown in Figure 6.101. The existing enclosure will be expanded by ~ 2 m upstream and 1 m inboard/outboard to accommodate the 10 T high field magnet, a platform required for safe top loading of samples, accessories such as dewars for cryogenic cooling and online Ruby/Raman systems for pressure calibration. A footprint of current and expanded enclosures is shown in Figure 6.101. A door is added in the outboard side of the station for user access from the (new) work area. Components in this enclosure include diamond XBPM, fixed curvature K-B mirrors, optical tables/mounts for detection of incident, transmitted, and fluorescence intensity, and Ruby fluorescence/Raman systems. The hutch ceiling ought to be raised to 6 m to enable top loading of a sample insert into a magnet with the crane operation.

Instruments 4-ID-D A high field superconducting magnet with 10 T longitudinal field and a bore large enough (~ 3”) to accommodate a membrane-driven diamond anvil cell is located @ ~ 73.2 m. This instrument is used for polarization-modulated XMCD and XMLD experiments (1 T transverse and vertical fields are provided by two additional pairs of split coils). X-ray focusing for this instrument ~ 200 (V) × 250 (H) nm^2 is provided by fixed-curvature K-B mirrors described in Section 6-9.4.1 and Section 6-9.4.2 (WD=0.4 m). This allows mapping electronic inhomogeneity as well as reaching extreme pressures up to 6 Mbar. Online Ruby fluorescence and Raman systems are used for in-situ pressure calibration. The sample is cooled with He vapor to avoid vibrations. Attocube stages compatible with 10 T fields and low temperatures are used to scan the DAC for real space mapping. Experiments in both transmission and fluorescence channels are accessible, the latter using axial (backscattering) or radial (gasket) geometries. A schematic of this instrument is shown in Figure 6.102.

6-9.4.4 Additional

Detectors

Experiments in the absorption channel require incident, transmitted, and fluorescence intensity monitors with high dynamic range and linearity. Calibrated photodiodes are preferred for incident

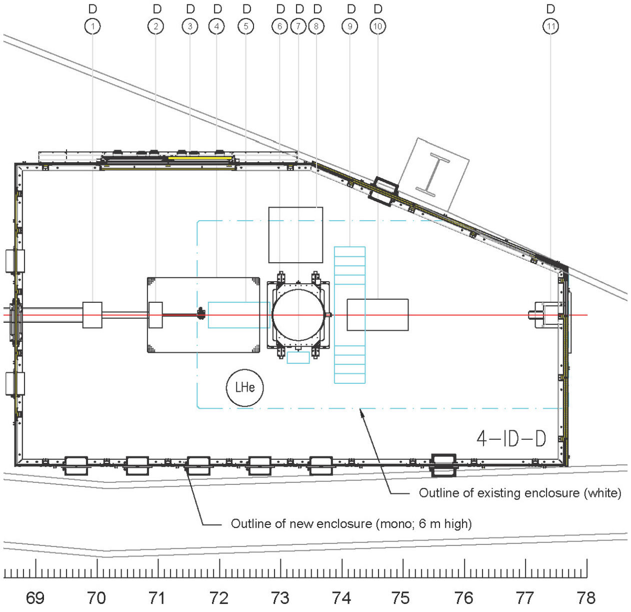

4-ID-D COMPONENTS		
No.	Name	Status
1	In-Vacuum Slits	Existing
2	Beam conditioning / Detection *	See *
3	Enclosure Doors, 1 m & 3 m	New
4	Optical Table: 6' x 4', X (2 motors) & Y (1 motor)	New
5	KB Mirrors - Fixed Curvature & I0 detector	New
6	10 T (longitudinal), 1 T (transverse), 1 T (vertical) Superconducting Magnet	New
7	Fluorescence detector	New
8	Support for Raman System	New
9	Platform Sample Loading	New
10	Detector Table & Detector (I) Photodiode	Existing
11	Beam Stop	Existing

* In-Vacuum Mono Slits, Diamond XBPM, Attenuators

Figure 6.101. Second experimental station 4-ID-D with list and status of components.

and transmitted intensity monitors due to better time response and linearity relative to gas ionization chambers. Dark current subtraction, especially fluctuations at high detector gains, is achieved with use of chopper. Fluorescence detectors ought to accept the largest solid angle compatible with setup and provide high dynamic range and energy resolution. Silicon drift diode arrays, coupled with fast digital signal processing (DSP), are the current method of choice for fluorescence detection. Although current diode and diode-array technology are sufficient to meet the needs of this beamline, new technologies for faster DSP and higher energy resolution detection compatible with experimental needs will be evaluated as they evolve, including use of crystal analyzers and transition edge sensor detectors.

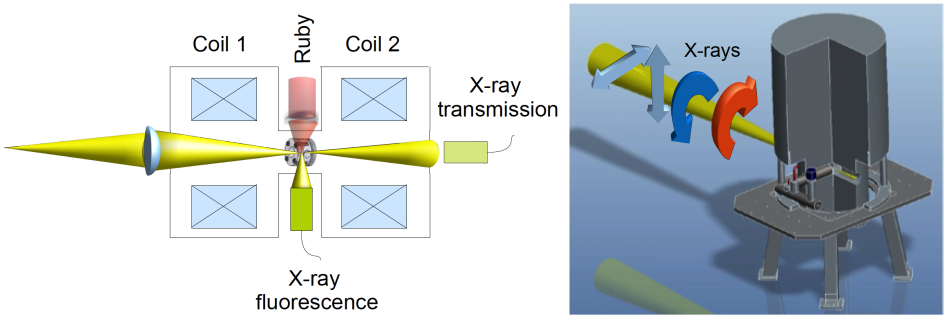

Figure 6.102. Schematic of XMCD/XMLD instrument in second experimental enclosure. The parameter space is P=6 Mbar, H=10 T (longitudinal), H=1 T (transverse/vertical), T=1.3 K. The split coil geometry (only one pair of coils is shown in the schematic at left) allows insertion of Ruby/Raman spectrometers and fluorescence detector into reentrant warm bores along the split direction.

Experiments in the scattering channel require single photon counting point detectors (e.g. avalanche photodiode- APD) or pixel array detectors- PAD with high dynamic range/linearity (e.g. Pilatus or Eiger). These are used to detect small dichroic differences in resonantly scattered intensities at electronic/magnetic Bragg peaks (either coincident with, or away from, lattice Bragg peaks) as well as weak scattering from short/long range electronic/magnetic ordering. Crystal analyzers are also used for background suppression (energy filtering) and for polarization analysis. Current APD and PAD technology allows meeting the demands of this beamline. However, new detector technologies, including PADs with smaller pixel size and higher efficiency polarization analyzers, will be evaluated as they evolve.

Computing

Computing demands and data flow/storage needs are met with current technologies and we do not expect a need to push boundaries in this category.

Specific safety requirements

A few aspects of the operation of this beamline will require special safety procedures. The use of He-gas driven diamond anvil cells for in-situ pressure control at low temperatures requires operation of pressurized gas systems (up to $\sim$ 2000 psi). Class 3b lasers will be needed for in-situ pressure calibration using Ruby fluorescence or diamond vibron (Raman) methods. Operation of high field

(10 T) magnet will require user access restrictions when magnet is energized and elevated platform for top sample loading. Radioactive samples will require special handling. All of the above can be addressed with implementation of controls, interlocks, special operating procedures, and user training.

Specific conventional facilities requirements

Air temperature stability in the experimental enclosures will be needed to maintain spot size stability. This will be accomplished with installation of air conditioning units and curtains at door locations in experimental enclosures. Vibration isolation, also critical for spot size stability, will be achieved with use of He flow/vapor cooling in low temperature experiments, as opposed to compressor-based closed cycle refrigerators. Optical tables and instrument support tables/frames will be designed for optimal vibration isolation.

Support facilities

Helium capture facilities are needed to reduce the operational costs of running vibration-free He flow/vapor cryostats in low temperature experiments. The APS is currently planning the installation of such a system at selected locations around the ring, to be liquefied elsewhere at Argonne. It is expected that cost to users will be 1/3 of current cost. Facilities for work with diamond anvil cells are needed, especially for complex sample loading in multi-mbar experiments. This includes programmable micro-manipulators for DAC loading, a gas loading system, laser drilling facility for gasket drilling, glove box for reactive samples, and a facility for EDM drilling of Be gaskets. Finally, radioactive samples are currently loaded at the Actinide facilities (Argonne Bldg 200). These facilities are not optimized for loading of high pressure samples and it will be greatly beneficial for APS to explore having a designated, properly equipped laboratory for handling of radioactive samples, if this were to be feasible.

6-9.5 R&D Needs

R&D activities are also needed in the area of preservation of circular and L-V polarization (or L-H for a horizontally-diffracting mono) in a narrow range of energy around 2.8 keV where Si(111) crystals diffract at θ_{Bragg}=45°. While this narrow, low energy region is secondary in importance to the higher energy 3.5-27 keV range, it does provide a unique capability (L-edges of 4d metals Ru, Rh, Pd are in the 2.8-3.3 keV range). Note that XRMS experiments using L-H (L-V) polarization are unaffected with a vertically (horizontally) diffracting monochromator. The possibility of using 6H-SiC crystals as a monochromator is being explored in collaboration with the Optics group at APS. Its lowest order c-axis reflection (0006) is at θ_{Bragg}=61.5°at 2.8 keV. 6H-SiC has excellent thermal conductivity, peak reflectivity, and energy resolution. High quality single crystals have been secured (Section 6-9.4.2). Since beam footprint at this large Bragg angle is small ($\sim 1\times1$ mm) and penetration depth shallow at this energy (microns), only a small crystal is needed. Crystals may be placed on top of internally cooled Si(111) crystals for indirect (contact) cooling, or placed side by side with Si(111) crystals in the second bank of the monochromator with direct or indirect cooling. In circular mode, the on-axis power at closed gap through a 0.5×0.5 mm^2 aperture at 25 m is only 4 W which may enable use of water cooling (see Section 6-9.4.2 for more details).

6-10 APS-U XPCS Beamline

6-10.1 Executive Summary

XPCS characterizes fluctuations in condensed matter at a combination of mesoscale length scales and timescales not otherwise accessible. Signal strengths depend on the x-ray beam coherence and minimum accessible delay times scale inversely with the square of the source brilliance so XPCS will benefit tremendously from APS-U. The preliminary design of an in-place upgrade to existing beamline 8-ID has been completed. The goal is for this to become a facility fully dedicated to state-of-the-art WA- and SA-XPCS that fully leverages the outstanding gains in brilliance provided by APS-U. Features of the beamline include uniquely high time-averaged coherent flux, access to time delays as short as 100 ns and high coherent flux in the energy range of 8–25 keV with the higher x-ray energies providing penetration into diverse samples and sample environments. The preliminary beamline design achieves these objectives via maximally-bright IDs that span the entire 8-ID straight section, small horizontal offset mirror pairs and monochromators (single crystal and multilayer optics), and two experiment stations each with compound ("zoom") optical focusing, and dedicated and optimized experiment infrastructure for WA- and SA-XPCS, respectively.

Using WA-XPCS, the beamline will advance studies in a host of key areas in physics, materials science, and engineering that include dynamic heterogeneity, structural dynamics in super-cooled liquids, and fluctuations associated with competing mesoscale interactions in emergent materials. Using SA-XPCS, the beamline will enable dynamics-related studies in areas as diverse as *in situ* rheometry, nanofluidic flow, and high pressure that will significantly impact key problems in soft matter and advance their potential applications in technologies across an array of sectors including energy, transportation, health, agriculture, and national defense.

6-10.2 Scientific Objectives and Capabilities

6-10.2.1 Description of User Community/Stakeholders

Today, XPCS primarily serves a subset of the soft matter and hard condensed matter community. While XPCS has transformed from an "expert user only" technique 10 years ago to a productive General User program (the 2009 Arthur Compton award was presented at the APS to the pioneers of XPCS for this very reason), the limitations in coherent flux, and therefore accessible dynamical length and time scales, has limited systems that can be studied to slowly fluctuating materials. Even under these non-ideal conditions, XPCS at the APS is over subscribed with a steadily growing user community that produces many high impact publications.

With unprecedented gains in coherent flux provided by APS-U, the science enabled for XPCS will extend to a wide range of new and increasingly broad fields such as biological soft matter, materials under high pressure, geophysics and glass and super-cooled liquid physics. Moreover existing areas of study will see dramatic gains. With the APS-U providing access to 10–100 ns time scales and sensitivity to 1 nm or less length scales, systems in or buried under aqueous media, for example, can be readily examined.

The APS-U Early Science workshops and Early Science document [51], and the subsequent XPCS beamline workshop, generated significant enthusiasm from a diverse community and has produced specific lists of high impact first experiments. Partial lists of stakeholder names and affiliations are listed in the brief and full white papers submitted to APS-U as part of the beamline selection process. APS-U will surpass all the other synchrotron light sources (present and upgraded) by delivering more than 10× more coherent flux across a broad range of energies. XPCS stands to gain the highest amongst the many APS-U-enabled techniques as its merits scale quadratically with gains in brilliance.

6-10.2.2 Explicit Statement of Use of APS-U Characteristics and Analysis of Proposed Beamline's World Class/Leading Status

In its most common incarnation, XPCS measures fluctuations within a sample by determining the intensity autocorrelation function, $g_2(Q,t) = [\langle I(Q,t')I(Q,t+t')\rangle_{t'}]/[\langle I(Q,t')\rangle_{t'}^2]$, of the sample's x-ray speckle pattern versus delay time (t) and wavevector (Q), where the t' subscripts denote an average over time t'. The quantity $g_2(Q,t)$ is related to the sample's normalized intermediate scattering function (ISF) $[f(Q,t) = S(Q,t)/S(Q,0)]$ via $g_2(Q,t) = 1 + A[f(Q,t)]^2$, where A is the speckle contrast. The ISF, which is equivalent to the sample's Q- and t-dependent density-density autocorrelation function, is an important quantity for condensed matter systems and is often key in comparing theory to experiment. XPCS is nominally equivalent to its laser-light-based analogue, namely PCS, but is challenging because there are many fewer coherent photons in x-ray beams from even the brightest synchrotrons than from laser sources, and also because x-ray scattering cross-sections are typically small. As a result, a crucial aspect of an XPCS experiment is the SNR. To fully leverage XPCS, it is essential that the source be as bright as possible and it is for this reason that XPCS is particularly well poised to use the unprecedented source brightness that will be provided by APS-U.

The XPCS signal-to-noise (SNR) is proportional to $n\sqrt{Tt_aN_p}$ [136], where n is the number of photons per detector pixel per second, T is the measurement duration, t_a is the accumulation time (integration time of the detector), and N_p is the number of pixels. In this expression, n is proportional to $n_i(d\Sigma/d\Omega)d\Omega$, where n_i is the number of x-rays incident on the sample per second, $(d\Sigma/d\Omega)$ is the sample's x-ray scattering cross-section per unit volume, and $d\Omega$ is the solid angle per pixel. The quantity n_i is proportional to the incident coherent flux, F_c, which is directly proportional to the source brightness, B, via $F_c = B\lambda^2/4$ [137] —so the XPCS SNR is linearly proportional to the source brightness. Since the brightness of APS-U will exceed by a factor of 100× or more than that of the APS today, the APS-U XPCS beamline represents a revolution in the kinds of samples that will be accessible for study. Interestingly, while the SNR scales linearly with B, it also scales as the square root of the accumulation time (which should be a few times smaller than the sample's correlation time). It follows that for samples of a given scattering strength, XPCS measurements will be possible at APS-U on time scales that are about 10^4× faster than are possible today at the APS. Since the current state-of-the art for diffuse scattering measurements corresponds to accumulation times of about 1 ms, we anticipate time resolutions at APS-U of 100 ns (roughly the bunch spacing of APS-U in 99% coupling mode). The XPCS beamline will also leverage other unique characteristics of the APS-U source. First, APS-U's uniquely high SR brightness extends to higher x-ray energies than NSLS-II, for example. As described in the document *Early Science at the Upgraded APS* [51], this will allow access to fluctuations in considerably more extreme environments. Second, the peak brightness of APS-U ideally fills the span between the extremely high peak values at x-ray FELs that often result in sample damage or destruction and the much lower per pulse values at a more continuous source like NSLS-II that will preclude measurements at the pulse spacing. Third, the relatively high SR peak and average brightness of the APS-U XPCS beamline also promises to enable tests and development of more speculative ideas to extend XPCS time resolution below 100 ns to sensitivity as short as several ps [138, 139, 140, 141, 142].

The world-leading capabilities that will be provided by the APS-U XPCS beamline are summarized in Table 6.32. Though operating and proposed optics schemes at peer beamlines are largely similar, there are differences between them. Accordingly, the table lists just the coherent flux derived from $F_c = B\lambda^2/4$, where B is the source brilliance and λ is the wavelength of the radiation.

Table 6.32. Worldwide comparison of the proposed APS-U XPCS beamline with other recent or newly proposed beamlines. Results are for 1×1 *transverse coherence modes and assume 0.01% relative bandwidth. For APS-U we have assumed a 4.6-m-long 21-mm-period device at 12 keV and a 4.6-m-long 25-mm-period device at 20 keV while for ESRF-EBS we assume* $2\times$ *CPMU19 IDs. The per pulse number for APS-U assumes* $\kappa = 0.99$ *(48 MHz) operations, for Petra-III it assumes 40-bunch timing mode operations (192 ns bunch separation), while for NSLS-II it assumes 2 ns bunch separation.*

Capability	**P10 (Petra-III)**	**CHX (NSLS-II)**	**XPCS (ESRF-EBS)**	**XPCS (APS-U)**
Flux at 12 keV (ph/s)	8×10^{10}	8×10^{10}	?	6×10^{12}
Flux at 20 keV (ph/s)	2×10^{10}	5×10^{9}	?	9×10^{11}
Flux/pulse at 12 keV (ph)	1.5×10^{3}	1.6×10^{2}	?	4.3×10^{5}
Broad bandpass operation?	No	No	?	Yes
XPCS-dedicated operations?	No	No	?	Yes

6-10.2.3 Statement of Key Beamline Characteristics

The XPCS beamline will be situated entirely on the experiment floor and within one sector. The ID will span the entire straight section. The beamline will be uncanted and operate from 8–25 keV. Since XPCS requires maximal brightness, most likely the ID will be a vertical gap revolver pair but continued scrutiny of a HGVPU is required. The beamline will have 4 shielded enclosures: i) the FOE will produce a stable monochromatic or pink beam for the downstream enclosures via mirrors and a monochromator; ii) the SOE contains the common first optic for the WA- and SA-XPCS setups; iii) the WA-XPCS enclosure contains a higher demagnification optic, a heavy duty multi-circle diffractometer, exit flight paths and detector positioning stages and detectors (2 of each) and it contains a higher demagnification optic for the SA-XPCS setup; and iv) the SA-XPCS enclosure contains beam conditioning apertures, a sample platform enabling rapid switching between sample environments, a variable length (< 10 m) exit flight path, and a detector positioning stage with detectors. In the WA-XPCS station, the spot size at the sample will be tunable from 0.3–3 μm, while in the SA-XPCS station it will be tunable from 3–10 μm. The maximum 0.01% relative bandwidth and several coherence areas flux delivered to the sample positions in both experiment set-ups is the unprecedentedly large and world-leading value of up to 5×10^{13} ph/s.

In summary, the XPCS beamline design features world-leading average brightness, a broad range of x-ray energies, access to a broad dynamic range, tunable spot sizes, and powerful sample positioning and detector capabilities—all are necessary to advance the science themes described elsewhere in this report.

6-10.3 Source and Front End Requirements

6-10.3.1 Insertion Device

The SNR for XPCS is proportional to the brilliance, B, so an ID that spans an entire straight section is critical. The required energy range for the beamline is 8–25 keV and is based on the balance between the peak brilliance deliverable by APS-U, detector efficiency, and the need for transmission through various sample environments. Continuous tunability over this range is not required as there is not a particular scientific motivation to access specific absorption edges. It is useful, however, to consider 3 broad x-ray-energy ranges, namely low (8–12 keV), medium (12–20 keV), and high (20–25 keV), that are targeted towards different scientific themes. Specifics of the different energy ranges are provided below:

1. The low range is suitable for experiments where penetration through sample environments and radiation damage are not concerns. This regime provides the highest coherent flux.
2. The medium range is best suited for sample environments such as rheometers, shear cells, and cryostats and ovens. The need for increased x-ray penetration mitigates the reduced coherent flux.
3. The high range is well suited to biophysical and DNA-templated systems because of the extreme sensitivity of such systems to radiation damage. It will also advance work such as studies of polyamorphic phase transitions using high pressure environments where penetration through thick diamond anvil cells is often required.

Since XPCS is a time domain technique, source (and optical) considerations that facilitate stability or are less sensitive to vibrations are also important. We therefore strongly prefer a monochromator and experiment goniometer that deflect in the horizontal, providing a strong impetus for a HGVPU because this allows scattering to occur in the horizontal scattering plane without polarization penalties.

There are not any special needs with respect to non-planar polarization or rapid tuning. Examining the list of possible planar IDs for APS-U, we conclude that, for the moment, a vertical gap revolver device is required to provide the maximum brightness over the broad tuning range specified above. Figure 6.103 shows tuning curves for a combination of APS-U planar IDs that meet the needs discussed above. For comparison, we have also plotted the tuning curve for a HGVPU that is closest to meeting our needs. The two features in this tuning curve that dampen our enthusiasm for a HGVPU are the approximate factor two decrease in brilliance relative to the vertical gap pair and the tuning gap between 10–13.5 keV.

6-10.3.2 Other Source Requirements

Excluding more speculative split and delay units [138, 139, 140, 141] or speckle-visibility techniques performed at the level of the bunch length or between the bunch spacing [142], the ultimate time resolution of XPCS is set by the bunch spacing. Time fluctuating speckle patterns must therefore be read out at the bunch frequency. Such measurements will be challenging because of the relatively low signal level per bunch (when compared to an x-ray free electron laser, for example). To perform experiments at this limit, therefore, the highest per bunch signal is required. Accordingly, we request operation of the APS-U SR at least a part of the time in the $\kappa = 0.99$ mode. Suitably jitter-reduced

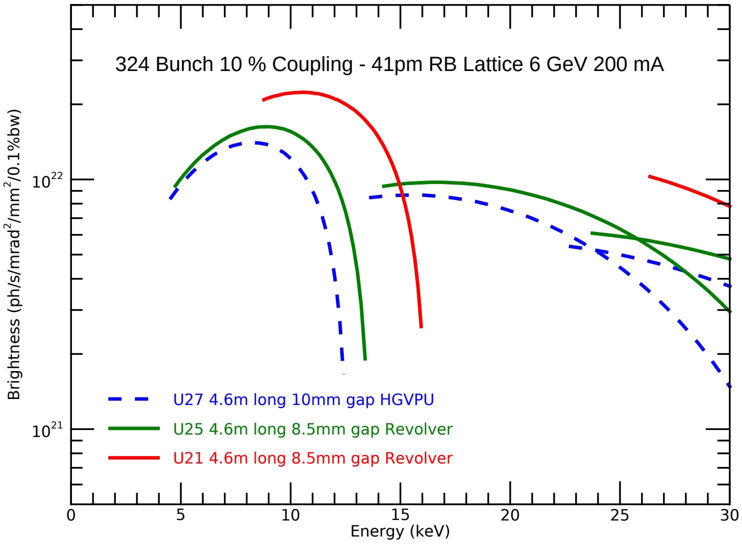

Figure 6.103. Brightness versus energy for a 4.6-m-long revolver undulator with two periods: 21 and 25 mm. The brightest ID would be selected using the revolver device for a particular x-ray energy. Also shown (dashed lines) is the tuning curve for a 4.6-m-long HGVPU with a 27 mm period.

and phase adjustable timing signals are required to synchronize emerging detectors, such as the VIPIC [143, 144, 145], to the bunch structure of the SR.

An additional requirement is SR beam stabilization over a considerably broader frequency bandwidth than is done today at the APS. Figure 6.104 shows an FFT of the scattered intensity recorded as a function of time from a nominally static reference sample. Evidently, there is is a strong oscillation at 147 Hz that subsequent conversations with Accelerator Systems Division (ASD) Diagnostics and XSD Optics group members has revealed originates from SR corrector magnet fluctuations. Though this parasitic signal can be smoothed away under some (but not all) circumstances, eliminating such fluctuations over a broad bandwidth is greatly preferred.

6-10.3.3 Front End Requirements

We require a standard uncanted FE. The maximum required acceptance aperture is 40 × 40 μrad^2.

6-10.4 Beamline Layout

6-10.4.1 X-Ray Optical Layout

Overall Layout The optical design of the XPCS beamline has to achieve variable (zoom) spot sizes at two locations along the beamline. The upstream WA-XPCS set-up requires spot sizes of 0.3–3 μm over 8–25 keV while accepting 1–10 coherent modes while the SA-XPCS station requires 3–10 μm spot sizes across the same energy range and span of coherent modes. Smaller spot sizes allow probing fluctuations at the mesoscale and smaller with high sensitivity and, technically, it ensures that the speckled scattering pattern can be resolved with sufficient resolution in the far field

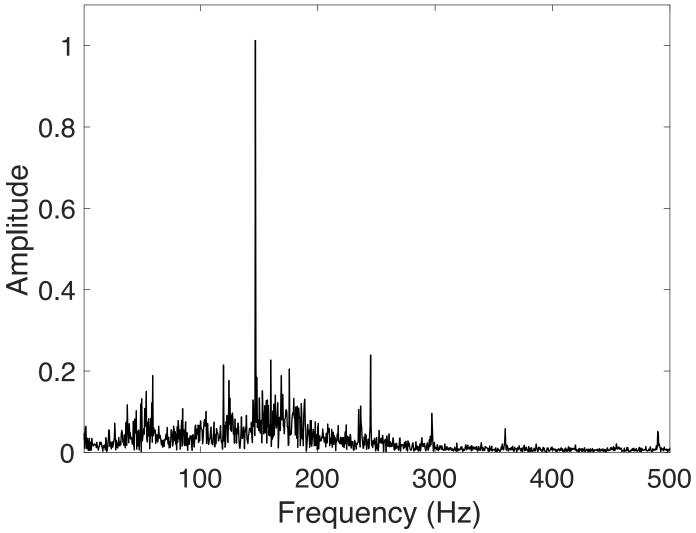

Figure 6.104. FFT of the time series of intensity from a nominally static speckle pattern. The 147 Hz oscillation arises from fluctuations arising from the SR corrector magnets.

using realistic anticipated pixel sizes for high gain area detectors and moderate sample-to-detector distances. With respect to the latter, we note that the speckle size, s, at the detector position, R_{det}, for a coherent beam size, a, at the sample is given by $s = \lambda R_{\mathrm{det}}/a$, where λ is the x-ray wavelength. Figure 6.105 shows necessary sample-to-detector distances for 1:1 sampling of speckles using a detector with pixel pitches of 25 (Mönch detector; green curves), 55 (Medipix3-based detectors; red curves) or 75 μm (Eiger, ultra fast x-ray camera (UFXC) or vertically integrated photon imaging chip (VIPIC) detectors; black curves). For SA-XPCS, the maximum sample-to-detector distance available at 8-ID is 10 m, so for measurements at the highest energies, a detector with still smaller pixels may be desirable or some speckle contrast will be sacrificed at higher x-ray energies. For WA-XPCS, detectors with a pixel size of 55 μm or less are required. Separately, we note that for all these cases, the detector is in the far field ($R_{\mathrm{det}} > a^2/\lambda$).

To achieve variable focal spot sizes, a compound focusing scheme is required with two optics upstream of each sample position. The optical layout shown in Figure 6.106 is for two different configurations of the beamline. In the first configuration, experiments are performed in the SA-XPCS end station (8-ID-D) and Optic 1 and Optic 3 are in place (with the WA-XPCS infrastructure including Optic 2 translated out of the way) while in the second configuration, experiments are performed in the WA-XPCS station (8-ID-C) and Optic 1 and Optic 2 are in place. Optic 1 is common for both configurations (but the lenses being used will vary) while Optic 2 and 3 are different and are in different locations.

To achieve the optics requirements above, focusing elements are required. For XPCS, inline optics such as 2-D CRLs are well suited to this task. Principal advantages are: i) because of near-normal incidence they are relatively forgiving with respect to the necessary beam stability requirements; ii) they work well at moderate x-ray energies and for achieving moderate demagnifications (spot sizes to a few μm); and iii) they are readily available from commercial sources with ongoing efforts to use better grades of beryllium for their fabrication (producing less small-angle scattering). In fact,

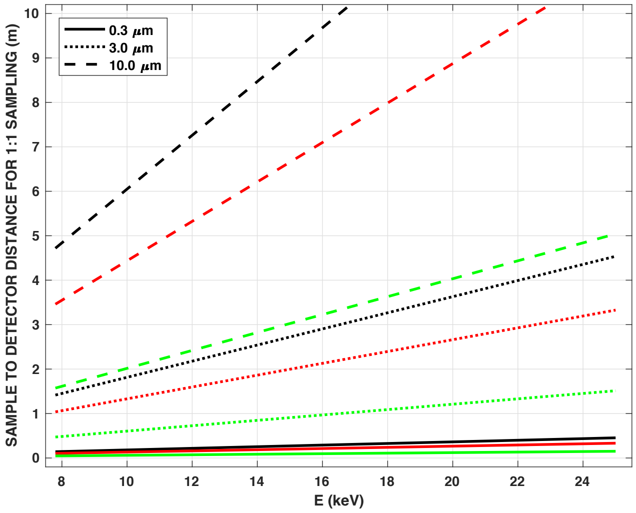

Figure 6.105. Sample-to-detector distances to achieve 1:1 speckle sampling for different spot sizes and x-ray energies relevant to the XPCS beamline. The green curves are for a detector pixel size of 25 µm, red are for 55 µm and black are for 75 µm.

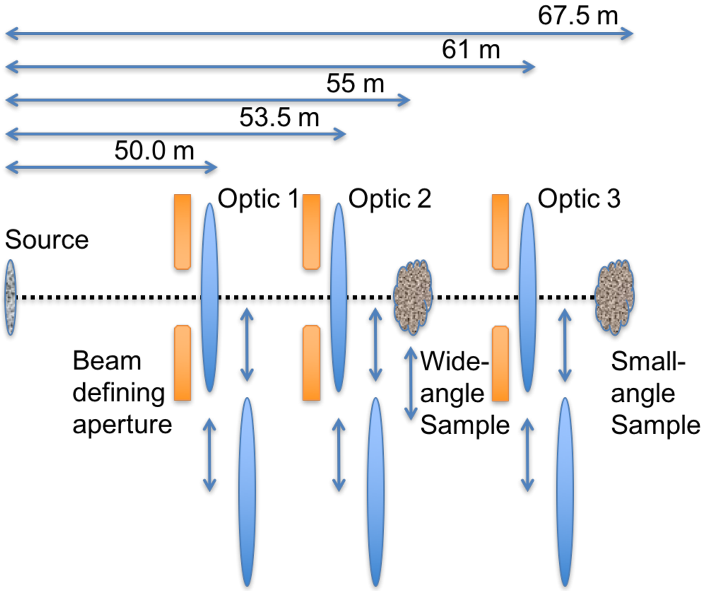

Figure 6.106. Optical layout for the XPCS beamline. Either Optic 1 and 2 are in the beam (for WA-XPCS) or Optic 1 and 3 (for SA-XPCS).

CRLs have been successfully used for coherence-driven experiments at the APS, ESRF, Petra-III, and LCLS [19, 146, 147]. Key disadvantages are that they are chromatic and they are rather bulky along the beam direction for higher demagnification applications like achieving the smaller spot sizes for WA-XPCS. Accordingly, we require a multi-component solution to achieve the necessary focusing. Optic 1 will be a beryllium CRL transfocator [19, 146], Optic 2 is still being evaluated but almost certainly will be a variable curvature KB mirror, and Optic 3 will be another beryllium CRL transfocator.

Tables 6.33 and 6.34 list the lens combinations, calculated by Xianbo Shi, that are required to achieve the focusing needs of the SA-XPCS station while Tables 6.35 and 6.36 do the same for the WA-XPCS station. As specific examples of how zoom focusing works, Tables 6.37 and 6.38 list lens combinations (Optic 1) and transmission factors for WA-XPCS at 15 keV for $\kappa = 0.1$ and $\kappa = 0.99$ operations, respectively. In both cases, the entrance slit for Optic 1 is set to accept 3.2×3.2 coherent modes and the KB mirror (Optic 2) is tuned to focus at the WA-XPCS sample position. Analogous calculations are available (not presented here) for the SA-XPCS but in this case the longitudinal position of Optic 3 must be moved to place the focus on the sample.

Table 6.33. Focusing at the SA-XPCS sample position (67.5 m) with 2-D CRLs at two different locations for 1×1 coherence mode. All sizes are calculated at the sample position, not at the best focus. Transmission numbers include the entrance slit acceptance and the CRL transmission.

	$\kappa = 0.99$ mode		$\kappa = 0.1$ mode	
Optics	Optic 3 only	Optic 1 only	Optic 3 only	Optic 1 only
Desired focusing (μm)	3	10	3	10
Optic-to-sample distance (m)	6	17.5	6	17.5
		10 keV		
Entrance slit (H × V) (μm)	89 × 131		79 × 199	
Osculating radius (μm)	300	1000	300	1000
Number of lenses	8	11	8	11
Focal size H (μm)	6.6	23	7.0	25
Focal size V (μm)	4.2	15	2.8	11
Transmission	3.1%	3.1%	5.3%	5.4%
CRL transmission	96%	96%	95%	96%
		15 keV		
Entrance slit (H × V) (μm)	61 × 93		54 × 154	
Osculating radius (μm)	300	1000	300	1000
Number of lenses	18	25	18	25
Focal size H (μm)	5.9	21	6.7	24
Focal size V (μm)	3.9	14	2.6	9.3
Transmission	1.8%	1.9%	3.8%	3.8%
CRL transmission	96%	96%	96%	96%
		25 keV		
Entrance slit (H × V) (μm)	37 × 59		33 × 110	
Osculating radius (μm)	100	200	100	200
Number of lenses	17	14	17	14
Focal size H (μm)	6.2	23	6.2	21
Focal size V (μm)	3.0	12	2.2	6.8
Transmission	0.9%	0.9%	2.3%	2.3%
CRL transmission	98%	98%	97%	98%

Table 6.39 lists the flux in the SA-XPCS station at various x-ray energies and focal spot sizes. The calculated numbers are for Si(111) monochromatic beam; for experiments that can be performed

Table 6.34. Focusing at the SA-XPCS sample position (67.5 m) with 2-D CRLs at two different locations for 3.2×3.2 *coherence modes. All sizes are calculated at the sample position, not at the best focus. Transmission numbers include the entrance slit acceptance and the CRL transmission.*

	$\kappa = 0.99$ mode		$\kappa = 0.1$ mode	
Optics	Optic 3 only	Optic 1 only	Optic 3 only	Optic 1 only
Desired focusing (μm)	3	10	3	10
Optic-to-sample distance (m)	6	17.5	6	17.5
		10 keV		
Entrance slit (H × V) (μm)	283 × 418		253 × 636	
Osculating radius (μm)	300	1000	300	1000
Number of lenses	8	11	8	11
Focal size H (μm)	3.9	15	4.3	16
Focal size V (μm)	3.3	15	3.3	17
Transmission	25%	26%	33%	36%
CRL transmission	89%	94%	86%	93%
		15 keV		
Entrance slit (H × V) (μm)	194 × 296		172 × 494	
Osculating radius (μm)	300	1000	300	1000
Number of lenses	18	25	18	25
Focal size H (μm)	3.6	13	4.1	15
Focal size V (μm)	2.7	9.5	2.5	9.9
Transmission	16%	17%	26%	27%
CRL transmission	92%	94%	89%	94%
		25 keV		
Entrance slit (H × V) (μm)	119 × 188		105 × 351	
Osculating radius (μm)	100	200	100	200
Number of lenses	17	14	17	14
Focal size H (μm)	3.9	12	3.9	14
Focal size V (μm)	3.2	7.7	4.8	5.7
Transmission	8.4%	8.7%	17%	18%
CRL transmission	95%	98%	91%	96%

Table 6.35. Focusing at the WA-XPCS sample position (55 m) with 2-D CRLs at the upstream location and a KB mirror in the downstream location for 1×1 *coherence modes. All sizes are calculated at the sample position, not at the best focus.*

	$\kappa = 0.99$ mode		$\kappa = 0.1$ mode	
Optics	Optic 1 only	Optic 2 only	Optic 1 only	Optic 2 only
Desired focusing (μm)	3	0.3	3	0.3
Optic-to-sample distance (m)	4.5	0.4	4.5	0.4
		10 keV		
Entrance slit (H $\times$ V) (μm)	89×131		79×199	
Osculating radius (μm)	500		500	
Number of lenses	18		18	
Focal size H (μm)	6.0	0.5	6.2	0.4
Focal size V (μm)	3.9	0.4	2.6	0.3
Transmission	2.7%	3.0%	4.7%	5.1%
Optics transmission	85%	91%	84%	91%
		15 keV		
Entrance slit (H $\times$ V) (μm)	61×93		54×154	
Osculating radius (μm)	300		300	
Number of lenses	24		24	
Focal size H (μm)	5.3	0.4	6.1	0.5
Focal size V (μm)	5.5	0.3	2.1	0.2
Transmission	1.4%	1.5%	2.8%	2.9%
Optics transmission	71%	74%	71%	74%
		25 keV		
Entrance slit (H $\times$ V) (μm)	37×59		33×110	
Osculating radius (μm)	100		100	
Number of lenses	22		22	
Focal size H (μm)	6.0	0.4	5.9	0.4
Focal size V (μm)	3.2	0.3	1.8	0.3
Transmission	0.7%	0.7%	1.7%	1.8%
Optics transmission	74%	76%	73%	76%

Table 6.36. Focusing at the WA-XPCS sample position (55 m) with 2-D CRLs at the upstream location and a KB mirror in the downstream location for 3.2 × 3.2 *coherence modes. All sizes are calculated at the sample position, not at the best focus.*

	$\kappa = 0.99$ mode		$\kappa = 0.1$ mode	
Optics	Optic 1 only	Optic 2 only	Optic 1 only	Optic 2 only
Desired focusing (μm)	3	0.3	3	0.3
Optic-to-sample distance (m)	4.5	0.4	4.5	0.4
		10 keV		
Entrance slit (H × V) (μm)	283×418		253×636	
Osculating radius (μm)	500		500	
Number of lenses	18		18	
Focal size H (μm)	3.3	0.3	3.8	0.3
Focal size V (μm)	2.4	0.3	1.5	0.2
Transmission	22%	21%	29%	28%
Optics transmission	79%	76%	76%	72%
		15 keV		
Entrance slit (H × V) (μm)	194×296		172×494	
Osculating radius (μm)	300		300	
Number of lenses	24		24	
Focal size H (μm)	3.2	0.2	3.6	0.3
Focal size V (μm)	2.1	0.2	1.2	0.2
Transmission	12%	13%	19%	21%
Optics transmission	68%	74%	66%	72%
		25 keV		
Entrance slit (H × V) (μm)	119×188		105×351	
Osculating radius (μm)	100		100	
Number of lenses	22		22	
Focal size H (μm)	3.3	0.2	3.6	0.2
Focal size V (μm)	2.1	0.2	1.1	0.1
Transmission	6.4%	6.7%	13%	14%
Optics transmission	72%	76%	69%	73%

Table 6.37. Sample WA-XPCS zoom system calculation for $\kappa = 0.1$. *The CRL osculating radius for Optic 1 is 300* μ*m and the KB mirrors (Optics 2) are tuned to focus at the sample position (54 m). The entrance slit size at Optic 1 is 0.17 mm × 0.49 mm.* T_{total} *is the transmission of the entire source and optical system while* T_{CRL} *is the transmission through the CRLs (Optic 1).*

Number of CRLs	Focal size (μm) H	Focal size (μm) V	$\mathrm{T_{total}}$ (%)	$\mathrm{T_{CRL}}$ (%)
0	0.3	0.2	21	72
8	0.4	0.3	21	71
12	0.5	0.4	20	70
15	0.7	0.5	20	69
17	0.8	0.5	20	68
18	0.9	0.6	20	68
19	1.1	0.7	20	68
20	1.2	0.7	20	67
21	1.3	0.7	19	67
22	1.8	0.8	19	67
23	2.4	1.0	19	66
24	3.6	1.2	19	66

Table 6.38. Sample WA-XPCS zoom system calculation for $\kappa = 0.99$. *The CRL osculating radius for Optic 1 is 300 μm and the KB mirrors (Optics 2) are tuned to focus at the sample position (54 m). The entrance slit size at Optic 1 is 0.19 mm × 0.30 mm.* T_{total} *is the transmission of the entire source and optical system while* T_{CRL} *is the transmission through the CRLs (Optic 1).*

Number of CRLs	Focal size (μm) H	V	T_{total} (%)	T_{CRL} (%)
0	0.2	0.2	13	74
8	0.4	0.4	13	72
12	0.5	0.6	13	71
15	0.6	0.7	12	70
17	0.7	0.7	12	70
18	0.8	0.7	12	70
19	0.9	0.8	12	69
20	1.0	0.8	12	69
21	1.3	1.0	12	69
22	1.6	1.2	12	69
23	2.1	1.6	12	68
24	3.2	2.1	12	68

with pink beam, the flux numbers will be roughly 100× higher. Table 6.40 lists the flux in the WA-XPCS station at various x-ray energies and focal spot sizes for a Si(111) monochromatic beam.

Table 6.39. Flux estimation in the $\kappa = 0.1$ *mode using a 2.1 and 2.5 cm period revolver ID for SA-XPCS. Included in the calculation are two horizontally-deflecting mirrors at glancing angles of 3.0 mrad and the Si(111) DCM.*

Energy (keV)	10		15		25	
Central cone flux (ph/s/0.1%bw)	3.20×10^{15}		1.60×10^{15}		9.80×10^{14}	
			Optic 3 only (smallest focal size)			
Coherence modes	1	10	1	10	1	10
Optic 1 entrance slit (H × V) (μm)	79×199	253×636	54×154	172×494	33×110	105×351
Flux (ph/s)	1.70×10^{13}	1.10×10^{14}	7.20×10^{12}	4.90×10^{13}	2.00×10^{12}	1.40×10^{13}
			Optic 1 only (largest focal size)			
Coherence modes	1	10	1	10	1	10
Optic 1 entrance slit (H × V) (μm)	79×199	253×636	54×154	172×494	33×110	105×351
Flux (ph/s)	1.70×10^{13}	1.20×10^{14}	7.20×10^{12}	5.10×10^{13}	2.00×10^{12}	1.40×10^{13}

Description of Optical Components

Mirrors

The beamline requires the option of pink beam to the SA-XPCS end station for experiments requiring the highest transverse coherent flux but that are forgiving with respect to longitudinal coherence. Also important are higher harmonic reduction and reducing the power load on the monochromator. These needs are best met by a flat horizontal-inboard-offset mirror pair in the FOE. In the limit

Table 6.40. Flux estimation in the $\kappa = 0.1$ mode using a 2.1 and 2.5 cm period revolver ID for WA-XPCS. Included in the calculation are two horizontally-deflecting mirrors at glancing angles of 3.0 mrad and the Si(111) DCM.

Energy (keV)	10		15		25	
Central cone flux (ph/s/0.1%bw)	3.20×10^{15}		1.60×10^{15}		9.80×10^{14}	
	Optic 2 only (smallest focal size)					
Coherence modes	1	10	1	10	1	10
Optic 1 entrance slit (H × V) (μm)	79×199	253×636	54×154	172×494	33×110	105×351
Flux (ph/s)	1.60×10^{13}	9.20×10^{13}	5.60×10^{12}	3.90×10^{13}	1.50×10^{12}	1.10×10^{13}
	Optic 1 and Optic 2 (flattened KB) (largest focal size)					
Coherence modes	1	10	1	10	1	10
Optic 1 entrance slit (H × V) (μm)	79×199	253×636	54×154	172×494	33×110	105×351
Flux (ph/s)	1.50×10^{13}	9.70×10^{13}	5.30×10^{12}	3.60×10^{13}	1.50×10^{12}	1.00×10^{13}

of small incidence angles, θ_i, the horizontal offset, H, achieved by a pair of mirrors transversely separated by D is $H = 2D$. H should be set to the offset required to separate Bremsstrahlung from synchrotron radiation so that the Bremsstrahlung can be stopped in the FOE. The longitudinal spacing, L_z, of the mirror pair, also in the limit of small θ_i, is $L_z = H/(2\theta_\mathrm{i})$. Since the incidence angles of the mirror are fixed, mirror energy cutoffs (low pass filtering) are achieved using the bare Si substrate as well as metal stripes such as Cr, Rh and Pt. The incidence angle for the mirrors has not been decided yet but it will be in the range of 2.5–3.0 mrad. A smaller incidence angle means larger (more expensive) mirrors, increased longitudinal separation between the mirror pair (that must fit in 8-ID-A atop a single plinth), and higher cutoff energies, while a larger angle means less use of the base silicon substrate. As a reference, Figure 6.107 shows the critical angles calculated for various mirror materials (substrate or stripe) as a function of x-ray energy.

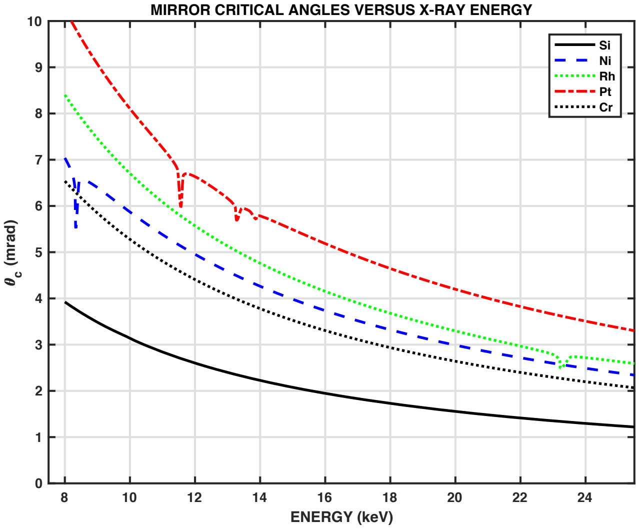

Figure 6.107. Critical angles as a function of x-ray energy for various mirror materials or stripes.

The maximum required transverse beam acceptance of 1 mm and the incidence angle defines the minimum longitudinal dimension (z) of the mirror. The overall mirror dimensions will be determined based on cooling and mechanical design, but are expected to be around 100 × 100 × 500 mm^3. Requirements for each mirror of the mirror pair and the mirror pair itself are summarized in Table 6.41, while the mirror geometry is illustrated in Figure 6.108. Optical specifications are state-of-the-art and are based on conversations with Dr. Lahsen Assoufid. Per conversations with XSD Optics group member Xianbo Shi, the second mirror may require extra length and a mechanical bending assembly to correct any thermally-induced wavefront error produced by the first mirror.

Table 6.41. Mirror specifications.

Item	Specification	Comment
Geometry	Flat	
Clear aperture	$\geq 1/\theta_\text{i}$ mm	Along the tangential direction
Max. rms roughness	0.1 nm	Over an area of 2 × 2 mm^2 and a wavelength band from 5–2000 μm
Max. rms slope error	0.1 μrad	For spatial frequencies $\geq$ 2 mm to the size of the clear aperture
Min. radius of curvature	>100 km	Along tangential direction
Max. PTV slope (raw surface profile)	0.4 μrad	No curvature removed
Material	Si	
Stripes	Yes	Si (bare) and TBD based on θ_i
Incidence angle	θ_i	TBD. $2.5 \leq \theta_\text{i} \leq 3.0$ mrad
Dimensions	≈ 500 × 100 × 100 mm^3	L × W × H
Transverse separation (D)	8.75 mm	To achieve $H \geq 17.5$ mm (inboard)
Longitudinal separation (Z)	$H/(2\theta_\text{i})$ m	≈ 3 m

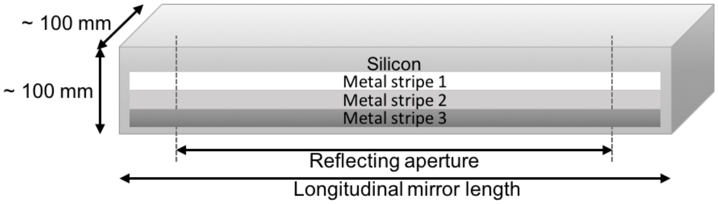

Figure 6.108. Geometry for the flat high heat-load mirrors in the FOE.

Monochromator

The XPCS beamline requires one double crystal monochromator and one double multilayer monochromator. A principal function of the monochromator crystals is to tune the longitudinal coherence length of the x-ray beam to match the coherent interference requirements of XPCS experiments.

The longitudinal coherence length, l_c, of the x-ray beam is $\lambda^2/\Delta\lambda$ and, to yield the coherent interference that is required for an XPCS measurement, this length must be comparable to or greater than the maximum PLD of the scattered x-ray beam (which depends on the scattering geometry and other factors like the x-ray absorption length of the sample) [137]. The DCM will use Si(111) and Si(311) crystals; Figure 6.110 shows the Bragg angles for these crystals for x-ray energies spanning 8–25 keV.

The relative energy bandwidths for Si(111) and Si(311) are 1.3×10^{-4} and 2.7×10^{-5}, respectively

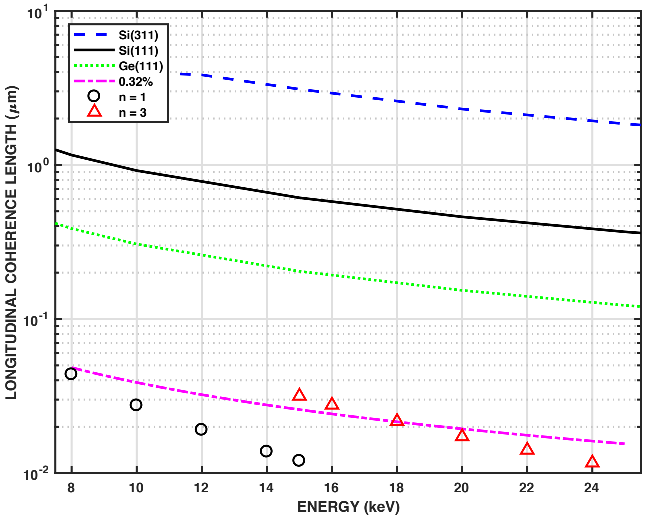

Figure 6.109. Longitudinal coherence lengths for Si(111), Si(311), Ge(111), 0.32% ($\delta\lambda/\lambda$, multilayer) and undulator harmonics $n = 1$ (circles) and $n = 3$ (triangles) through a 3 × 3 coherence lengths aperture.

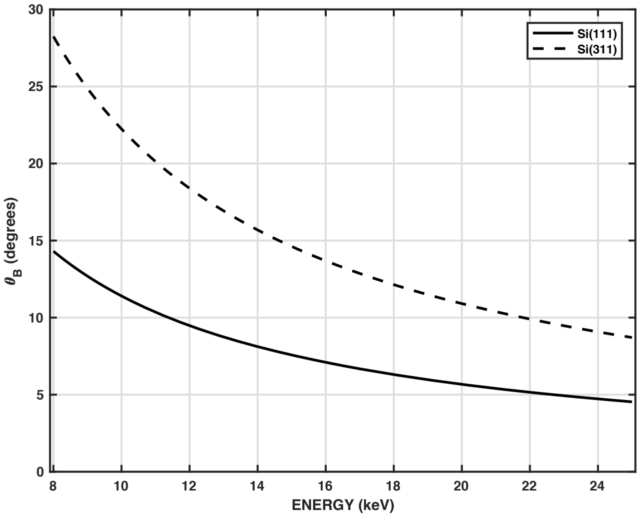

Figure 6.110. Monochromator Bragg angles as a function of x-ray energy.

and from these the longitudinal coherence lengths for σ polarization are plotted in Figure 6.109. We have also plotted the same for a Ge(111) monochromator crystal pair (see Section 6-10.5) and a 0.32% multilayer (see the SOE monochromator section below). Lastly, we have plotted the relative bandwidths of the first and third harmonics of the ID assuming transmission through a 3 × 3 coherence length aperture. For a WA-XPCS experiment, the PLD must be less than or comparable to several longitudinal coherence lengths.

In addition, the monochromator should allow the incident beam to be transmitted through the monochromator unimpeded, for both pink beam experiments and alignment purposes. DCM optical specifications are summarized in Table 6.42; specifications for the DMM are under development in collaboration with XSD Optics group member Ray Conley.

Table 6.42. Monochromator optical specifications.

Item	Specification	Comment
Geometry	Constant, small horizontal offset. 2 crystal reflection.	TBD but $\approx$ 10 mm anticipated. (Not required for radiation shielding purposes.)
Crystals	Si(111) or Si(311)	Symmetric reflection geometry
Bragg angles (θ_B)	0° and 4–29°	0° for pink beam and alignment purposes
Surface finish	< 0.1 nm and $< \lambda/50$	State-of-the art

Additional Focusing Elements

For two of the three focusing optics required for the beamline, CRLs (housed in transfocators) will be used. The CRLs will be commercially-available 2-D lenses fabricated from beryllium. Per Tables 6.33, 6.34, 6.35 and 6.36, lens osculating radii of 0.1, 0.2, 0.3, 0.5, and 1.0 mm are needed. For the second focusing optic for WA-XPCS, we require a compact KB mirror system since the optic-to-sample distance is not large. (A KB mirror also has the advantage of being achromatic.) Per conversations with XSD Optics group member Xianbo Shi, the mirrors should have state-of-the-art surface finishes with slope errors less than 100 nrad. The vertical-focusing mirror should be upstream and its length is 200 mm while the downstream mirror is horizontal-focusing and has a length of 100 mm. Bimorph benders are required to optimize the shape of the optics.

6-10.4.2 Beamline Physical Layout

Overall Beamline

General Description

Leveraging existing enclosure infrastructure at 8-ID to the greatest extent possible, the shielded enclosure and major optical component layout is listed below and illustrated in Figure 6.111.

1. Existing FOE 8-ID-A spanning 24–36 m and containing a windowless connection to the FE, WB slits, Bremsstrahlung and synchrotron radiation collimators, and stops and diagnostics to aid alignment. It also contains a pair of flat HHL mirrors, pink beam slits, and a HHL DCM.
2. Shielded transport and a new or re-purposed mini-hutch at 43.5 m (8-ID-A-MH-1) containing

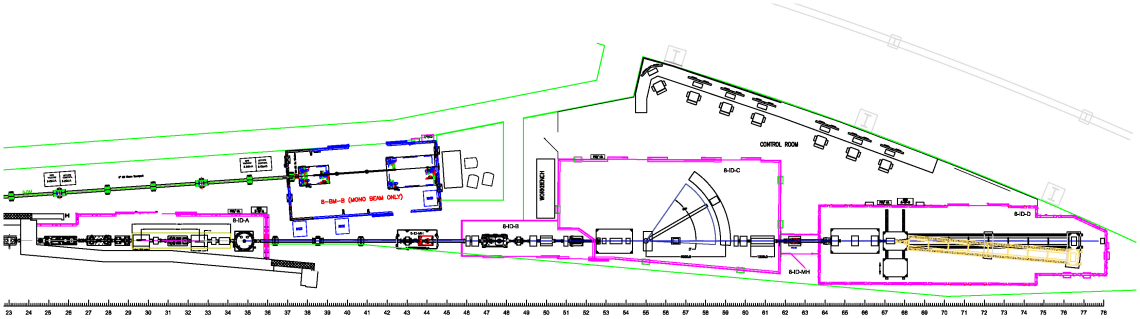

Figure 6.111. Overall plan view of the APS-U XPCS beamline situated at 8-ID.

the 8-ID-B shutter and connecting the FOE to the SOE.

3. New SOE 8-ID-B spanning 46–52 m (encompassing existing enclosure 8-ID-D) housing a DMM, pink beam slits (2), a CRL transfocator (Optic 1), diagnostics and the 8-ID-C pink beam shutter/stop.
4. Existing experiment enclosure 8-ID-C (née 8-ID-E) for WA-XPCS spanning 50.5–61.5 m and containing a higher demagnification optic (Optic 2), monochromatic beam slits and a heavy-duty multi-circle diffractometer, and exit flight paths and detectors (2). It also contains diagnostics, monochromatic beam slits, the second optic for SA-XPCS (Optic 3), and the 8-ID-D pink beam shutter/stop.
5. Existing enclosure 8-ID-C-MH-1 (née 8-ID-D-MH-1) spanning 61.5–63.5 m and containing the 8-ID-D pink and mono beam compatible shutter.
6. Existing experiment enclosure 8-ID-D (née 8-ID-I) for SA-XPCS spanning 63.5–78 m and containing pink-beam-compatible slits; a sample area supporting multiple sample environments such as flow, high pressure, and shear cells, as well as a rheometer; a variable length and angle ($2\theta \leq 70$ mrad) exit flight path, and a multi-detector support and positioning assembly.

Table 6.43 lists the major optical components and their position along the beamline in both distance from the source and location inside a shielded enclosure.

Radiation Safety

The beamline will meet or exceed all APS radiation safety standards. We do not anticipate any special circumstances or anticipate extensive studies of radiological samples or use of radioactive sources.

Vacuum

To preserve the beam brilliance, we require a UHV windowless connection to the front end. We also require brilliance preserving pink beam capable windows at the entrances to 8-ID-C and 8-ID-D and at the exit of 8-ID-C. To preserve the mirror and monochromator finishes and the transfocator lenses and to be compatible with a windowless connection to the SR, the beamline should be UHV until the 8-ID-C entrance window and contain no direct coolant-to-vacuum joints. Beyond this window, 10^{-8} mbar (HV) vacuum levels will suffice. Since the beamline will need to switch operations back and forth between 8-ID-C and 8-ID-D, a convenient way to assemble and disassemble flight path through 8-ID-C and bring it rapidly to the required vacuum levels is needed.

Table 6.43. Major XPCS beamline components.

Item	Location (m)	Location (station etc.)	Comment
Differential pump	25	8-ID-A	Connection to FE
White beam slits	27.5	8-ID-A	
Collimator	28.5	8-ID-A	
Mirror 1 (M1)	29.5	8-ID-A	First of pair
Diagnostic	30.5	8-ID-A	
White beam stop	31.5	8-ID-A	
Mirror 2 (M2)	32.5	8-ID-A	Second of pair. Position depends on θ_i
Diagnostic	33.2	8-ID-A	
Pink beam slits	33.8	8-ID-B	
HHL DCM	35	8-ID-A	Horizontal offset.
Collimator	36	8-ID-A	
Shielded transport and mini hutch	36–46	Experiment floor	
8-ID-B shutter	44	8-ID-A-MH-1	
Diagnostic	46	8-ID-B	Pink beam
Pink beam slits	46.5	8-ID-B	
HHL DMM	47.5	8-ID-B	
Pink beam slits	49.5	8-ID-B	
Transfocator (Optic 1, Figure 6.106)	50	8-ID-B	First optic for WA- and SA-XPCS
Diagnostic	51	8-ID-B	Pink and mono beam
8-ID-C shutter	51.5	8-ID-B	
Motorized high load optical table (TC1)	52.5–54.5	8-ID-C	
Mono beam slits	53, 54	8-ID-C	On TC1
KB mirror (Optic 2, Figure 6.106)	53	8-ID-C	On TC1 Second optic for WA-XPCS
Diffractometer	55	8-ID-C	
Diagnostic	59.5	8-ID-C	Pink and mono beam
Pink beam slits	60	8-ID-C	
Transfocator (Optic 3, Figure 6.106)	61	8-ID-C	Second optic for SA-XPCS
8-ID-D shutter	62.5	8-ID-C-MH-1	
Motorized high load optical table (TD1)	64–66.5	8-ID-D	
Pink beam slits	64.5, 65.5, 66.5	8-ID-D	On TD1
Sample environment support assembly	67.5	8-ID-D	
Exit flight path	67.5–76	8-ID-D	
Detector positioning	76.5	8-ID-D	
and support assembly	76.5	8-ID-D	

First Optics Enclosure and Infrastructure The beamline will use existing FOE 8-ID-A. Figure 6.112 illustrates the new component layout. One required improvement is temperature control of the station to ≤ ± 0.05 °C to help ensure positional stability of the optical components. This specification is arrived at by assuming a typical thermal expansion coefficient for granite (anticipated plinth material for slits, mirrors, and monochromators) of 5×10^{-6} K^{-1} and 1 m of support material yielding a change in height of 0.5 μm with a temperature of 0.1 °C. This is acceptable since it is comparable to the needed positioning accuracy for the slits.

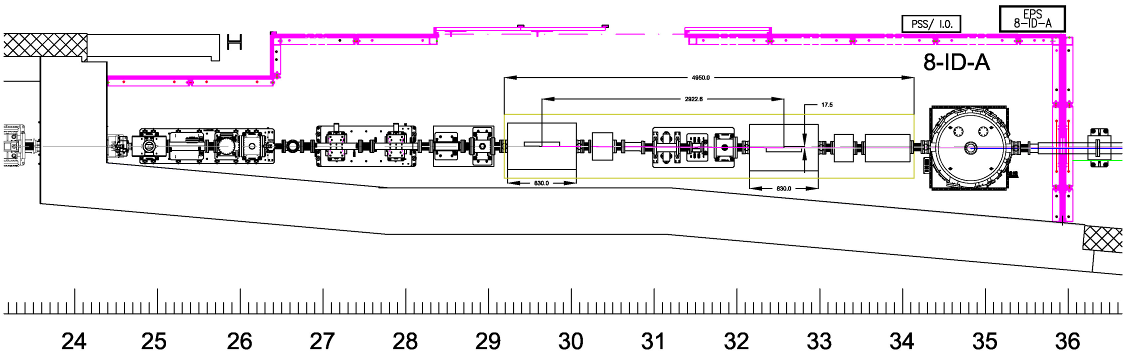

Figure 6.112. Plan view of the component layout in 8-ID-A. The mirror pair assumes 3.0 mrad incidence angles and, for shielding purposes, a minimum lateral synchrotron-Bremsstrahlung beam offset of 17.5 mm.

Windows

To help preserve the beam brilliance, a windowless, i.e., differential pump, connection to the FE is required. The exit aperture should subtend an angle of 40 μrad × 40 μrad (1×1 mm^2).

Slits

The first slits are HHL slits, have a maximum aperture of 5×5 mm^2, and provide a sharp-edged aperture over the beamline operating energy of 8–25 keV. The entire slit assembly should be located atop a stable motorized table so that once an aperture has been set, it can be scanned in the x-ray beam without moving the slit blades. The required table translation in the X and Y directions is ±6 mm.

Collimators

Collimators and stops are required in the FOE to contain the Bremsstrahlung radiation to the FOE. The FOE Bremsstrahlung collimators work in concert with collimators in the FE to achieve the necessary offsets and apertures.

Shutters/Stops

The beamline requires three pink beam shutters, one white beam stop and one pink beam stop. Requirements are summarized in Table 6.44.

Table 6.44. Beamline shutters and stops.

Item	**Location**	**Function**
White beam stop	8-ID-A between the HHL mirrors	Stop WB while allowing pink beam deflected by upstream HHL mirror to pass downstream
Pink beam stop	Downstream end of 8-ID-D	Stop pink beam from hitting downstream wall of 8-ID-D
8-ID-B shutter	8-ID-A-MH-1	Stops beam from entering 8-ID-B
8-ID-C shutter	Downstream end of 8-ID-B	Stops beam from entering 8-ID-C. Functions as a pink beam stop for experiments in 8-ID-C
8-ID-D shutter	8-ID-C-MH-1	Stops beam from entering 8-ID-D

High-Heat-Load Mirrors

The FOE will have two plane Si mirrors with metal stripes to achieve a fixed horizontal offset pink beam sufficiently well-separated from the primary Bremsstrahlung radiation cone. The upstream mirror will be exposed to white beam while the downstream mirror will see only pink beam. Both mirrors require cooling with the cooling geometry and medium to be determined after a more detailed engineering study. HHL power loads and power densities on the mirrors and the monochromator (next section) can be calculated using some working assumptions for the beamline design (subject to change). Specifically, we assume the APS-U 41 pm lattice, $\kappa = 0.1$ coupling, an effectively 4.6-m-long ID with period (21 or 25 mm) and harmonic chosen to maximize the flux through a 1 × 1 mm^2 aperture 25 m from the source. Table 6.45 calculates the power and power densities through this aperture and incident upon the first mirror (M1), the second mirror (M2), and the HHL DCM. We also assume that the incidence angle on the mirrors is 3.0 mrad, the mirrors reflect from stripes as indicated in the table, and the HHL DCM is set to reflect Si(111). Lastly, we assume that the beam does not diverge appreciably between the FOE entrance aperture and the HHL optics so that the power density can be calculated assuming a 1 × 1 mm^2 transverse beam size. The power density on the DCM is less than from Undulator A at closed gap at the APS today [148] so we do not anticipate any showstoppers working with these power levels, but it is important to realize that the finely collimated APS-U beams and our beamline will be much more sensitive to thermal bump wavefront perturbations. We also emphasize that the analysis documented above should be extended to all operating energies of the beamline to ensure that we have documented worst-case power loads and it should also be extended to Si(311).

Table 6.45. Power transmitted though a 1 × 1 mm^2 aperture at 25 m and incident upon successive HHL optics in the FOE. The column entitled ID lists the period of the ID.

E (keV)	ID (mm)	κ	Harmonic	Stripe	→M1 (W)	M1$_{\text{abs}}$ (W/mm^2)	→M2 (W)	M2$_{\text{abs}}$ (W/mm^2)	→DCM (W)	DCM$_{\text{abs}}$ (W/mm^2)
8	25	1.119	1	Si	335	0.53	157	0.03	147	36.8
10	21	1.119	1	Si	479	0.79	215	0.05	197	39.3
12	21	0.843	1	Cr	358	0.41	223	0.07	201	33.3
16	25	1.768	3	Cr	506	0.94	194	0.05	176	21.8
20	25	1.449	3	Rh	437	0.60	239	0.06	217	21.5
24	25	1.120	3	Pt	335	0.28	243	0.09	214	17.6

With respect to motion, each mirror requires one motorized angular degree of freedom (pitch) and two motorized linear degrees of freedom. We also anticipate the second (downstream) mirror of the pair requiring a bender to correct any wavefront perturbations introduced by the high heat load on the first mirror. Figure 6.113 show the axis orientations for the mirror degrees of freedom. Fine positioning and subsequent lockdown of the yaw and roll degrees of freedom is required only during installation so for these axes, manual adjustment is suitable.

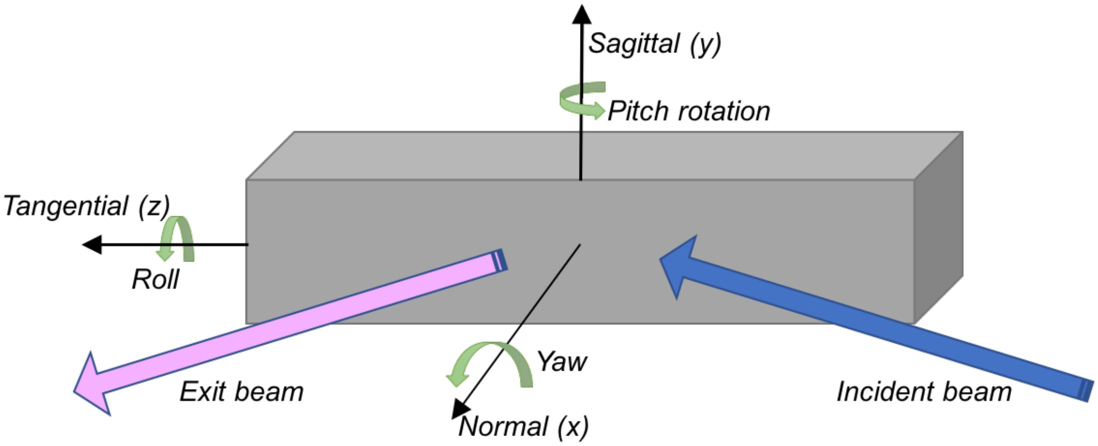

Figure 6.113. Mirror axis orientation.

The most critical motorized degree of freedom is the pitch. The nominal incidence angle is to be determined (in the range of 2.5–3.0 mrad with 3.0 mrad = 0.172° used in this document). The required travel range is small, requiring motion from 0 to 0.20°. Allowing for some beam and/or survey alignment errors, we request motion in the range -0.05–0.22°. Table 6.46 summarizes the motion requirements for the horizontally deflecting HHL mirrors.

Monochromators

As evidenced by the operational experience of XPCS beamlines at APS, ESRF, Petra-III, and NSLS-II, the beamline monochromator requires exceptional mechanical stability since XPCS measurements are performed in the time domain. A horizontal offset design is required as this will facilitate a more stable mechanical design. Figure 6.114 is a schematic representation of the monochromator geometry.

The horizontal offset monochromator is preferred because the degrading effect of any residual vibrations is ameliorated in this direction because the horizontal source size is bigger than in the vertical. Specifically, for an optic located a distance, p, from the source having an rms angular vibration amplitude, σ_v, the effective source size is broadened by $\sqrt{\Sigma^2 + (2p\sigma_v)^2}/\Sigma$, where $\Sigma_{x,y}$ is the rms source size in the x (horizontal) or y (vertical) direction $= \sqrt{\sigma_{x,y}^2 + \sigma_r^2}$, $\sigma_{x,y}$ is the rms electron beam size and σ_r is the rms photon beam size. Figure 6.115 shows the source broadening for different vibration amplitudes. The thicker black lines are relative vertical source broadening while the thinner blue lines are relative horizontal broadening. The calculations assume APS-U brightness mode operation (41 pm emittance and 10% coupling) and an optic 35 m from the source vibrating with the rms amplitudes shown in the legend. Not surprisingly, the relative source blurring is much larger in the vertical than the horizontal.

Table 6.46. Motion and mechanical specifications for the horizontally-deflecting mirrors in 8-ID-A.

Motion	Parameter	Specification
Pitch	Drive	Motorized and encoded
	Nominal angle	3 mrad
	Range	-1–4 mrad
	Resolution	$\leq$ 10 nrad
	Angular stability	$\leq$ 30 nrad (rms)
	Axis position	On the mirror surface
Roll	Drive	Manual with lock-in
	Nominal angle	0°
	Range	± 10 mrad
	Axis position	On the mirror surface
Yaw	Drive	Manual with lock in
	Nominal angle	0°
	Range	± 10 mrad
	Axis position	Perpendicular to the mirror surface
Sagittal (Y) (Stripe selection)	Drive	Motorized and encoded
Surface normal (X)	Drive	Motorized and encoded
Longitudinal (Z)	Drive	Not required
Bender/Corrector	Drive	Required for the second mirror
Vacuum	$< 10^{-9}$ mbar	UHV

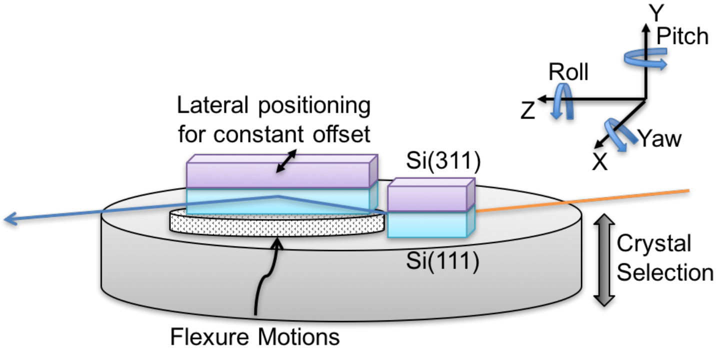

Figure 6.114. Schematic representation of the horizontal monochromator. Key motion requirements, as well as the coordinate system, are illustrated.

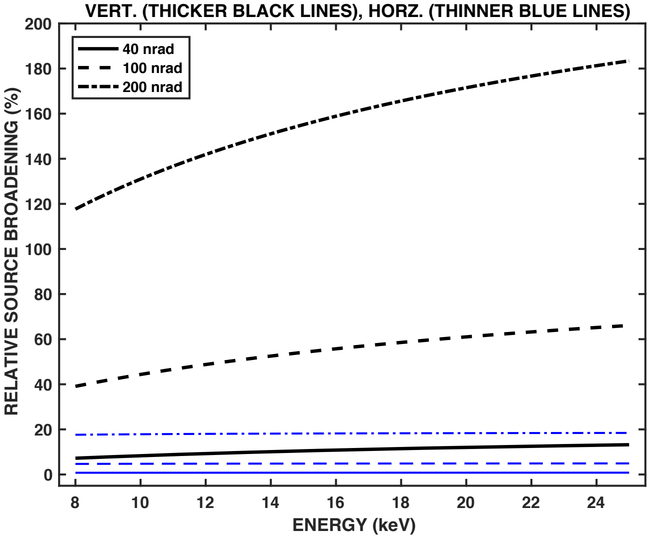

Figure 6.115. Relative source broadening induced by a vibrating optic with the rms vibration amplitudes shown. Calculation performed for the APS-U $\kappa = 0.1$ mode. Thinner blue lines: horizontal vibration; thicker black lines: vertical vibration.

The smallest vibration amplitude plotted, 40 nrad, is roughly the state-of-the-art of published cryo-cooled monochromator vibration studies [149, 150, 151]. Moreover, a so-called artificial channel cut monochromator has demonstrated suitable stability for XPCS measurements [152] (albeit with water cooling) and vendors have documented LN2-cooled designs on their web sites, demonstrating 50 nrad rms (`http://www.idtnet.co.uk/mono_stability.html`) and 25 nrad rms (`http://www.idtnet.co.uk/ultra_stable_horizontal_dcm.html`) stability, respectively. In short, the stability specifications should be achievable.

The monochromator cooling must also be able to withstand the high-power loads and power densities generated by the ID with minimal distortion of the first crystal face. The monochromator mechanical requirements are summarized in Table 6.47 while power loads on the first Si(111) crystal at selected operating energies are documented in Table 6.45.

Other Optics

We do not anticipate the need for any additional optics in the FOE.

Diagnostics

Beam diagnostics are required in two locations in the FOE to aid the alignment of the undulator central cone through the fixed upstream beamline mask and for alignment of the mirrors. A suitable diagnostic would provide a white beam BPM, a yttrium aluminum garnet (YAG) screen that could function with the undulator gap almost wide open, a photocurrent monitor, and a bypass aperture.

Table 6.47. HHL DCM mechanical requirements.

Motion	Parameter	Specification
	Assembly	
Pitch	Drive	Motorized and encoded
	Range	0° and 2°–14.5°
	Angular stability	$\leq$ 40 nrad (rms)
	Axis position	On the first crystal surface
	First Crystal	
Face adjustment	Drive	Manual with lockdown (Adjust first crystal to COR)
	Second Crystal	
Coarse Pitch (miscut)	Drive	Piezo-driven flexure
	Range	± 1.5 mrad
	Axis position	On the crystal surface
Fine Pitch (feedback)	Drive	Piezo-driven flexure
	Range	± 0.2 mrad
	Axis position	On the crystal surface
Roll	Drive	Piezo-driven flexure
	Range	± 20 mrad
	Nominal angle	0°
	Axis position	On the crystal surface
Y (Crystal selection)	Drive	Motorized and encoded
	Range	TBD
Cooling	LN2 for crystals.	
	Water for Compton shielding.	
Vacuum	$< 10^{-9}$ mbar	UHV
Vibration amplitude	$<$ 40 nrad rms	Pitch (tangential) direction

Secondary Optics Enclosure and Infrastructure The SOE is a new enclosure for the beamline. It is a pink- and mono-beam compatible enclosure located immediately upstream of 8-ID-C. Its overall dimensions are 7 m (L) × 2 m (W) × 3 m (H). An SOE is necessary for housing critical optical components like the multilayer monochromator and first focusing optic (Optic 1 in Figure 6.106) as well as beam defining apertures and diagnostics.

Since this is a new shielded enclosure, Figure 6.116 shows the siting of this enclosure on the experiment floor immediately upstream of 8-ID-C (née 8-ID-D/E). From left-to-right, the components in 8-ID-B are an ion pump, a diagnostic, slits, a DMM, slits, a transfocator, a diagnostic, the 8-ID-C shutter, and a pink beam window. The upstream wall between 8-ID-B and the small, existing 8-ID-D enclosure will need to be removed.

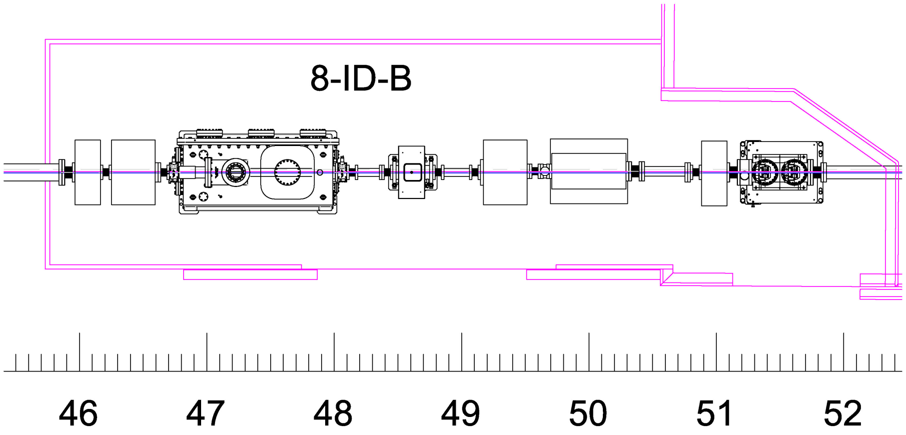

Figure 6.116. Preliminary plan view of the SOE and its components.

Windows

The SOE requires a pink- and mono beam compatible coherence-preserving window at its downstream end. Upstream of the window is UHV with a windowless connection to the FE. The exit aperture should be 6 mm × 6 mm. The beam will translate horizontally by 10 mm when switching between pink and monochromatic beam operation so this window must be atop a motion stage capable of this while the beamline is under vacuum.

Slits

Two sets of pink beam compatible slits are required in the SOE. The first set of slits is located near the upstream end of the SOE and are used to define the size of the beam incident on the multilayer monochromator. They have a maximum opening aperture of 10 mm × 10 mm and provide sharp beam-defining edges across the beamline operating energy of 8–25 keV. The second set of slits are immediately upstream of the transfocator. They serve as adjustable apertures for both pink and monochromatic beam. Their maximum opening aperture is 10 mm × 10 mm and they should provide an effectively “hard” aperture from 8–25 keV.

Collimators

No collimators are needed in the SOE because the primary Bremsstrahlung is stopped in the FOE.

Shutters/Stops

The SOE requires a pink- and monochromatic-beam compatible shutter at its downstream end. Table 6.44 lists all the shutters and stops in the beamline.

High-heat-load Mirrors

There are no HHL mirrors in the SOE.

Monochromators

In many instances the relative energy bandwidth provided by a DCM ($\leq 0.01\%$) is finer than is necessary for SA-XPCS. One solution is to use entire relative bandwidth of an undulator ($\approx 1\%$) and this option is provided by our beamline design. There are many other cases, however, where a relative bandwidth between these two extremes is needed; this option will be provided by a horizontal offset DMM. Suitable multilayers are being developed by Ray Conley of the XSD Optics group, but likely candidates include bilayers composed of $MoSi_2$ and Si or $MoSi_2$ and B_4C. Since Bragg angles are small, limited flexure-based motion is preferred. Moreover, because the monochromator will only be used for some experiments (none of the WA-XPCS measurements, for instance), it must include sufficient degrees and ranges of motion so that the incident beam can pass through unperturbed when it is not being used.

The DMM cooling scheme must also be able to withstand the high-power loads and power densities transmitted from the FOE. A very rough approximation of the power density on the first crystal can be obtained by using the entries in the column labeled →DCM in Table 6.45, assuming an incident beam cross section of 1×1 mm^2 and assuming an incidence angle on the first crystal of 25 mrad. From this we obtain a power density estimate of 4 W/mm^2. The monochromator mechanical requirements are summarized in Table 6.48.

Table 6.48. HHL DMM mechanical requirements.

Motion	Parameter	Specification
Pitch (assembly)	Drive	Flexure-based and encoded
	Range	0° and 1°–3°
	Angular stability	$\leq$ 40 nrad (rms)
	Axis position	On the first crystal surface
Pitch (2nd crystal)	Drive	Closed loop piezo-driven flexure
	Range	TBD
	Axis position	On the 2$^{\text{nd}}$ crystal surface
Roll (2nd crystal)	Drive	Closed loop piezo-driven flexure
	Range	TBD
	Nominal angle	0°
	Axis position	On the 2$^{\text{nd}}$ crystal surface
Y	Drive	Motorized and encoded
(Multilayer selection)	Range	TBD
Cooling	TBD	
Vacuum	$< 10^{-9}$ mbar	UHV
Vibration amplitude	$<$ 40 nrad rms	Pitch (tangential) direction

Other Optics

Evident from the lens and focusing optic configurations listed in Tables 6.33, 6.34, 6.35 and 6.36, variable numbers and radii of CRLs are required to achieve the focusing requirements of the beamline. In the two locations where CRLs are specified, a so-called transfocator is a device to achieve this. Requirements for the transfocator are UHV compatibility, x, y and z translations, pitch and yaw rotations, and the ability to remove and insert variable numbers of lenses. The number of lens banks required will be determined when the final optical design is complete. As an example, Figure 6.117 shows a transfocator designed for the P10 beamline at Petra-III that contains 12 banks allowing for $2^{12} = 4,096$ combinations of lenses.

Figure 6.117. Left: transfocator designed for P10 at Petra-III [19].

Preliminary specifications for the Optic 1 and Optic 3 transfocator systems are listed in Table 6.49.

Table 6.49. Specifications for the transfocators to be used in the Optic 1 and Optic 3 locations.

Item	**Specification**	**Comment**
Vacuum level	UHV	
Cooling	Water required	Pink beam operation
Motions	X, Y, Z, pitch and yaw	Motorized and encoded
X	±15 mm	To switch between monochromatic and pink beam as well as between the lenses and the clear aperture
Y	±5 mm	For centering lenses in the beam
Z	±300 mm	Optic 3 only. To adjust the lens position to focus on the sample over the entire energy range
Pitch	±2°	
Yaw	±2°	
Lenses	Yes	For inserting and removing lens stacks in the beam

Diagnostics

Beam diagnostics are required in two locations in the SOE. The first location is the most upstream position in the SOE while the second position is immediately upstream of the beam-defining aperture for Optic 1. In the upstream location, the diagnostic will aid in the alignment and monitoring of the stability of the beam from the FOE. A suitable diagnostic would provide a diamond BPM, a YAG screen that could function with the undulator gap almost wide open to facilitate alignment, and a bypass aperture. In the downstream location, the diagnostic will be used to aid in the alignment of the multilayer monochromator and as a beam position feedback source for experiments being performed in 8-ID-C. The diagnostic must be compatible with both pink and monochromatic beam with the same suite of capabilities mentioned immediately above.

Wide-Angle XPCS Enclosure and Infrastructure The 8-ID-C enclosure is for performing wide-angle (diffraction) XPCS experiments. A preliminary plan view of the station layout is shown in Figure 6.118. The station will have upstream beam preparation optics [mono beam slits and a higher demagnification focusing optic (KB mirror), attenuators and an experiment shutter] supported on a heavy-duty motorized optical table. It will also have a sample positioning goniometer and two flight path and detector positioning assemblies (with detectors)—one horizontal and one vertical. Additional components in 8-ID-C are for the SA-XPCS program in 8-ID-D. These include a BPM, pink and monochromatic-beam compatible precision slits, a pink and monochromatic beam transfocator, and the 8-ID-D shutter/stop assembly (8-ID-C-MH-1). All components past the detector positioning assembly are for components related to the SA-XPCS program that will be hosted in 8-ID-D.

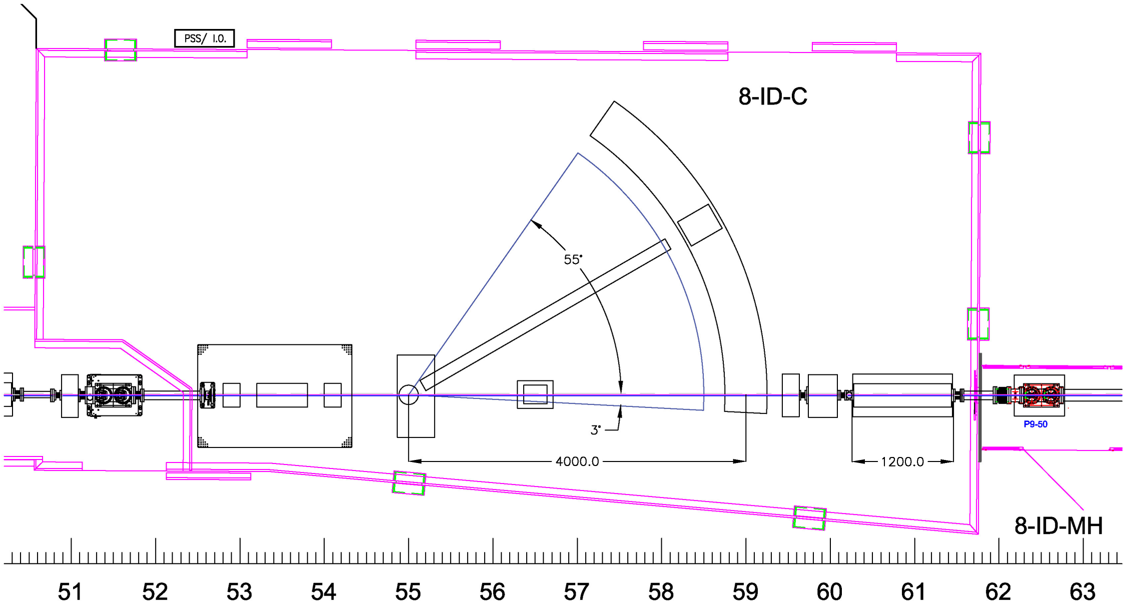

Figure 6.118. Plan view of the component layout in 8-ID-C.

Other Optics

Optic 2 combines with Optic 1 to produce variable spot size focused beams for WA-XPCS. In the

Optic 2 location, which will be a monochromatic beam UHV environment, a KB mirror pair is needed. The specifications for a KB mirror in the Optic 2 location are listed in Table 6.50.

Table 6.50. KB mirror specifications for the Optic 2 location.

Item	**Specification**	**Comment**
Vacuum level	UHV	To preserve the mirror surface
Cooling	To stabilize temperature of the device	Monochromatic beam.
Upstream mirror	Vertical focusing. 200 mm length	Bimorph bender
Downstream mirror	Horizontal focusing, 100 mm length	Bimorph bender
Mirror coating	Pt	
Grazing incidence angle	2.5 mrad	
Curvature error tolerance	≤ 0.1 μrad rms	
Roughness	≤ 0.1 nm rms	

Components

The first component in 8-ID-C is a heavy-duty, precise motorized table with 6 degrees of freedom. Atop this table sit attenuators, an experiment shutter, monochromatic beam slits, a moderate to high demagnification KB mirror pair, and guard slits. All of these components are for use in monochromatic beam only.

The key component in 8-ID-C is a heavy-duty, yet precise, diffractometer. Because of the small focal spot sizes and the wide dynamic range of correlation times that will be measured, being able to support the sample and any ancillary chambers or environments independent of the detector positioning is important. Being able to access a wide range of reciprocal space is also important. A final requirement is being able to position the sample for scattering in either the vertical or horizontal scattering plane. The horizontal plane, within the limits of the existing station size, allows for a larger sample-to-detector distance while the vertical scattering plane provides access to larger scattering angles without a reduction of scattered intensity because of polarization effects. Separate from the diffractometer are detector and flight path positioning assemblies for scattering in the horizontal and vertical scattering plane. The former supports detectors up to 4 m from the sample while the latter provides a sample-to-detector distance of 1.5–2 m.

Instruments

Diffractometer

To precisely position the sample in the beam and to move the diffractometer out of the way for experiments in 8-ID-D, the base of the diffractometer needs X- and Y-translations.

Independent of the sample positioning goniometer are two detector positioning arms. The first arm should move in the stability-facilitating horizontal plane and support a detector located 4 m from the sample (Figure 6.105). This arm and detector span angles from $2\theta = -1°$ to $55°$ The sample-to-detector distance should be spanned with rough vacuum tubing and a pair of low resolution X-Y slits on each end of the flight path. The vertical detector arm should span angles from $2\theta = -1°$ to $120°$ and support a more lightweight detector at a distance of 1.5–2 m. This detector arm will not be able to sample speckle patterns as finely as the horizontal arm but will provide extinction-free scattering to large values of 2θ. For positioning samples in reciprocal space, the sample goniometer must provide a full range of θ motion and χ and ϕ motions of limited range in both horizontal and vertical scattering planes. For the horizontal scattering plane, this might be accomplished using a large θ base (atop X and Y translations) with vertically stacked χ and ϕ tilt stages, while for the vertical scattering plane, the χ and ϕ tilt stages would be mounted at 90° atop the θ stage with a counterweight opposite. Atop these stages are X-Y-Z translation stages with varying degrees of precision and accuracy depending on the experiment needs. Figure 6.119 is a schematic of such a diffractometer with precision motion stages shown atop the vertical stack.

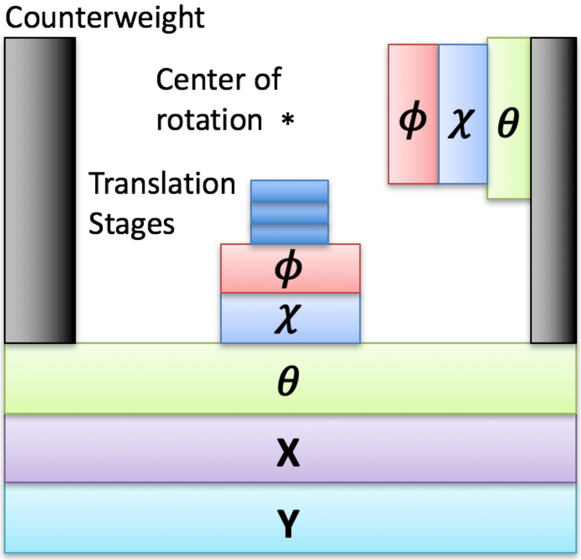

Figure 6.119. Schematic of the WA-XPCS sample-positioning goniometer.

The remaining components in 8-ID-C are for the operations in 8-ID-D. These items are a pink and mono beam compatible diagnostic, followed by pink and mono beam compatible slits, a beryllium lens transfocator (Optic 3) and, finally, a pink and mono beam shutter inside 8-ID-C-MH-1.

The diagnostic will aid in the alignment and monitoring of the stability of the pink or monochromatic beam being delivered to 8-ID-D. A suitable diagnostic would have a diamond BPM, a YAG screen, and a bypass aperture. When operations are being performed in 8-ID-D, the diagnostic will serve as a position feedback source to correct any slow drifts arising from the DCM or HHL mirror pair.

Pink and mono-beam compatible slits are needed to serve as the beam defining aperture for Optic 3. The slits must be able to withstand pink beam heat load, have a maximum opening aperture of $10 \times 10\ \mathrm{mm}^2$, and provide a sharp-edged aperture from 8–25 keV.

A transfocator, as described above, serves as Optic 3 for the SA-XPCS experiments in 8-ID-D. The required lens configuration is different than that for the first transfocator. Like the slits described above, the transfocator requires a large horizontal translation to accommodate switches between pink and monochromatic beams. It also requires significant longitudinal translation (±300 mm or more) so that the beam is focused on the sample.

The last component is in 8-ID-C-MH-1 and is a pink- and monochromatic-beam compatible shutter for 8-ID-D.

Small-Angle XPCS Enclosure and Infrastructure The 8-ID-D end station is optimized for performing XPCS experiments at small and medium scattering angles. A preliminary plan view of the station layout is shown in Figure 6.120. The station will have series of high precision high vacuum slits, a fast opening/closing experiment shutter (< 1 msec), a set of polished attenuators operating over the energy range of 8–25 keV, sliding stages for selecting sample environments, and an adjustable sample-to-detector distance flight path and detector assembly.

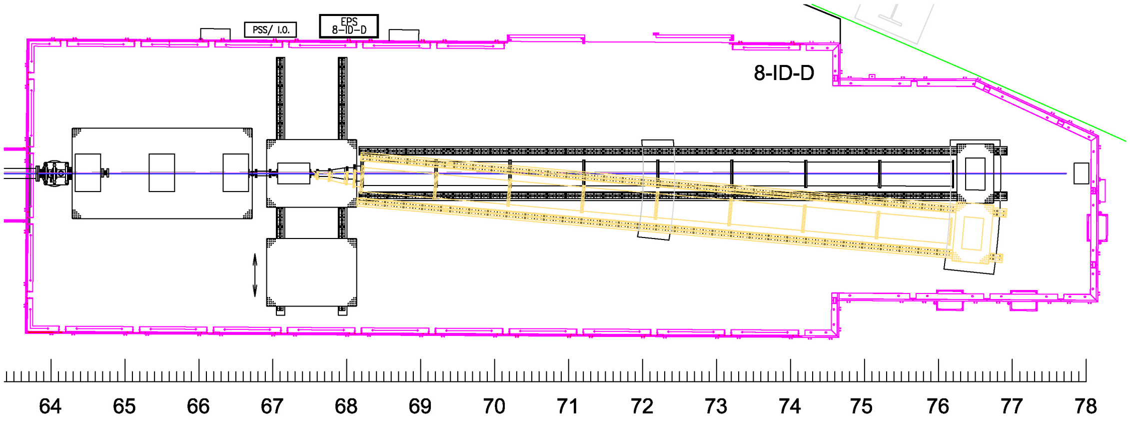

Figure 6.120. Plan view of the component layout in 8-ID-D.

Components

The first component in 8-ID-D is a heavy-duty, precise motorized optical table (2.5 m × 1.5 m) with 6 degrees of freedom. The focused beam for experiments in this station ranges from 3–10 μm. The optical table will house the following components: beam diagnostic, fast shutter, attenuators, and a series of 4–5 precision slits. The slits serve as guard slits which progressively condition the tails of the beam to minimize the parasitic scattering from the focusing optics as well as Fraunhofer diffraction from the guard slits themselves. It will also be desirable to have differential pumping (2–3 orders of magnitude difference) between the above components and the sample environment so that the slits can be maintained at high vacuum to prevent contamination.

Sample environments are critical and a few types are required: a commercial rheometer with capability for *in situ* scattering measurements, a microfluidic flow and mixing device equipped with a pressure driven flow pump, a vacuum chamber with temperature controlled sample stage, and diamond anvil cells for high pressure research.

In order to minimize labor intensive and inefficient switching of these sample environments, we require two independent motorized optical tables (each with 6 degrees of freedom) mounted transverse to the beam propagation direction (1 m lateral × 1.25 m longitudinal) using guide rails on or in the floor (see APS beamline 1-ID-D, for example). Two different sample environments can be set up and switched back and forth in an efficient manner. Based on projected scientific demand, we anticipate the rheometer permanently occupying one of the optical tables while other set ups will be mounted on the other optical table based on need. While the positioning of the rheometer with respect to the beam can be carried out using the table motion, the other set up will require high precision linear translations stages (3 degrees of freedom) atop the optical table.

For optimal SNR, the sample to detector distance has to be adjusted based on the x-ray energy and the focal spot size so that the speckle size equals the detector pixel size. Further, as shown in Figure 6.105, the sample-detector distance has to be varied over a range of 1–15 m, but in 8-ID-D this distance is limited to < 10 m and so operation above 16 keV may be non-optimal in terms of SNR depending on future detector developments. A suite of detectors will be mounted at the end of the flight path on a dedicated table with long-travel X and Y translation stages. The most downstream section of the flight path will comprise motorized translation stages to precisely position the direct beam stop before a thin Kapton (polyimide) window that separates the flight path from the detector assembly. We propose that this last section of the flight path and the detector assembly will move as a single unit when the sample-detector distance is adjusted based on the operating x-ray energy. A final requirement is the ability to rotate the exit flight path and detector support assembly around a (virtual) pivot point defined at the sample position. This feature is necessary since when the detector is far from the sample, it only subtends a small range of reciprocal space. Rotation around the pivot point will provide access to a larger range of reciprocal space. Figure 6.111 shows the exit flight path rotated inboard by 4°. The exact amount of rotation will be determined based on the design of the exit flight path and the detector support assembly, as well as required space for personnel egress.

Instruments

The major instruments required are (i) a commercially-available stress-controlled rheometer and (ii) a pressure driven microfluidic flow pump with a microchip based flow and mixing device. The temperature-controlled sample cell in a vacuum chamber will be built in-house and the high-pressure diamond anvil cells and the accessories will be developed via collaboration.

The rheometer allows the measurement of the real and imaginary parts of the viscosity that are respectively related to the modulus and dissipation in materials. These macroscopic properties can be directly correlated to the nanoscale dynamic properties using *in situ* XPCS measurements. While shear cells today are made of polycarbonate that are well suited for lower energy (8–12 keV) operations, their chemical incompatibility with several systems limit their use.

A compact pressure driven and controlled microfluidic flow control system will also have to be procured. This technology offers advantages over the traditional syringe pump based flow systems that are known to introduce instabilities in the flow. The flow cell will involve custom fabrication as it has to be made of x-ray transparent material such as Si_3N_4 or silicon.

6-10.4.3 Additional Needs

Detectors Equal in importance to the source, area detectors are critical to the XPCS beamline. In general, suitable detectors should be fast with relatively small pixels and the ability to resolve small numbers of scattered photons per pixel per frame with high fidelity. Rapid frame rates or sampling rates and high efficiency to higher x-ray energies (25 keV) are important to take advantage of the brilliance gains that will be provided by APS-U. Appropriate detectors have advanced considerably in recent years. Today, commercial detectors that warrant consideration are those based on sensors and systems developed at the Paul Scherrer Institute [153, 154, 155] and around the Medipix-3 [156] sensor. Ongoing research and development detectors such as the UFXC [157, 158] and VIPIC [143, 144, 145] among others [159] also warrant continued examination. Detector requirements are summarized in Table 6.51.

Table 6.51. XPCS detector needs.

Item	**Requirement**	**Comment**
Form factor	2-D (area)	10^6 pixels or more
Pixel size	$\leq 100\ \mu$m	
Efficiency	$\geq$80%	$\leq$ 25 keV
Type	Integrating	Preferred. Counting almost always works well
Dynamic range	Small	Depends on sampling time or frame rate. Can be as small as 2 bits (0–4)
Frame rate	$\geq$ 1 MHz	Pixel occupancy is very low
Readout	Sparse	
Energy resolution	Not required	LLD and photon centroiding
Synchronization	External timing signals Multiple detectors	$\leq$ SR bunch frequency
Other	Rolling buffer	Trigger storage of prior accumulated data

At a minimum, the WA-XPCS station requires two appropriate detectors—one for the long horizontally rotating detector arm and one for the vertical detector arm. The SA-XPCS station also requires two—one for the end of the long detector flight path and another closer to the sample for the simultaneous monitoring of scattering at larger scattering angles. Depending on developments over the next few years, additional detectors may be necessary to span gaps in frame rate or pixel size (speckle resolution).

Computing and Controls Motion control requirements for the XPCS beamline are relatively standard and therefore should be achievable within a modern, relatively standard synchrotron beamline motion control framework. For the most part, XPCS measurements are accomplished by moving the sample and detector(s) to a certain position and set of conditions and then measuring the scattering for a certain length of time. Some measurements will require translating the sample during the detector data acquisition. For measurements under these conditions, it will be helpful to have precise, synchronizable timing signals available to coordinate motion and data acquisition. This might be accomplished using a user-programmable FPGA such as SoftGlue. The control system should support both a GUI interface as well as text-based scriptable input. Python has emerged as a ubiquitous tool for scientific computing so a combined GUI/text input/scriptable interface based on this language is desirable. Large amounts of data will be acquired rapidly using fast XPCS-relevant detectors. To estimate data flows, we assume 5×10^{13} ph/s incident on the sample and assume that on average, 10^{-6} of the incident photons are collected by the detector. Assuming that we only record "hits," then each hit consists of the x and y position on the detector, a time stamp, and the intensity, or approximately 10 bytes/event. Very roughly, therefore, we expect a data rate from the detector of 0.5 GB/s. Assuming 50% duty cycle, we anticipate a data accumulation rate of tens of TB per day. Appropriate networking and storage systems are required to sustain data collection, reduction, and analysis with these data volumes.

Specific Safety Requirements We do not anticipate any programs at the beamline using unusually hazardous materials or conditions. A ventilation system will be required for some gases and an interlock and curtain system that allows safe operation of a laser system or ion gun might be required for some experiments. We do not anticipate measuring radioactive materials.

Specific Conventional Facilities Requirements The temperature in the experiment stations should be stabilized with gentle air handling systems to ±0.05°C to avoid slow temperature-induced drifts in the position of critical optical components. Also important are curtains at the station entrances to minimize temperature instabilities and turbulence when the station doors are opened. Avoiding strongly directed airflows by ventilating through diffusers should make for a more stable and comfortable working environment. Temperature stabilization in the experiment enclosures will be facilitated by a temperature-controlled control room encompassing the main entry doors to 8-ID-C and 8-ID-D. Since XPCS is a time domain technique, minimizing vibrations is important. Locating equipment in water-cooled racks on the station roofs is required. Specific locations include the roofs atop 8-ID-A, 8-ID-B, and the downstream end of 8-ID-D

Support Facilities Limited and basic laboratory space is required for minimal sample preparation such as epoxying samples to mounts, loading samples in glove boxes, or attaching leads to samples. It will also be necessary to have a small space with a ventilated work area in a corner or end of the experiment control area. Digital macroscopes and microscopes will be required for inspecting samples.

6-10.5 R&D Needs and Outstanding Issues

The following are R&D topics and outstanding questions related to the design of the APS-U XPCS beamline:

1. CRL quality and performance specifications vis-à-vis suitability for the highly-coherent APS-U x-ray beams need to be determined. Simulations are required to determine the amount of coherence degradation from commercially-available lenses so that a decision can be made about whether CRLs are suitable for focusing at APS-U.
2. Do metal mirror stripes such as Cr, Ni, Rh, or Pt on the surface of otherwise state-of-the-art polished silicon reduce the quality, i.e, degrade the coherence of the reflected x-ray beam? Are there specific coatings in this regard that are better or worse than others?
3. Thermal analysis is required for the beamline mirrors and monochromator so that the adequacy of various cooling schemes can be determined.
4. Determine whether Ge(111) monochromator crystals would work well enough at LN2 temperatures for APS-U. (Germanium's thermal properties improve with decreasing temperature [160] but not nearly so dramatically and favorably as the properties of silicon do.) Adding a Ge(111) option to the XPCS beamline monochromator [along with Si(111) and Si(311)] would provide a dramatic factor of 3× more coherent flux for almost all SA-XPCS experiments requiring monochromatic radiation and might be useful for a few WA-XPCS experiments.
5. Examine the coherence preservation for narrower bandpass (0.1–0.5% relative bandwidth) multilayer optics. In a similar vein, evaluate the performance and cooling requirements for multilayer optics under moderate heat loads (≈ 5 W/mm^2).

6-11 Nano-focusing Optics Development for the APS-Upgrade

Nano-focusing Optics Development for the APS-Upgrade involves research and development of a zone plate based optical system that can focus X-rays efficiently down to 20 nm focus size and up to 25 keV X-ray energy. Zone plates are circular diffraction optics similar to gratings, but with changing period as a function of radius. The numerical aperture, or the focusing power, is proportional to the outermost zone width, and for hard X-ray energy, the focusing efficiency is largely determined by the zone thickness. A high resolution and efficient hard X-ray zone plate will have a thin outermost zone width while also being very thick, i.e. a 20 nm wide, 4000 nm tall outer most zone. To accomplish the stated goals, the project involves developing high-resolution zone plate fabrication capabilities at the Center for Nanoscale Materials (CNM), simulation software to test ideas, and a zone plate stacking apparatus to align up to six zone plates for high efficiency due to increased total zone thickness. Several XSD scientists and engineers have worked on the stacking device, including Sophie Gleber, Deming Shu, Michael Wojcik, Barry Lai, Christian Roehrig, Jie Liu, and Stefan Vogt, while Michael Wojcik has developed the zone plate fabrication methods.

Development of the fabrication methods for zone plates corresponds with the fabrication of the sets of zone plates needed for stacking experiments. Several sets of zone plates used for the first high energy stacking experiments were fabricated with 80 nm outer zone width and 10 aspect ratio structures using a previously established recipe (Figure 6.121). We then developed a higher contrast lithography technique to fabricate up to 20 aspect ratio zone plates with 50 nm outer zone width. We have also fabricated zone plates with smaller zones using atomic layer deposition and have fabricated several sets of zone plates for future stacking experiments, and a single zone plate shown in Figure 6.122. Similar fabrication methods resulted in sets of 16 nm outer zone width zone plates with greater than 20 aspect ratio and these optics were designed for the 20 nm focus spot size stacking experiments in the future. The research and development of zone plate fabrication has progressed to reach the goals set by APS-U on schedule.

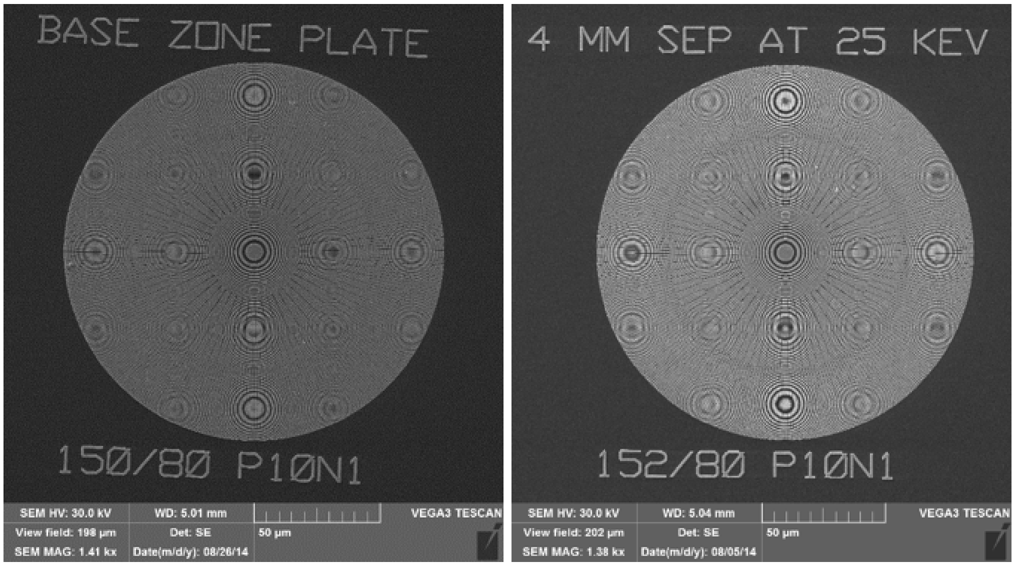

Figure 6.121. The base (left) and six (right) zone plate used for stacking experiments with 80 nm outer zone width, the six zone plate should be positioned 4 mm away from the base zone plate at 25 keV X-ray energy focusing.

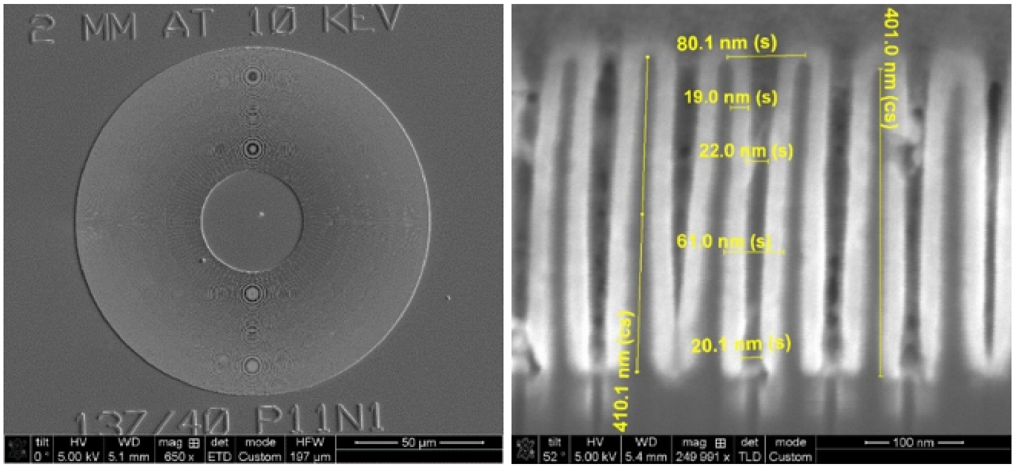

Figure 6.122. Zone plate with 20 nm outer zone width and 20 aspect ratio designed to be 2 mm from the base zone plate at 10 keV X-ray energy for a future stacking experiment.

Simulations designed to test the concept for zone plate stacking and validate new ideas for zone plate development played a relatively small but useful part in the development. We based the simulation code on free space propagation after X-rays interact with the zone plates to determine the focusing spot size and efficiency. We used the simulation results to compare with experimental data and found good agreement, after taking into account the fabrication errors. These results for stacking experiments with larger zone width zone plates brought confidence that the experiments with smaller outer zone width would work.

We have demonstrated intermediate zone plate stacking towards high efficiency at high X-ray energy and towards fine focus for X-ray energy around 10 keV. The first high energy X-ray experiment was done with a set of five zone plates with 80 nm outer zone width and we measured close to 20% efficiency at 25 keV [*Opt. exp.* **22**, 23 (2014)]. After some improvements, for the next experiment we stacked six at 27 keV X-ray energy and achieved 28% focusing efficiency, which was about 20 times larger than the efficiency of a single zone plate while maintaining the same focal spot size [*SPIE Opt. Eng. + Appl.* (2015)]. The stacking apparatus setup is show in Figure 6.123. The next step taken was decreasing outermost zone width to 60 nm and using three stacked zone plates to achieve 22% focusing efficiency at 10 keV. Towards the end of the three-year period, an experiment stacking four zone plates with 40 nm outer zone width was done and achieved 6.5% efficiency at 10 keV, though each individual zone plate had close to 0.5% focusing efficiency. The misalignment was also measured and after 8 hours was less than 7 nm total between the four zone plates. We are planning upcoming experiments to stack six zone plates with 20 nm and 16 nm outer zone width, to achieve the goals for the APS-Upgrade zone plate R&D project. The US patent related to the zone plate stacking apparatus granted is Patent #9,613,729 B2.

We have made tremendous progress the last few years: starting from an idea, to engineering the stacking apparatus and developing the fabrication methods, to the first stacking tests, and finally advancement to stacking smaller zone width zone plates. Completing the nano-focusing optics development on time will result in capabilities available to APS beamlines and will dovetail into the next generation of nano-focusing optics with incredibly high resolution capabilities.

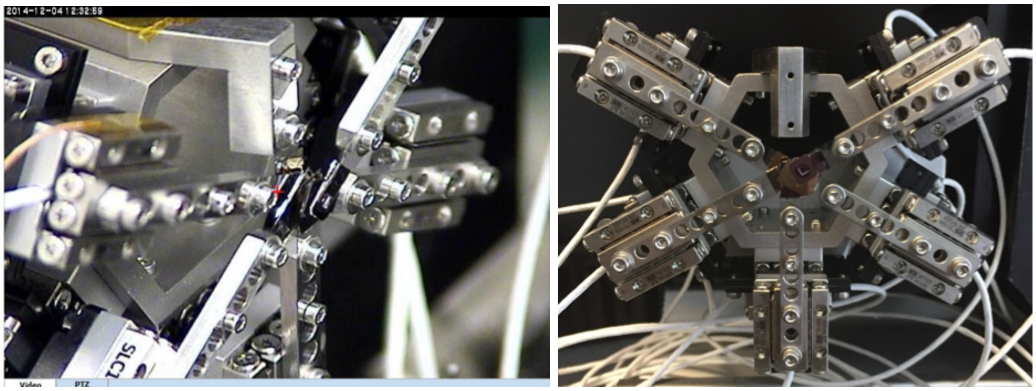

Figure 6.123. (left) A profile view of six zone plates stacked from the experiment at 27 keV during the test, (right) looking at the stacking apparatus from the front side with five zone plates out of beamline.

6-12 Beamline Enhancements

The APS-U Feature Beamline scope is designed to deliver a relatively small number of new or significantly upgraded beamlines that will be recognized as world-leading or world-class in performance, and are explicitly designed to capitalize on the strengths of the APS-U storage ring. What should not be overlooked is that the current APS has over sixty operating beamlines, many of which are state-of-the-art for a particular x-ray technique. A relatively small investment in key areas (e.g., optics) allows for many beamlines to utilize the improved emittance of the APS-U storage ring and tremendously leverages the APS-U Project.

The APS-U Beamline Enhancements process and scope is designed to address the opportunity that exists to make relatively minor investments in existing beamlines with resultant large increases in a beamline's ability to utilize the improvements of the APS-U. Two guiding principles were used for the Beamline Enhancements: 1) No beamline should lose ground in its performance after the APS-U is finished – "do no harm," and 2) it is prudent to make relatively minor investments that significantly improve a beamlines performance – "bang for the buck." For the APS-U Beamline Enhancements process, the do-no-harm items that fall under the first principle are considered "Non-Discretionary," and those that fall under the second bang-for-the-buck principle as "Discretionary."

To establish a baseline for the APS-U Beamline Enhancements, APS-U staff solicited a self-evaluation from every APS beamline. The items in the self-evaluation were costed and evaluated for merit to produce a top-down cost estimate and proposed budget that was presented at the APS-U DOE CD-3B review. The self-evaluation also provided information that was used to identify the Non-Discretionary items for APS-Beamlines. These items could be sorted as:

- Realignment of bending-magnet beamlines
- Shielding enhancements
- Beam choppers for bunch separation
- Optics (typically needed because of heat-load performance)
- High-heat-load safety components (e.g., stops, shutters)
- Beamline canting components

Using the remaining Beamline Enhancement budget as a starting point, a call was made in December, 2016 for any APS beamline to submit short proposals with items to be considered as a Discretionary Beamline Enhancement. Items in proposals were evaluated for feasibility and costed. In total, 47 proposals were submitted, nearly all with multiple items. An ad-hoc review committee met and evaluated the proposals on March 21, 2017. Subsequently, APS/APS-U management used that evaluation and a discussion with the APS SAC to select the preliminary Beamline Enhancement scope. This scope is shown in Table 6.52.

Table 6.52. Beamline Enhancement Scope

Beamline	Proposal	Item
1-ID	Upgrade Enhancements for the 1-ID Beamline for APS-U	1-ID-E station extension Added tilt stage Hexapod
1-ID	1-ID Enhancement–High-Energy Monochromator Upgrade	Monochromator upgrade
2-ID	Enhancement of the 2-ID Beamline and Microprobe	Two vertical focusing mirrors Beam Defining Aperture Figured KB mirrors mounted inside vacuum chamber Compact laser interferometers, two on each KB mirror High-stiffness fast-scanning sample stages
3-ID	Beamline Enhancement Request for 3-ID	KB-mirror system
5-ID	APS Upgrade Project: DND-CAT Beamline Enhancement Request	Refinished Mirrors Upgraded Monochromator
6-ID	6-ID-D: Disorder in materials at extreme conditions	Focusing capabilities using CRLs
6-ID	Studying Mesoscopic Principles underlying Emergent Behaviors in Condensed Matter Physics	CRLs for horizontal and vertical focusing
7-ID	7-ID Beamline Enhancement Proposal	Mirror for diffraction branch Nanodiffraction focusing optics Detector arm
11-ID	11-ID-D/E: A multi-modal high-energy X-ray beamline	Cant 11-ID beamline Bent Laue, double crystal monochromator Multiple sets of compound refractive lenses
12-ID	Upgrade of 12-ID SAXS Programs	Long SAXS tube/USAXS Enclosure modification CRL System
13-ID	APS-U Beamline Enhancement Proposals for Sector 13 (GSECARS)	Dual horizontal mirrors (500 mm) Two sets of KB mirrors Double crystal monochromator End station instrumentation (Table upgrade for stability) 1.0 m long mirrors (one vertical and one horizontal focusing) KB system - 350 mm long mirrors
15-ID	ChemMatCARS (15-ID) Beamline Enhancement Proposal	2D CRL focusing system One harmonic rejection mirror system Bent-Flat Vertical Focusing Mirror System

Beamline	Proposal	Item
20-ID	Proposed Enhancements to the 20-ID LERIX Endstation	Movable analyzers
20-ID	Multilayer Monochromator for 20-ID	Multi-layer monochromator
26-ID	APS-Upgrade Beamline Discretionary Enhancement Proposal: The 4D Nanoprobe (N4D) Controlling Strain in Space and Time at the CNM/APS Hard X-ray Nanoprobe	High-speed high-range Nanoprobe scanning capabilities Rebuild of mirror system M1 interior components Rebuild of double crystal monochromator Stacked zone plate optics
27-ID	Ultra-high Energy Resolution Resonant Inelastic X-ray Scattering (RIXS) at 27-ID Beamline Enhancement Proposal	Extension of the high-energy-resolution monochromator Sphere of confusion
30-ID	Next Generation High Energy Resolution Inelastic X-ray Spectrometer (HERIX-30) at Beamline 30-ID at the Advanced Photon Source	Cryogenic conversion of Kohzu monochromator Cryogenic high-energy resolution monochromator
32-ID	Proposal for 32-ID Enhancement	Cant 32-ID beamline White beam shutter, and additional mask White beam slits, filters Be window(s) Aluminum pipes and adapters Slightly modification to the manual shutter, and new Be window Slightly modified end shutter Pair of small deflecting mirrors (ML) and hardware Double (vertical) mirrors (harmonics rejection) CRLs (Small transfocator), with alignments stages Precision slits Granite table Two sets of KB, with ML optimized for $\sim$ 25 keV and 12 keV energy ranges Nano-CT stack, with high speed air bearing rotation stage
XX-ID	USAXS facility upgrade for APS-MBA	Major revision of the main Bonse-Hart USAXS instrument
XX-ID	BNP-II: 10 nm cryogenic XRF nanoprobe	Polycapillary detector collimator Upgrade scanning stages Upgrade rotation stage Upgrade laser interferometer system Vacuum chamber Delta tau control system High-resolution and high-efficiency zone plate optics

References

[1] G Kwon, O Kokhan, A Han, K W Chapman, P J Chupas, P Du, D M Tiede, and IUCr. Oxyanion induced variations in domain structure for amorphous cobalt oxide oxygen evolving catalysts, resolved by X-ray pair distribution function analysis. *Acta Crystallographica Section B: Structural Science, Crystal Engineering and Materials*, 71(6):713–721, December 2015.

[2] David M Tiede. Private Communication (2016).

[3] A Ulvestad, A Tripathi, S O Hruszkewycz, W Cha, S M Wild, G B Stephenson, and P H Fuoss. Coherent diffractive imaging of time-evolving samples with improved temporal resolution. *Physical Review B*, 93(18):184105, May 2016.

[4] Wael Z Abuzaid, Michael D Sangid, Jay D Carroll, Huseyin Sehitoglu, and John Lambros. Slip transfer and plastic strain accumulation across grain boundaries in Hastelloy X. *Journal of the Mechanics and Physics of Solids*, 60(6):1201–1220, June 2012.

[5] Golden Kumar, Amish Desai, and Jan Schroers. Bulk Metallic Glass: The Smaller the Better. *Advanced Materials*, 23(4):461–476, January 2011.

[6] S H Dietze, O G Shpyrko, and IUCr. Coherent diffractive imaging: towards achieving atomic resolution. *Journal of Synchrotron Radiation*, 22(6):1498–1508, November 2015.

[7] B C Larson, Wenge Yang, G E Ice, J D Budai, and J Z Tischler. Three-dimensional X-ray structural microscopy with submicrometre resolution. *Nature*, 415(6874):887–890, February 2002.

[8] Takashi Kimura, Satoshi Matsuyama, Kazuto Yamauchi, and Yoshinori Nishino. Coherent x-ray zoom condenser lens for diffractive and scanning microscopy. *Opt. Express*, 21(8):9267, 2013.

[9] B Blank, T Kupp, E Johnson, and A Deyhim. Development of a goniometer with nanoradian accuracy. *… Engineering Design of …*, 2002.

[10] S. Vogt. Personal communication. 2014.

[11] T. Graber. Efficiency of horizontal monochromators for aps-u beamlines. Technical report, APS, ANL/APS/LS-347, 2017.

[12] Yury Ivanyushenkov. Modeling of magnetic structure. 2017.

[13] M. Suzuki and et al. *Jpn. J. App. Phys.*, 37:L1488, 1998.

[14] S. Francoual and et al. *Journal of Physics: Conference Series*, 425:132010, 2013.

[15] Scagnoli and et al. *J. Synchrotron Radiat.*, 16:778, 2009.

[16] T. Hara and et al. *Nucl. Instr. and Meth. in Phys. Res. A*, 498:496, 2003.

[17] X. Shi and et al. *J. Synchrotron Rad*, 21:669.

[18] T. Kolodziej, H. XianRong, Y. Shvydko, and et al.

[19] A V Zozulya, S Bondarenko, A Schavkan, F Westermeier, G Grübel, and M Sprung. Microfocusing transfocator for 1D and 2D compound refractive lenses. *Optics Express*, 20:18967, July 2012.

[20] J. Sidarous and StudioGC. Argonne national laboratory long beamline feasibility study. November 28 2016.

[21] Simon J L Billinge and Igor Levin. The problem with determining atomic structure at the nanoscale. *Science*, 316(5824):561–565, April 2007.

[22] Wenge Yang, Xiaojing Huang, Ross Harder, Jesse N Clark, Ian K Robinson, and Ho-kwang Mao. Coherent diffraction imaging of nanoscale strain evolution in a single crystal under high pressure. *Nature Communications*, 4:1680–, April 2013.

[23] Xiaojing Huang, Wenge Yang, Ross Harder, Yugang Sun, Ming Lu, Yong S Chu, Ian K Robinson, and Ho-kwang Mao. Deformation Twinning of a Silver Nanocrystal under High Pressure. *Nano Lett.*, 15(11):7644–7649, October 2015.

[24] H D Coughlan, C Darmanin, N W Phillips, F Hofmann, J N Clark, R J Harder, D J Vine, and B Abbey. Radiation damage in a micron-sized protein crystal studied via reciprocal space mapping and Bragg coherent diffractive imaging. *Structural Dynamics*, 2(4):041704, July 2015.

[25] Qun Shen, Ivan Bazarov, and Pierre Thibault. Diffractive imaging of nonperiodic materials with future coherent X-ray sources. *Journal of Synchrotron Radiation*, 11(5):432–438, September 2004.

[26] Andreas Schropp and Christian G Schroer. Dose requirements for resolving a given feature in an object by coherent x-ray diffraction imaging. *New Journal of Physics*, 12(3):035016, March 2010.

[27] Brian Abbey, Lachlan W Whitehead, Harry M Quiney, David J Vine, Guido A Cadenazzi, Clare A Henderson, Keith A Nugent, Eugeniu Balaur, Corey T Putkunz, Andrew G Peele, G J Williams, and I McNulty. Lensless imaging using broadband x-ray sources. *Nature Photonics*, 5(7):420–424, June 2011.

[28] Bo Chen, Ruben A Dilanian, Sven Teichmann, Brian Abbey, Andrew G Peele, Garth J Williams, Peter Hannaford, Lap Van Dao, Harry M Quiney, and Keith A Nugent. Multiple wavelength diffractive imaging. *Physical Review A*, 79(2):023809, February 2009.

[29] W. Cha, W. Liu, R. Harder, R. Xu, P.H. Fuoss, and S.O. Hruszkewycz. Utilizing broadband x-rays in a bragg coherent x-ray diffraction imaging experiment. 2016.

[30] *Early Science at the Upgraded Advanced Photon Source https://www1.aps.anl.gov/APS-Upgrade*. 2015.

[31] W Cha, A Ulvestad, M Allain, V Chamard, R Harder, S J Leake, J Maser, P H Fuoss, and S O Hruszkewycz. Three Dimensional Variable-Wavelength X-Ray Bragg Coherent Diffraction Imaging. *Physical review letters*, 117(22):225501, November 2016.

[32] Robert P Winarski, Martin V Holt, Volker Rose, Peter Fuesz, Dean Carbaugh, Christa Benson, Deming Shu, David Kline, G Brian Stephenson, Ian McNulty, and Jörg Maser. A hard X-ray nanoprobe beamline for nanoscale microscopy. *Journal of Synchrotron Radiation*, 19(Pt 6):1056–1060, November 2012.

[33] Satoshi Matsuyama, Hiroki Nakamori, Takumi Goto, Takashi Kimura, Krishna P Khakurel, Yoshiki Kohmura, Yasuhisa Sano, Makina Yabashi, Tetsuya Ishikawa, Yoshinori Nishino, and Kazuto Yamauchi. Nearly diffraction-limited X-ray focusing with variable-numerical-aperture focusing optical system based on four deformable mirrors. *Scientific reports*, 6:24801, April 2016.

[34] Paul Kirkpatrick and A V Baez. Formation of Optical Images by X-Rays. *JOSA*, 38(9):766–774, September 1948.

[35] Jonathan Logan, Ross Harder, Luxi Li, Daniel Haskel, Pice Chen, Robert Winarski, Peter Fuesz, Deborah Schlagel, David Vine, Christa Benson, and Ian McNulty. Hard X-ray polarizer to enable simultaneous three-dimensional nanoscale imaging of magnetic structure and lattice strain. *Journal of Synchrotron Radiation*, 23(5):1210–1215, 2016.

[36] Satoshi Matsuyama, Hiroki Nakamori, Takumi Goto, Takashi Kimura, Krishna P Khakurel, Yoshiki Kohmura, Yasuhisa Sano, Makina Yabashi, Tetsuya Ishikawa, Yoshinori Nishino, and Kazuto Yamauchi. Nearly diffraction-limited X-ray focusing with variable-numerical-aperture focusing optical system based on four deformable mirrors. *Scientific reports*, 6(1):srep24801, April 2016.

[37] J Morse, B Solar, H Graafsma, and IUCr. Diamond X-ray beam-position monitoring using signal readout at the synchrotron radiofrequency. *Journal of Synchrotron Radiation*, 17(4):456–464, July 2010.

[38] Klaus Giewekemeyer, Hugh T Philipp, Robin N Wilke, Andrew Aquila, Markus Osterhoff, Mark W Tate, Katherine S Shanks, Alexey V Zozulya, Tim Salditt, Sol M Gruner, and Adrian P Mancuso. High-dynamic-range coherent diffractive imaging: ptychography using the mixed-mode pixel array detector. *Journal of Synchrotron Radiation*, 21(5):1167–1174, September 2014.

[39] J Fienup. Phase retrieval algorithms: a comparison. *Applied optics*, 21(15):2758–2769, 1982.

[40] S Marchesini, H He, H Chapman, S Hau-Riege, A Noy, M Howells, U Weierstall, and J Spence. X-ray image reconstruction from a diffraction pattern alone. *Physical Review B*, 68(14):140101, 2003.

[41] Jesse N Clark, Loren Beitra, Gang Xiong, David M Fritz, Henrik T Lemke, Diling Zhu, Matthieu Chollet, Garth J Williams, Marc M Messerschmidt, Brian Abbey, Ross J Harder, Alexander M Korsunsky, Justin S Wark, David A Reis, and Ian K Robinson. Imaging transient melting of a nanocrystal using an X-ray laser. *Proceedings of the National Academy of Sciences of the United States of America*, 112(24):7444–7448, June 2015.

[42] M R Howells, T Beetz, H N Chapman, C Cui, J M Holton, C J Jacobsen, J Kirz, E Lima, S Marchesini, H Miao, D Sayre, D A Shapiro, John Spence, and D Starodub. An assessment of the resolution limitation due to radiation-damage in X-ray diffraction microscopy. *Journal of Electron Spectroscopy and Related Phenomena*, 170(1-3):4–12, 2009.

[43] Elbio Dagotto. Complexity in strongly correlated electronic systems. *Science*, 309(5732):257–262, 2005.

[44] GE Jellison, John D Budai, Charlee JC Bennett, Jonathan Zachary Tischler, Chad E Duty, V Yelundur, and A Rohatgi. High-resolution x-ray and light beam induced current (lbic) measurements of multcrystalline silicon solar cells. In *Photovoltaic Specialists Conference (PVSC), 2010 35th IEEE*, pages 001715–001720. IEEE, 2010.

[45] John D Budai, Wenge Yang, Nobumichi Tamura, Jin-Seok Chung, Jonathan Z Tischler, Bennett C Larson, Gene E Ice, Chan Park, and David P Norton. X-ray microdiffraction study of growth modes and crystallographic tilts in oxide films on metal substrates. *Nature Materials*, 2(7):487–492, 2003.

[46] Gene E Ice and Judy WL Pang. Tutorial on x-ray microlaue diffraction. *Materials Characterization*, 60(11):1191–1201, 2009.

[47] Wenge Yang, BC Larson, GM Pharr, GE Ice, JD Budai, JZ Tischler, and Wenjun Liu. Deformation microstructure under microindents in single-crystal cu using three-dimensional x-ray structural microscopy. *Journal of materials research*, 19(01):66–72, 2004.

[48] BC Larson, Wenge Yang, GE Ice, JD Budai, and JZ Tischler. Three-dimensional x-ray structural microscopy with submicrometre resolution. *Nature*, 415(6874):887–890, 2002.

[49] Jonathan Z. Tischler. Reconstructing 2d and 3d x-ray orientation maps from white-beam laue. In Rozaliya Barabash and Gene Ice, editors, *Strain and Dislocation Gradients from Diffraction*, chapter 10, pages 358–375. Imperial College Press, London, 2014.

[50] Challenges at the Frontiers of Matter and Energy: Transformative Opportunities for Discovery Science. Technical report, Basic Energy Sciences Advisory Committee, November 2015.

[51] Early Science at the Upgraded APS. `https://www1.aps.anl.gov/files/download/Aps-Upgrade/Beamlines/APS-U%20Early-Science-103015-FINAL.pdf`, 2015.

[52] M. H. Yang and C. P. Flynn. *Phys. Rev. Lett.*, 62:2476, 1989.

[53] J. Y. Tsao. Materials fundamentals of molecular beam epitaxy. *Academic, San Diego*, 1993.

[54] F. Jiang, A. Munkholm, R.-V. Wang, S. K. Streiffer, Carol Thompson, P. H. Fuoss, K. Latifi, K. R. Elder, and G. B. Stephenson. *Phys. Rev. Lett.*, 101:086102, 2008.

[55] J. E. Millburn, J. F. Mitchell, and D. N. Argyriou. *Chem. Commun.*, 15:1389–1390, 1999.

[56] A. Yeckel, P. Daoutidis, and J. J. Derby. *J. Cryst. Growth*, 361:16, 2012.

[57] D.J. Duquette and et al. *Research Opportunities in Corrosion Science and Engineering.* The National Academies Press, 2011.

[58] A Ulvestad, A Singer, J N Clark, H M Cho, J W Kim, R Harder, J Maser, Y S Meng, and O G Shpyrko. Topological defect dynamics in operando battery nanoparticles. *Science*, 348(6241):1344–1347, June 2015.

[59] S. Ravy. *Acta Cryst. A*, 69:543, 2013.

[60]] S.O. Hruszkewycz, M. Allain, M. V. Holt, C. E. Murray, J. R. Holt, P. H. Fuoss, and V. Chamard. High resolution three dimensional structural microscopy by single angle bragg ptychography. *[cond.mat. mtrl. sci] arxiv:1506.01262*, 2015.

[61] P. Fenter. 2016.

[62] M. G. Rainville, C. Wagenbach, J. G. Ulbrandt, S. Narayanan, A. R. Sandy, Hua Zhou, R. L. Headrick, and Jr. K. F. Ludwig. *Phys. Rev. B*, 92:214102, 2015.

[63] E. M. Dufresne, S. Narayanan, A. R. Sandy, D. M. Kline, Q. Zhang, E. C. Landahl, and S. Ross. *Optics Express*, 24:355, 2016.

[64] M. Altarelli, R. P. Kurta, and I. A. Vartanyants. Phys. rev. B 82:104207, 2010.

[65] M. Sutton. 2016.

[66] In situ characterization of surface and interface structures and processes. In *Workshop*. APS, Argonne Natational Laboratory, Sept 8-9 2005.

[67] Catalysis research. In *Workshop*. APS, Argonne Natational Laboratory, Sept 12-13 2005.

[68] Interfacial and surface science. In *Woorkshop*. APS, Argonne Natational Laboratory, june 29 2006.

[69] In situ studies of interfacial reflectivity. In *Workshop*. APS, Argonne Natational Laboratory, May 10 2007.

[70] Aps renewal project workshop. Lisle, IL, Oct 20-21 2008.

[71] M. Bedzyk, P. Fenter, and P. Fuoss. X-ray interfacial science collaborative development team proposal to the aps. Technical report, Dec 2008.

[72] *APS Upgrade Conceptual Design Report*. 2011.

[73] X-ray interface science at the advanced photon source: New sector development. APS, Argonne National Laboratory, Jan 10-12 2012.

[74] *APS Upgrade Preliminary Design Report*. 2012.

[75] New science opportunities provided by a multi-bend achromat lattice at the aps. In *Workshop*. APS, Argonne National Laboratory, Oct 21-22 2013.

[76] http://www.ne.anl.gov/xmat/.

[77] H.M. Jaeger and A.J. Liu. *cond-mat.soft*, 2010. arXiv:1009.487v1.

[78] T.Sun, Z. Jiang, J. Strzalka, L. Ocola, and J. Wang. *Nat. Photon*, 6:586–590, 2012.

[79] J. Miao, T. Ishikawa, I.K. Robinson, and M.M. Murnane. *Science*, 348:530–535, 2015.

[80] Murphy and et al. *J. Synchrotron Radiat.*, 21:45–56, 2014.

[81] https://www.dectris.com/EIGER.html.

[82] Tate and et al. *J. Physics: Conf. Series*, 425, 2013.

[83] A.F. Isakovic and et al. *J. Synchrotron Rad.*, 16:8–13, 2009.

[84] M. Pellin. eXtreme MATerials (XMAT) beamline. *Argonne National Laboratory*, website:http://www.ne.anl.gov/xmat/.

[85] S. D. Shastri, P. Kenesei, and R. M. Suter. Refractive lens based full-field x-ray imaging at 45–50 keV with sub-micron resolution). *SPIE*, 9592:95920X–1–9, 2015.

[86] A. Ulvestad, H. M. Cho, R. Harder, J. W. Kim, , S. H. Dietze, E. Fohtung, Y. S. Meng, , and O. G. Shypyrko. Nanoscale strain mapping in battery nanostructures. *Appl. Phys. Lett.*, 104:073108–1–5, 2014.

[87] H. Simons, A. King, W. Ludwig, C. Detlefs, W. Pantleon, S. Schmidt, I. Snigireva, A. Snigirev, and H. F. Poulsen. Dark-field x-ray microscopy for multiscale structural characterization. *Nature Communications*, 6:6098–1–6, 2015.

[88] B. Jakobsen, H. F. Poulsen, U. Lienert, J. Almer, S. D. Shastri, H. Sorenson, C. Gundlach, and W. Pantleon. Formation and subdivision of deformation structures during plastic deformation. *Science*, 312:889–892, 2006.

[89] S. D. Shastri, K. Fezzaa, A. Mashayekhi, W.-K. Lee, P. B. Fernandez, and P. L. Lee. Cryogenically-cooled, bent double-Laue monochromator for high-energy undulator x-rays (50–200 keV). *J. Synchrotron Radiation*, 9:317–322, 2002.

[90] S. D. Shastri. Combining flat crystals, bent crystals, and compound refractive lenses for high-energy x-ray optics. *J. Synchrotron Radiation*, 11:150–156, 2004.

[91] S. D. Shastri, K. Evans-Lutterodt, R. L Sheffield, A. Stein, M. Metzler, and P. Kenesei. Kinoform lens focusing of high-energy x-rays (50–100 keV). *SPIE*, 9207:920704–1–9, 2014.

[92] S. D. Shastri, J. Almer, C. Ribbing, and B. Cederström. High-energy x-ray optics with silicon saw-tooth refractive lenses. *J. Synchrotron Radiation*, 14:204–211, 2007.

[93] S. O. Hruszkewycz, M. V. Holt, M. Allain, V. Chamard, S. M. Polvino, C. E. Murray, and P. H. Fuoss. Efficient modeling of Bragg coherent x-ray nanobeam diffraction. *Optics Letters*, 40:3241–3244, 2015.

[94] D. J. Batey, T. B. Edo, C. Rau, U Wagner, Z. D. Pesic, T. A. Waigh, and J. M. Rodenburg. Reciprocal-space up-sampling from real-space oversampling in x-ray ptychography. *Phys. Rev*, A89:043812–1–5, 2014.

[95] M. Stuckelberger, B. West, T. Nietzold, B. Lai, J. M. Maser, V. Rose, and M. I. Bertoni. Review: Engineering solar cells based on correlative x-ray microscopy. *Journal of Materials Research*, 32(10):1825–1854, 2017.

[96] M. Stuckelberger, T. Nietzold, G. N. Hall, B.West, J. Werner, B. Niesen, C. Ballif, V. Rose, D. P. Fenning, and M.Bertoni. Charge collection in hybrid perovskite solar cells: relation to the nanoscale elemental distribution. *IEEE J. Photovolt.*, 7(2):590–597, 2017.

[97] G. Martinez-Criado, J. Segura-Ruiz, B. Alèn, J. Eymery, A. Rogalev, R. Tucoulou, and A. Homs. Exploring single semiconductor nanowires with a multimodal hard x-ray nanoprobe. *Adv. Mater.*, 26:7873–7879, 2014.

[98] M. P. Nikiforov, B. Lai, W. Chen, S. Chen, R. D.Schaller, J. Strzalka, J. Maser, and S. B. Darling. Detection and role of trace impurities in high-performance organic solar cells. *Energy Environ. Sci.*, 6:1513, 2013.

[99] M. I. Bertoni, D. P. Fenning, M. Rinio, V. Rose, M. Holt, J. Maser, and T. Buonassisi. Nanoprobe x-ray fluorescence characterization of defects in large-area solar cells. *Energy Environ. Sci.*, 4:4252–5257, 2011.

[100] R. L. Z. Hoye, R. E. Brandt, A. Osherov, V. Stevanović, S. D. Stranks, M. W. B. Wilson, H. Kim, A. J. Akey, J. D. Perkins, R. C. Kurchin, J. R. Poindexter, E. N. Wang, M. G. Bawendi, V. Bulović, and T. Buonassisi. *Chem. Eur. J.*, 2016. doi:10.1002/chem.201505055.

[101] V. K. Kapur, B. M. Basol, and E. S. Tseng. Low cost methods for the production of semiconductor films for cuinse2/cds solar cells. *Solar Cells*, 21:65–72, 1987.

[102] M. Kaelin, D. Rudmann, F. Kurdesau, H. Zogg, T. Meyer, and A. N. Tiwari. Low-cost cigs solar cells by paste coating and selenization. *Thin Solid Films*, 480âĂŞ481:486–490, 2005.

[103] D. P. Fenning, J. Hofstetter, A. E. Morishige, D. M. Powell, A. Zuschlag, G. Hahn, and T. Buonassisi. Darwin at high temperature: Advancing solar cell material design using defect kinetics simulations and evolutionary optimization. *Adv. Energy Mater.*, 4(13):1400459, 2013.

[104] D. Starodub and et al. Dose, exposure time and resolution in serial x-ray crystallography. *Journal of Synchrotron Radiation*, 15:62–73, 2008.

[105] Q. Shen, I. Bazarov, and P. Thibault. Diffractive imaging of nonperiodic materials with future coherent x-ray sources. *Journal of Synchrotron Radiation*, 11:432–438, 2004.

[106] D. Vine. Personal communication. 2015.

[107] J.C. Da Silva and et al. Efficient concentration of high-energy x-rays for diffraction-limited imaging resolution. *Optica*, 4(5):492–495, 2017.

[108] H. N. Chapman and et al. High-resolution ab initio three-dimensional x-ray diffraction microscopy. *Journal of the Optical Society of America a-Optics Image Science and Vision,*, 23(5):1179–1200, 2006.

[109] J. Miao and et al. Direct determination of the absolute electron density of nanostructured and disordered materials at sub-10-nm resolution. *Physical Review B,*, 68(1), 2003.

[110] C. G. Schroer and et al. Coherent x-ray diffraction imaging with nanofocused illumination. *Physical Review Letters*, 101(9), 2008.

[111] Y. Takahashi and et al. High-resolution diffraction microscopy using the plane-wave field of a nearly diffraction limited focused x-ray beam. *Physical Review B*, 80(5), 2009.

[112] D.J. Vine and et al. Simultaneous x-ray fluorescence and ptychographic microscopy of cyclotella meneghiniana. *Opt. Express*, 20(16):18287–18296, 2012.

[113] J. Uhlig and et al. High-resolution x-ray emission spectroscopy with transition-edge sensors: present performance and future potential. *J Synchrotron Radiat*, 22(Pt 3):766–775, 2015.

[114] L. Mandel and E. Wolf. *Optical Coherence and Quantum Optics*. Cambridge University Press, 1995.

[115] G.G. Lonzarich. *Nat. Phys.*, 1:11, 2005.

[116] C. Pfleiderer. *Rev. Mod. Phys.*, 81:1551, 2009.

[117] L. Dubrovinsky and et al. *Nature*, 525:226–229, 2015.

[118] M. Eremets and et al. *Nature*, 411:170, 2011.

[119] Drozdov and et al. *Nature*, 525:73, 2015.

[120] L. Mirebeau and et al. *Nature*, 420:54, 2002.

[121] Aronson and et al. *Phy. Rev. Let.*, 63:2311, 1989.

[122] N. Souza-Neto and et al. *Phy. Rev. Let.*, 109:026403, 2012.

[123] N. Ishimatzu and et al. *Phy. Rev. B*, 83:180409, 2011.

[124] R. Torchio and et al. *PHY. REV. B*, 84:060403, 2011.

[125] H. H. Kung and et al. *Science*, 347:6228.

[126] J. C. Lashley and et al. *Phys. Rev. B*, 72:054416, 2005.

[127] R. H. Heffner and et al. *Phys. Rev. B*, 73:094453, 2006.

[128] S. Maekawa and et al. Physics of transition metal oxides. *Springer Series in Solid State Sciences*, 144:337, 2004.

[129] C.N.R. Rao and B. Raveau. *Transition Metal Oxides: Structure, Properties, and Synthesis of Ceramic Oxides*. Number 392. Wiley-VCH., 1998.

[130] C. M. Pepin and et al. *Phys. Rev. Lett.*, 113:265504, 2014.

[131] A. Kitaev. *Ann. Phys. (N.Y.)*, 321:2.

[132] Roger Dejus. Tuning curves calculated. 2016.

[133] T. Hara and et al. *J. Synchotron Rad.*, 5:426, 1998.

[134] Ruben Reininger and Xianbo Shi. Calculations. 2017.

[135] R. Reininger and et al. In *AIP Conf. Proc*, volume 1234, page 383, 2010.

[136] E Jakeman. *Photon Correlation and Light Beating Spectroscopy*. Plenum, New York, 1973.

[137] Friso van der Veen and Franz Pfeiffer. Coherent x-ray scattering. *Journal of Physics: Condensed Matter*, 16(28):5003–5030, July 2004.

[138] W Roseker, H Franz, H Schulte-Schrepping, A Ehnes, O Leupold, F Zontone, A Robert, and G Grübel. Performance of a picosecond x-ray delay line unit at 8.39 keV. *Optics Letters*, 34(12):1768–1770, June 2009.

[139] Wojciech Roseker, Hermann Franz, Horst Schulte-Schrepping, Anita Ehnes, Olaf Leupold, Federico Zontone, Sooheyong Lee, Aymeric Robert, and Gerhard Grübel. Development of a hard X-ray delay line for X-ray photon correlation spectroscopy and jitter-free pump–probe experiments at X-ray free-electron laser sources. *Journal of Synchrotron Radiation*, 18(3):481–491, March 2011.

[140] Wojciech Roseker, Sooheyong Lee, Michael Walther, Horst Schulte-Schrepping, Hermann Franz, Amber Gray, Marcin Sikorski, Paul H Fuoss, G Brian Stephenson, Aymeric Robert, and Gerhard Grübel. Hard x-ray delay line for x-ray photon correlation spectroscopy and jitter-free pump-probe experiments at LCLS. In Stefan P Moeller, Makina Yabashi, and Stefan P Hau-Riege, editors, *SPIE Optical Engineering + Applications*, pages 85040I–7. SPIE, October 2012.

[141] Yuri P Stetsko, Yuri V Shvyd'ko, and G Brian Stephenson. Time-delayed beam splitting with energy separation of x-ray channels. *Applied Physics Letters*, 103(17):173508–5, 2013.

[142] J Wingert, A Singer, and O G Shpyrko. A new method for studying sub-pulse dynamics at synchrotron sources. *Journal of Synchrotron Radiation*, 22:1141–1146, August 2015.

[143] Grzegorz W Deptuch, Gabriella Carini, Pawel Grybos, Piotr Kmon, Piotr Maj, Marcel Trimpl, David P Siddons, Robert Szczygiel, and Raymond Yarema. Design and Tests of the Vertically Integrated Photon Imaging Chip. *IEEE Transactions on Nuclear Science*, 61(1):663–674, February 2014.

[144] Grzegorz W Deptuch, Gabriella Carini, Paul Enquist, Pawel Grybos, Scott Holm, Ronald Lipton, Piotr Maj, Robert Patti, David Peter Siddons, Robert Szczygiel, and Raymond Yarema. Fully 3-D Integrated Pixel Detectors for X-Rays. *IEEE Transactions on Electron Devices*, 63(1):205–214, December 2015.

[145] A K Rumaiz, D P Siddons, G Deptuch, P Maj, A J Kuczewski, G A Carini, S Narayanan, E M Dufresne, A Sandy, R Bradford, A Fluerasu, and M Sutton. First experimental feasibility study of VIPIC: a custom-made detector for X-ray speckle measurements. *Journal of Synchrotron Radiation*, pages 1–6, February 2016.

[146] G B M Vaughan, J P Wright, A Bytchkov, M Rossat, H Gleyzolle, I Snigireva, and A Snigirev. X-ray transfocators: focusing devices based on compound refractive lenses. *Journal of Synchrotron Radiation*, 18:125–133, December 2010.

[147] M Sikorski, S Song, A Schropp, F Seiboth, Y Feng, R Alonso-Mori, M Chollet, H T Lemke, D Sokaras, T C Weng, W Zhang, A Robert, and D Zhu. Focus characterization at an X-ray free-electron laser by coherent scattering and speckle analysis. *Journal of Synchrotron Radiation*, 22:599–605, April 2015.

[148] Undulator A magnetic properties and spectral performance. Technical report, Advanced Photon Source, Argonne National Laboratory, 05 2002.

[149] P Kristiansen, J Horbach, R Dohrmann, and J Heuer. Vibration measurements of high-heat-load monochromators for DESY PETRA III extension. *Journal of Synchrotron Radiation*, 22:879–885, May 2015.

[150] P Kristiansen, U Johansson, T Ursby, and B N Jensen. Vibrational stability of a cryocooled horizontal double-crystal monochromator. *Journal of Synchrotron Radiation*, 23:1076–1081, July 2016.

[151] I Sergueev, R Dohrmann, J Horbach, and J Heuer. Angular vibrations of cryogenically cooled double-crystal monochromators. *Journal of Synchrotron Radiation*, pages 1–7, August 2016.

[152] S Narayanan, A Sandy, D Shu, M Sprung, C Preissner, and J Sullivan. Design and performance of an ultra-high-vacuum-compatible artificial channel-cut monochromator. *Journal of Synchrotron Radiation*, 15:12–18, December 2007.

[153] I Johnson, A Bergamaschi, J Buitenhuis, R Dinapoli, D Greiffenberg, B Henrich, T Ikonen, G Meier, A Menzel, A Mozzanica, V Radicci, D K Satapathy, B Schmitt, and X Shi. Capturing dynamics with Eiger, a fast-framing X-ray detector. *Journal of Synchrotron Radiation*, 19:1001–1005, September 2012.

[154] I Johnson, A Bergamaschi, H Billich, S Cartier, R Dinapoli, D Greiffenberg, M Guizar-Sicairos, B Henrich, J Jungmann, D Mezza, A Mozzanica, B Schmitt, X Shi, and G Tinti. Eiger: a single-photon counting x-ray detector. *Journal of Instrumentation*, 9(05):C05032–C05032, May 2014.

[155] M. Ramilli, A. Bergamaschi, M. Andrae, M. BrÃijckner, S. Cartier, R. Dinapoli, E. FrÃűjdh, D. Greiffenberg, T. Hutwelker, C. Lopez-Cuenca, D. Mezza, A. Mozzanica, M. Ruat, S. Redford, B. Schmitt, X. Shi, G. Tinti, and J. Zhang. Measurements with mönch, a 25 μm pixel pitch hybrid pixel detector. *Journal of Instrumentation*, 12(01):C01071, 2017.

[156] R Ballabriga, J Alozy, G Blaj, M Campbell, M Fiederle, E Frojdh, E H M Heijne, X Llopart, M Pichotka, S Procz, L Tlustos, and W Wong. The Medipix3RX: a high resolution, zero dead-time pixel detector readout chip allowing spectroscopic imaging. *Journal of Instrumentation*, 8(02):C02016–C02016, February 2013.

[157] P Grybos, P Kmon, P Maj, and R Szczygiel. 32k Channel Readout IC for Single Photon Counting Pixel Detectors with Pitch, Dead Time of 85 ns, Offset Spread and 2% rms Gain Spread. *IEEE Transactions on Nuclear Science*, 63(2):1155–1161, April 2016.

[158] Q Zhang, E M Dufresne, P Grybos, P Kmon, P Maj, S Narayanan, G W Deptuch, R Szczygiel, and A Sandy. Submillisecond X-ray photon correlation spectroscopy from a pixel array detector with fast dual gating and no readout dead-time. *Journal of Synchrotron Radiation*, 23:679–684, April 2016.

[159] G Blaj, P Caragiulo, G Carini, S Carron, A Dragone, D Freytag, G Haller, P Hart, J Hasi, R Herbst, S Herrmann, C Kenney, B Markovic, K Nishimura, S Osier, J Pines, B Reese, J Segal, A Tomada, and M Weaver. X-ray detectors at the Linac Coherent Light Source. *Journal of Synchrotron Radiation*, pages 1–7, April 2015.

[160] Donald H. Bilderback, Andreas K. Freund, Gordon S. Knapp, and Dennis M. Mills. The historical development of cryogenically cooled monochromators for third-generation synchrotron radiation sources. *Journal of Synchrotron Radiation*, 7(2):53–60, March 2000.